RICE UNIVERSITY

Biomedical Nanocrystal Agents: Design, Synthesis, and Applications

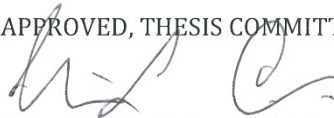by

Minjung Cho

A THESIS SUBMITTED
IN PARTIAL FULFILLMENT OF THE
REQUIREMENTS FOR THE DEGREE

Doctor of Philosophy

APPROVED, THESIS COMMITTEE
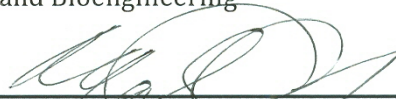
Vicki L. Colvin
Kenneth S. Pitzer-Schlumberger
Professor of Chemistry and Professor of
Chemical & Biomolecular Engineering,
Chair

John T. McDevitt
Brown-Wiess Professor of Chemistry
and Bioengineering

Michael S. Wong
Professor of Chemical and Biomolecular
Engineering and Chemistry

HOUSTON, TEXAS
April 2013

ABSTRACT

Biomedical Nanocrystal Agents: Design, Synthesis, and Applications

by

Minjung Cho

In these days, nanomaterials are applied in a variety of biomedical applications including magnetic resonance imaging (MRI), cell imaging, drug delivery, and cell separation. Most MRI contrast agents affect the longitudinal relaxation time (T_1) and transverse relaxation time (T_2) of water protons in the tissue and result in increased positive or negative contrast. Here, we report the optimization of r_1 ($1/T_1$) or r_2 ($1/T_2$) relaxivity dynamics with diameter controlled gadolinium oxide nanocrystals (2~22 nm) and iron based magnetic nanocrystals (4 ~33 nm). The r_1 and r_2 MR relaxivity values of hydrated nanocrystals were optimized and examined depending on their core diameter, surface coating, and compositions; the high r_1 value of gadolinium oxide was 40-60 $S^{-1}mM^{-1}$, which is 10-15 fold higher than that of commercial Gd (III) chelates (4.3~4.6 $S^{-1}mM^{-1}$). Moreover, *in vitro* toxicological studies revealed that polymer coated nanocrystals suspensions had no significant effect on human dermal fibroblast (HDF) cells even at high concentration. Towards multimodal imaging or multifunctional ability, we developed the iron oxide/QDs complexes, which consist of cores of iron oxide that act as nucleation sites for fluorescent QDs. The choice of variable QDs helped to visualize and remove large iron oxide materials in a magnetic separation.

Additionally, diluted materials concentrated on the magnet could be fluorescently detected even at very low concentration. The designed MRI or multifunctional nanomaterials will give great and powerful uses in biomedical applications.

Acknowledgments

First, I would like to express my gratitude to Prof. Vicki L. Colvin who is my advisor. She provided me great opportunities to explore the nanomaterial science and nanotechnology. Her guidance, support, and endless trust encouraged me to have valuable trial and errors, attitude toward science, and thoughts for scientific research. She gave me a lot of freedom to explore scientific questions and trials as well as to develop my own experiments with creativity. At various stages of my Ph.D. work, she taught me how to organize scientific thoughts, write scientific documents, and present research effectively.

I am very grateful to other members of my Ph.D. committee: Prof. John. T. McDevitt and Prof. Michael Wong for their guidance and time to support this dissertation work. I am also grateful to Dr. Paolo Decuzzi in the department of translational Imaging & nanomedicine at the Methodist Hospital Research Institute (TMHRI). He supported me to get important scientific results for my dissertation work and allowed me to do experiments at TMHRI as a visiting research fellow. He was very kind advisor and trying to understand what my researches are and how my researches go. I also thank to Prof. Robia Pautler in the department of Molecular Physiology and Biophysics, Baylor College of Medicine (BCM) for the collaboration of my research.

I was very lucky to come and have a graduate student life in colvin group at Rice. I would like to thank all of my group members. I enjoyed working with them, sharing scientific ideas, learning scientific skills each other. Specially, I was very

Contents

List of Figures

List of Tables

Chapter 1

Literature Review: The Preparation and Biomedical Applications of Inorganic Nanoparticles

1.1. Introduction

Nanotechnology is used to describe materials with a size below 100 nm and covers diverse fields including chemistry, material science, bioengineering, and even medicine. Nanotechnology makes use of the unique chemical and physical properties of nanoscale materials, which cannot be acquired in bulk state. In particular, magnetic iron oxide nanoparticles below 30 nm are superparamagnetic and exhibit high magnetization but have no residual magnetization in the absence of an external magnetic field.[1-5] This superparamagnetic behavior of iron oxide nanoparticles, combined with low toxicity, makes them useful as carriers for driving drugs to the specific target cells (targeted drug delivery) and is able to use in

multiplexed cell separation.[6] Iron oxide magnetic nanoparticles have widely used as contrast agents for magnetic resonance imaging (MRI). [7,8]

Among various imaging technologies, MRI is currently one of the most powerful imaging tools since it has several advantages including high spatial resolution, excellent contrast in soft tissue, non-usage of radioisotopes or X-rays. [9] It monitors the response of water protons to external magnetic field and visualizes the contrast in the image. MRI is a non-invasive method and provides real-time images of internal anatomy and physiology of living organisms. However, there is no little difference in normal and disease tissues in relaxation time, additional chemical supplements have been used for more accurate diagnosis. The most effective supplement is a contrast agent that accelerates T_1 or T_2 relaxation time.

The most widely used clinically MRI contrast agents are T_1 contrast agents using paramagnetic gadolinium (Gd) chelates.[10,11] In particular, Gd-DTPA is a popular agent whose applications are focused on detecting the disruption of the blood brain barrier (BBB), the degree of vascularity, and flow dynamics.[12] However, the Gd chelates have still very low relaxivity values ($4.3 \sim 4.6$ mM^{-1}S^{-1}), so a high dosage must be used for MR enhancement.[13] In recent years, gadolinum based nanoparticles could be good candidates for T_1 MRI contrast agents because the surface of nanoparticles contains a large number of metal ions with high magnetic moments. Gadolinium oxide (Gd_2O_3), gadolinium fluoride (GdF_3), and gadolinium phosphate ($GdPO_4$) nanoparticles have been applied as T_1 MRI contrast agents showing bright contrast.[14-21] In contrast, iron oxide nanoparticles induce a

shortening of T_2 relaxation time and show a darker image. For example, superparamagnetic iron oxide nanoparticles with biocompatible dextran coating exhibit large r_2 relaxivity ($\sim$200 mM^{-1}S^{-1}) and are used for tumor evaluations.[22,23]

Fluorescent labeling is also an important technique that has been widely applied to the cell and tissue imaging. Specially, semiconductor nanocrystals, referred as quantum dots (QDs) are well known as fluorescent labeling probes.[24-26] The important characteristics of QDs are high photoluminescence quantum yield (PLQYs, 20$\sim$80 %) comparing with fluorescent dyes, size tunable fluorescence spectra, and high photo stability. They allow for multiplex cell imaging and analysis using size tunable QDs.[27-30] Furthermore, QDs can be useful for *in vivo* cell imaging and targeting. [31,32]

The combination of different nanomaterials provides multifunctional biomedical applications such as multimodal imaging and simultaneous diagnosis and treatment.[33-36] For example, the combination of MRI contrast agent (iron oxide, gadolinium oxide) and fluorescent probe (QDs, fluorescent dye, or rare earth dopants) allows the detection of cancer through pre-MRI diagnosis and optical imaging during surgery. Moreover, the combination of magnetic nanoparticles and sensing probes can manipulate the carriers under the external magnetic field and visualize the disease area for the treatment simultaneously. In this chapter, the preparation of various nanomaterials and their biomedical applications are discussed. [33-36]

1.2. Preparation and properties of inorganic nanoparticles

1.2.1. Gadolinium based nanoparticles

Since Gd^{3+} has seven unpaired electrons with a large magnetic moment, most T_1 contrast agents are Gd^{3+} based agents.[35] Due to the toxicity of Gd^{3+} ion, the contrast agents are in the form of complexes with chelates, which are most stable and less toxic. Due to interaction with blood, Gd-chelates have short life spans in the body and circulate in a non-specific manner. Moreover, the relaxivity (r_1) of Gd-chelates is relatively low (4.6 $mM^{-1}S^{-1}$) at 1.5 T.[12,37,38] Very recently, gadolinium based nanoparticles such as gadolinium oxide (Gd_2O_3), gadolinium fluoride (GdF_3), and gadolinium phosphate ($GdPO_4$) are developed as new T1 contrast agents with high relaxivity.[19,39-43]

Ion	Configuration		Magnetic moment
	3d	4f	
Transition metal ion $^{24}Cr^{3+}$	↿ ↿ ↿ — —		3.88
$^{25}Mn^{2+}$	↿ ↿ ↿ ↿ ↿		5.92
$^{26}Fe^{3+}$	↿ ↿ ↿ ↿ ↿		5.92
$^{29}Cu^{2+}$	⇅ ⇅ ⇅ ⇅ ↿		1.73
lanthanide metal ion $^{63}Eu^{3+}$		⇅ ↿ ↿ ↿ ↿ ↿ ↿	3.4
$^{64}Gd^{3+}$		↿ ↿ ↿ ↿ ↿ ↿ ↿	7.94
$^{66}Dy^{3+}$		⇅ ⇅ ↿ ↿ ↿ ↿ ↿	10.65

Figure 1-1 Electron configuaration and magnetic moment of metal ions, adapted from ref. [35]

The Gd_2O_3 nanoparticle-based agents have been prepared with small core sizes (< 5 nm) and stabilizing biocompatible coatings of poly (ethylene glycol) (PEG)[19,43], dextran[39], and silica[40] since non-coated nanoparticles are pH unstable and are not very water-soluble. The Fortin and coworkers prepared ultra-small gadolinium oxide nanoparticles stabilized by PEG.[43] The resulting Gd_2O_3 nanoparticles had uniform size of 3 nm and they are well soluble in water. The relaxivity was twice as high as that of Gd-DTPA. The Lee and coworkers also explored the ultrasmall Gd oxide nanoparticles (< 2 nm) that had a high r_1 value and obtained better contrast *in vivo* MR imaging.[19] Moreover, dextran stabilized small gadolinium oxide nanoparticles were synthesized by the reduction and co-precipiation reaction of gadolinium salt ($GdCl_3$) in aqueous media in the presence of dextran as a stabilizer.[39] Due to their large hydrodynamic size (> 50 nm), it is hard to apply them as MRI contrast agents due to the particle agglomeration and polydispersity.

GdF_3 (or GdF_3/LaF_3) nanoparticles were investigated as T_1 contrast agents with the surface functionalization with 2-aminoethyl phosphate group or negatively charged citrate group.[41] Dextran coated $GdPO_4$ nanoparticles were synthesized by a hydrothermal process in the presence of dextran.[42] These Gd based nanoparticles showed strong positive contrast effect. The Table 1-1 shows the T_1 contrast agents based on the gadolinium based nanoparticles.

Table 1-1 T_1 contrast agents based on gadolinium based nanoparticles, adapted from ref. [35]

Name	Core Material	Surface	Diameter of Core [nm]	Hydrodynamic Diameter [nm]
Dextran-SPGO	Gd_2O_3	Dextran		26
PEG-Gd_2O_3	Gd_2O_3	PEG	3	
GadoSiPEG	Gd_2O_3	Polysiloxane-PEG	2.2	3.3
			3.8	5.2
			4.6	8.9
GdF_3:cit	GdF_3	Citric acid		129.3
GdF_3/LaF_3:AEP	GdF_3/LaF_3	2-Aminoethyl Phosphate		51.5
PGP/dextran-K01	$GdPO_4$	Dextran		23.2

1.2.2. Iron oxide magnetic nanoparticles

Superparamagnetic iron oxide nanoparticles (SPIOs) can serve as MRI contrast agents in diagnosis, heat mediators in hyperthermia treatments, and colloidal carriers for drug delivery targeted at cancer.[4,5,44-46] Among several types of iron oxide, magnetite (Fe_3O_4) or maghemite(γ-Fe_2O_3) are widely used for biomedical application because they include high magnetic moments, have chemical stability in physiological conditions, and low toxicity.[4]

The simplest way of synthesizing iron oxide nanoparticles is the co-precipitation, which involves the simultaneous precipitation of Fe^{2+} and Fe^{3+} ions in basic aqueous solution.[47,48] After preparation, the iron oxide nanoparticles are usually coated with hydrophilic polymers such as dextran in order to guarantee their stability. However, the resulting iron oxide nanoparticles have low crystallinity and large polydispersity. Another method of synthesis is water-in-oil microemulsions. [49] In this method, a certain amount of water is added to a large

amount of non-polar solvent such as oil and homogeneous droplets of water are stabilized by amphiphilic surfactants. However, limited reaction temperature leads to low crystallinity and low product yield.

In the last, iron oxide nanocrystals were synthesized by high temperature thermo-decomposition of organometallic precursors in the presence of organic surfactant and solvent.[50,51] This method can control the nucleation and growth kinetics of the particles and offer high crystallinity, particle monodispersity, and high yield. These iron oxide nanoparticles can be functionalized with biocompatible coating including dextran or PEG polymers for biomedical applications.

1.2.3. Semiconductor nanocrystals (quantum dots)

Quantum dots (QDs) are inorganic semiconductor fluorophores and have emerged as sensing probes for biomedical applications.[26,27,32,52,53] The optical properties such as absorption and emission spectra can be tunable from ultraviolet (UV) to near infrared (NIR) by confining the electrons in variable sizes and energy band gaps.[53-58] For example, CdSe QDs were synthesized by high-temperature decomposition of organometallic precursors in the presence of organic surfactants and solvents. [59-62] Small CdSe QDs (~2 nm diameter) show blue fluorescence emission from 380 to 440 nm, whereas, large QDs (4~6 nm) emit red fluorescence from 605 to 630 nm.[24,63] QDs have high brightness and photo stability compared to the fluorescent organic dye. Furthermore, the PLQY can be enhanced to 80 % by the deposition of a shell of higher band-gap QDs (e.g. ZnS or CdS) on the CdSe core.[64] By

over coating with biocompatible polymers, QDs are widely used for biomedical imaging as a fluorescent sensing probe *in vitro* or *in vivo*. [24,25,32,53,65-67]

1.2.4. Multifunctional magnetic-fluorescent nanoparticles

The combination of a magnetic and a fluorescent component may provide a new multifunctional nanomaterial with a broad range of biomedical applications. The multifunctional magnetic-fluorescent nanomaterials have either organic dyes or QDs as fluorescent domains and iron oxide or iron based magnetic nanoparticles as magnetic domains. There are three types of strategies to prepare multifunctional nanomaterials: 1) the encapsulation of the magnetic and fluorescent domains inside one domain; 2) the direct reaction between the fluorescent and magnetic domains using ligand linking; 3) the seed mediated inorganic synthesis.[36]

First, in encapsulation, the magnetic and fluorescent domains are embedded together in a nano or a micro-sized shell. The encapsulating materials have been explored from polypeptides to polyelectrolytes, styrene/acrylamine, and silica materials.[68-71] For example, CdSe/ZnS QDs (3-5 nm) and Fe_3O_4 nanoparticles (6 nm) were embedded in the meso-porous silica beads (3-5 *u*m diameter).[70] This method is relatively simple and suitable for *in vitro* applications,[72-74] but the resulting materials are relatively large (>100 nm) and easily aggregated. In addition, magnetic nanoparticles quench the fluorescence of QDs through electron energy transfer when packed together inside the shell.[75,76]

Second, a magnetic nanoparticle is linked covalently to the fluorescent probe.[77-82] Simply, hydroxyl-functionalized iron oxide nanoparticles are covalently linked to the NHS-Cy5.5 fluorescent dye by means of amino-PEG silane molecules.[78] Magnetic nanoparticles are also conjugated with fluorescent dyes or QDs via m-2-3-dimercaptosuccinic acid (DMSA) ligand or dodecylamine (DDA) cross linkers.[77,80] This method can keep the particle size small but is limited by low product yield and the complicated functionality of linkers.

The recent reported method for multifunctional magnetic-fluorescent nanoparticles is based on the direct synthesis via seed mediation. In this method, QDs nucleate and grow directly on the surface of magnetic nanoparticles including iron oxide.[83-90] It can be extended to the preparation of various hybrid nanostructures including metal-semiconductor, metal oxide-metal, and metal oxide-semiconductor and it offers the products with small size, homogeneous structure, and tunable stoichiometry.[91-96] The Figure 1-2 shows the summary of types of multifunctional magnetic-fluorescent nanomaterials.
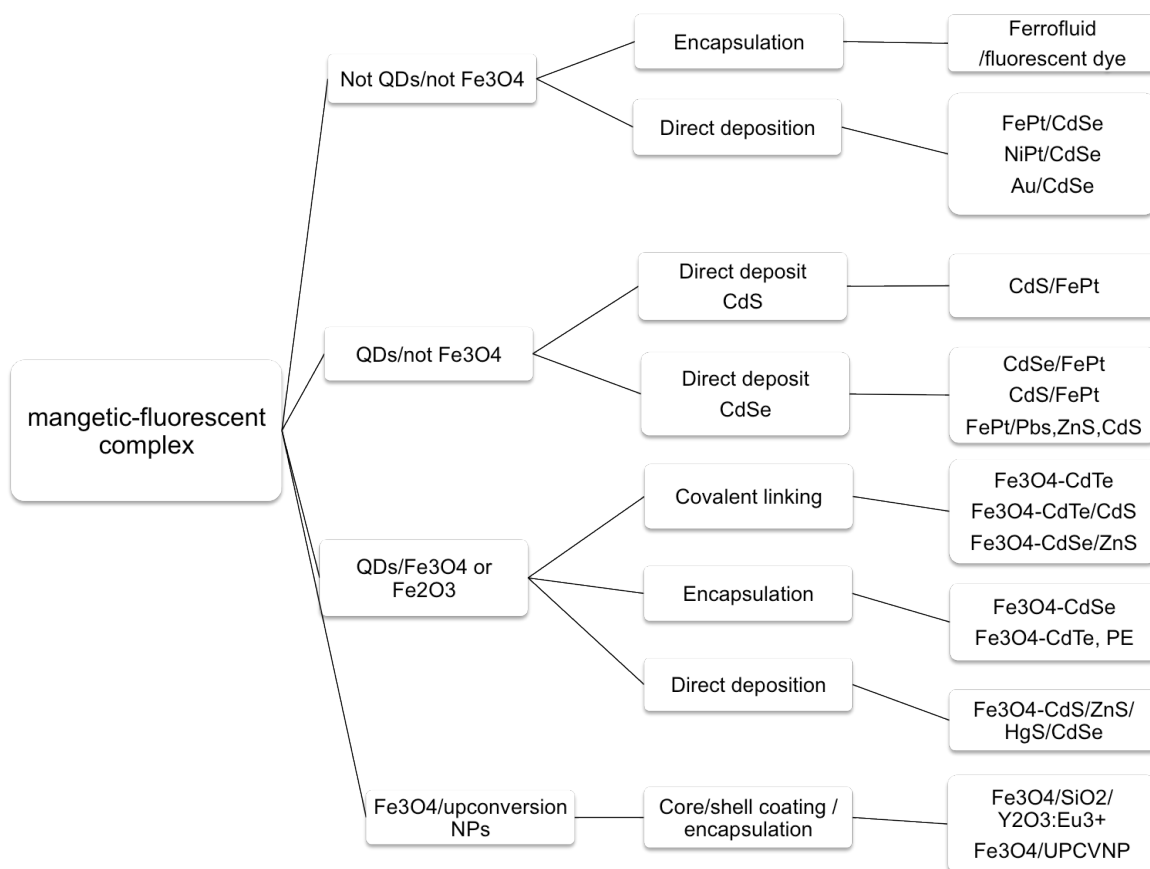
Figure 1-2 The summary of multifunctional magnetic-fluorescent nanocomposites

1.3. Biomedical applications of inorganic nanoparticles

1.3.1. Magnetic resonance imaging (MRI)

1.3.1.1. Basic principle of MRI contrast agents

Magnetic resonance imaging (MRI) is currently one of the most powerful and non-invasive diagnostic tools and is based on nuclear magnetic resonance (NMR) with the relaxation of proton spins in a magnetic field.[97-99] The contrast

enhancement in MRI occurs from the interaction between the contrast agent and neighboring water molecules. Adding contrast agents help to get more specific and enhanced contrast images in MRI. [37,38]

Once the nuclei of protons is exposed to a strong magnetic field, their spins align in a parallel or antiparallel direction to the field.[35,100] When inducing by a resonant lamor frequency ($\omega_0 = \gamma B_0$, where ω_0 = lamor frequency, γ= gyromagnetic ratio, and B_0= magnetic field), the nuclei absorbs the electromagnetic energy and excites to the antiparallel state (Figure 1-3 (a)). As antiparallel spin population increases, the longitudinal magnetization (M_z), which is parallel to the external magnetic field, decreases and transverse magnetization (M_{xy}) is generated (Figure 1-3 (b)). When removing lamor frequency, the nuclear spin returns to their initial state. It is called as a relaxation. There are two relaxation pathways. First is longitudinal magnetization recovery (T_1 relaxation). T_1 is the time required for longitudinal magnetization recovering to 63 % of the initial state (Figure 1-3 (c)). The second calls transverse magnetization decay (T_2 relaxation). It involves the induced magnetization on the perpendicular plane disappearing by the dephasing of spins (Figure 1-3 (d)). T_2 is the time required for transverse magnetization to drop to 37 % of its initial magnitude.
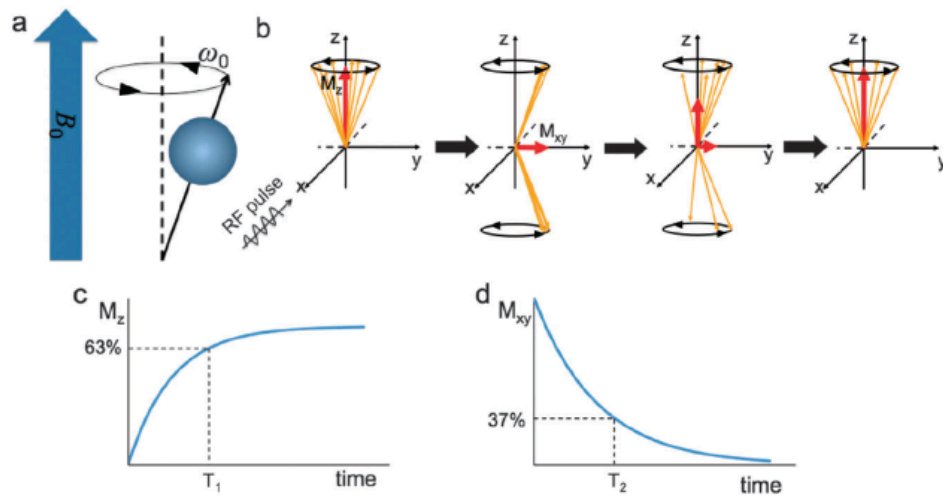
Figure 1-3 Principles of magnetic resonance imaging (MRI).

(a-b) the process for the relaxation (c) T_1 relaxation (d) T_2 relaxation, adapted from ref. [35,100]

Contrast agents are used to improve the visualization of substances by accelerating their relaxation times. [35] The relaxivity (r_i) is defined as the increase in relaxation rate of water protons (R_i) per concentration of agents or the slope of a plot of ($1/T_i$-$1/T_o$) versus the concentration of agents (mM).

$$R_i = \frac{1}{T_i} = \left(\frac{1}{T_o}\right) + r_i C$$

where R_i is the relaxation rate of the aqueous solution, T_o is the relaxation time of water without contrast agent, T_i is the relaxation time in the presence of contrast agent, C is the concentration of contrast agent (mM), and r_i is its relaxivity ($S^{-1}mM^{-1}$).

1.3.1.2. Gd_2O_3 based T_1 MRI contrast agents

The paramagnetic gadolinium ions on the surface of Gd_2O_3 nanoparticles make a shorten T_1 relaxation time. The Bridot and coworkers reported that gadolinium oxide nanoparticles act as T_1 contrast agents.[40] They synthesized Gd_2O_3 nanoparticles with diameters of 2.2, 3.8, and 4.6 nm, coated with dye doped silica shells and evaluated the effect of the size of Gd_2O_3 core on the T_1 MR relaxivity. The r_1 relaxivities of the Gd_2O_3 nanoparticles with 2.2, 3.8, and 4.6 nm core sizes were 8.8, 8.8, and 4.4 $mM^{-1}S^{-1}$ at 1.5 T, respectively. These r_1 values are higher than the value of Gd-DTPA (4.1 $mM^{-1}S^{-1}$).[12,37,38] Moreover, the dye-doped silica shell acts as a fluorescent probe as well as prevents the release of toxic Gd^{3+} ion to the outside. They showed the use of biocompatible gadolinium oxide nanoparticles (GadoSiPEG2C) as *in vivo* dual MRI and fluorescence imaging (Figure 1-4).[40] The MRI and fluorescence imaging after injection revealed that the GadoSiPEG2C particles accumulated in the kidney and bladder.
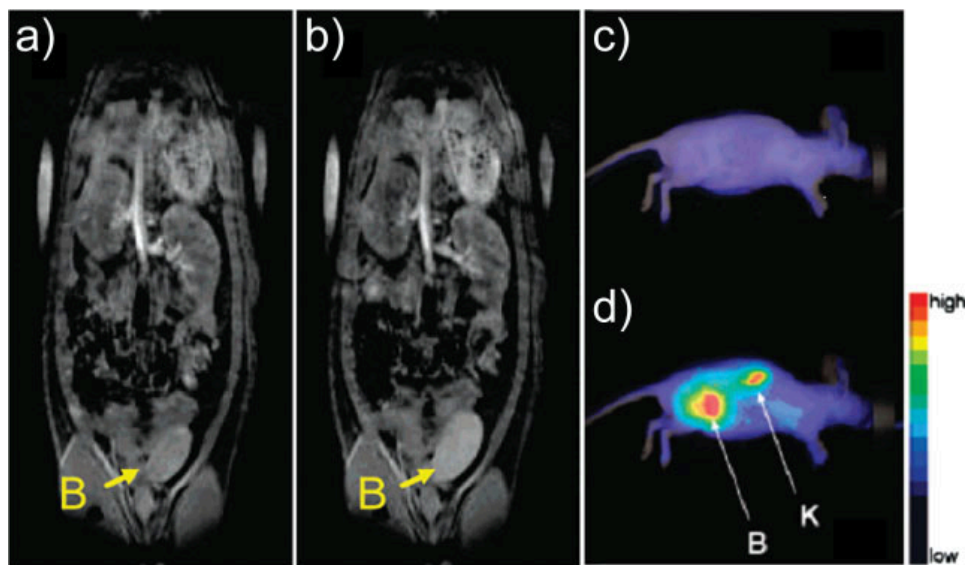
Figure 1-4 T_1 weighted MR images and fluorescence imaging

T_1-weighted images of rat a) before and b) 1 h after injection of GadoSiPEG2C; Fluorescence reflectance imaging of a mouse c) before and d) 3 h after the injection of GadoSiPEG2C (B: bladder, K: kidney), adapted from ref.[40]

In 2009, the Lee and coworkers prepared ultra-small gadolinium oxide nanoparticles with an average diameter of 1.0 nm.[19] They provided the r_1 relaxivity value of 9.9 mM^{-1}S^{-1}, which is much higher than those of Gd (III) chelates (4.1 mM^{-1}S^{-1}) at 1.5 T.[37,38] The Gd (III) ions in the particles accelerates the longitudinal relaxation of water proton, providing large r_1 values. They also addressed the size effects on relaxivity and took *in vivo* MR images of a rat with brain tumor using d-glucuronic acid coated gadolinium oxide nanoparticles. Figure 1-5 showed *in vitro* cell toxicities using different cell lines and MR contrast enhancement images of brain tumor after injection. Moreover, Figure 1-6 monitored *in vivo* MR images of both kidney and bladder after vein injection of the sample.
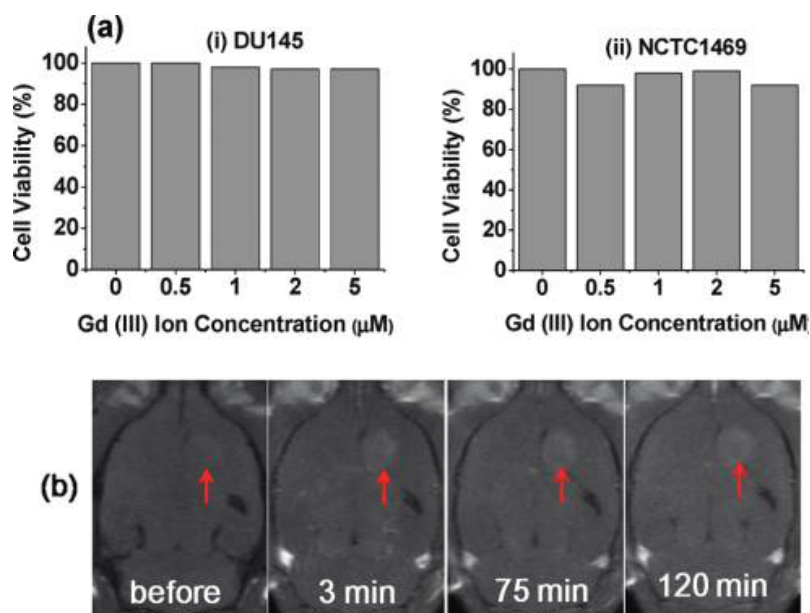
Figure 1-5 *In vitro* cytotoxicity and T_1 MR images of a brain tumor

(a) *In vitro* cytotoxicity test of (i) DU145 and (ii) NCTC1469 cell lines. (b) *In vivo* T_1 MR images of a brain tumor of a rat, adapted from ref. [19]
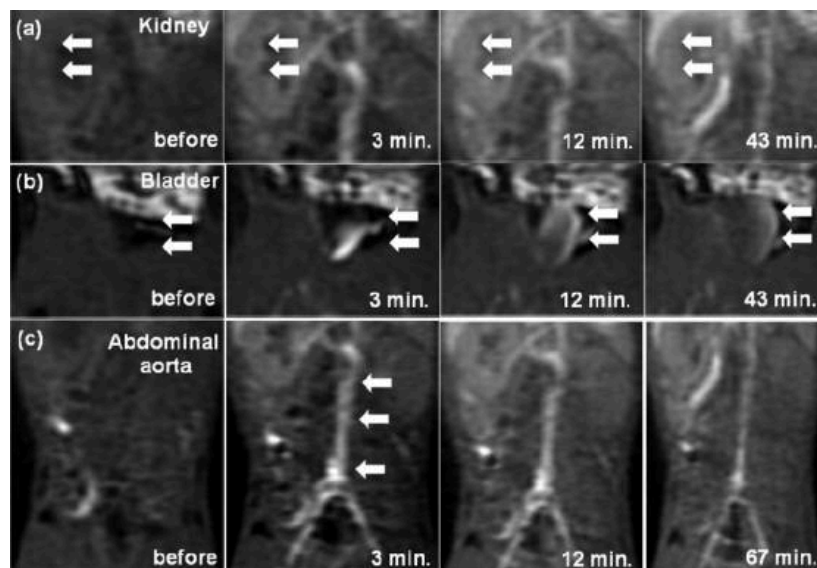
Figure 1-6 *In vivo* T_1 MR images of a rat with a brain tumor.

(a) Kidney, (b) bladder contrast enhancement, and (c) blood pool effect, adapted from ref.[19]

Table 1-2 shows the summary of Gd_2O_3 nanoparticle based T_1 MRI contrast agents. The size uniformity of nanoparticle, low relaxivity, and the dependences of size and surface coating on the relaxation are still undergoing researches. For future clinical diagnosis and active target molecular imaging, the long-term stability, long blood circulation time, and bio-distribution of Gd_2O_3 nanoparticles are essential to achieve ideal MRI contrast agent.

Table 1-2 The summary of r_1 relaxivities of gadolinium oxide T_1 contrast agents

Sample	Coating	Size (nm)	r1 ($mM^{-1}S^{-1}$)	B_0 Field (T)	Reference
Gd-DTPA(Magnevist)	DTPA	-	4.1	1.5	ref[12,37,38]
Gd-DTPA-BMA (Omniscan)	DTPA-BMA	-	3.84	1.5	ref[37,38]
Gd-TETA	TETA		2.1	1.5	ref[38]
PEG Gd_2O_3	PEG	3	9.4	1.5	ref[43]
PEG Gd_2O_3	PEG-dialysis	3-5	(3 days) 22.8 (6 days)	1.5	ref[17]
Gd_2O_3	D-glucuronic acid	1.5	9.9	1.5	ref[19]
Gd_2O_3	PEG-silane	2.2	8.8	7	ref[40]
Gd_2O_3	PEG-silane	3.8	8.8	7	ref[40]
Gd_2O_3	PEG-silane	4.6	4.4	7	ref[40]
Gd_2O_3	PEG-silane	30	0.1	7	ref[43]
Gd_2O_3 nanorod	APS silinization	2.5/18	1.5	9.4	ref[101]
Gd_2O_3	DEG	3	2.64	1.5	ref[102]
Gd_2O_3	DEG	60	2.22	1.5	ref[102]
Gd_2O_3	DEG	75	2.05	1.5	ref[102]
Gd_2O_3	DEG	105	1.86	1.5	ref[102]
Gd_2O_3	SiO2	10	3.48	1.5	ref[103]

1.3.1.3. Iron oxide based T_2 MRI contrast agents

Iron oxide nanoparticles are superparamagnetic, losing their magnetization in the absence of an external magnetic field. On the other hand, when applying an external magnetic field, they exhibit strong magnetization, which induces inhomogeneous local magnetic field and activates the dephasing of protons. As a result, iron oxide nanoparticles make a shorten T_2 relaxation time and produce a decreased signal in T_2 weighted MR image.[35]

The iron oxide nanoparticles are classified by their sizes; 1) micrometer-size paramagnetic iron oxide (MPIO, < 5 um); 2) superparamagnetic iron oxide (SPIO, < 100 nm); 3) ultra small superparamagnetic iron oxide (USPIO, < 40 nm).[35] The SPIO or USPIO is widely used as MRI contrast agent.[104] Due to the large magnetic moments, SPIO or USPIO can induce local magnetic field under the external magnetic field and thus yield an enhancement in the image. USPIO with diameters less than 40 nm have been clinically investigated as contrast agents that accumulate at the margins of brain tumors and offers prolonged delineation due to lower diffusion from tumor sites.[105]

The detection of lymph nodes is critical for checking an accurate tumor stage and planning a subsequent therapy. Since USPIO is very small (< 40 nm), they can travel through blood vessels and transport to lymph nodes through lymphatic vessels.[105,106] Figure 1-7 (b) showed the lymph-node metastases in patients with prostate cancer using USPIO. A SPIO or USPIO based T_2 contrast agent leads to

contrast enhancement of tumors as well as conjugation with biological target probes, antibodies, and other imaging probes. Therefore, iron oxide T_2 contrast agents can be used for target specific *in vivo* MR imaging and tracking of cells.
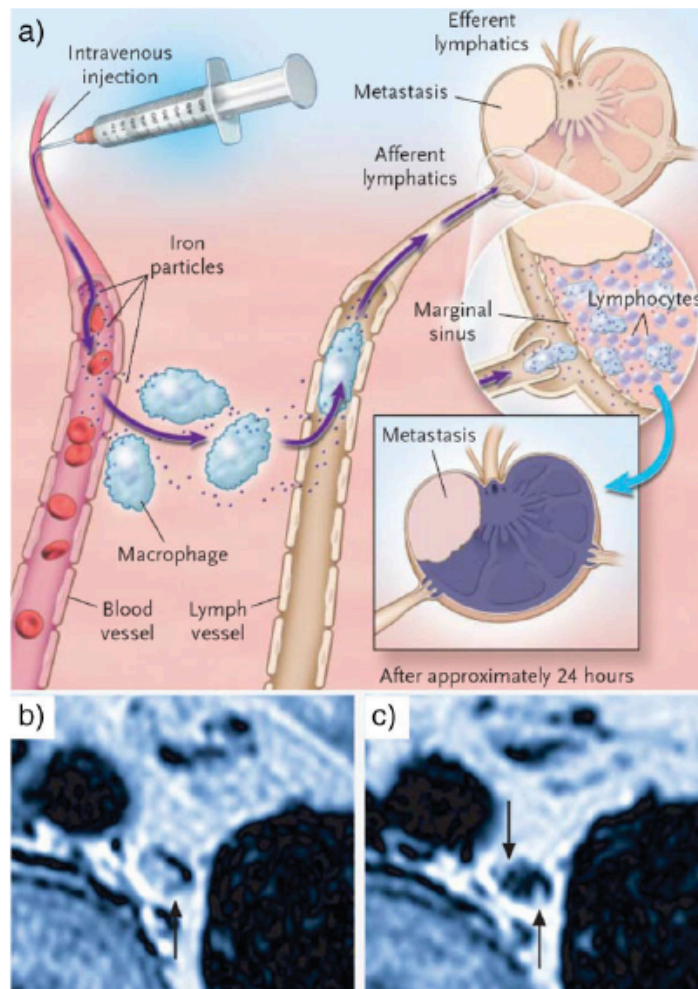
Figure 1-7 MR images of a metastatic lymph node using USPIO

(a) Schematic diagram of an action of USPIO, (b) MR images of a metastatic lymph node and c) after USPIO, adapted from ref.[105,106]

1.3.2. Imaging and sensing

1.3.2.1. Cellular labeling and sensing

Fluorescence imaging is widely used in clinical diagnosis. The Alivisatos and coworkers established the utility of QDs for fluorescent labeling.[25] The 3T3 mouse fibroblast cell was fluorescently labeled using two different CdSe/CdS core/shell nanocrystals (2 nm green QDs and 4 nm red QDs).[25] Figure 1-8 shows that the nucleus was labeled with green QDs and f-actin filaments were labeled with red QDs.[25]
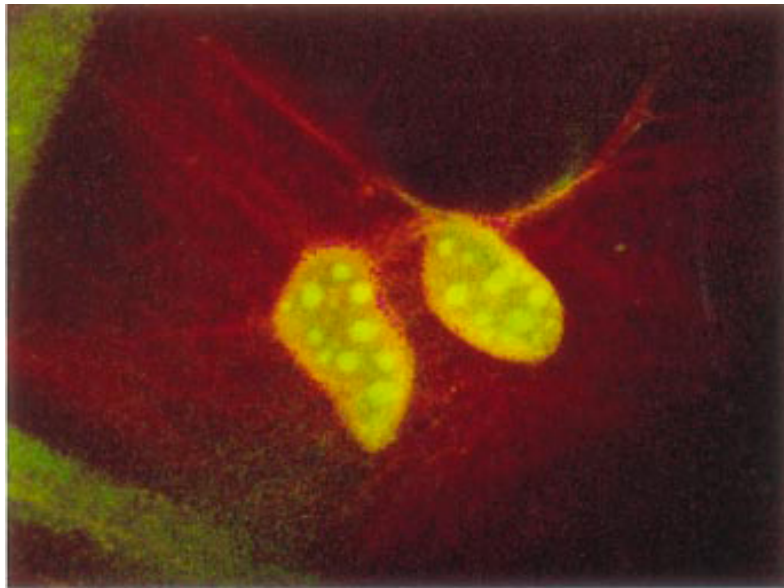
Figure 1-8 Cross section of a dual-labeled sample with mouse 3T3 fibroblast cell, adapted from ref.[25]

1.3.2.2. Tumor targeting and sensing

Antibody-conjugated QDs have allowed the real-time tracking of single molecule on the surface of living cells with high sensitivity. The Nie and coworkers reported the development of bio-conjugated QDs probes suitable for *in vivo* targeting and imaging of cancer cells.[32] They examined how functional groups on the QD probe affect targeted *in vivo* imaging. Figure 1-9 compared *in vivo* images from three types of QDs with COOH, PEG, and PEG_PSMA antibody. With COOH probe, no tumor signal was observed and only weak tumor signal was detected with PEG probe (passive targeting). When using PEG-PSMA antibody conjugated QD probe (active targeting), the high tumor signal was shown. This result shows that the active tumor targeting using tumor-specific ligand is the most efficient probe.

They also explored *in vivo* imaging with multicolor QDs-encoded micro-bead. The 0.5-μm polymer beads were doped with green, yellow or red QDs and they were injected into a mouse at three different locations. Three different QDs encoded beads were fluorescently detected simultaneously in a mouse (Figure 1-10). Approximately 1,000 of the QD-labeled cells were injected on the right flank of a mouse, while the same number of GFP-labeled cells was injected on the left flank.
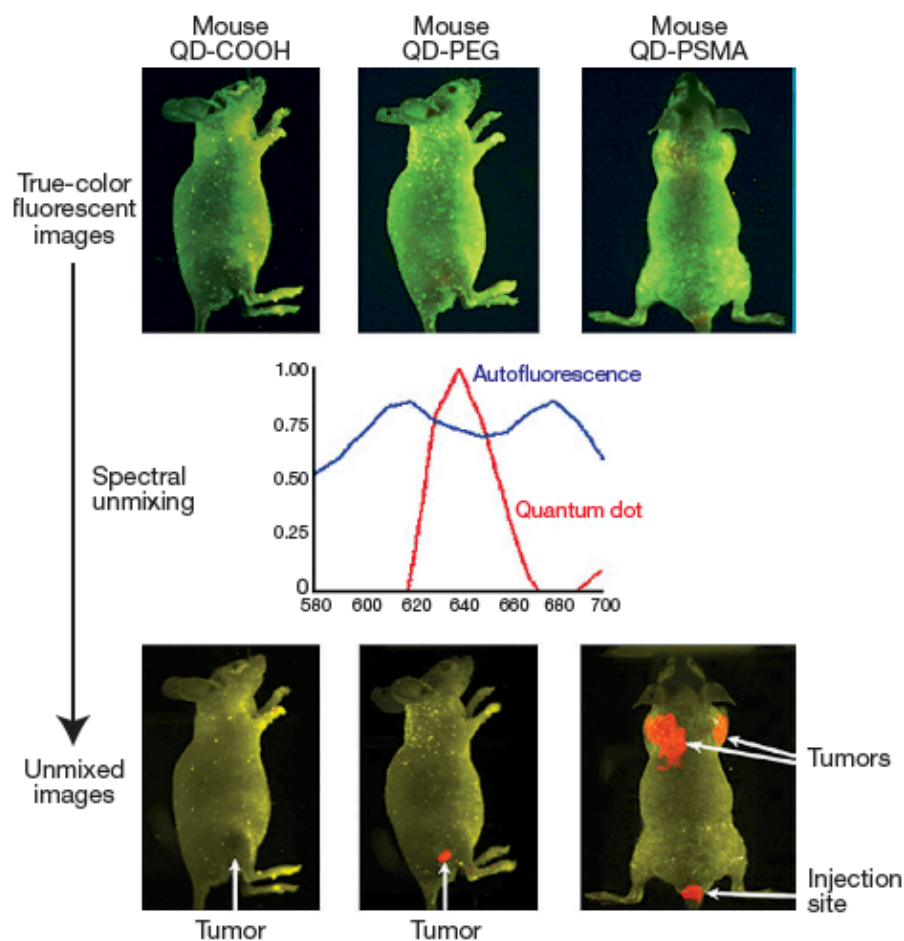
Figure 1-9 *In vivo* fluorescence images of tumor-bearing mice using QD probes

QD probes with carboxylic acid groups (left), PEG groups (middle) and PEG-PSMA Ab conjugates (right); A color image (top), two fluorescence spectra from QD and animal skin (middle), and a spectrally resolved image (bottom) were obtained from the live mouse models bearing C4-2 human prostate tumors (0.5–1.0 cm in diameter). The site of QD injection was observed as a red spot on the tail, adapted from ref. [32]
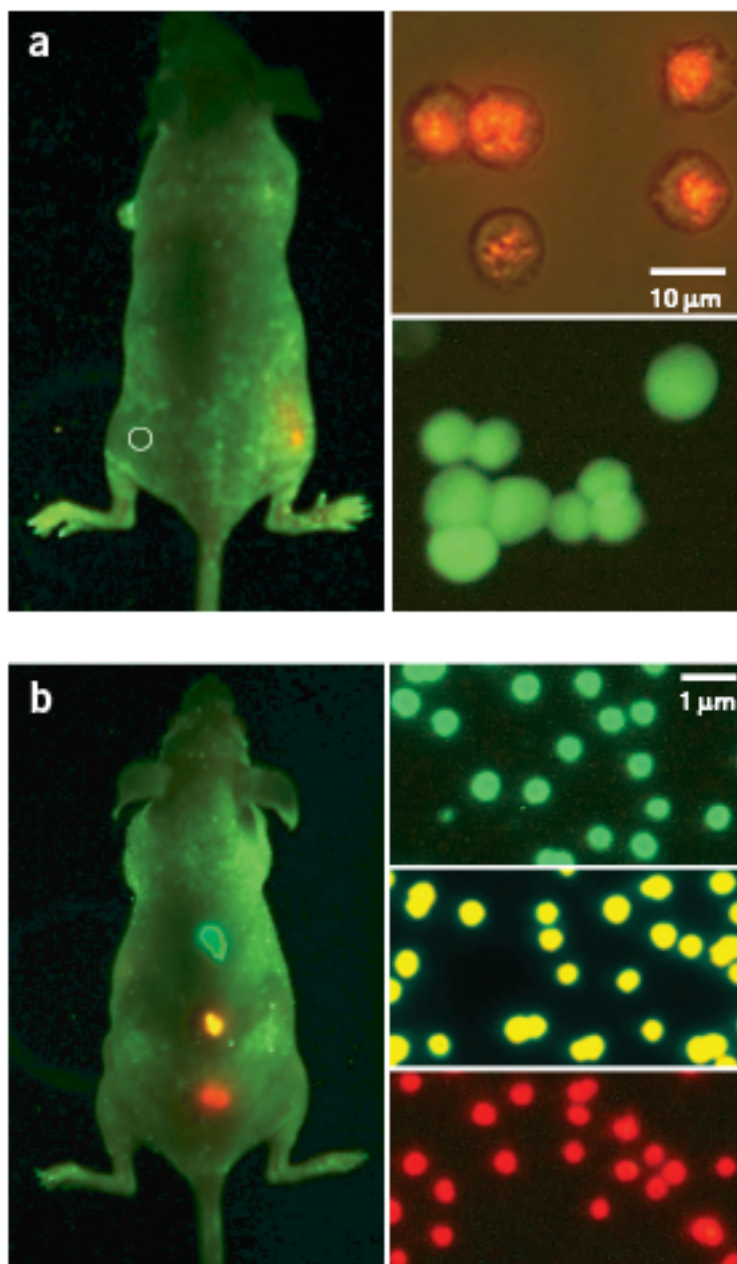
Figure 1-10 Sensitivity and multicolor capability of QD imaging in live animals.

The comparison between QD-tagged and GFP transfected cancer cells (a) and simultaneous *in vivo* imaging of multicolor QD-encoded microbeads (b) The right-hand images show QD-tagged cancer cells (orange, upper) and GFP-labeled cells (green, lower), adapted from ref. [32]

Multifunctional imaging and separation

Figure 1-11 shows the biomedical applications of multifunctional magnetic-fluorescence nanocomposites via different routes. The popular applications are multimodal imaging, multiplexed cells separation, and targeted drug delivery. [36]
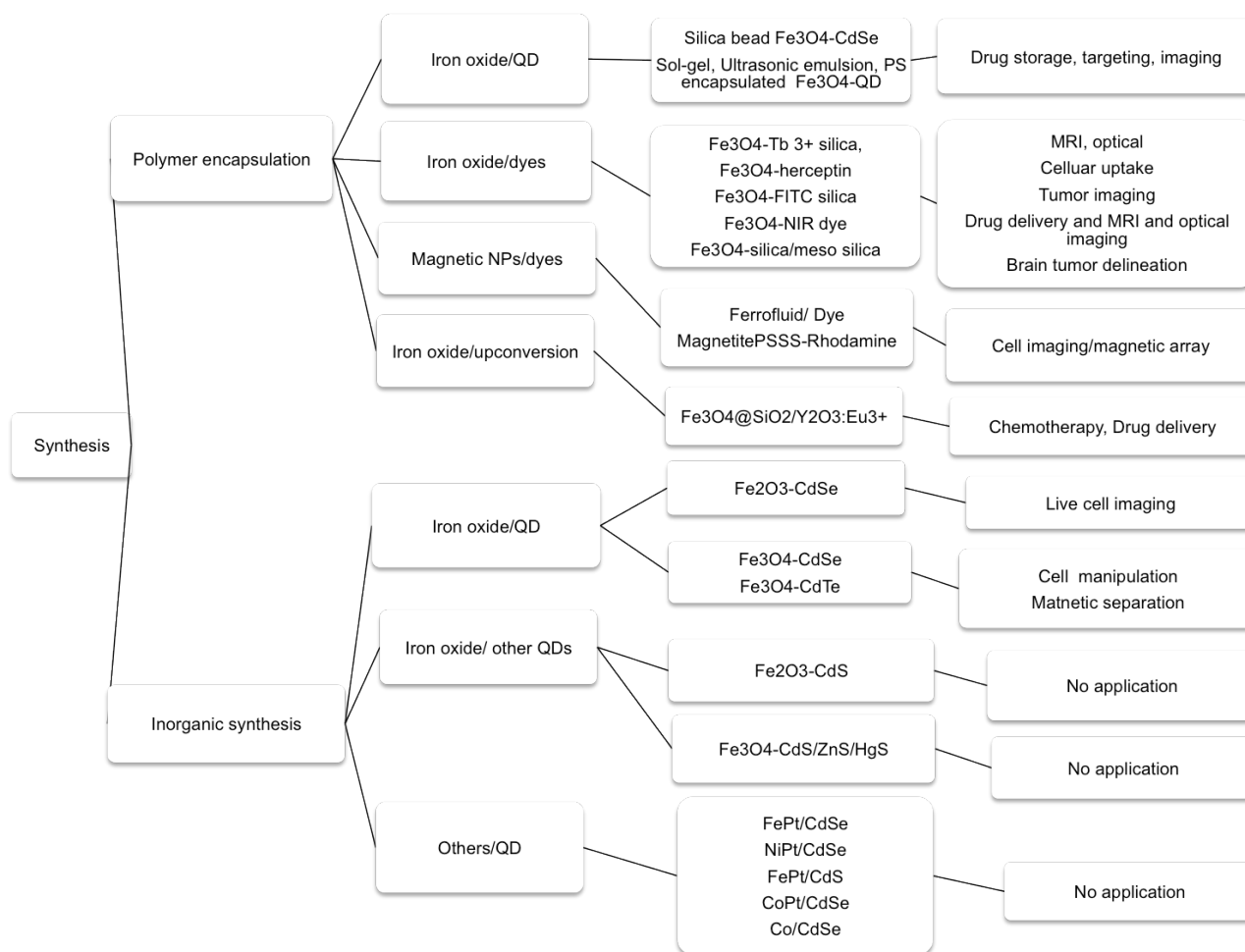
Figure 1-11 Biomedical applications of magnetic-fluorescence complexes.

1.3.2.3. Multimodal imaging

The popular multimodal imaging probe is the superparamagnetic iron oxide nanoparticles coupled with fluorescent organic dyes. The cross-linked iron oxide nanoparticles (CLIO) have been used for *in vivo* as well as *in vitro* MR imaging. The Josephson and coworkers developed multimodal imaging probe consists of CLIO conjugated with NRI fluorescent dye.[81] The optical imaging in the near IR (NIR) range from 700 to 900 nm allows the light to penetrate several centimeters into the tissue and minimizes the auto-fluorescence of tissue. By injection of this probe into nude mice, the lymph nodes were darkened on MRI and detected by NIR fluorescent imaging (NIRF) at the same time (Figure 1-12).

The Mulder and coworkers prepared quantum dot with paramagnetic Gd^{3+} coating in PEG lipids.[107] The *in vitro* MR and fluorescent imaging capabilities of paramagnetic QDs (pQDs) were demonstrated for human umbilical vein endothelial cells (HUVECs). Figure 1-13 shows the fluorescence imaging and T_1 MR image of cells with RGD-pQDs and pQDs. The multimodal imaging probes could potentially map the lymph nodes or tumors with MRI prior to surgical resection and give a fluorescent imaging guide during surgery.

Figure 1-12 MR and NIRF images from tissues of mice injected with Cy5.5-CLIO
(A) MR enhancement of lymph nodes with ax) axillary and br) brachial. (B) Contrast enhanced coronal image of the axillary node. (C) white light and (D) NIRF images, showing intense regions of NIRF in axillary and brachial nodes, adapted from ref. [81]
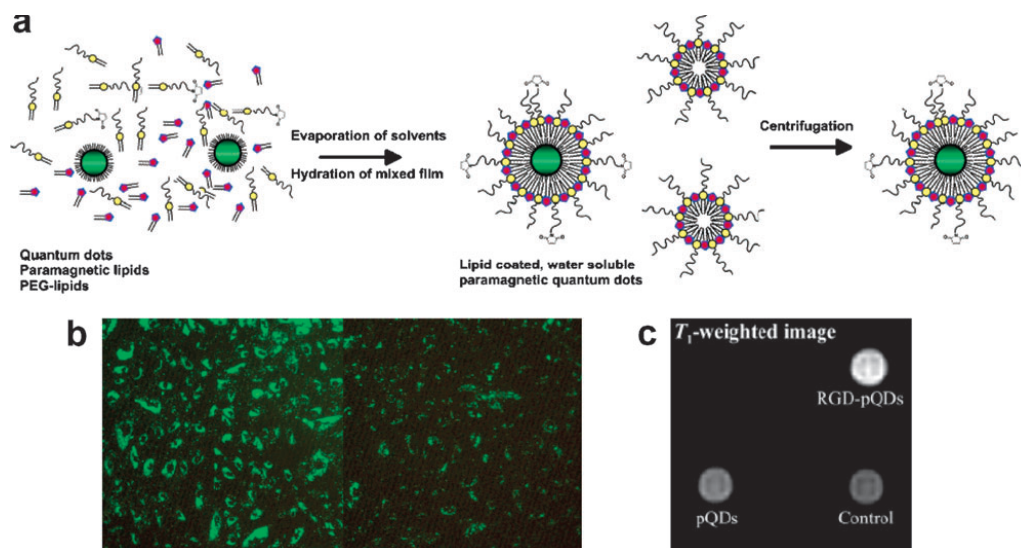
Figure 1-13 pQDs and their fluorescence and MR imaging

(a) Schematic diagram of the preparation of QDs with a paramagnetic Gd (III) coating. (b) Fluorescence imaging of HUVEC incubated with RGD-pQDs and bare pQDs. (c) T_1-weighted image of cells incubated with RGD-pQDs, pQDs, or without contrast agent, adapted from ref. [107]

1.3.2.4. Magnetic enrichment, manipulation, and separation

The enrichment, manipulation, and separation of different biomolecules including enzymes, proteins, and genes, which are present in a blood are important for the early diagnosis and detection of disease.[36] Moreover, the manipulation of tumor in tissue is crucial for the treatment. A multifunctional magnetic-fluorescent nanoprobe would be able to operate the enrichment of specific target molecules or cells by the application of external magnetic field. At the same time, fluorescent domain would act as a sensing code to distinguish target molecules. For example, silica/iron oxide/fluorescein (FITC) nanocomposites were functionalized with anti-

CD-10 antibody and specifically targeted with floating SP tumor cells (Figure 1-14).[108] By applying an external magnetic field, the tumor cells were moved to the area where the magnet was located.
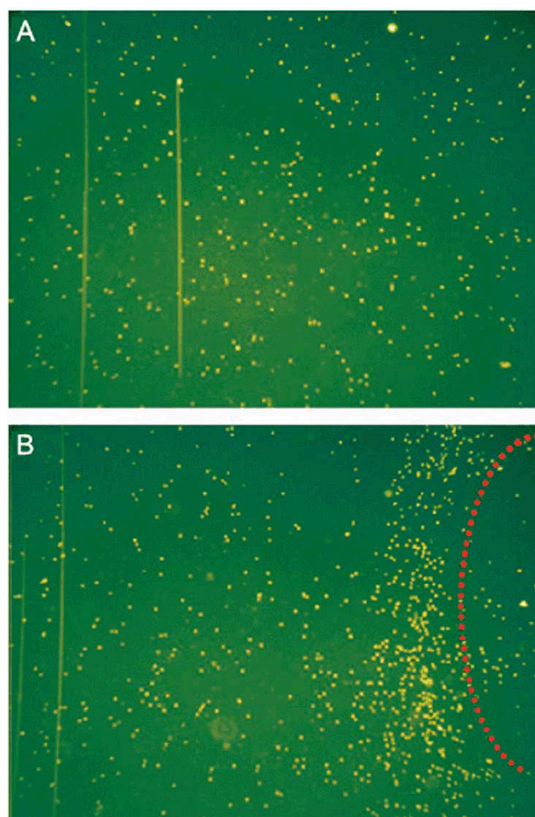
Figure 1-14 Magnetic-fluorescent nanocomposites for cell separation

SP2/0 floating cells have been labeled with silica coated $CoFe_2O_4$–FITC NPs. Optical microscopy images taken (A) before and (B) after applying an external magnetic field show how the cells moved under the magnetic attraction, adapted from ref. [108]

Recently, using Fe_3O_4/CdSe@GSH nanoparticles, the Xu and coworkers demonstrated the intracellular manipulation by applying a magnetic field (Figure 1-15).[109] The Fe_3O_4/CdSe@GSH nanoparticles were mainly distributed in the cytosol

without magnetic field. But after applying a strong magnet for 8 hours, the nanoparticles were aggregated on the side of the cell nearest the magnet. This intracellular manipulation can be used to move and control the tumor sites for the treatment.
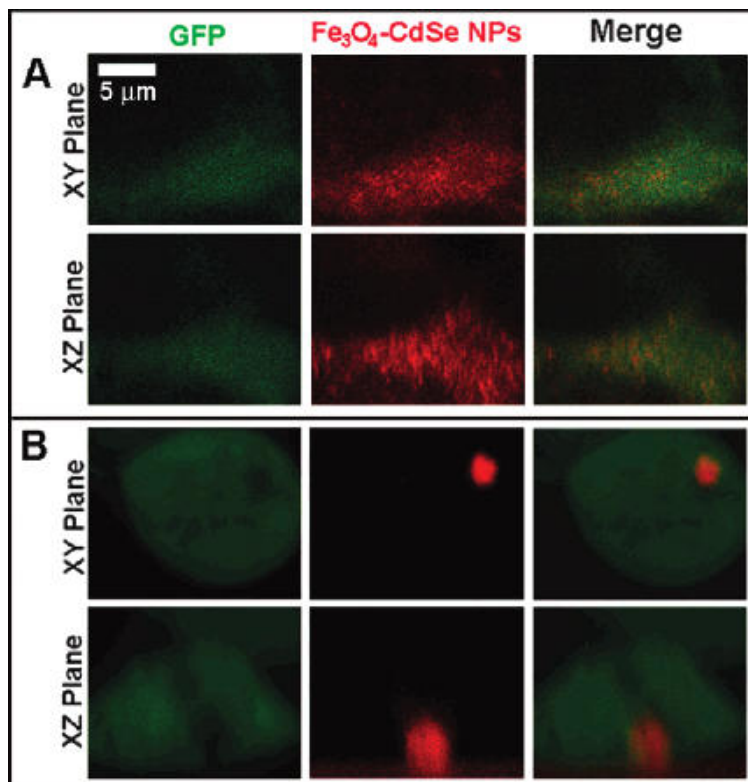
Figure 1-15 Magnetic manipulation of HEK293T cells with Fe_3O_4-CdSe@GSH
HEK293T cells are incubated with the Fe_3O_4-CdSe@GSH nanoparticles and pEGFP-N1 vectors, these fluorescence images were taken of the cell (A) without a magnetic field and (B) under a magnetic field for 8 hours, adapted from ref.[109]

1.4. Conclusion and future outlook

Fundamental inorganic nanoparticles and multifunctional nanomaterials are widely used in biomedical applications such as MRI and fluorescence sensing. This chapter reviewed the preparation of numerous inorganic nanoparticles, their properties, and biomedical applications. In these days, there are lots of research reports on the development of fundamental inorganic nanoparticles and multifunctional nanostructures for diagnosis, imaging, and therapy. In order to get an effective diagnosis and specific treatment of diseases in clinics for the future, many issues including bio-distribution, toxicity, *in vivo* targeting efficacy, and long-term stability need to be addressed. The development of efficient nanomaterials and exact investigation of their properties will give a right route for diagnosis and therapy of diseases in the future.

Chapter 2

Tutorial Review: The Synthesis and Characterization of Fundamental and Multifunctional Nanomaterials

2.1. Introduction

Nanotechnology is a fast-growing area, which currently involves usage of various nanomaterials in modern science and technology. Magnetic and fluorescent inorganic nanoparticles are of particular importance due to their broad range of potential applications.[104] For instance magnetic iron oxide nanoparticles can be used as contrast agents in magnetic resonance imaging (MRI).[35] For the MRI contrast agent, gadolinium oxide nanoparticles are also used for brighter contrast.[101] And also external magnetic fields could get multiplexed cell separation

using magnetic nanoparticles and bring nanoparticles to a specific site thereby acting as site-specific drug delivery vehicles.[6]

Fluorescent semiconductor nanocrystals (QDs) have a strong characteristic spectral emission, which is tunable to a desired energy by selecting variable particle size and compositions. As a fluorescent probe, QDs have important biomedical applications including *in vivo* cell targeting, imaging, and multiplexed biological detection.[25,53] However, there are still many questions for the toxicity of QDs containing Cd, Pb, Hg, Te, and Se. These elements are toxic and can damage the tissues. In recent years, rare earth (RE) nanoparticles are proposed as attractive candidates for imaging.[110] RE ions, composed of the lanthanide (Ln) series (terbium (Tb), europium (Eu), erbium (Er), and ytterbium (Yb)) exhibit sharp fluorescent spectra (4f or 4f-5d transition) with multicolor emission and photostability. Most importantly, RE nanoparticles have lower toxicity compared to QD probes.

A combination of magnetic and fluorescent properties in a nanocomposite would have great advantages such as multimodal imaging probe and magnetic separation with optical imaging.[36,111,112] For multimodal imaging and separation with fluorescence detection, iron oxide/quantum dot or fluorescent dye complexes are generally prepared.[112] Moreover, RE ions (Tb or Eu) doped gadolinium oxide nanoparticles are also used for multimodal imaging probe. [113]

In this chapter, we explore the preparation of a variety of nanomaterials including QDs, iron oxide magnetic nanocrystals, gadolinium oxide nanoparticles,

magnetite quantum dot complexes, and rare-earth ion (Eu^{3+}) doped gadolinium oxide nanoparticles and their characterizations for the evaluation of nanomaterials.

2.2. Experimental sections

2.2.1. Materials

Cadmium oxide (CdO, powder 99.99 %), zinc oxide (ZnO, 99.99 %), lead (III) oxide (PbO, 99.99 %), selenium (Se, 99.99 %), tellurium (Te, 99.99 %), sulfur (S, 99.5 %), iron(III) oxide, hydrated (FeO(OH), catalyst grade, 30-50 mesh), gadolinium nitrate hexahydrate ($Gd(NO_3)_3 \cdot 6H_2O$, 99.99 %), europium(III) nitrate hydrate ($Eu(NO_3)_3 \cdot 5H_2O$, 99.99 %), oleic acid (technical grade, 90 %), , stearic acid (98.5 %), trioctylphosphine oxide (TOP, technical grade 90 %), hexadecylamine (HDA, 98 %), trioctylphosphine oxide (TOPO, 99 %), octadecylamine (ODA, 97 %), 1-octadecene (1-ODE, technical grade 90 %) were all purchased from Sigma-Aldrich. All nanocrystals were synthesized under ultra-high purity nitrogen (N_2, 99.99 %). Hexanes (95 %), acetone (99 %), ethanol (99.5 %), and methanol (99 %) were obtained from Sigma-Aldrich. All chemicals were used as received.

2.2.2. Synthesis of semiconductor nanocrystals (QDs)

2.2.2.1. Synthesis of CdSe QDs

CdSe semiconductor nanocrystals were prepared using a modified synthetic protocol from literature.[63] For a typical reaction, CdO (0.192 g) and stearic acid

(0.85 g) were mixed into 50 ml three neck flask and heated to 200 °C under N_2 flow to obtain a colorless clear solution. After cooling down to room temperature, hexadecylamine (HDA) (1.875 g), TOPO (1.875 g), and 1-ODE (10 g) were added into the flask. The mixture was reheated to 283 °C. At this temperature, 0.356 g of 10 % Se-TOP (Se (0.64 g) in TOP (8 mmol)) diluted with toluene (0.06 g) and 1-ODE (1.375 g) was swiftly injected into reaction flask. The reaction was allowed to cool down to 250 °C to grow CdSe QDs. At various time intervals (10 sec to 5 min) aliquots mixture was taken out using syringe and quenched in chloroform.

2.2.2.2. Synthesis of CdS QDs

The synthesis of CdS QDs was modified by reported method.[114] CdO (0.0384 g), oleic acid (0.338 g), and 1-ODE (total volume 12 g) were loaded into 50 ml three-neck flask and heated to 300 °C under N_2 flow. At this temperature, a solution of S-ODE (0.15 mmol, 0.006 g S in ODE 6 g) was swiftly injected into the hot solution. After injection, the temperature was allowed to cool down to 250 °C for the growth of CdS QDs. At various time intervals (10 sec, 30 sec, 1 min, 5 min, 10 min), aliquots with a needle tip were removed and diluted with cool hexanes.

2.2.2.3. Synthesis of CdTe QDs

CdTe QDs was prepared via a modified reported procedure.[63] CdO (0.0384 g), oleic acid (0.338 g), and 1-ODE (total 12 g) were added into 50 ml three neck flask and heated to 200 °C under N_2 flow. At 280 °C, 0.174 g Te-TOP 10 % solution,

prepared by dissolving 42.2 mg of Te in 0.8 ml TOP and diluted with 5 ml 1-ODE, was quickly injected into the hot reaction mixture. After injection, the temperature was allowed to cool to 250 °C for the growth of CdTe QDs.

2.2.2.4. Synthesis of CdSe@CdS and CdSe@ZnS QDs

To synthesize core/shell QDs, CdSe QDs were first prepared and purified. The procedure for the synthesis of core/shell CdSe@CdS QDs and CdSe@ZnS QDs was modified by the reported reference.[62] The CdS or ZnS shell was deposited onto the CdSe QDs by introducing the calculated amounts of Zn and S. The cadmium precursor solution (0.04 M) was prepared by dissolving CdO (0.615 g) in oleic acid (10.83 g) and 1-ODE (108 ml) at 250 °C. The zinc precursor solution (0.04 M) was made by dissolving ZnO (0.39 g) in oleic acid (10.83 g) and 1-ODE (108 ml) at 250 °C. The sulfur stock solution (0.04 M) was prepared by dissolving sulfur powder (0.128 g) in 1-ODE (100 ml) at 200 °C. Both precursor solutions were prepared under the N_2 flow. The Zn or Cd precursor solution needs pre-heating to ensure complete dissolution before injection. For each injection to make a shell, a certain amounts of stock solution were taken by syringe.

Following the reference, the successive ionic layer adsorption and reaction (SILAR) method is based on the alternating injection of Cd or Zn and S precursors into the solution containing purified CdSe QDs for the growth of CdSe/CdS core/shell or CdSe/ZnS core/shell QDs.[62] The amount of cadmium/zinc or sulfur precursors required for each layer was calculated by the number of surface atoms of

a given size of a core/shell QDs. The average thickness of one monolayer of CdS was 0.35 nm, so additional layer growth would increase the diameter of a nanocrystal by 0.7 nm. In a typical reaction with 3.7 nm core, 2.13×10^{-3} mmol of Cd and S precursor is needed for the first layer of the shell growth, and an additional 2.85×10^{-3} mmol of Cd and S completes the growth of the second layer.

CdSe QDs (3.5 nm, 1×10^{-4} mmol of particles) dissolved in 2 ml hexanes were mixed with 1.5 g ODA and 5 g 1-ODE in a 25 ml three neck flask. To remove hexanes, the reaction mixture was allowed to preheat at 100 °C or vacuum. Then, under N_2 atmosphere, the mixture was further heated to 240 °C for making core/shell QDs. The Cd or Zn precursor solution (0.04 M) was injected with the volume of 0.49 ml and stirred for 5 min at this temperature (240 °C). Amount of solution required for subsequent injection was calculated using the method described above. After 5 min, 0.49 ml of the sulfur precursor solution was injected to the mixture and stirred for 10 min for the first layer of CdS or ZnS shell. After that, the reaction mixture was cooled down to room temperature and purified using methanol and acetone three times.

2.2.2.5. Synthesis of PbSe QDs and PbSe@PbS QDs

The PbSe QDs was prepared via a modified procedure.[115] Typically, PbO (0.892 g, 4 mmol), oleic acid (2.825 g, 10 mmol), and 1-ODE (total weight was 16 g) were loaded to the three neck flask and heated to 180 °C under N_2 flow until the solution becomes colorless. Then 6.4 g of Se-TOP 10 % solution, prepared by 0.64 g

of Se (8 mmol) in 6.4 g TOP was quickly injected into the solution at 180 °C. Then, the reaction mixture was cooled down to 150 °C for the growth of PbSe QDs. The aliquots of reaction mixture were collected using syringe for getting various sizes of PbSe QDs (10 sec (3-5 nm core size) and 800 sec (9 nm)).

2.2.3. Synthesis of iron oxide nanocrystals

The iron oxide magnetic nanocrystals were synthesized following the previous work.[51] Experimentally, 0.178 g of FeO(OH) was added with 2.26 g oleic acid and 5 g of 1-ODE into three neck flask and heated to 120 °C for 3 hours to make first iron oleates and finally refluxed to 320 °C for 2 hours.

2.2.4. Synthesis of gadolinium oxide nanocrystals

2 mmol of gadolinium nitrate hexahydrate was mixed with oleic acid (4 mmol) and 1-ODE (5 g) into three neck flask and stirred for 2 hours at 110 °C until the Gd precursor was completely dissolved in the solvent as Gd-oleate precursors. After increasing the temperature from 110 to 290 °C, the reaction mixture was refluxed at 290 °C for 3-18 hours. After the reaction is done, the temperature was cooled down to room temperature. Finally, the gadolinium oxide nanoparticles (5 nm) were prepared and stored in hexanes. To make larger nanoparticles (8, 11, 13, and 22 nm), the oleylamine (2, 6, 8, and 12 mmol) and more 3 g 1-ODE were added into the gadolinium-oleate mixture (2 mmol gadolinium nitrate hexahydrate, 4 mmol oleic acid, 5 g 1-octadecene) after heating at 110 °C for 2 hours and then refluxed at 290 °C for 3-18 hours. For making smaller 2 nm gadolinium oxide

nanoparticles, the refluxed reaction temperature was increased from 290 to 320 °C with the amount of gadolinium nitrate hexahydrate (2 mmol), oleic acid (4 mmol), and 1-ODE (5 g).

2.2.5. Purification of nanocrystals

The resulting colloidal solution (5 mL) was centrifuged with methanol (20 mL) and acetone (20 mL) at 4150 rpm for 30 minutes and redispersed with hexanes. This purification was repeated six times resulting in purified nanocrystal solutions with minimal residual surfactants. The resulting nanocrystal solution is stored in hexanes and ready for further synthesis and characterization.

2.2.6. Synthesis of iron oxide/CdSe QD complexes

For the synthesis of iron oxide/CdSe QD complexes, the iron oxide nanocrystals were first prepared and purified. Using iron oxide nanocrystals as seeds, the QDs were nucleated and grown onto the surface of iron oxide. CdO (0.3 mmol), ODA (11 mmol), and ODE (40 mmol) were added in a 50 mL three neck flask. This mixture was ramped to 200 °C and held there for one hour under nitrogen (N_2) flow. After cooling down to room temperature, 1 mL iron oxide nanocrystal solution stored in hexanes at the concentration of 6,000 mg/L Fe was injected into the mixture and the mixture was heated to 100 °C for 30 minutes for the evaporation of hexanes completely. Afterwards, the reaction mixture was allowed to heat at 280 °C for one hour under nitrogen (N_2) flow. Se (0.9 mmol) dissolved in trioctylphosphine (TOP, 2 ml) was slowly injected into the solution with

the speed of 0.4 ml/min at lower temperature 220 °C and the temperature was set to 250 °C allowing to grow CdSe QDs on the iron oxide surface. Aliquots of reaction mixture at the different time intervals from 1 to 25 min, gave iron oxide/QD complexes emitting distinctive fluorescence colors from green to red. The aliquots of growth solution were quenched with hexanes and further purified. The Figure 2-1 shows the synthesis setup for nanocrystals.

2.2.7. Synthesis of iron oxide/PbSe QD complexes

For the reaction of iron oxide/PbSe QD complexes, PbO (0.15 mmol), oleic acid (0.8 mmol), and 1-ODE (10 g) were mixed and heated to 180 °C for 1 hour. After cooling down to room temperature, ODA (4 g) and preformed iron oxide nanocrystal solution (0.1 mmol Fe_3O_4 in 2 ml hexanes, 6,000 mg/L Fe) were injected into the reaction mixture. After evaporation of hexanes using vacuum or heating at 100 °C for 30 minutes, the reaction was reheated to 180 °C. At this temperature, the Se (0.9 mmol) dissolved in trioctylphosphine (TOP, 2 ml) was slowly injected to the mixture. The PbSe QDs were grown on the surface of iron oxide at 150 °C for 30 min. The resulting iron oxide/PbSe QDs complexes were purified with methanol/acetone several times and were kept in hexanes.

2.2.8. Synthesis of Eu (III) doped gadolinium oxide nanoparticles

2 mmol of gadolinium nitrate hexahydrate (0.9 g) and 0.5 mmol europium nitrate hydrate (0.2 g) were mixed with oleic acid (4 mmol) and 1-ODE (5 g) into three neck flask and stirred for 2 hours at 110 °C for making Gd/Eu oleates. After

increasing the temperature from 110 to 290 °C, octadecylamine (6 mmol, 1.6 g) was added and the reaction mixture was refluxed at 290 °C for 3-18 hours. After the reaction is done, the temperature was cooled down to room temperature. Finally, the europium doped gadolinium oxide nanoparticles (12 nm) were prepared and further purified with methanol and acetone by centrifugation at 4150 rpm for 30 minutes three times. By changing the reflux time, monomer concentration, surfactant (oleic acid and oleylamine) ratio and Gd/Eu ratio, the particle diameter was varied from 2 to 15 nm.
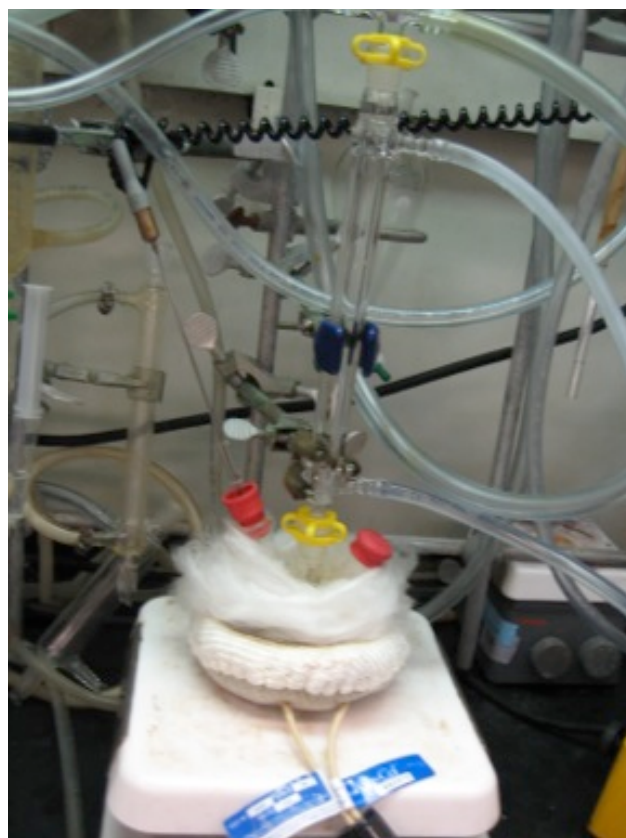
Figure 2-1 Nanoparticle synthesis setup

2.2.9. Instruments and characterization

2.2.9.1. Absorbance detection

Ultraviolet-visible absorption spectrometer (Varian Cary 5000 UV-visible-NIR) was used for the absorbance of QDs.

2.2.9.2. Photoluminesccence detection

Photoluminescence (PL) spectra of quantum dots or iron/oxide QD complexes were recorded on a Jobin Yvon Spex Fluorolog 3 fluorescence spectrophotometer. The absolute photoluminescence quantum yield (PLQY) was calculated by the gradient method of comparing the PL integrated intensity of the CdSe QDs and that of the solution of rhodamine 6G (R6G) in ethanol. The absorption spectra of iron oxide/QDs complexes, CdSe QDs, and R6G were recorded at 480 nm excitation, with the optical intensities of all samples below 0.10 absorbance. The following equation was used to calculate the quantum yield. [116,117]

$$\Phi_x = \Phi_r \cdot \left[\frac{A_r}{A_x}\right] \cdot \left[\frac{I_r}{I_x}\right] \cdot \left[\frac{n_x^2}{n_r^2}\right] \cdot \left[\frac{D_x}{D_r}\right]$$

At room temperature, Φ_x and Φ_r are the absolute quantum yield of the CdSe QDs and rhodamine 6G. The Φ_r of R6G in ethanol is 95 %. A_r and A_x are, respectively, compared to the absorption value at the excitation wavelength, e.g. 480 nm in this study. I_r and I_x are the intensities of excitation, and those of the sample in our

experiment are equal to the values of the standard sample. n_r and n_x are the refractive indicies of the solvents. Ethanol (n=1.359) and hexanes (n=1.372) are used in this study. D_x and D_r are the PL integrated intensities excited at 480 nm of the CdSe QDs and R6G.

2.2.9.3. Transmission electron microscopy (TEM)

TEM specimens were carried out by JEOL 2100 field emission gun TEM operating at 200 kV with a single tilt holder. The TEM sample was made by evaporating one drop of purified solution in hexanes on ultra thin carbon type-A 400 mesh copper grids (Ted Pella Inc.). Energy-filtering transmission electron microscopy (EFTEM) provides the gatan imaging filter (GIF) mapping, which gives the chemical information from the nanostructured regions. For the analytical technique, energy-dispersive x-ray spectrometry (EDXS) was performed to get the chemical composition from the complex area. The size and size distribution data were obtained by counting over 500 individual nanocrystalline particles using Image-Pro Plus 5.0 (Media Cybernetics, Inc., Silver Spring, MD).

2.2.9.4. X-ray diffraction (XRD)

The XRD patterns were recorded using a Rigaku D/Max Ultima II with a zero background sample holder and analyzed by JCPDS card. The 2θ range was measured from 10 to 80 degree with Cu Kα radiation. The X-ray was generated at 40 KV and 40 mA.

2.3. Results and discussions

The core CdSe QDs and core/shell CdSe@ZnS QDs were prepared by thermo-decomposition in the presence of organic surfactants and 1-ODE. The size tunable CdSe QDs have multiple fluorescent colors from blue to red under the UV light as shown in Figure 2-2. And the TEM image (Figure 2-3) shows the monodisperse CdSe QDs with the growth for 180 sec. The size of CdSe QDs was 3.4 ± 0.4 nm. The photographs of size tunable CdS and CdTe QDs are also in Figure 2-4 and Figure 2-5. Moreover, the PbSe QDs emitted in Near IR region were prepared and showed in Figure 2-6.
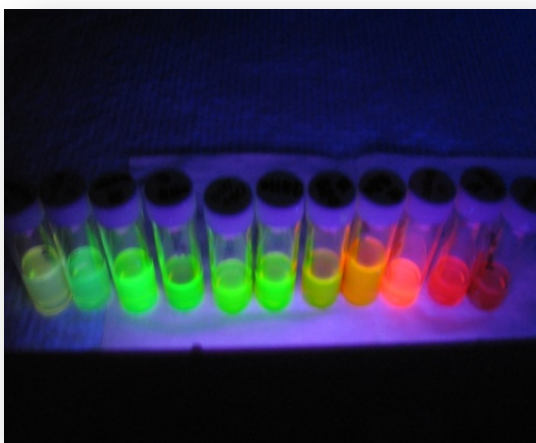
Figure 2-2 The CdSe QDs excited by UV light
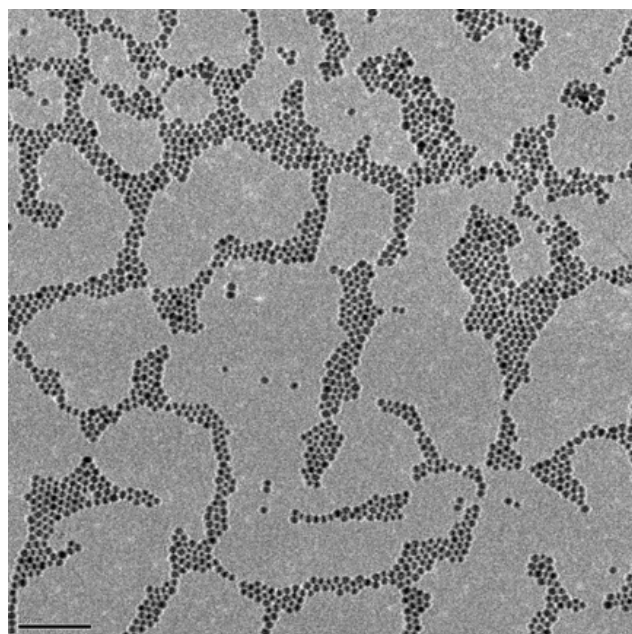
Figure 2-3 The TEM image of CdSe QDs
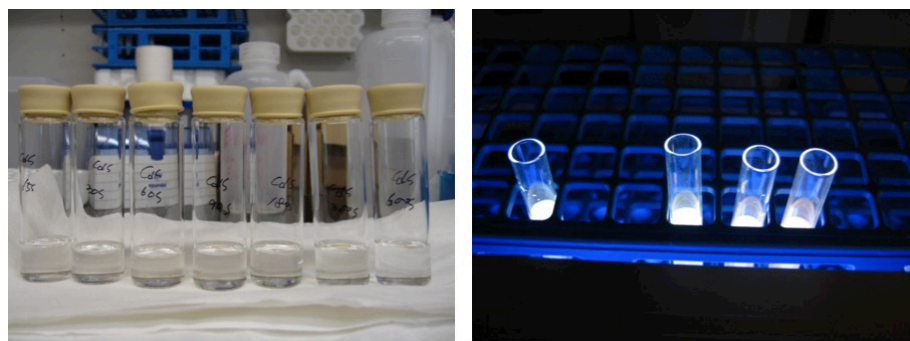
Figure 2-4 Size tunable CdS QDs under the day light and UV light
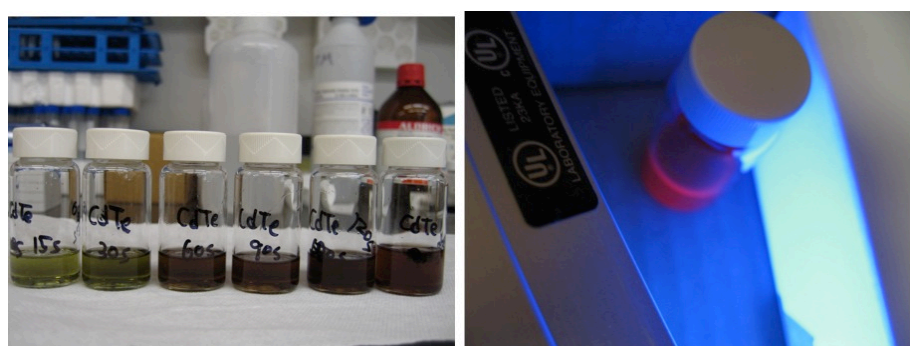
Figure 2-5 Size tunable CdTe QDs under the day light and UV light
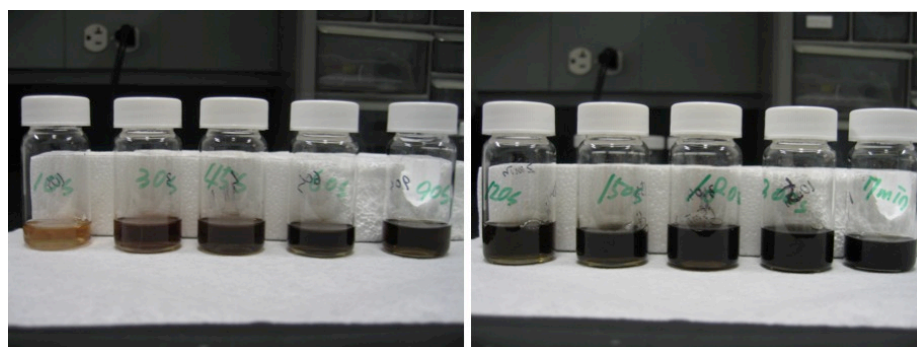
Figure 2-6 Size tunable PbSe QDs by taking aliquots at different time intervals

When taking aliquots at the different time intervals, the absorbance spectrum is red-shifted. The CdSe QDs were red shifted from 557 nm to 589 nm at the different time growth from 10 sec to 180 sec as shown in Figure 2-7. The size dependent emission spectra of QDs can be explained by quantum confinement and band gap energy theory[118]. The exciton transition shifted to higher energy with an increase of molar absorption coefficient as QD diameters decreased. The Figure 2-8 shows that the absorbance (529 nm) and photoluminescence (540 nm) spectra of CdSe QDs (2 nm size, green emission). The absorbance of CdS QDs and CdTe QDs confirmed the red shift from 352 to 378 nm and 593 nm to 689 nm, respectively (Figure 2-9 and Figure 2-10). Moreover, the PbSe QDs absorb near IR region and were red-shifted over 1800 to 2200 nm with different growth time (Figure 2-11). The Table 2-1 shows the summary of wavelength (nm) and full width at half maximum (FWHM).
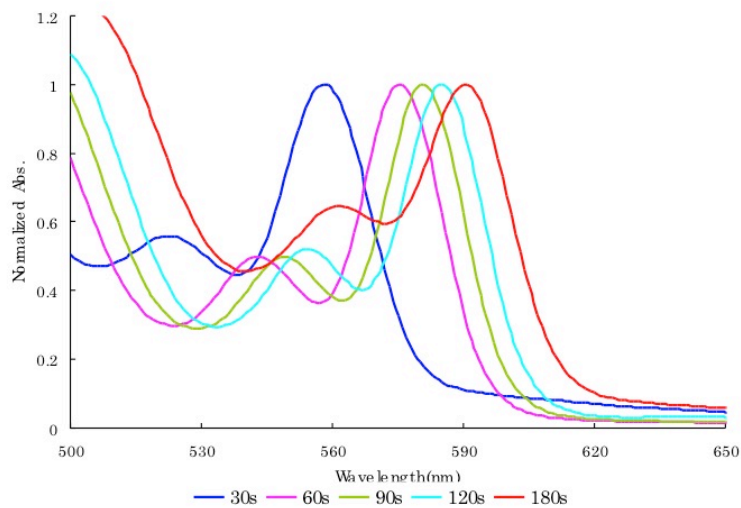
Figure 2-7 The absorbance of CdSe QDs at the different time intervals
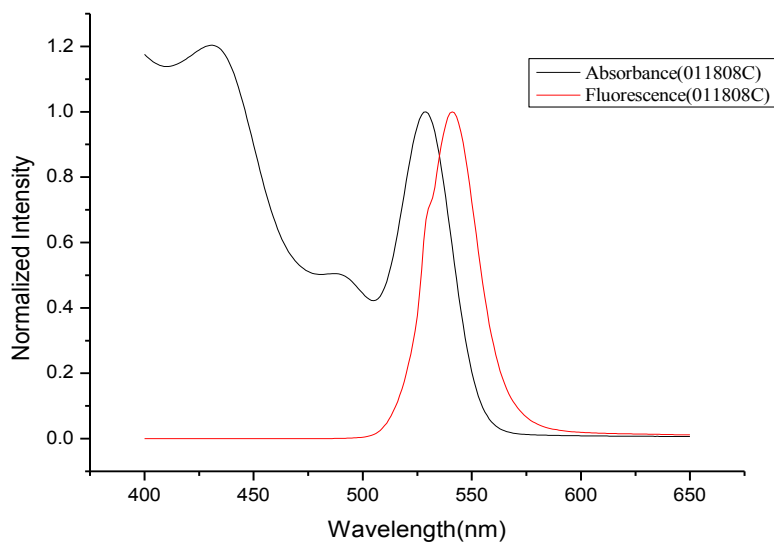
Figure 2-8 The absorbance and photoluminescence (PL) spectra of CdSe QDs.
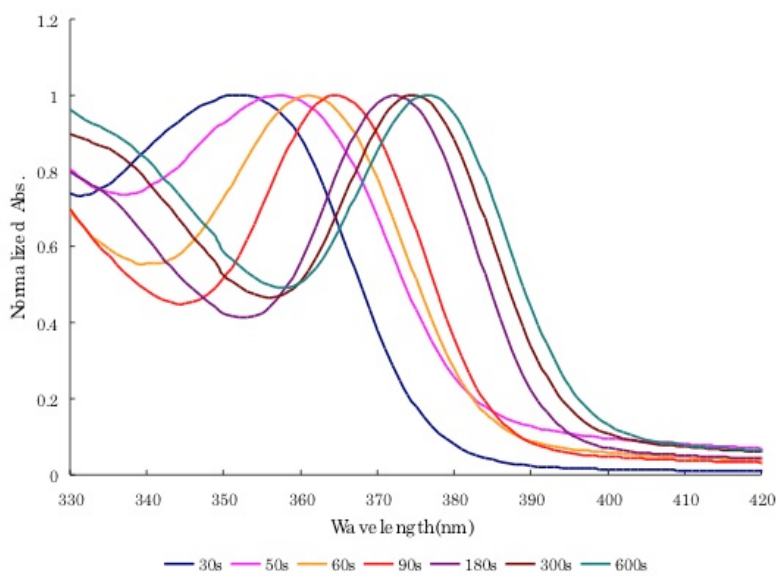
Figure 2-9 The absorbance of CdS QDs at the different time intervals
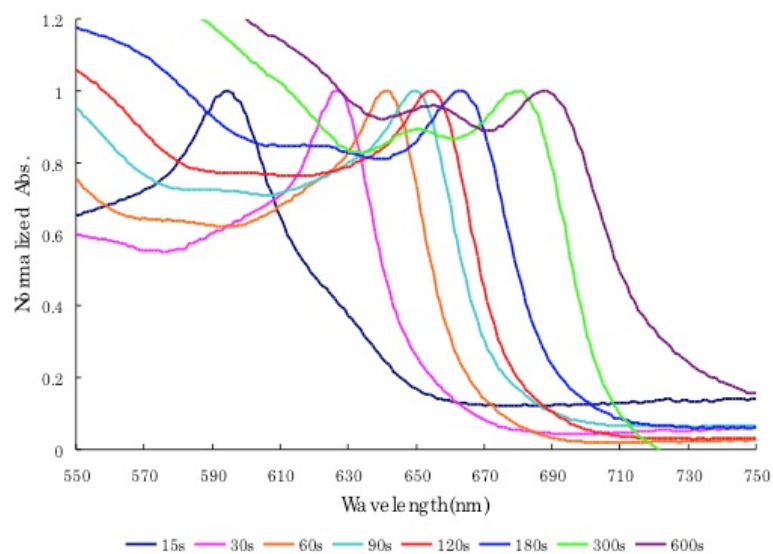
Figure 2-10 The absorbance of CdTe QDs at the different time intervals
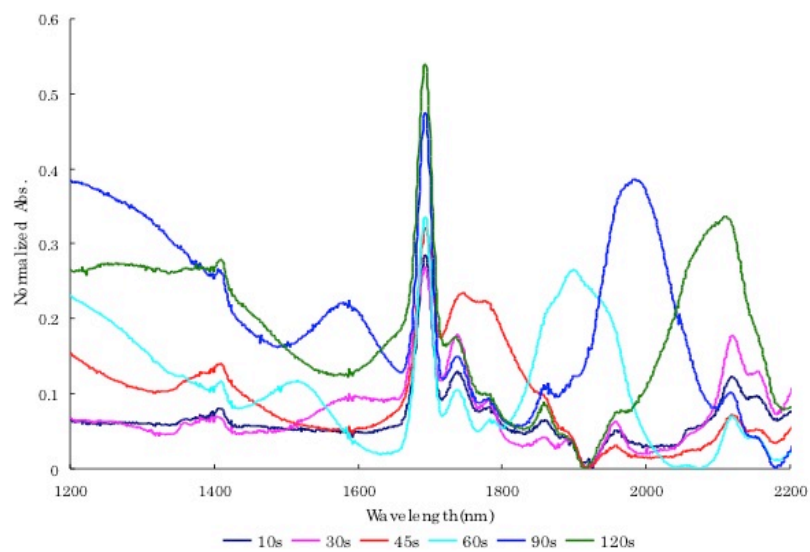
Figure 2-11 The absorbance of PbSe QDs at the different time intervals

Table 2-1 The absorbance wavelength and full width at half maximum (FWHM) of QDs

	CdSe QDs			CdS QDs			CdTe QDs	
	λ_{max}	FWHM		λ_{max}	FWHM		λ_{max}	FWHM
30s	557nm	28nm	30s	352nm	32nm	15s	593nm	3onm
45s	575nm	30nm	60s	361nm	30nm	60s	641nm	28nm
180s	579nm	28nm	180s	371nm	26nm	180s	663nm	32nm
420s	584nm	26nm	300s	375nm	26nm	300s	679nm	34nm
3000s	589nm	28nm	600s	378nm	24nm	600s	689nm	36nm

The core QDs can be used for making core/shell QDs to improve PLQY and prevent toxic Cd leakage to the outside. When ZnS shell deposited on the CdSe QDs, the wavelength of absorbance and PL spectra was red-shifted as depicted in the fluorescent colors under UV light (Figure 2-12). The TEM images (Figure 2-13) verified the change of size from 3.6 nm to 4.3 nm after capping ZnS shells. The XRD data confirmed that the peak positions of CdSe QDs and CdSe/ZnS QDs were matched with reference (Figure 2-14). The references were taken from JCPDS card 02-0330 and 01-0667.
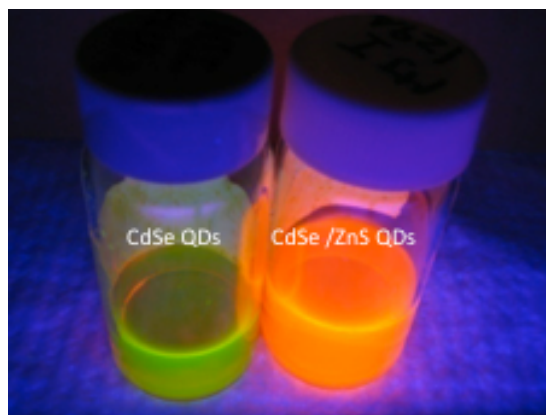
Figure 2-12 The photograph of CdSe QDs (green emission) and CdSe/ZnS QDs (organe emission)
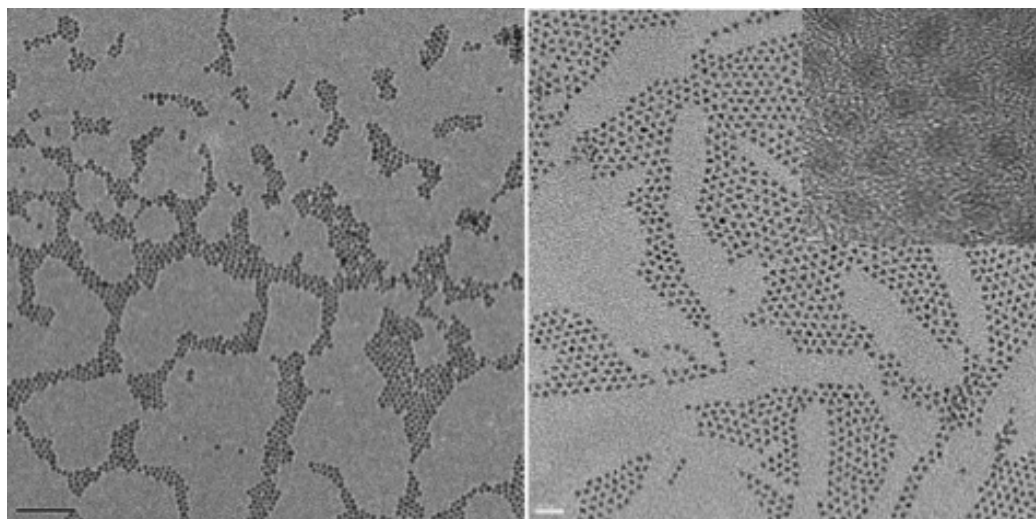
Figure 2-13 The CdSe QDs (3.6 nm, left) and CdSe/ZnS QDs (4.3 nm, right).

The inset indicated the high resolution images showing crystal lattice fringes.
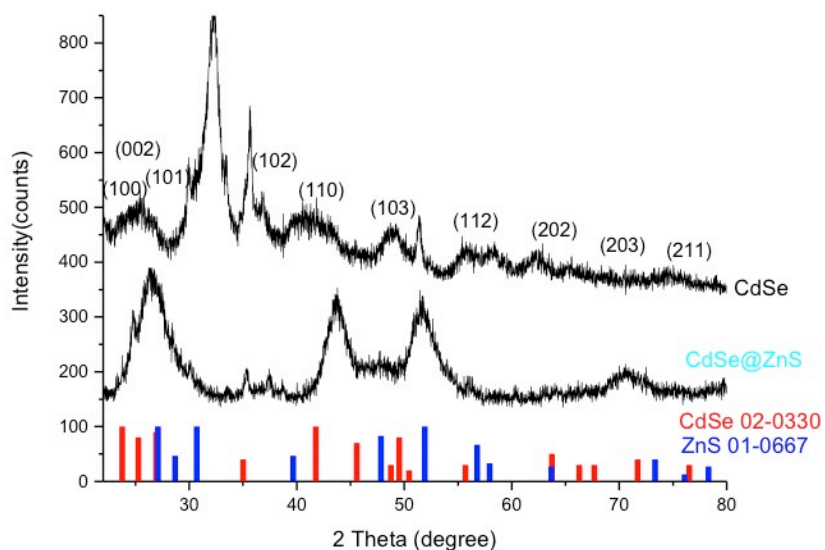
Figure 2-14 The XRD pattern of CdSe QDs and CdSe@ZnS QDs

The iron oxide nanocrystals were prepared by thermo-decomposition in the presence of FeOOH precursor with oleic acid and ODE solvent. By changing the molar ratio between FeOOH precursor and oleic acid from 1:3 to 1:5, the core diameters of iron oxide nanocrystals were changed from 8 to 17 nm.[51] The TEM images shows the diameters of monodisperse iron oxide nanocrystals were 10.2 ± 1.2 nm and 17.5 ± 1.3 nm (Figure 2-15 and Figure 2-16). The high resolution TEM image shows that iron oxide nanoparticles has crystalline structure showing lattice fringes (Figure 2-17). And also XRD confirmed that the diffraction peaks of iron oxide nanoparticles were matched with the iron oxide reference peaks (Figure 2-18).
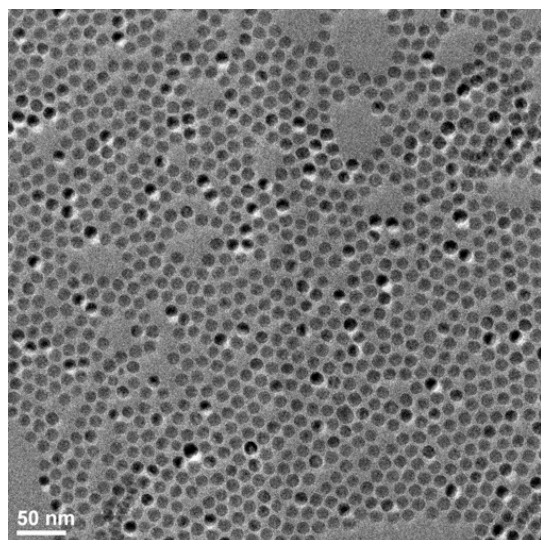
Figure 2-15 TEM image of iron oxide nanocrystals with the size of 10.2 nm
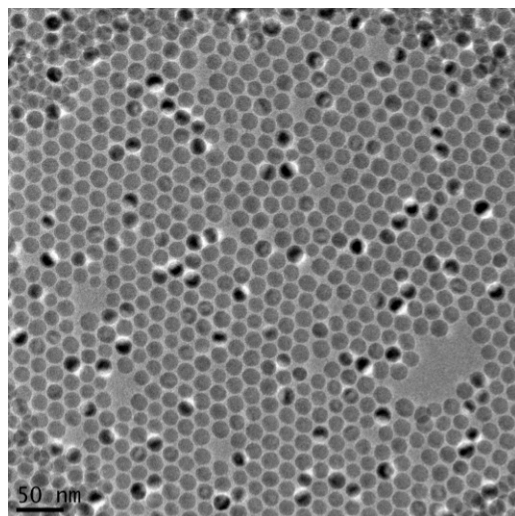
Figure 2-16 TEM image of iron oxide nanoparticles with the size of 17.5 nm
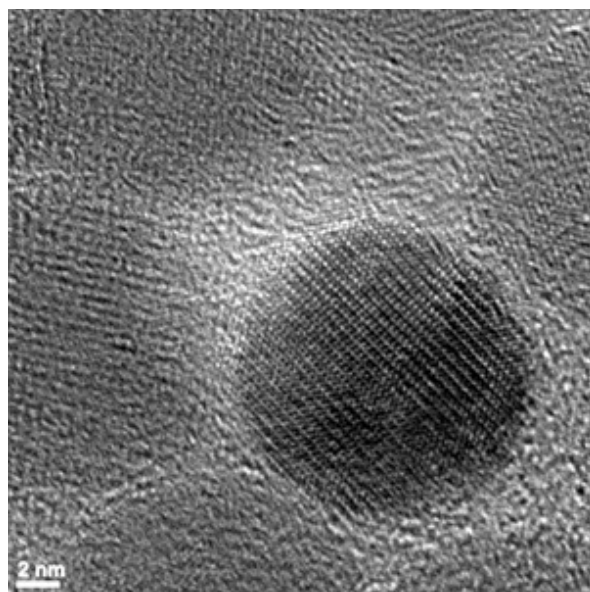
Figure 2-17 The high resolution TEM image of iron oxide nanocrystals (10 nm)
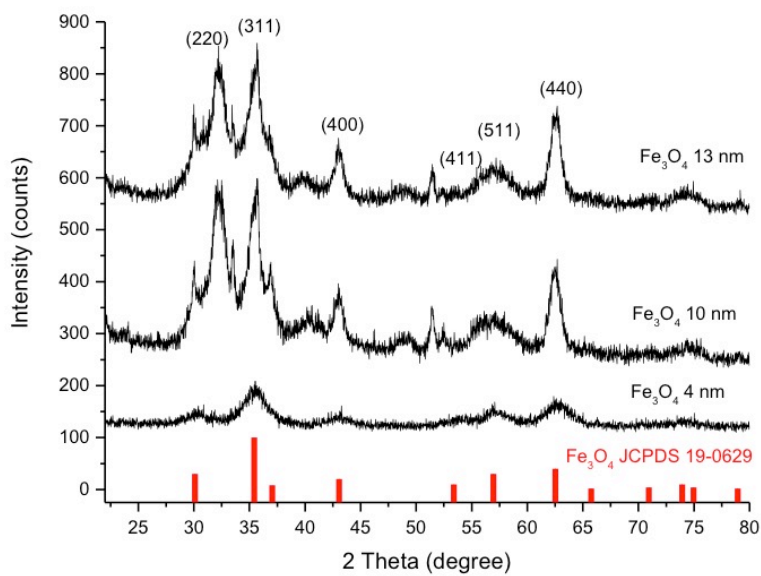
Figure 2-18 The XRD pattern of iron oxide nanoparticles.

Based on the iron oxide nanoparticle synthesis, the multifunctional iron oxide/QDs complexes were prepared in a reaction that relied on the nucleation of CdSe QDs or PbSe QDs on preformed iron oxide nanocystals. Monodisperse iron oxide nanocrystals were used as seeds for the nucleation sites of QDs. By controlling growth time from 1 to 25 minutes, the size tunable iron oxide/CdSe QDs complexes were synthesized with multiple fluorescence colors from green to red. (Figure 2-19) The Figure 2-20 shows very uniform pincushion iron oxide/CdSe QD complexes using 12 nm iron oxide seeds by thermo-decomposition. Figure 2-21 indicated the iron oxide/PbSe QDs complexes using 18 nm iron oxide nanocrystals by high temperature thermo-decomposition. The gatan image filter (GIF) analytical mapping confirmed that the CdSe or PbSe QDs nucleated directly at the interface with iron oxide core (Figure 2-22 and Figure 2-23).
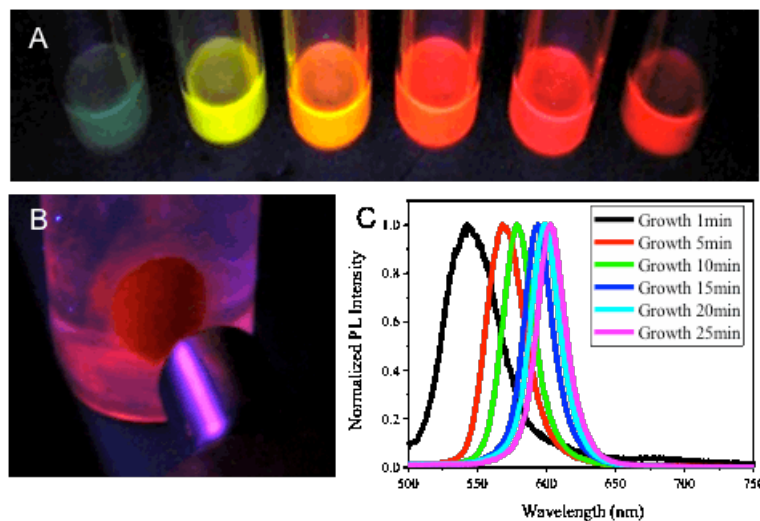
Figure 2-19 Size tunable iron oxide/CdSe QDs complexes
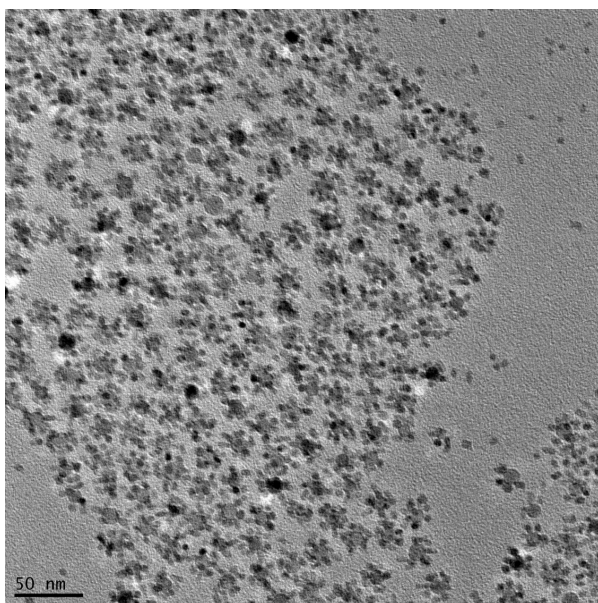
Figure 2-20 The TEM image of iron oxide/CdSe QD complexes
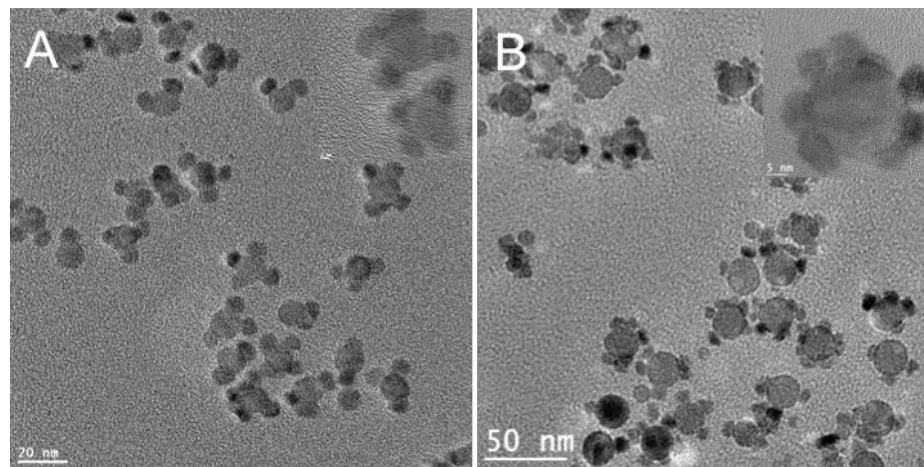
Figure 2-21 The TEM image of iron oxide/PbSe QDs complexes using iron oxide 10 nm (A) and 18 nm (B)
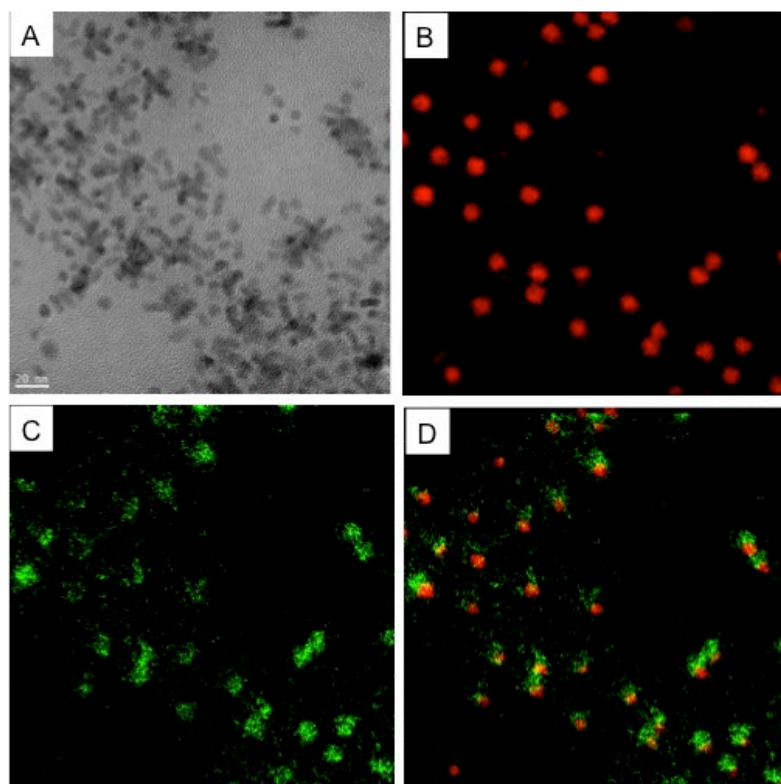
Figure 2-22 The GIF mapping of iron oxide-CdSe QDs complexes

(A) frame image, (B) Fe (red) mapping, (C) Cd(green) mapping, and (D) mixed image (Fe : red, Cd: green)
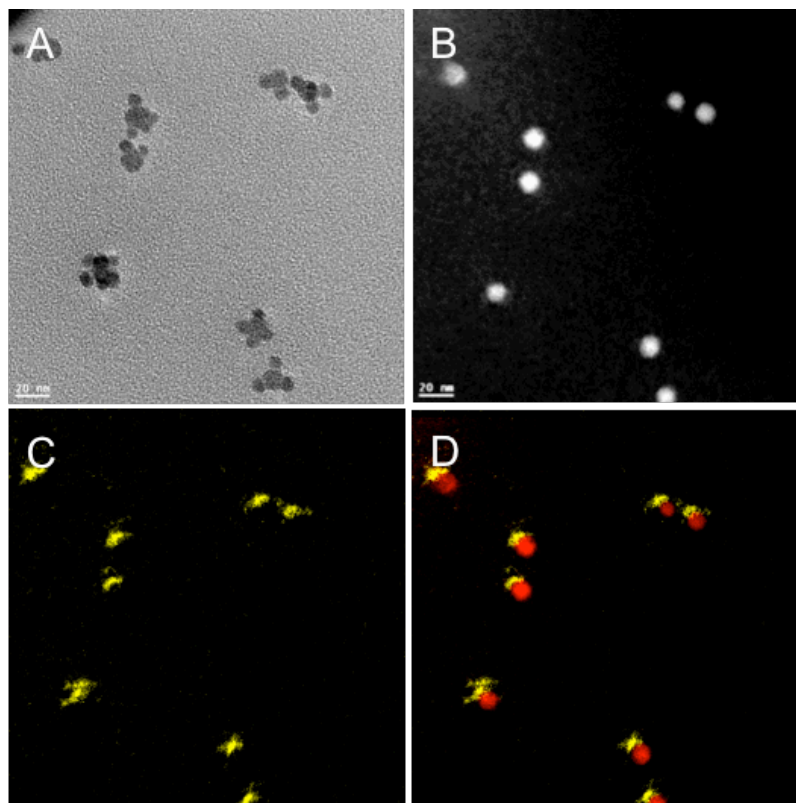
Figure 2-23 The GIF mapping of iron oxide-PbSe QDs complexes
(A) frame image, (B) Fe (white) mapping, (C) Pb (yellow) mapping, and (D) mixed
image (Fe : red, Cd: yellow)

The gadolinium oxide nanoparticles (11 nm) were synthesized by thermodecomposition of gadolinium nitrate hexahydrate in the presence of oleic acid and ODE (Figure 2-24). Based on the gadolinium oxide synthesis, we simply prepared europium (Eu^{3+}) doped gadolinium oxide nanoparticles for multimodal imaging probe. By controlling reaction parameters (e.g. reaction time, concentration of monomer, the ratio of Gd/Eu, the ratio of oleic acid/oleylamine), the diameter of europium doped gadolinium oxide nanoparticles was tunable from 2 to 15 nm

(Figure 2-25). The ratio between oleic acid and oleylamine or the ratio between gadolinium and europium nitrate hydrate is important parameter to make a wide size range (Figure 2-26). When increasing the oleylamine and europium nitrate precursors, the size was dramatically increased because more labile gadolinium promoted the particle growth. The GIF mapping reveals that the europium and gadolinium elements were mixed in a nanoparticle structure (Figure 2-27).
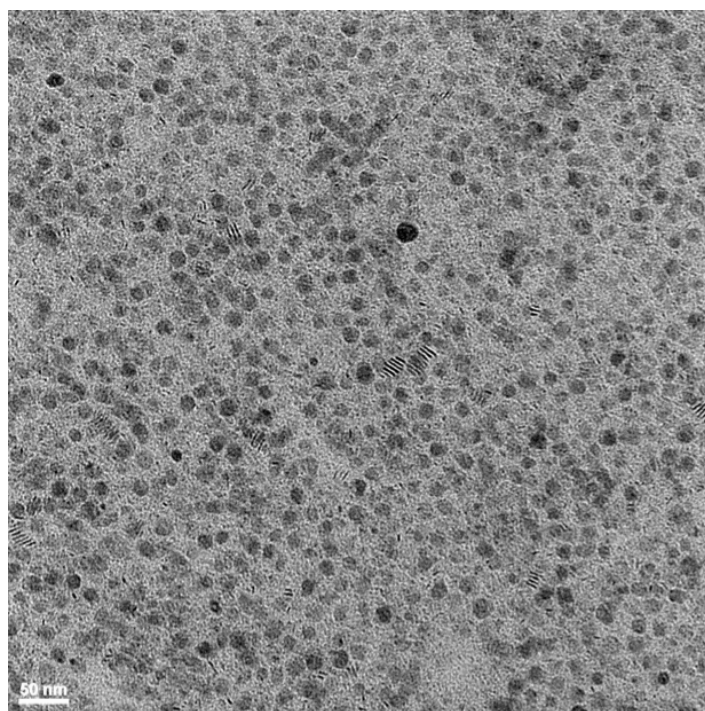
Figure 2-24 The TEM image of gadolinium oxide nanoparticle (11 nm)
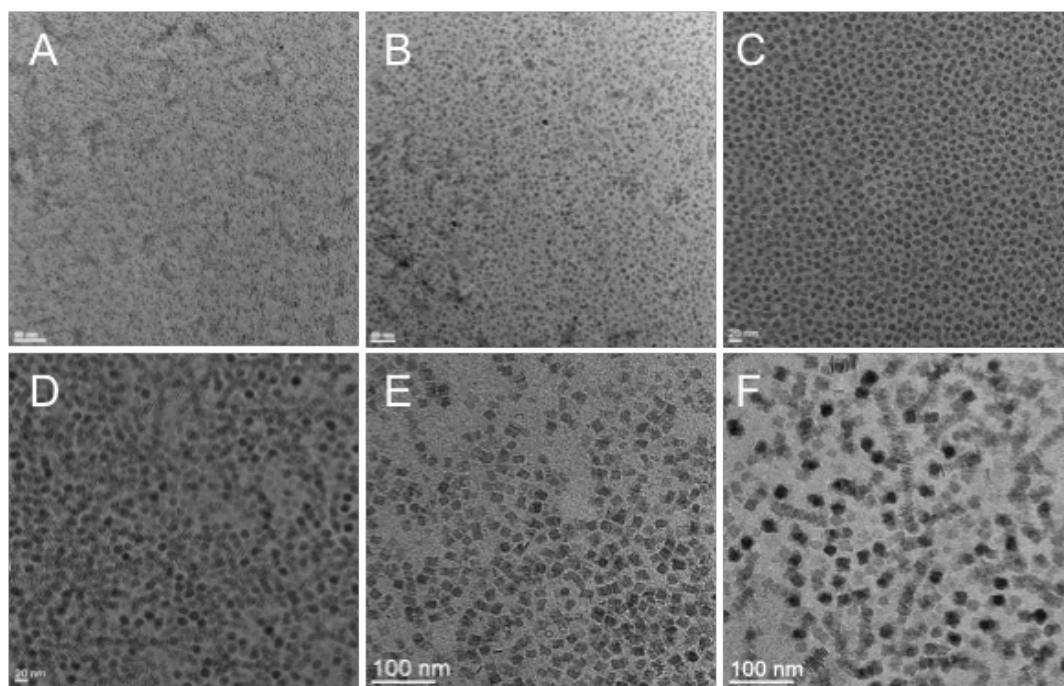
Figure 2-25 TEM images of europium doped gadolinium oxide nanoparticles

The diameter of nanoparticle was 2.1 ± 0.4 nm (A), 6.0 ± 0.7 nm (B), 8.2 ± 0.9 nm (C), 11.4 ± 1.6 nm (D), 13.2 ± 2.0 nm (E), and 15.5 ± 2.4 nm (F), respectively.
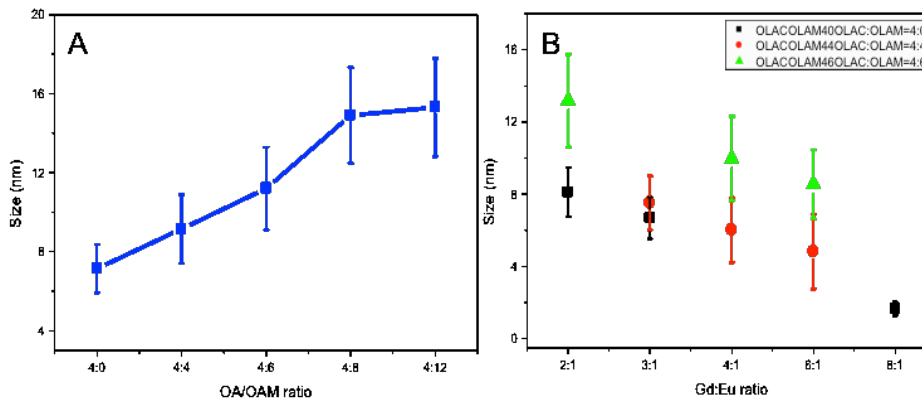
Figure 2-26 The reaction parameters for size tunability

(A) the ratio of oleic acid (OA)/oleylamine (OAM) and (B) the ratio of Gd/Eu precursor
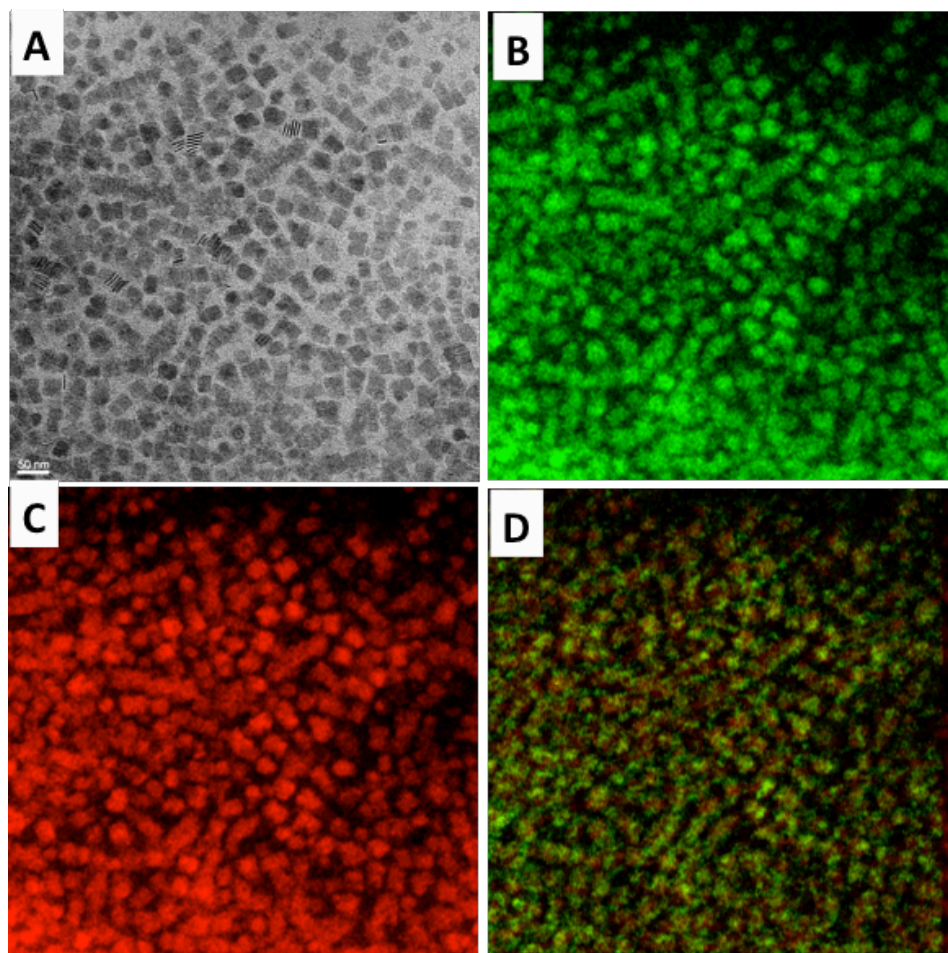
Figure 2-27 The GIF mapping of europium doped iron oxide nanoparticle
(A) frame image, (B) Gd mapping, (C) Eu mapping, and (D) Gd and Eu mixed mapping

2.4. Conclusions

In this tutorial chapter, the various inorganic nanoparticles including quantum dots, iron oxide nanoparticles, gadolinium oxide, iron oxide/QD complexes, and europium doped gadolinium oxide nanoparticles have been prepared. These inorganic fundamental and multifunctional nanocrystals have size tunable optical or magnetic properties. Therefore, the preparation of various nanomaterials gives great possibilities towards a variety of biomedical applications including MRI, cell imaging, manipulation, separation, and toxicological study.

Chapter 3

High r_1 Relaxivity Dynamics for Gadolinium Oxide Nanoparticle MR Contrast Agents

In this work, uniform gadolinium (Gd) oxide nanoparticles ranging from 1.8 to 22 nm were prepared using the thermal decomposition of gadolinium salts. Particles could be transferred to water using oleic acid bilayers, octylamine modified poly (acrylic acid) (PAA-OA), and lauryl acrylate (LA)-poly (2-acrylamido-2-methyl-1-propanesulfonic acid) (PAMPS) (PAMPS-LA) copolymers. Because of the control over both particle size and surface chemistry, it was possible to study how the longitudinal relaxivity (r_1) of gadolinium oxide nanoparticle was affected by both variables. Particle diameter had only a moderate effect on relaxivity; larger particles were not as effective on average as smaller ones, an observation attributed to the fact that in larger particles there are fewer surface-available gadolinium. On

the other hand, surface chemistry was a key parameter for maximizing the relaxivity, as this interface will define the access of water to the particle surface. PAA-OA and PAMPS-LA coatings were the best coating. The highest r_1 value observed was 58.2 $S^{-1}mM^{-1}$, a value 15 fold higher than Gd(III)-chelates[13] (4.3~4.6 $S^{-1}mM^{-1}$) at 1.41 T. Moreover, *in vitro* cell toxicological studies revealed that various gadolinium oxide suspensions, especially PAMPS-LA coated nanocrystals, had no significant effect on human dermal fibroblasts (HDF) up to 300 μM. This work illustrates that surface engineered gadolinium oxide nanoparticles may be a strong candidate for MRI contrast agents that offer r_1 relaxivities in excess of commercially available agents.

3.1. Introduction

Magnetic Resonance Imaging (MRI) has emerged as a powerful noninvasive imaging technique because it allows non-invasive *in vivo* examination of biological samples with excellent spatial resolution.[97-99] Because there is little difference between normal and diseased tissue in MRI, contrast agents are an important way to gather more specific information about the health of a patient.[37,38] They work by either shortening the longitudinal relaxation time (T_1) or the transverse relaxation time (T_2) of water protons. Two contrast agents in use clinically are gadolinium (Gd)-based chelates and iron oxide nanoparticles.[12,37,119-124] Gadolinium chelate MR contrast agents are positive contrast agents because they shorten T_1 relaxation time leading to increase signal intensity. Gadolinium-diethylenetriaminepentaacetate

(Gd-DTPA, Magnevist®) is the most popular clinical agent; it can be used to enhance tissue pathology, detect leaks in the blood-brain barrier (BBB), and in some cases identify physiological changes in tissue.[12]

Iron oxide nanoparticles induce a shortening of T_2 relaxation time, resulting a reduction of signal and negative contrast. Dextran coated superparamagnetic iron oxide nanoparticles (SPIOs) possess very large transverse relaxivity ($r_2 = 100\sim200$ mM^{-1}S^{-1}) and are used specifically in the evaluation of the tumors.[7,22,23,104,105,125-127] Following intraveneous injection, 80 % of injected dose of SPIOs is taken up by macrophages in the liver and the rest portion of SPIOs is taken up by those in spleen or bone marrow.[7,127] The reticuloendothelial system (RES) macrophage-mediated uptake SPIOs has been used to detect liver tumors or their accumulation in lymph node has been used to diagnose lymph node metastases.[105,106,128,129] Specially, ultrasmall superparamagnetic iron oxide nanoparticles (USPIOs) with diameters less than 40 nm have been clinically investigated as contrast agents because they offer prolonged delineation due to lower diffusion from tumor sites and increased internalization by tumor cells.[105] As blood-pool agents, they are readily distributed in the intravascular extracellular space and transported to lymph nodes through lymphatic vessels.[7,105,126,127]

Each of these contrast agents has strengths and weaknesses in medical applications. Iron oxide nanoparticles are particularly well suited for molecular and cellular imaging. Because they concentrate a large number of magnetic ions in a small volume, they offer a high signal to noise ratio which translates into high

anatomic resolution.[123,130] Moreover, because they are formed as nanoparticles they have longer blood circulation times and increased retention by cells. In contrast, gadolinium chelates T_1 agents are rarely used in high sensitivity applications such as cellular imaging and tracking because they are rapidly cleared and poorly taken up by cells. [131] Therefore, iron oxide nanoparticles have emerged for MRI contrast agents suitable for molecular/cellular labeling. However, the negative T_2 contrast agent based on iron oxide nanoparticles have significant drawbacks in MRI. The resulting dark contrast image is easily confused with the signal from bleeding, calcification, and susceptibility artifacts, and as a result can be quite misleading in diagnoses.[123] For these more practical reasons the FDA approved brighter Gd chelates including Magnevist® and Omiscan™ are generally the choice of clinicians for MR enhancement of brain tumor, blood vessels, central nervous system, and other abnormal structures or lesions.[132-141]

It would be of great value to develop a T_1-based contrast agent that had the advantages of a nanoparticle form with the benefits of the gadolinium r_1 relaxivity. Gadolinum is the material of choice for this application as it has seven unpaired 4f electrons, providing a large electric magnetic moment and high total electronic spin (S state, S=7/2).[37]   If the S value is high, a slow electron spin relaxation of S-state electrons will closely match the slow water proton spin-relaxation. Thus, S state electrons can induce the longitudinal water proton relaxation.[37,38,142] However, free gadolinium in biological systems can be toxic hence the use of Gd-chelates is limited by toxicity for higher doses. A number of studies have reported out on

nephrologenic system fibrosis (NSF) issue and other potential side effects from the use of Gd-chelates above recommended doses (0.1 mmol Gd/kg of body weight). [143-147]

Such a material could provide: 1) positive (brighter) contrast so as to provide accurate, reliable information for clinical decisions; 2) high relaxivity values with the injection of a small dose; 3) a nanoparticle form to allow for cellular uptake and accumulation as well as longer circulation times; 4) easy surface modification for efficient labeling with target molecules; and 5) low toxicity to minimize potential side effects.

Given the potential there has been recent interest in producing gadolinium containing nanoparticles for use as contrast agents.[17,19,40,43,101,102,113,148-154] Gadolinium oxide, one of the rare earth sequioxide nanoparticles, was synthesized using high boiling polyalcohol solution (polyol method).[14,17,40,43,102,148,155-158] It is direct precipitation in a high boiling point of diethylene glycol (DEG), which acts as a surface capping agent for preventing particle agglomeration. The amount of NaOH in the reaction controlled the reaction yield resulting in gadolinium oxide nanoparticles in the range of 2 to 5 nm. Based on the polyol method, the Tillement group only showed different sizes of gadolinium oxide nanoparticles (2.2, 3.8, and 4.6 nm) by controlling the reaction.[40] Another synthesis approach is the decomposition of rare-earth complexes in the presence of fatty acid or organic ligands in high boiling point solvent.[101,113,152-154,159,160] Single crystalline, monodisperse nanostructures including ultrathin nanoplates, nanorings, nanorods,

and nanodisks were synthesized and the sizes were from 3 to 20 nm. For example, Holloway group demonstrated the shape of gadolinium oxide were changed with spheres, plates, and curved rods by depending on the synthesis factors including metal precursors, surfactants and their ratio.[152] Using decomposition method, there was no report in size control of gadolinium oxide.

Based on polyol method, gadolinium oxide nanoparticles showed r_1 relaxivity values (< 9.5) and act as MRI contrast agent *in-vitro.*[17,43,102,148] Very recently, ultrasmall gadolinium oxide nanoparticles were used for *in-vivo* contrast agents with r_1 relaxivity values (<15).[19,40,103,161-163] The Lee and other research groups considered the toxicity of the gadolinium oxide nanoparticles.[19,103,162-164] For example, Lee group demonstrated the d-glucuronic acid coated lanthanide doped gadolinium oxide was not toxic from 5 μM to 279 μM of Gd(III) ions.[19,163] While promising the extent to which gadolinium nanoparticle r_1 can be optimized so that they can compete with existing clinical contrast agents remains an open question.

In this work, we reported a study of how the diameter and surface chemistry of gadolinium oxide nanoparticles affect their r_1 relaxivity. Gadolinium oxide nanoparticles prepared in organic solvents were transferred to water using different phase transfer agents with high yields ($\sim$80 %). Core diameters and different surface coatings of gadolinium oxide nanoparticles affect the MR relaxivity values since the number of Gd metal ions in a nanoparticle, water proton exchange rate, and rotation are dependent on both variables. Optimized gadolinium oxide nanoparticles exhibit 10-15 fold higher r_1 relaxation than that of Gd-DTPA (4.3 $\sim$ 4.6

$mM^{-1}S^{-1}$) at 1.41 T.[12,13] Moreover, the gadolinium present in the particles is not as labile as Gd-chelates. For example, a screen of acute toxicity with HDF cells found low to no toxicity up to 350 µM (LD_{50}) in contrast to 5.7mmol/kg of body weight of Gd-DTPA (LD_{50}).

3.2. Experimental sections

3.2.1. Chemicals

Gadolinium nitrate hexahydrate ($Gd(NO_3)_3 \cdot 6H_2O$, 99.99 %),oleic acid (OLAC, technical grade 90 %), oleylamine (OLAM, technical grade 70 %), 1-octadecene (1-ODE, technical grade 90 %), poly(acrylic acid) (PAA, Mw=1800), octylamine (OA, 99 %), acrylic acid 2-Acrylamido-2-Methylpropane sulfonic acid copolymer (AA/AMPS), lauryl acrylate (LA, technical grade 90 %), dulbecco's modified eagle's medium (DMEM), fetal bovine serum (FBS), penicilin-streptomycin (PS), and trypsin-EDTA were purchased from Sigma-Aldrich. The synthesis was under high purity nitrogen (N_2, 99.99 %) flow. Methanol (99.8 %), acetone (99.5 %), hexanes (98.5 %), sodium bicarbonate (99.7 %), and dimethylformamide (DMF, 99.8 %), nitric acid (HNO_3, 70 %) and hydrogen peroxide (H_2O_2, 30 %) were purchased from Fisher Scientific; 1-ethyl-3-[3-dimethylaminopropyl] carboiimide hydrochoride (EDC) was purchased from Thermo Scientific; The CellTiter 96® Aqueous One solution Cell Proliferation Assay (MTS assay) was purchase from Promega; Human derman fibroblast (HDF) cells were purchased from Cambrex.

3.2.2. Synthesis of gadolinium oxide (Gd$_2$O$_3$) nanoparticles

2 mmol of gadolinium nitrate hexahydrate was mixed with oleic acid (4 mmol) and 1-octadecene (5 g) and stirred for 2 hours at 110 °C until the Gd precursor was completely dissolved in the solvent as Gd-oleate precursors. After increasing the temperature from 110 to 290 °C, the reaction mixture was refluxed at 290 °C for 3-18 hours. After the reaction is done, the temperature was cooled down to room temperature. The resulting colloidal solution (5 mL) was centrifuged with methanol (20 mL) and acetone (20 mL) at 4150 rpm for 30 minutes and redispersed with hexanes. This purification was repeated six times resulting in purified gadolinium oxide nanoparticle solution. Finally, the Gd$_2$O$_3$ nanoparticles (5 nm) were prepared and stored in hexanes. To make larger Gd$_2$O$_3$ nanoparticles (8, 11, 13, and 22 nm), the oleylamine (2, 6, 8, and 12 mmol) and more 3 g 1-octadecene were added into the gadolinium-oleate mixture (2 mmol gadolinium nitrate hexahydrate, 4 mmol oleic acid, 5 g 1-octadecene) after heating at 110 °C for 2 hours and then refluxed at 290 °C for 3-18 hours. For making smaller 2 nm Gd$_2$O$_3$ nanoparticles, the refluxed reaction temperature was increased from 290 to 320 °C with the amounts of gadolinium nitrate hexahydrate (2 mmol), oleic acid (4 mmol), and 1-octadecene (5 g).

3.2.3. Oleic acid coated Gd$_2$O$_3$ nanoparticles

The oleic acid coated Gd$_2$O$_3$ nanoparticles were followed and modified by a previously published procedure.[165] A specific amount of oleic acid (from 30 μL to

300 μL) was introduced to 1 mL of Gd_2O_3 nanoparticles solution dispersed in ethyl ether (1,500 - 4,000 mg/L of Gd ion concentration). After stirring for 24 hours, ultra pure water (Milipore, 18.2 MΩ·cm) or 0.1 M sodium bicarbonate (pH 9) solution was introduced and stirred for 2 hours. Then a probe sonicator (UP 50H, Dr. Hielscher) was used with 60 % amplitude for 10 minutes for the dispersion in water. The Gd_2O_3 aqueous solution was further stirred for 1 day to evaporate ethyl ether completely by opening the cap. The purification of water-soluble Gd_2O_3 nanoparticles was carried out using ultracentrifugation (optima L-90K ultracentrifuge, Beckman coulter) at 40,000 rpm for 3 hours twice and followed by syringe filtration (pore size of 0.45 uM, Whatman NYL). The resulting clear brown aqueous solution was acquired after purification. To calculate the transfer yield of oleic acid coating, the concentrations of gadolinium ion were compared in both original and transferred solution. Finally, Gd_2O_3 nanoparticles were dispersed in ultra pure water.

3.2.4. Octylamine (OA) modified poly acrylic acid (PAA) (PAA-OA) polymer synthesis

The preparation of PAA-OA polymer and PAA-OA coated Gd_2O_3 nanoparticles followed a previously published procedure.[166] To make PAA-OA copolymer, first PAA (0.6 g, 0.33 mmol) was dissolved in DMF (10 g). After stirring for 10 minutes, EDC (0.58 g, 3 mmol) was added to the PAA/DMF solution, and octylamine (0.5 mL, 3 mmol) was sequentially introduced to the PAA/EDC/DMF solution. After stirring overnight, rotavap was used to remove DMF and keep the PAA-OA solution in a

vacuum. The final PAA-OA solution (15 mg/mL) was redispersed in chloroform (40 mL).

3.2.5. PAA-OA coated Gd_2O_3 nanoparticles

The varied amounts of PAA-OA polymer from 1 to 7 mL were mixed with 1mL Gd_2O_3 nanoparticle/chloroform solution (typically 1,500 to 4,000 mg/L of Gd ion concentration). The mixed solution was stirred for 24 hours and then evaporated the chloroform by using vacuum or air. After adding 0.05 M sodium bicarbonate solution (10 mL), a probe sonicator with 60 % amplitude was used for 10 minutes. The resulting solution was purified with ultracentrifugation (40,000 rpm for 3 hours, twice) and filtered out with syringe filter (0.45 uM, Whatman NYL). The clear brown Gd_2O_3 nanoparticle solution was acquired and completely dissolved in ultrapure MQ water.

3.2.6. Poly (acrylic acid 2-Acrylamido-2-Methylpropane sulfonic acid) (PAMPS)- lauryl acrylate (LA) (PAMPS-LA) polymer synthesis

The PAMPS-LA polymer is synthesized by copolymerization of 30 g of AMPS (0.1447 mol, 207.23 g/mol) and 22.5 mL of LA monomers (240.38 g/mol, 0.0827 mol) in 300 mL of DMF solution under UV light. The polymer solution can be used to coat nanocrystals directly without further purification.

3.2.7. PAMPS-LA coated Gd_2O_3 nanoparticles

The varied amounts of PAMPS-LA polymer from 1 to 7 mL were mixed with 1mL nanocrystal/ethyl ether solution (typically 1,500 to 4,000 mg/L of metal ion concentration). When the solution was cloudy after adding certain amounts of polymer, more DMF solution helped to get a clear mixture solution. The nanocrystal/polymer solution was stirred for 24 hours. After adding ultra pure MQ water, the solution was kept to stir for another 24 hours and allowed to evaporate ethyl ether via air. The resulting solution was purified with ultracentrifugation (40,000 rpm for 3 hours, twice) and filtered out using syringe filter (0.45 uM, Whatman NYL). The clear nanocrystal solution was acquired and completely dissolved in ultra pure MQ water.

3.2.8. MRI relaxivity measurements

MR relaxivity measurement. Various concentration of Gd_2O_3 (0.01 ~2 mM) was prepared by dilution from the stock solution of Gd_2O_3 nanoparticles capped with oleic acid, PAA-OA, and PAMPS-LA polymers for MR relaxivity measurement. To measure r_1 and r_2 of Gd_2O_3 nanoparticles, the MR relaxometer (NMR analyzer, mq 60, Bruker) at 1.41T was used. The r_1 and r_2 values were calculated by determining the slope of $1/T_1$ or $1/T_2$ (s^{-1}) at varying T_R and T_E values against gadolinium concentration (mM).

MR phantom imaging. To image phantoms in MR, a MRI clinical 3T scanner was used. T_1 weighted contrast enhancement was performed running a standard

spin-echo (SE) sequence with 500 ms T_R and 23 ms T_E. The voxel size is 0.4 X 0.4 mm and slice thickness was 1 mm. For this measurement, the different concentration of Gd_2O_3 aqueous solutions (oleic acid, PAA-OA, PAMPS-LA) were used and compared the contrast with Magnevist® (Gd-DTPA) at same concentration

3.2.9. Cell culture and MTS assay

Cell Culture: Human derman fibroblast (HDF) were used and cultured in Dulbecco's Modified Eagle's Medium (DMEM) with 10% fetal bovine serum (FBS) and 1 % penicilin-streptomycin (PS). The cells were lifted by trypsin-EDTA and re-suspended in media (DMEM with 10% FBS and 1% PS) solution for the passaging.

Cell Viability test (MTS assay): To determine the cell toxicity depending on their sizes and surface coatings (oleic acid, PAA-OA, and PAMPS-LA), the standard colorimetric assay, MTS (CellTiter 96, Promega) was used. HDF cells were placed and grown in 96 well culture plates with over 80 % confluency. Each set was prepared with different concentration of Gd_2O_3 nanoparticle solutions (0-500 uM). One set was treated as a blank (no nanoparticles) and last set was used for the untreated control (ethanol). The treated cells with Gd_2O_3 nanoparticle aqueous solution were incubated for 24 hours. The solution was then suctioned out and replaced with 100 uL fresh media (DMEM with FBS 10 % and 1 % PS) solution and 20 uL MTS agent to each well. After incubating for 1 hour at 37 °C and 5 % CO_2, the absorbance at 490 nm of the solution was measured with a plate reader (SPectraMax, M2, Molecular devices). The experiment was repeated three times for

the average. The LD_{50}, which gives the lethal dose required for half of the cells to die, was calculated by the percentage of the cell viability.

3.2.10. Instruments and characterization

Transmission electron microscope (TEM). To measure the diameter of the Gd_2O_3 nanoparticles a JEOL 2100 field emission TEM operating at 200 kV with a single tilt holder was used. TEM sample was prepared by evaporation of one drop of Gd_2O_3 nanoparticle solution on the ultrathin 400 mesh copper grids (Ted Pella Inc.). The size and size histograms of Gd_2O_3 nanoparticles were calculated by counting over 500 particles with Image-Pro Plus 5.0 (Media Cybernetics, Inc., Silver Spring, MD).

X-ray diffraction (XRD). X-ray powder diffraction of Gd_2O_3 nanoparticles was carried out using a Rigaku D/Max Ultima II with a zero background sample holder. The X-rays were generated at 40 KV and 40 mA and the range of 2θ was 10 to 80 degrees. For reference the JCPDS card was used.

X-ray photoelectron spectroscopy (XPS). XPS data was recorded by PHI quantera with a monochromatic aluminium 38.6 W. An x-ray source,with an x-ray spot size (200 um) with a pass energy of 26 eV at 45° was used for the measurement.

Dynamic light scattering (DLS) and zeta potential. The hydrodynamic size (nm) and zeta potential (mV) of oleic acid and PAA-OA coated Gd_2O_3

nanoparticles were measured by Malvern Zetasizer Nanoseries (Malvern, UK). The measurement was repeated five times for the average.

Inductive coupled plasma-optical emission spectroscopy (ICP-OES). To measure the gadolinium concentration in a nanoparticle, Perkin Elmer ICP-OES equipped with auto sampler was used. The preparation of sample for ICP-OES was prepared by acid digestion using nitric acid (HNO_3, 70 %) and hydrogen peroxide (H_2O_2, 30%).

Total organic carbon (TOC). A Shimadzu TOC-L was used to measure the carbon concentration for surface functionalized gadolinium nanoparticles in water. Three replicates of each sample were prepared by adding 1 ml of the stock nanoparticle sample and diluting to 8.5 mL with Milli-Q 18 MΩ pure water. Each sample was run on a total nonpurgeable organic carbon (NPOC) assay with triplicate 50 µL injections. The calibrations from 0.5 to 60 ppm were prepared using TOC standard solution (Sigma-Adrich) with high R^2 (0.998) value.

Calculation of grafting density (GD). The calculation of grafting density (σ) was calculated from TOC data using the equation below, similar to previously published method.[167]

$$\sigma = \frac{[C] * MW_n}{MW_p * C_n * [NP] * (4\pi r_{core}^2)}$$

The nonpurgeable organic carbon concentration ([C]) from TOC analysis must be converted from mg/L (ppm) to mol/liter (molarity) by considering molar

mass of carbon (12,010 mg/mol). To determine the number of polymer molecules the carbon concentration is multiplied by the molecular weight of the monomer (MW_n) and divided by the polymer molecular weight (MW_p) times the number of carbons per monomer (C_n). By dividing by the molar concentration of nanoparticles, [NP], and the surface area of the particle the resulting grafting density is achieved.

3.3. Result and discussions

3.3.1. Synthesis of size tunable gadolinium oxide nanoparticles

A central goal of this work was to examine how particle diameter and surface coating affects the relaxivity of (Gd_2O_3) nanoparticles in aqueous suspensions. Towards that end, we adapted synthetic methods used to form uniform metal oxide nanocrystals in organic solutions to gadolinium oxide synthesis. This synthesis proceeds via the thermal decomposition of gadolinium nitrate precursors in the presence of organic surfactants (oleic acid or the mixture of oleic acid and oleylamine) (Schematic 3-1). Decomposition occurs at high temperature (290 °C).

In a typical reaction, a Gd-oleate precursor was first prepared by heating gadolinium nitrate hexahydrate and oleic acid at 110 °C for two to three hours. This pre-treatment led to much better particle uniformity than reported before, perhaps because of the ordering of the fatty acid chains.[168] This treatment resulted in a black-brownish Gd-oleate complex, which was then refluxed system at 290 °C under N_2 for three to eighteen hours. The Gd_2O_3 nanoparticles are nearly monodisperse

with narrow diameter distributions (<15 %) (Figure 3-1, Figure 3-2, and Figure 3-3). Moreover, they can be formed with a wide range of diameters, from 1.8 to 22 nm, by tailoring the reflux time, temperature, precursor concentration, and surfactant type and amount. Transmission electron microscopy (TEM) shows gadolinium oxide nanoparticles with different core diameters from 1.8 to 22 nm (Figure 3-1).
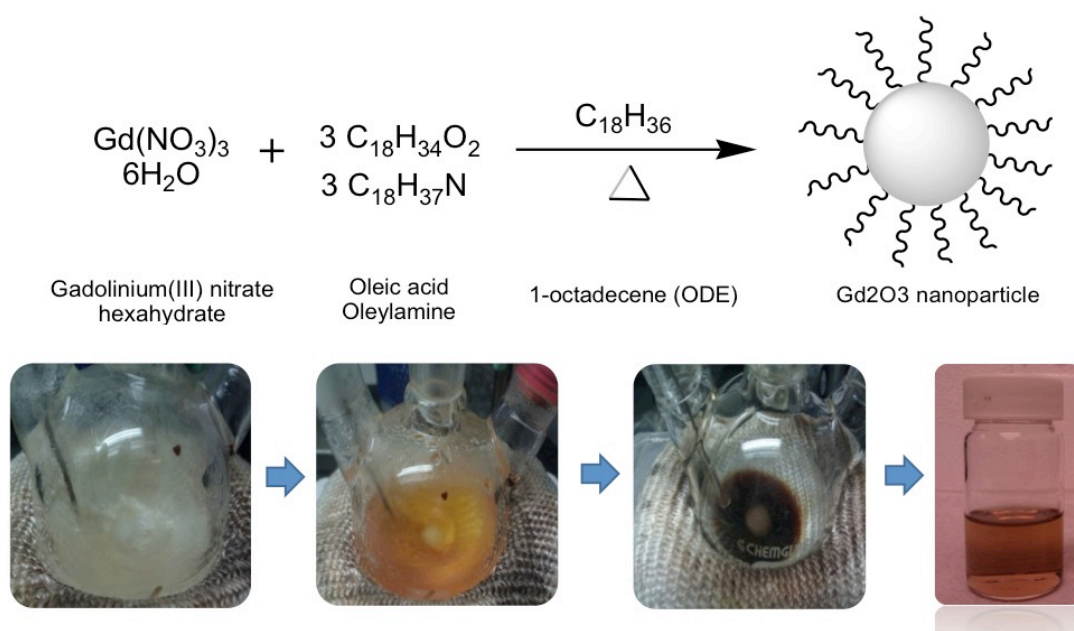
Schematic 3-1 Schematic diagram of Gd oxide synthesis

Schematic diagram and photographs showing the synthesis of Gd_2O_3 nanoparticles based on thermodecomposition of gadolinium(III) nitrate hexahydrate in the presence of organic surfactant (oleic acid and oleylamine) and 1-octadecene.
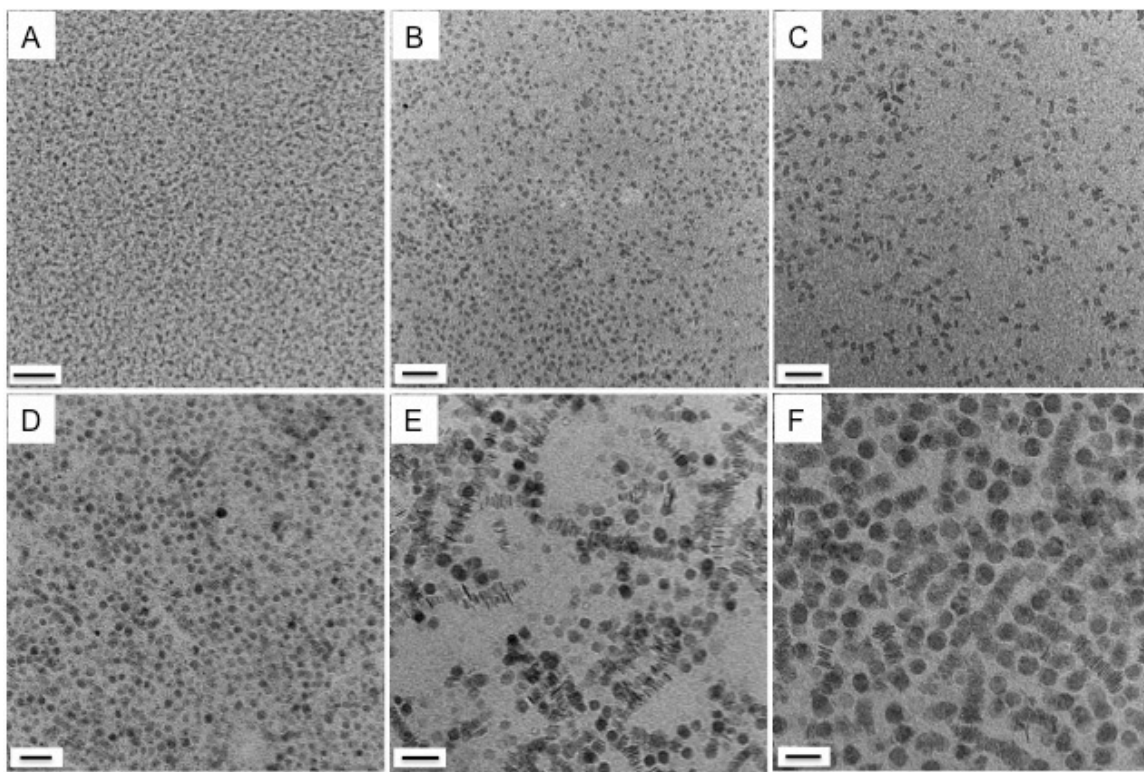
Figure 3-1 TEM images of Gd_2O_3 nanoparticles

TEM images of Gd_2O_3 nanoparticles ranging from 1.8 nm to 22 nm. The diameter of Gd_2O_3 nanoparticles (A-F) are 1.79 ± 0.23, 5.02 ± 0.45, 7.95 ± 0.82, 10.82 ± 1.75, 13.18 ± 2.09, and 21.97 ± 2.78 nm, respectively. The scale bars are 50 nm except A (20 nm). The histograms for the size distribution of Gd_2O_3 nanoparticles are shown in Figure 3-2.
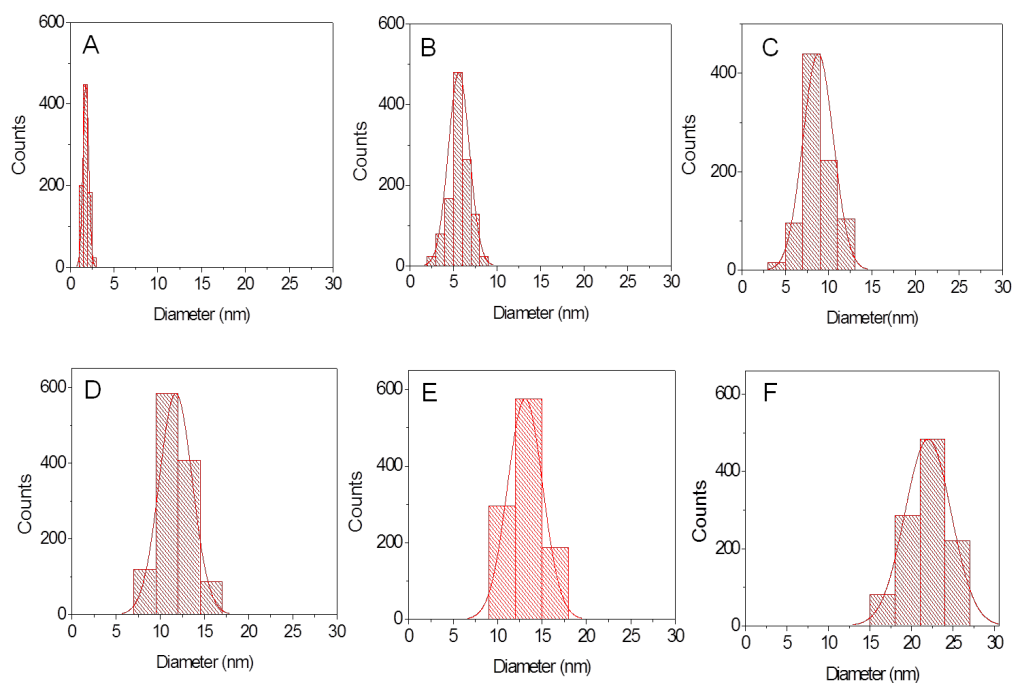
Figure 3-2 The histograms of Gd_2O_3 nanoparticles

The histograms of Gd_2O_3 nanoparticles ranging from 1.8 to 22 nm. The average diameters with standard deviataion are (A) 1.79 ± 0.23 nm, (B) 5.02 ± 0.45 nm, (C) 7.95 ± 0.82 nm, (D) 10.82 ± 1.75 nm, (E) 13.18 ± 2.09 nm, and (F) 21.97 ± 2.78 nm, respectively.
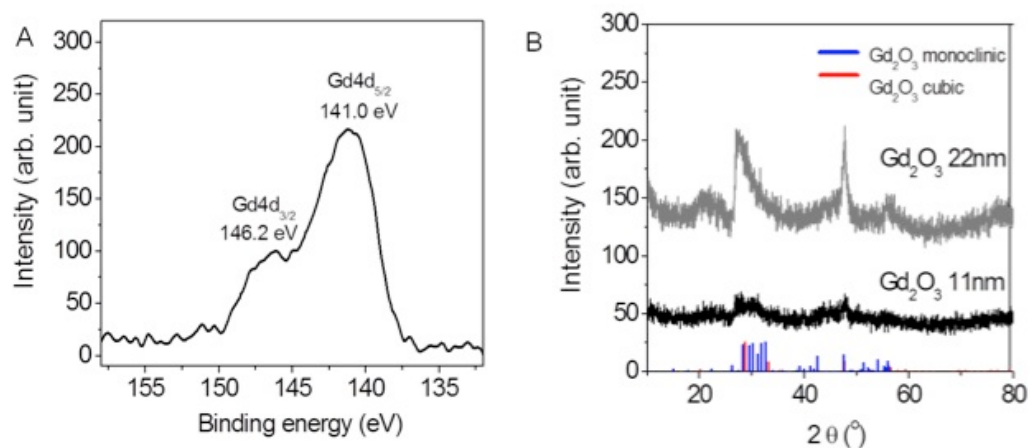
Figure 3-3 XRD and XPS data of Gd_2O_3 nanoparticles

A) XPS data of Gd_2O_3 nanoparticles (11 nm diameter) showing Gd $4d_{3/2}$ at 146.2 eV and (B) XRD Data of Gd_2O_3 nanoparticles with diameter 11 nm and 22 nm. For the references, JCPDS Gd_2O_3 monoclinic (# 43-1015) and cubic (# 43-1014) were used.

The shape, morphology, crystal structure, and composition of Gd_2O_3 nanoparticles were evaluated by transmission electron microscopy (TEM), X-ray photoelectron spectroscopy (XPS), and X-ray diffraction (XRD) measurement (Figure 3-1 and Figure 3-3) In the TEM images, the Gd_2O_3 nanoparticles appear as ultrathin nanoplates or nanodisks; in the case of plates/discs they can be visualized both parallel to the underlying carbon coated copper grid as well as perpendicular and standing on their edge (Figure 3-1). When perpendicular it was possible to measure edge thicknesses on the order of 1.1 to 1.2 nm. Sometimes the plates/discs would stack on top of each other, giving very dark contrast in the images. Due to high oxophilicity, the oleic acid ligand was strongly bound to the gadolinium nanoparticles rather than oleylamine.[169] The capped oleic acid ligand prevented

self-aggregation of nanoparticles via inter-particle dipolar-dipolar repulsive force, and was well dispersed in non-polar solvent (1-octadecene) with good dispersibility (side to side).[160] When adding only oleic acid, the nuclei of gadolinium oxide underwent a fast growth and finally they would form dynamically stable nanoplates with smaller size.[160] Increasing the amount of oleylamine with oleic acid, resulted in particle size increase from 8 to 22 nm. Gd_2O_3 nanoparticles above 11 nm in diameter typically aligned parallel to the surface without a preferred direction to minimize their surface energy due to interfacial tension (self assembled face to face behavior) (Figure 3-4). The formation of gadolinium oxide nuclei with oleylamine prefered a slow growth and they transformed to a thermodynamically stable nanodisks.[40] When changing the reaction conditions including time, concentration, temperature, and surfactant ratio, the average diameter of nanoplates/nanodisks increased from 1.8 to 22 nm, but their thickness remained constant (~1.1 nm). Over the last few years, others have observed that gadolinium oxide and rare earth doped Gd_2O_3 nanoparticles often form unusual shapes including nanorings, nanoplates, and ultra-narrow nanorods. However, those reactions proceeded at lower temperatures using gadolinium acetate hydrate or gadolinium acetylacetonate hydrate precursors with no size tunability.[101,113,152-154]
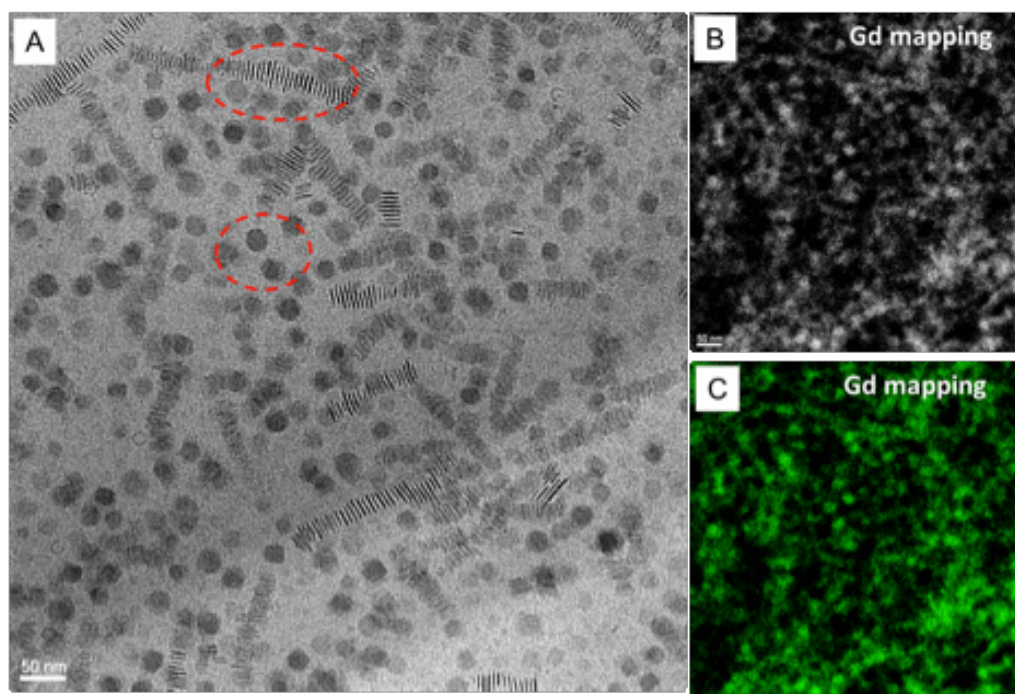
Figure 3-4 The TEM image of 22 nm diameter gadolinium oxide nanodisks

In the TEM images, some ultrathin nanodisks were aligned parallel with face-to-face direction. From GIF mapping, these nanodisks have gadolinium in a nanoparticle.

The chemical composition and structure of the products were consistent with Gd_2O_3 nanoparticles. X-ray photoemission spectroscopy (XPS) found Gd 4d 3/2 and Gd 4d 5/2 features at 146.2 eV and 141 eV, respectively (Figure 3-3 (A)). This corresponds to an oxidation state of Gd in keeping with Gd^{3+}. The crystalline structure of Gd_2O_3 nanoparticle was determined by x-ray diffraction (XRD) of two different diameters of Gd_2O_3 nanoparticles. As is apparent in the data (Figure 3-3 (B)), the peaks are quite broad as would be expected for this plates/disks (< 1.2 nm).[152,154,159] By overlapping the reference peaks using JCPDS card, the Gd_2O_3

nanoparticles contained both cubic and monoclinic structures.[152]   Larger 22 nm diameter Gd_2O_3 nanoparticles, had more intense monoclinic features.

Diameter control was best achieved through control over the type and amount of surfactant (oleic acid/oleylamine), though monomer concentration and temperature also played a role (Figure 3-5). Most particle growth occurs through the dissolution and reformation of particles rather than from soluble monomers. Smaller particles have higher surface energies or chemical potentials. Thus, they dissolve and grow faster than the large ones, leading size focusing effect, as described by the Gibbs-Thomson equation.[170-172]   When gadolinium (III) nitrate hexahydrate reacted with oleic acid at 110 °C, the intermediate gadolinium oleate precursor was generated. When refluxed to high temperature at 290 °C, the nucleation and subsequent growth of gadolinium oxide undergo with selective addition of oleylamine. The Yan group proposed the formation mechanism of rare earth oxide nanocrystals (RE_2O_3) via two steps of rare-earth oleates and subsequent decomposition of catalyzed oleylamine.[160] The ultrathin nanoplates and nanodisks RE_2O_3 nanocrystals were produced by fast growth with [100] facets and slow growth of [111] facets, respectively. The molar ratio of oleic acid and oleylamine was very important to control the diameter of gadolinium nanoparticles (nanoplates/nanodisks).

As the amounts of oleylamine increased from 0 to 12 mmol, the particle diameters of Gd_2O_3 nanoparticles increased from 5 to 22 nm with fixed amounts of gadolinium nitrate hexahydrate (2 mmol) and oleic acid (4 mmol) (Figure 3-1 and

Figure 3-5). In contrast, as increasing the amounts of oleic acid from 4 to 8 mmol with 2 mmol gadolinium nitrate hexahydrate, the particle diameters were decreased from 10 to 7 nm. The high ratio of organic surfactants between oleic acid and oleylamine (4:0 to 4:12) may result in more labile gadolinium; as the particles are more soluble, growth increased. Increasing concentration of precursors (Gd nitrate/oleic acid/oleylamine) from 2/4/6 to 40/80/120 produced larger particle diameters from 11 to 22 nm. Likewise, reducing the amounts of 1-octadecene from 15 g to 4 g with 2 mmol gadolinium nitrate hexahydrate also the particle diameter increased from 7 to 13 nm. Higher concentration of precursors increased higher monomer concentration and allowed particle growth.

Under a fixed concentration of precursor (gadolinium nitrate/oleic acid/oleylamine = 4/12/12) and reflux time (6 hours), as the temperature increased from 260 to 320 °C, the particle size was not changed significantly. Without oleylamine, as increasing temperature (290 to 320 °C), the particle diameter was reduced from 5 to 1.8 nm. High temperature may cause a higher concentration of nuclei and decreasing the growth. The reflux time is not a significant factor for the size change. The synthetic parameters related to the size control of gadolinium oxide are described in Figure 3-5. In summary, to get highly monodisperse particles requires first that the Gd-oleate complex be stabilized for several hours at 110 °C;, second that the reaction temperatures be high - 260 to 320 °C;, and finally a long reflux time to fully sharpen size distributions as small particles dissolved and added to larger particles.
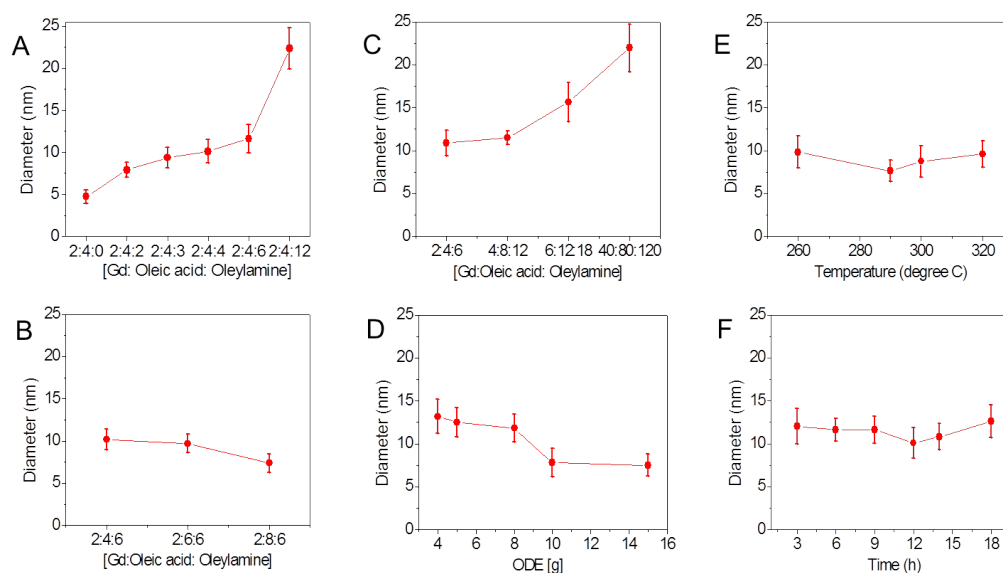
Figure 3-5 Important parameters for size tunability

The size controllable Gd_2O_3 nanoparticles by changing synthetic parameters (A) oleylamine, (B) oleic acid, (C) concentration of precursors, (D) ODE, (E) temperature, and (F) reflux time; As increasing the amounts of oleylamine (A), the particle sizes were increased from 5 to 22 nm. As increasing oleic acid (B), the particle sizes were decreased from 10 to 7 nm. When increasing high concentration of precursors or reducing ODE amounts, the particle sizes were increased due to higher monomer concentration. The temperature (E) and (F) did not show any significant size change.

3.3.2. Phase transfer of gadolinium oxide nanoparticles

To evaluate Gd_2O_3 nanoparticles as T_1 MR contrast agents, the Gd_2O_3 nanoparticles need to be transferred to water with biocompatible coatings. These coatings must perform two seemingly opposite functions: first, they must prevent the release of toxic Gd(III), which is a major cause of NSF[143-147], but at the same time

allow for facile access of water to the surface gadolinium atoms. We evaluated two very different surface coatings for these reasons. One relied on the formation of a dense and thin oleic acid bilayer, while the others employed PAA-OA and PAMPS-LA co-polymers.[165,166,173] In all cases, the original organic layer present at the nanoparticle interface was not disturbed. Figure 3-6 illustrates the phase transfer process using oleic acid, PAA-OA, and PAMPS-LA copolymers. In the case of the oleic acid, the bilayer forms and a free acid group is present at the surface. The PAA-OA and PAMPS-LA on the other hand wrap the organic ligands to the particle leaving the PAA or PAMPS to impact stability in aqueous solutions.
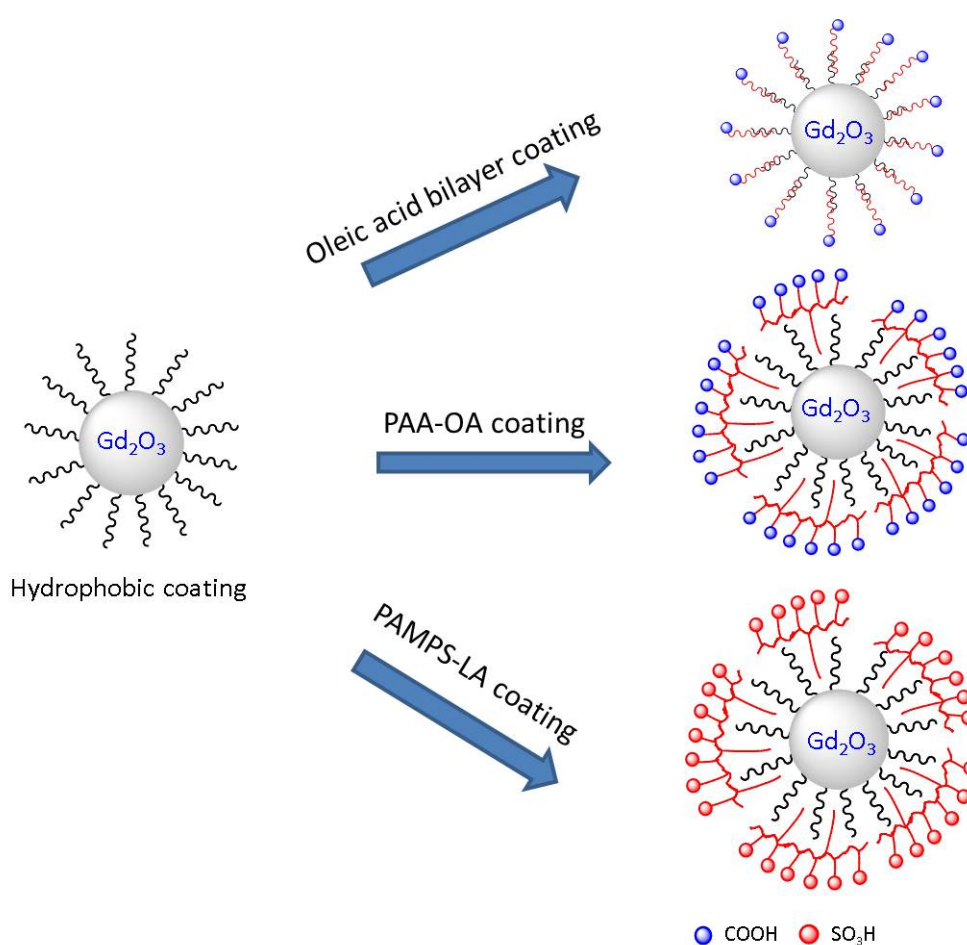
Figure 3-6. Phase transfer of Gd_2O_3 nanoparticles
Schematic diagram of phase transfer method of ligand exchange using oleic acid and polymer encapsulation using PAA-OA and PAMPS-LA.

The transfer of particles via bilayers was reported previously for iron oxide, and the process is similar in this work.[165] What results are materials with very small hydrodynamic diameters (< 30 nm) because of the small length of oleic acid (e.g. 1.97 nm). Such a rigid and dense bilayer coating is very effective for dispersing nanoparticles in water, and it can be applied for a wide range of core diameters

(Figure 3-7). The phase transfer efficiency (~50 %) was found by comparing the concentration of Gd(III) in hexanes to that found in the water. Several factors controlled the efficacy of the phase transfer process. If the amount of phase transfer agents (oleic acid, PAA-OA, and PAMPS-LA) were not large enough to cover the hydrophobic surface of Gd_2O_3 nanoparticles, then transfer efficiencies would drop substantially (10 - 30 %). Also, low yields (10 - 40 %) were observed when too much phase transfer agent was added. Both oleic acid and amphiphilic co-polymers can form micelles above the critical micelle concentration. Under the optimal conditions with amounts of phase transfer agents, the best transfer efficiencies of oleic acid, PAA-OA, and PAMPS-LA were 40~50 %, 70~80 %, and 70-80 %, respectively (Figure 3-7).
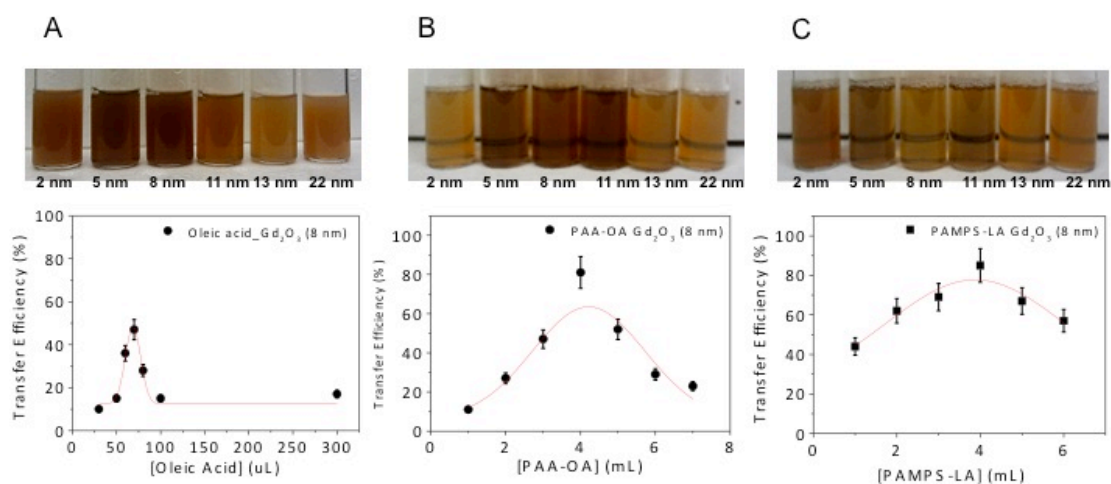
Figure 3-7 The phase transfer yields of oleic acid, PAA_OA and PAMPS-LA coated Gd$_2$O$_3$ nanoparticles

(A) The photograph of oleic acid coated Gd$_2$O$_3$ nanoparticles with different sizes from 1.8 nm to 22 nm and phase transfer efficiency (%) of oleic acid coating when using various amounts of oleic acid (30-300 uL) in 1ml Gd$_2$O$_3$ nanoparticle/ethyl ether solution (1.5~4 mg/ml). (B) The photograph of PAA-OA coated Gd$_2$O$_3$ nanoparticles ranging from 1.8 nm to 22 nm diameters and phase transfer efficiency (%) using various amounts of PAA-OA solutions (1 to 7 ml, 15 mg/ml PAA-OA) with 1 mL Gd$_2$O$_3$ nanoparticle/ethyl ether solution (1.5~4 mg/ml). (C) The photograph of PAMPS-LA coated Gd$_2$O$_3$ nanoparticles ranging from 1.8 nm to 22 nm diameters and phase transfer efficiency (%) using various amounts of PAMPS-LA solutions (1 to 6 ml) with 1 mL Gd$_2$O$_3$ nanoparticle/ethyl ether solution (1.5~4 mg/ml). The concentrations of Gd$_2$O$_3$ nanoparticles were analyzed by ICP-OES.

PAA-OA and PAMPS-LA copolymers represent a very different kind of surface coating as compared to the OA bilayers. These amphiphilic polymers contain both hydrophobic tails and hydrophilic COOH or SO$_3$H groups; the rationale is that the hydrophobic tail surrounds the hydrophobic Gd$_2$O$_3$ nanoparticles, while the

hydrophilic chain transfers them into water. This process does not require a direct ligand exchange of the nanoparticle surface coating, but rather encases the particles in another thicker layer of polymer. As a result, PAA-OA or PAMPS-LA polymer coated Gd_2O_3 nanoparticles are larger in hydrodynamic diameter (core size 22 nm, oleic acid coating 43 nm, PAA-OA coating 47 nm, PAMPS-LA coating 49 nm).

An important characteristic for both surfaces is the number of surface agents per particle; very densely covered surfaces should be less accessible to water for example, and led to less lower r_1 relaxivity in MRI. Previously, the surface coverage of polymers was determined by total organic carbon analysis (TOC).[167] The grafting density is strongly dependent on the molecular weight of polymers and decreased as molecular weight increased. A high molecular weight polymer has lower grafting density, and could offer more surface access. Using TOC measurement, we examined the grafting density of these transfer agents. The molecular weights of these agents of oleic acid, PAA-OA, and PAMPS-LA are 283, 2783, 4615 g/mol, respectively (Table 3-1).[165,166] With 5 nm gadolinium oxide nanoparticles, the grafting densities of oleic acid, PAA-OA, PAMPS-LA were 8.67, 0.86, and 0.94, respectively (Figure 3-8). These grafting densities of polymers are strongly related to the permeability and diffusion time of MR relaxivity.

Table 3-1 The grafting densities of phase transfer agents

Iron oxide	Polymer/nm2 (grafting density)		
Size	OA	PAA-OA	PAMPS-LA
Molecular weight (theoretical)	283	2783	-
Molecular weight (experimental)			4615
5 nm	8.67	0.86	0.94
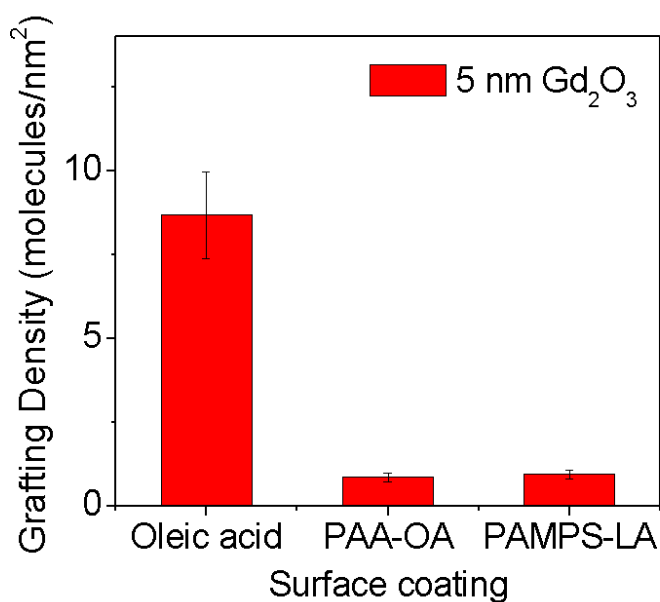
Figure 3-8 The grafting densities of oleic acid, PAA-OA, and PAMPS-LA

The dynamic light scattering (DLS) and zeta potential studies as well as visual changes for the stability confirmed that the Gd_2O_3 nanoparticles were not aggregated and stable in aqueous suspension. DLS measures the hydrodynamic diameter using 4 mW He-Ne laser at 633 nm and noninvasive 173° back scatter

geometry. When the particles are illuminated with a laser, the intensity of scattered light fluctuates at a rate dependent on the size of the particles. Particles in a suspension undergo Brownian motion and smaller particles moves more rapidly than the larger one. The intensity of fluctuations gives the velocity of the Brownian motions, or the diffusion coefficient D, the hydrodynamic size of the particle can be used by Stokes-Einstein relationship. [174,175]

$$D(h) = \frac{kT}{6\pi\eta D}$$

Where D is the diffusion coefficient, k is the Boltzmann constant, T the absolute temperature, η is the velocity, and D (h) is the hydrodynamic radii. The hydrodynamic size measures the radii of a sphere that diffuse at the same rate as the molecule. This sphere includes a hydration, which means the process of attraction between the molecules of a solvent and the molecules of a substance dissolved. Thus, the attracted molecules increase the radii.

DLS and zeta potential studies as well as visual observation indicated that once phase transferred, the Gd_2O_3 nanoparticles remained non-aggregated and stable in aqueous suspension (Figure 3-9 (A)). The hydrodynamic sizes of all oleic acid, PAA-OA, and PAMPS-LA coated Gd_2O_3 nanoparticles ranged from 23 to 49 nm (Figure 3-9 (A)). The hydrodynamic sizes by DLS increased as expected when the core diameters increased from 1.8 nm to 22 nm, and there was no evidence of aggregation. Both oleic acid and PAA-OA capped Gd_2O_3 nanoparticle solution with COOH ligands had large negative charges (-60~-80 mV) that varied with diameters

(Figure 3-9 (B)). The PAMPS-LA coating also had negative zeta (-65 ~ -68 mV) potential due to their sulfonyl group. The Table 3-2 summarizes the hydrodynamic size and zeta potential of gadolinium oxide nanoparticles with various coatings. Given the charge stabilization, hydrodynamic size was monitored over time for Gd_2O_3 nanoparticles at various temperatures, buffer conditions, pH, and ionic strengths. Additionally, particle stability was also screened in phosphate buffered saline (PBS), borate buffer, and cell medium (DMEM). While both particle surfaces imparted good stability in most of these conditions, the PAA-OA or PAMPS-LA Gd_2O_3 nanoparticle aqueous solutions were more stable than oleic acid capped Gd_2O_3 nanoparticle aqueous suspensions at PBS and cell medium (from Figure 3-10 to Figure 3-13). The Table 3-3 shows the stability of hydrodynamic size at various conditions.
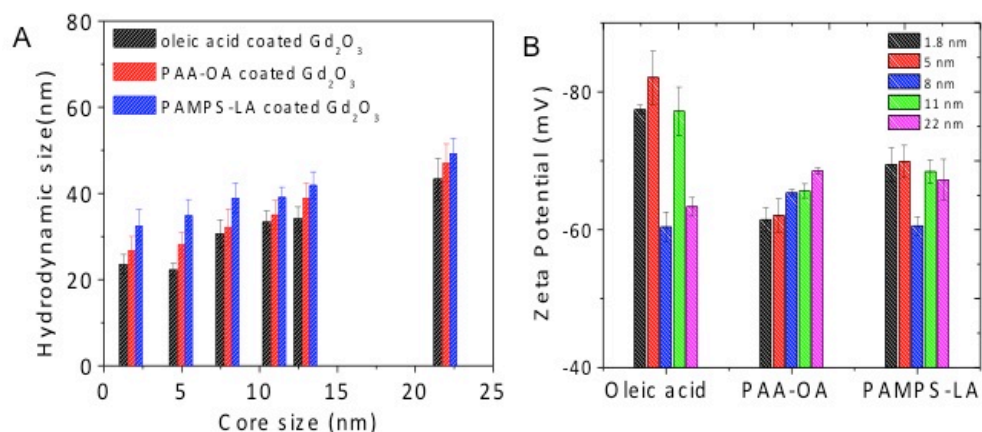
Figure 3-9 (A) The hydrodynamic size by DLS and (B) Zeta Potential of Gd_2O_3 nanoparticles with different coatings

(A) The hydrodynamic sizes of oleic acid, PAA-OA, and PAMPS-LA coated Gd_2O_3 nanoparticles with different core diameters (1.8 to 22 nm) using dynamic light scattering (DLS) analysis. The measurements were repeated 5 times and the average diameters with errors were shown. (B) Zeta Potential (mV) of oleic acid, PAA-OA, and PAMPS-LA coated Gd_2O_3 nanoparticles. Due to carboxylic acid (COOH) or surfurnyl group and basic solution, the zeta potential is around -60~80 mV. The average number with standard deviation was determined by the repeated measurement (5 times).

Table 3-2 The hydrodynamic size and zeta potential of gadolinium oxide nanoparticles with various coatings

Core Size (nm)	Hydrodynamic size (nm)			Zeta Potential (mV)		
	Oleic acid	PAA-OA	PAMPS-LA	Oleic acid	PAA-OA	PAMPS-LA
1.8	23.55± 2.25	26.78± 3.31	32.45± 2.78	-77.40±0.66	-61.47±1.72	-69.43 ± 2.46
5	22.25± 2.47	28.12 ± 2.77	34.86 ± 3.47	-82.07±3.86	-62.03±2.43	-69.9 ± 2.34
8	30.67± 3.22	32.18± 3.23	38.87 ± 4.22	60.40±2.17	-65.33±0.5	-60.57 ± 1.33
11	33.38 ± 2.59	35.03 ± 3.35	39.12 ± 3.59	-77.20±3.5	-65.63±1.02	-68.43 ± 1.73
13	34.14± 3.72	38.89 ± 4.49	41.88 ± 4.72	-64.65±4.24	-63.65±3.43	-67.23 ± 2.98
22	43.35± 4.79	47.05± 5.43	49.25± 5.79	-63.33±1.34	-68.5±0.46	-64.53 ± 3.46
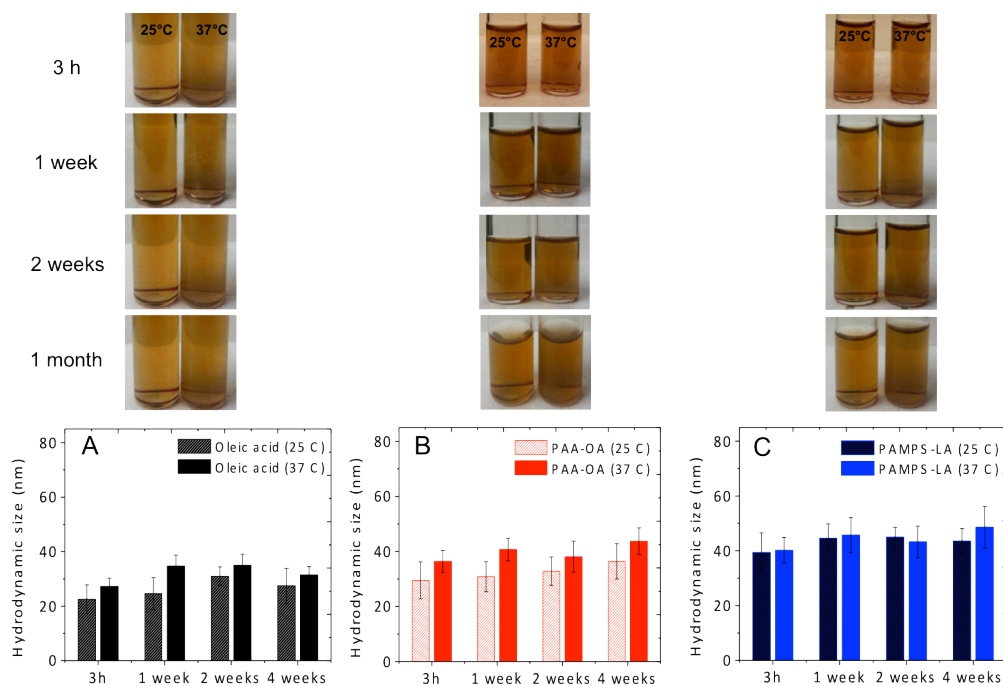
Figure 3-10 The stability of gadolinium oxide suspensions at 25 °C and 37 °C

The stability test of (A) oleic acid, (B) PAA-OA, and (C) PAMPS-LA coated Gd_2O_3 nanoparticles at room temperature (RT) and body temperature (37 °C) from 3 h to 4 weeks. The stability data were based on the photographs and the changes of hydrodynamic size (nm) for long-term duration (4 weeks).
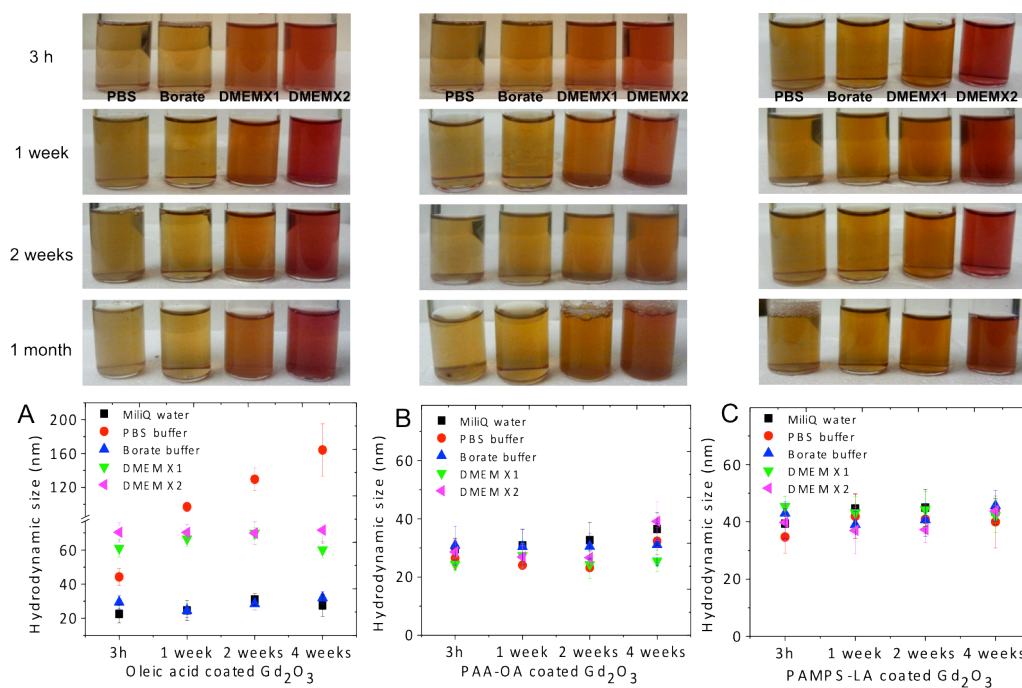
Figure 3-11 The stability of gadolinium oxide suspensions with different buffer conditions

The stability test of (A) oleic acid, (B) PAA-OA, and (C) PAMPS-LA coated Gd_2O_3 nanoparticles at different buffer conditions including PBS buffer, borate buffer (BB), DMEM 1 media solution with nanoparticles in water (1:1 v/v ratio), and DMEM2 cell media solution with nanoparticle solution in water (2:1 v/v ratio). The stability data were based on the visible change (photographs) and the differences of hydrodynamic size (nm) for long-term duration (up to 4 weeks).
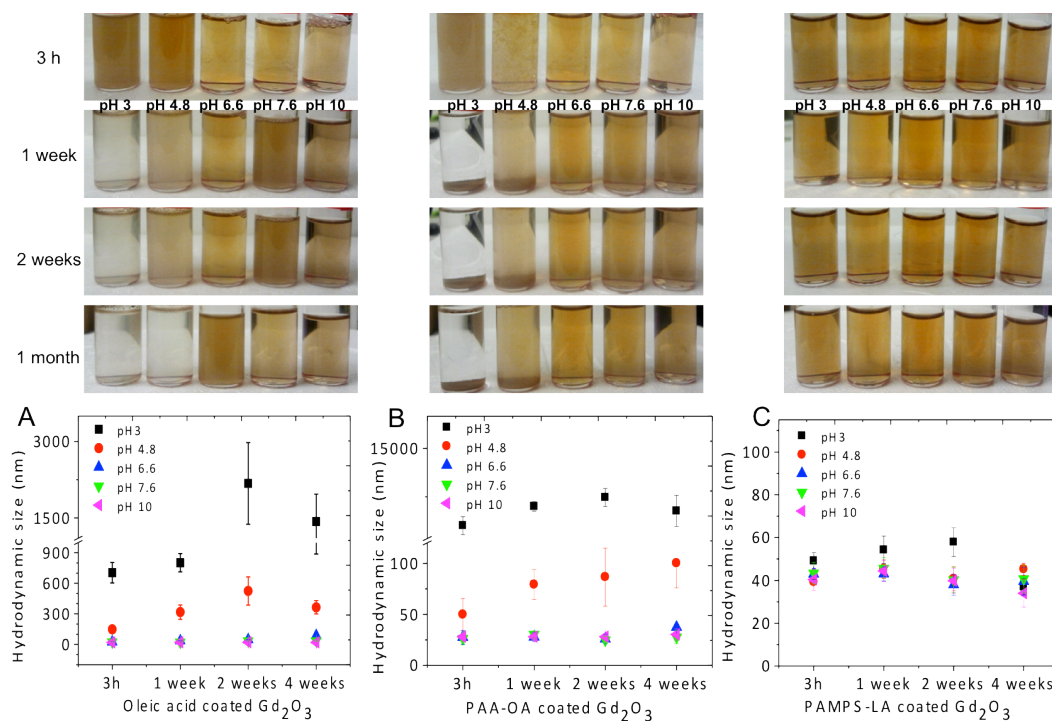
Figure 3-12 The stability of gadolinium oxide suspensions with different pH

The stability test of (A) oleic acid, (B) PAA-OA, and (C) PAMPS_LA coated Gd_2O_3 nanoparticles at different pH conditions from 3, 4.8, 6.6, 7.6, and 10. The stability was determined from the photographs and changes of hydrodynamic size for long-term duration (up to 4 weeks)
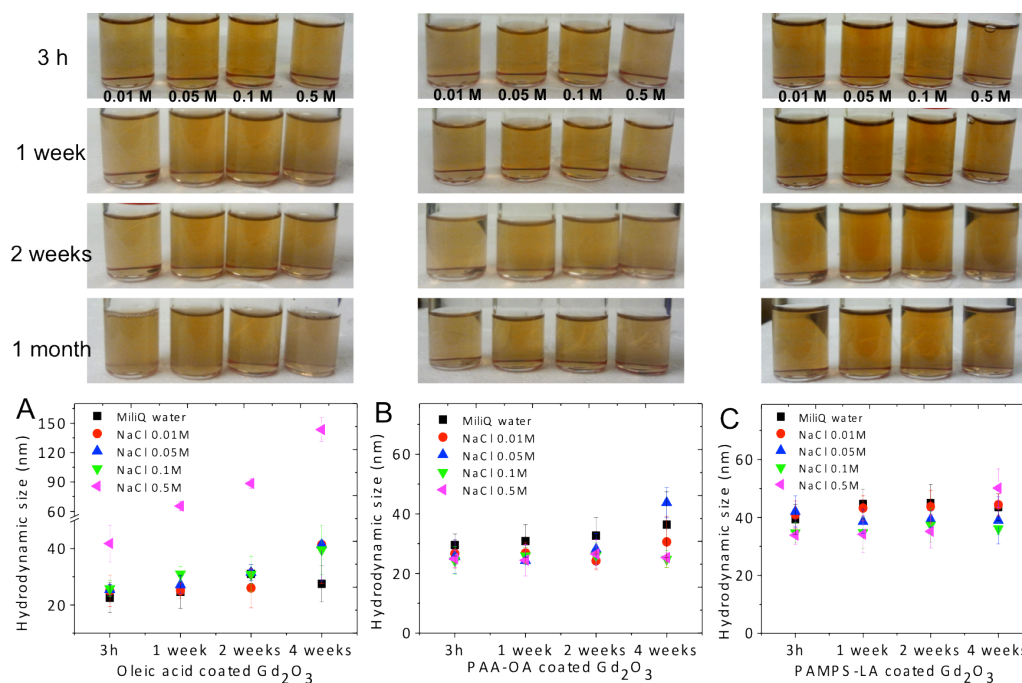
Figure 3-13 The stability of gadolinium oxide suspension with different ionic strengths

The stability test of (A) oleic acid, (B) PAA-OA, and (C) PAMPS-LA coated Gd_2O_3 nanoparticles at different ionic strengths (0.01 M NaCl to 0.5M NaCl). The stability data were based on the visible photographs and DLS measurements for long-term duration (up to 4 weeks).

Table 3-3 The hydrodynamic size stability of gadolinium oxide nanoparticle suspensions

	Hydrodynamic size (√ : stable, X : non-stable, △ : little stable)													
	Temperature		Buffers				pH					NaCl (M)			
	25C	37C	PBS	BB	DMEM (1:1)	DMEM (2:1)	3	4.8	6.6	7.6	10	0.01	0.05	0.1	0.5
Oleic acid	√	√	×	√	△	△	×	△	√	√	√	√	√	√	×
PAA-OA	√	√	√	√	√	√	×	△	√	√	√	√	√	√	√
PAMPS-LA	√	√	√	√	√	√	√	√	√	√	√	√	√	√	√

3.3.3. MR relaxation dynamics of Gd_2O_3 nanoparticles

The contrast agents can be evaluated by their relaxivity, or how much the relaxation rates of water protons are increased in the presence of the contrast agents (e.g. gadolinium oxide) at a given concentration. The relaxivity (r_i) is defined as the increase in relaxation rate per concentration of paramagnetic agents, or the slope of a plot of relaxation rate (R_i (S^{-1})= $1/T_i$)$_{obs}$ versus the concentration of agent (mM) (eq.1).[38,142,176] Total paramagnetic relaxation enhancement can include both an inner sphere component (Solomon-Bloembergen Equation) from the proton relaxation of a solvent molecule (e.g. water) directly coordinated to the Gd(III) and an outer-sphere component from solvent in the second coordination sphere and the bulk solvent.[38,142,176] (eq.2)

$$R_i = \left(\frac{1}{T_i}\right)_{obs} = \left(\frac{1}{T_i}\right)_{diamagnetic\ (e.g.water)} + r_i[Gd] \quad i = 1,2 \quad (eq.1)$$

$$\left(\frac{1}{T_i}\right)_p = \left(\frac{1}{T_i}\right)_{inner\ sphere} + \left(\frac{1}{T_i}\right)_{outer\ sphere} \qquad i = 1.2 \ (eq.\,2)$$

The inner sphere contribution is due to the direct interaction between the Gd electron spins and water protons, whereas outer sphere relaxation arises from the interactions between the Gd electrons spin and bulk water protons that are randomly diffusing.

In order to examine whether Gd_2O_3 nanoparticles could be applied as a T1 MRI contrast agent, we measured the longitudinal relaxation time (T_1) and transverse relaxation time (T_2) of various nanoparticle suspensions. Figure 3-14 shows the r_1 and r_2 relaxivity values for both PAA-OA and PAMPS-LA capped Gd_2O_3 nanoparticles with 1.8 nm and 5 nm core diameters. These parameters were found by plotting 1/T as a function of the Gd (III) concentration, and calculating the r_1 and r_2 by obtained from the slope.[17,19] The r_1 relaxivity values of PAMPS-LA capped Gd_2O_3 nanoparticles with 1.8 and 5 nm were 58.16 and 56.01 $S^{-1}mM^{-1}$, respectively (Figure 3-14). In addition, the r_1 relaxivities PAA-OA capped Gd_2O_3 nanoparticles with 1.8 nm and 5 nm were 47.20 and 43.76 $S^{-1}mM^{-1}$. Specifically, the r_1 relaxivity of 1.8 nm PAMPS-LA coated Gd_2O_3 nanoparticles is 15 times higher than that of Gd-DTPA (4.6 $S^{-1}mM^{-1}$)[13] at 1.41 T. This r_1 value is also six times higher than those reported r_1 values of PEG coated gadolinium oxide (8.8 ~ 9.4 $mM^{-1}S^{-1}$) with 2.2 nm core size[40,43] or d-glucuronic acid coated gadolinium oxide (9.9 $mM^{-1}S^{-1}$) with 1 nm core at 1.41 T.[19]
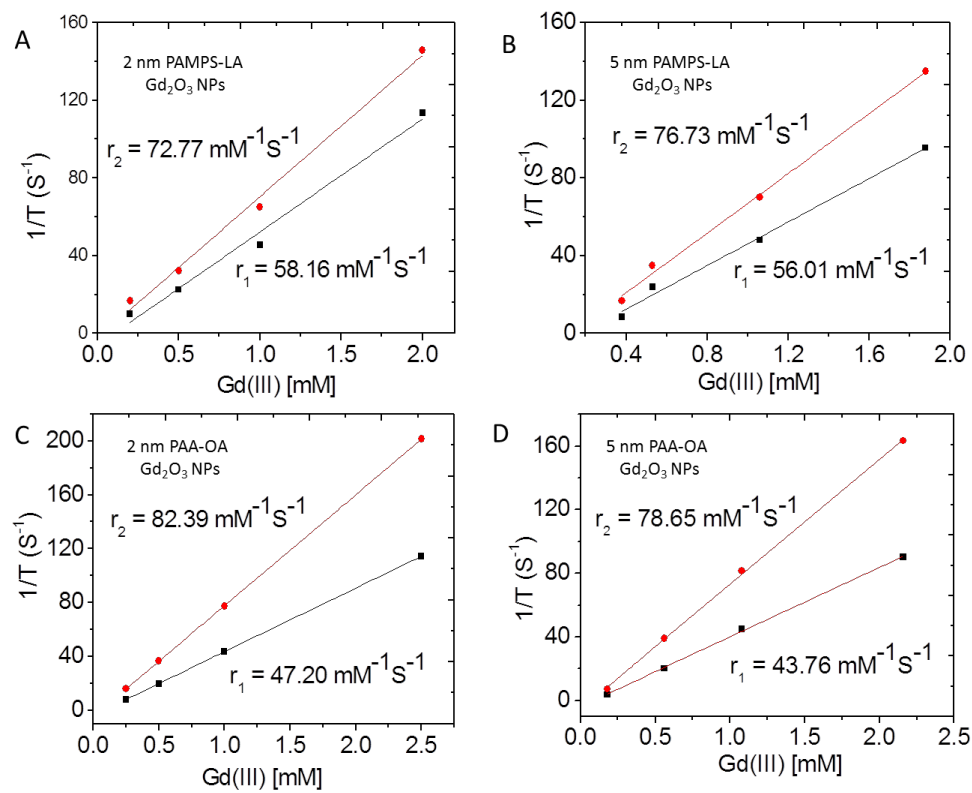
Figure 3-14 Plots of the R_1 and R_2 of gadolinium oxide suspensions
(A) and (B) Plots of the r_1 and r_2 of PAMPS-LA coated Gd_2O_3 nanoparticles as a function of Gd(III) ion concentration. (C) and (D) Plots of the r_1 and r_2 of PAA-OA coated Gd_2O_3 nanoparticles as a function of Gd(III) ion concentration. The r_1 and r_2 values were determined from the slopes.

The r_1 and r_2 relaxivity values of Gd_2O_3 nanoparticles with various surface coatings and core diameters were shown in Table 3-4. These values were obtained from the slope of the plot of $1/T$ as a function of Gd (III) concentration. Based on these values, the graphs on the effect on r_1, r_2, and r_2/r_1 ratios were plotted as function of the core diameters of Gd_2O_3 nanoparticles and surface coatings including

oleic acid, PAA-OA, and PAMPS-LA. These graphs show that both the r_1 and r_2 relaxivities decrease as the core diameter increases from 1.8 nm to 22 nm (Figure 3-15). The surface to volume ratio (S/V) and number of surface gadolinium ions are decreased as increasing core diameters. This may be considered as reducing factors on the relaxivity. The surface gadolinium (III) ions significantly contribute to the relaxation time of water protons.[19] Moreover, PAA-OA and PAMPS-LA coated Gd_2O_3 nanoparticles had 6-10 fold higher r_1 and r_2 relaxivities than those of oleic acid coated Gd_2O_3 nanoparticles with same core diameter. The average r_2/r_1 ratios of oleic acid, PAA-OA, and PAMPS-LA capped Gd_2O_3 nanoparticles were 2.44, 1.82, and 1.32, respectively. The r_2/r_1 ratio of Gd_2O_3 nanoparticle is an important factor to maximize T_1 contrast effect.[177-179] Although r_1 is high, the high r_2/r_1 limits T_1 weighted imaging. Thus, ideal T_1 MRI contrast agent should have high r_1 values as well as low r_2/r_1 ratio (1~3). In contrast, T_2 contrast MRI agent should keep high r_2/r_1 ratio (>10). The PAA-OA or PAMPS-LA coating had lower r_2/r_1 ratio than that of oleic acid and these values were similar with commercial Gd-DTPA (1.1) or PEG gadolinium oxide (1.3 ~ 3.4).[19]

Table 3-4 The r_1 and r_2 relaxivities and r_2/r_1 ratios of various Gd_2O_3 nanoparticles from the slopes of the plot of $1/T$ and concentration of Gd ions.

Coating	Core diameter (nm) by TEM	r_1 (mM^{-1}S^{-1})	STD	r_2 (mM^{-1}S^{-1})	STD	r_2/r_1	B_0 Field (T)
Gd-DTPA	-	4.3	-	-	-	-	1.5
PEG	3	9.4					1.5
Oleic acid	2	7.63	0.34	21.1	1.44	2.77	1.5
Oleic acid	5	5.99	0.50	11.2	2.30	1.87	1.5
Oleic acid	8	5.45	0.49	16.0	4.26	2.94	1.5
Oleic acid	11	4.56	0.54	10.3	2.21	2.26	1.5
Oleic acid	22	3.02	0.41	6.37	0.24	2.11	1.5
PAA-OA	2	47.2	5.81	82.4	10.9	1.74	1.5
PAA-OA	5	43.8	7.34	78.7	4.41	1.79	1.5
PAA-OA	8	33.7	0.93	70.0	6.52	2.08	1.5
PAA-OA	11	32.4	2.45	67.3	3.52	2.08	1.5
PAA-OA	22	21.1	6.55	32.4	10.6	1.54	1.5
PAMPS-LA	2	58.2	7.65	72.8	1.69	1.25	1.5
PAMPS-LA	5	56.0	4.17	76.7	4.51	1.37	1.5
PAMPS-LA	8	41.2	4.43	49.9	6.93	1.22	1.5
PAMPS-LA	11	43.6	4.42	63.9	6.56	1.46	1.5
PAMPS-LA	22	36.4	2.04	53.8	2.59	1.48	1.5
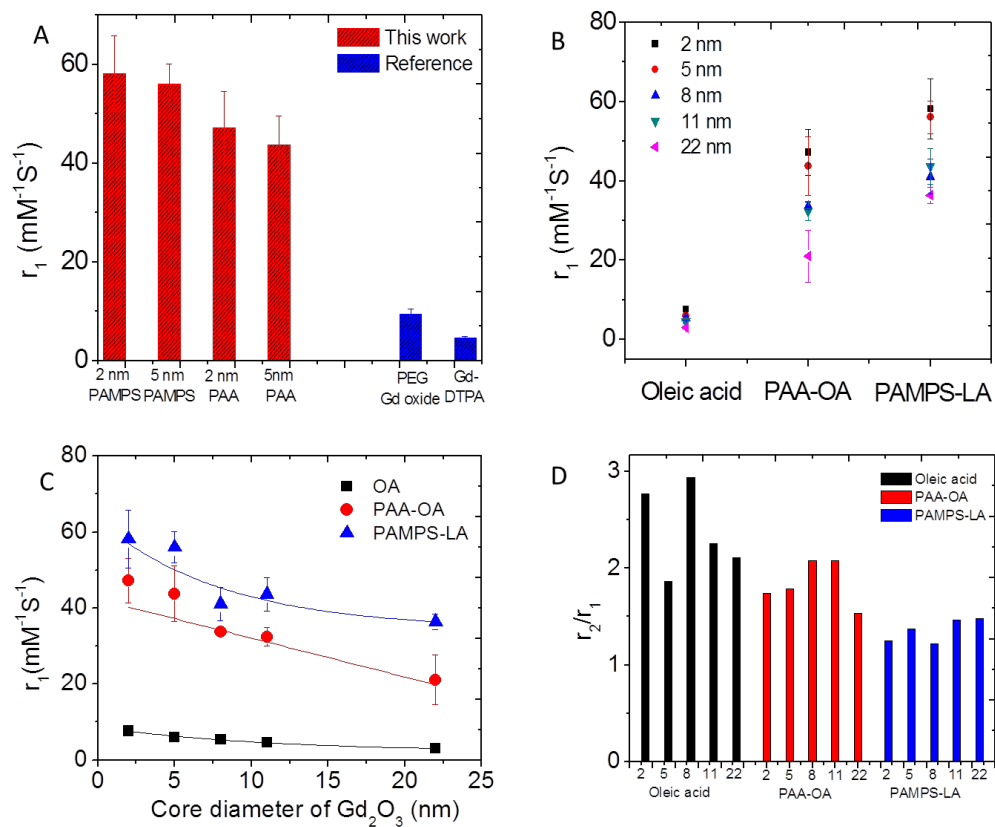
Figure 3-15 Plots of r_1 and r_2 depending on the core diameters and surface coatings (A) Plot of r_1 values of PAMPS-LA and PAA-OA coated Gd_2O_3 nanoparticles (B) Plot of r_1 values of different core diameters of Gd_2O_3 nanoparticles depending on the surface coatings (oleic acid, PAA-OA, PAMPS-LA) (C) Plot of r_1 values of different coatings of Gd_2O_3 nanoparticles depending their core sizes. (D) Plot of r_2/r_1 ratios of oleic acid, PAA-OA, and PAMPS-LA Gd_2O_3 nanoparticles.

The observed high relaxivity of surface coated Gd_2O_3 nanoparticles can be explained from the important parameters (e.g. electron spin of metal ion (S), strength of magnetic dipole moment (M), number of surface metal ions (N), and internal flexibility (diffusion), and rotation) of the inner/outer sphere relaxation. In

inner sphere contribution, the relaxivity (r_1 and r_2) is proportional to S(S+1) by dipole-dipole interaction modulated by the reorientation of the nuclear spin-electron vector and scalar interactions influenced by electron spin relaxation and water proton exchange.[142]   Due to high S state of Gd (III) (S=7/2), Gd_2O_3 nanoparticles have higher relaxivity.[16,38,180] Second, Gd_2O_3 nanoparticles have no magnetic dipole (μ) due to the paramagnetic spin structure. Since the strength of magnetic dipole moment (M) of Gd_2O_3 nanoparticle is zero the transverse relaxation ($1/T_2$) can be minimized by reducing the fluctuation of local magnetic field. So, the r_2/r_1 ratio can be retained to be small (1~3).

The r1 relaxivities with core diameters (d) were related to the number of surface metal ions (N) interacting with water protons. Gd_2O_3 nanoparticles have a high surface to volume ratio, as the core diameter is smaller. In contrast with Gd-DTPA (N=1), Gd_2O_3 nanoparticles concentrate a large number of Gd surface ions (N) possessing high electron spin (S= 7/2) in a small volume. Since Gd_2O_3 nanoparticles are ultrathin nanoplates/nanodisks, high number of Gd surface ions significantly induces and accelerates the longitudinal relaxations of the water proton.[19] As the core diameter of Gd_2O_3 nanoparticles get smaller, the number of surface Gd ions in a certain volume increases so that it gets a higher relaxivity. In 2009, the Lee group reported the dependence of r_1 relaxivity (9.9 to 0.1) with diameters (1.1 to 30 nm), combining other reference works.[19] With size tunable ultrathin gadolinium nanoplates/nanodisks by the control of reaction, we confirmed that diameter controlled Gd_2O_3 nanoparticles (1.8 to 22 nm) had high r_1 relaxivity and those values

of Gd_2O_3 nanoparticles in oleic acid, PAA-OA, and PAMPS-LA coatings decreased as the core size increased (Figure 3-15). The Table 3-5 shows the r_1 and r_2 relaxivities values of gadolinium oxide nanoparticles obtained by the relaxation rate ($1/T_1$ or $1/T_2$) per concentration of Gd atoms and per number of particles.

Table 3-5 The r_1 and r_2 relaxivities of gadolinium oxide nanoparticles obtained by the relaxation rate per concentration of Gd atoms and number of particles

Coating	Core diameter (nm)	Relaxivity based on concentration of Gd atoms		Relaxivity based on number of particles	
		$r_1(mM^{-1}S^{-1})$	$r_2(mM^{-1}S^{-1})$	$r_1(mM^{-1}S^{-1})$	$r_2(mM^{-1}S^{-1})$
Gd-DTPA	-	4.3	4.9	4.3	4.9
Oleic acid	2	7.20	20.0	5.9E+09	1.6E+10
Oleic acid	5	6.19	13.2	3.2E+10	6.8E+10
Oleic acid	8	5.36	12.8	7.0E+10	1.7E+11
Oleic acid	11	4.87	10.8	1.2E+11	2.7E+11
Oleic acid	22	2.95	6.8	1.0E+11	2.4E+11
PAA-OA	2	45.0	82.3	3.7E+10	6.8E+10
PAA-OA	5	41.4	77.8	2.1E+11	4.0E+11
PAA-OA	8	35.0	69.6	4.6E+11	9.2E+11
PAA-OA	11	30.4	65.1	7.6E+11	1.6E+12
PAA-OA	22	20.4	32.6	7.1E+11	1.1E+12
PAMPS-LA	2	54.1	74.3	4.4E+10	6.1E+10
PAMPS-LA	5	49.2	76.0	2.5E+11	3.9E+11
PAMPS-LA	8	40.5	64.6	5.3E+11	8.5E+11
PAMPS-LA	11	35.0	63.8	8.7E+11	1.6E+12
PAMPS-LA	22	27.9	51.0	9.7E+11	1.8E+12

Moreover, the surface coating would affect relaxivity dynamics regarding with the internal flexibility (diffusion) and rotation. The oleic acid (small molecular weight, Mw=283 g/mol) coated Gd_2O_3 nanoparticles has much lower r_1 relaxivity

values than PAA-OA (Mw = 2783 g/mol) and PAMPS-LA (Mw =4615 g/mol) coated Gd_2O_3 nanoparticles. The longitudinal relaxation is dependent on the rotation and rotational correlation time (τR).[38,142,181] When the rigid and small oleic acid introduces to coat the surface of the Gd_2O_3 nanoparticle, the proton relaxivity is limited by the fast rotation. The rotation is generally decreased by the increase of molecular weight of polymer. Moreover, the large polymer coating increases the internal flexibility and permeability that are important parameters for the exchange rate of the water proton and diffusion with bulk water. Therefore, more flexible, larger molecular weight PAA-OA and PAMPS-LA coated Gd_2O_3 nanoparticles can accelerate water proton relaxation.

These factors (rotation, flexivitiy, and diffusion) affected the relaxivity values and resulted in 15 fold higher r_1 relaxivity than commercial Gd-DTPA and 6 fold higher than that reported for other Gd_2O_3 nanoparticles.[19] T_1 weighted MR images clearly confirmed that r_1 maps were not only dose, surface, and size dependent (Figure 3-16). At the same concentration, T_1 weighted MR images of PAA-OA and PAMPS-LA capped Gd_2O_3 were much more brighter than those of oleic acid gadolinium nanopartices or the commercial Gd-DTPA. Moreover, small size of PAMPS-LA capped Gd_2O_3 nanoparticles has more brighter T_1 weighted images than those of large size.
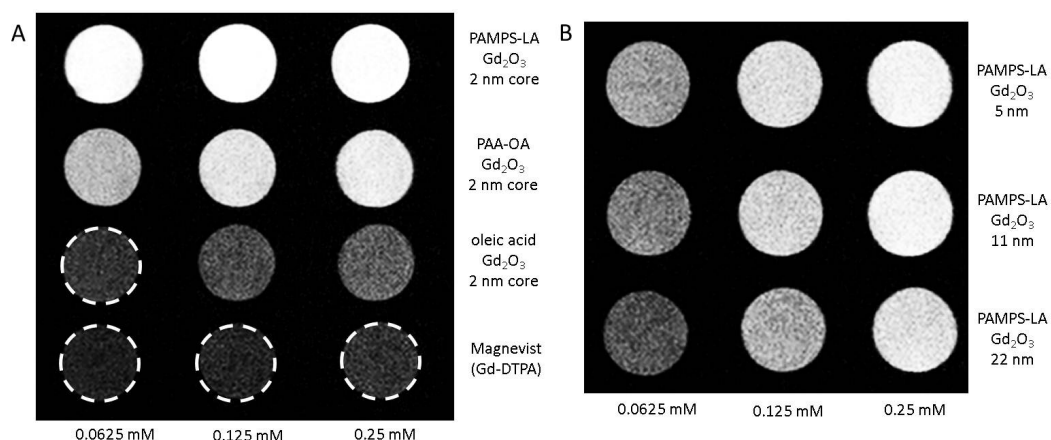
Figure 3-16 The T_1 weighted MR phantom images of gadolium oxide with different coatings (A) and different core diameters (B)

The r_1 relaxivity were also measured in various relevant media after both 1 day and 4 weeks (Figure 3-17 and Table 3-6). For most conditions, there was little to no change in r_1 relaxivity. The notable exceptions were PBS and cell media solution (DMEM with 10 % FBS and 1 % PS). In these conditions, the r_1 relaxivity values were decreased. The decreasing r_1 values in PBS and DMEM may be due to particle agglomerations and non-specific protein binding effect, respectively.[182,183] The non-specific protein itself may interfere the hydration of the inner water proton exchange and outer sphere diffusion so that the relaxivity was limited by fast rotation. This is a challenge common for all nanoparticle-based contrast agents, and it will become more of an issue for *in-vivo* MR imaging. Some reports mentioned that the relaxivity values can be improved when targeting with specific protein or linking with multiple targets.[182,183] The effects of the protein association on MR relaxivity values are the subject of ongoing studies.
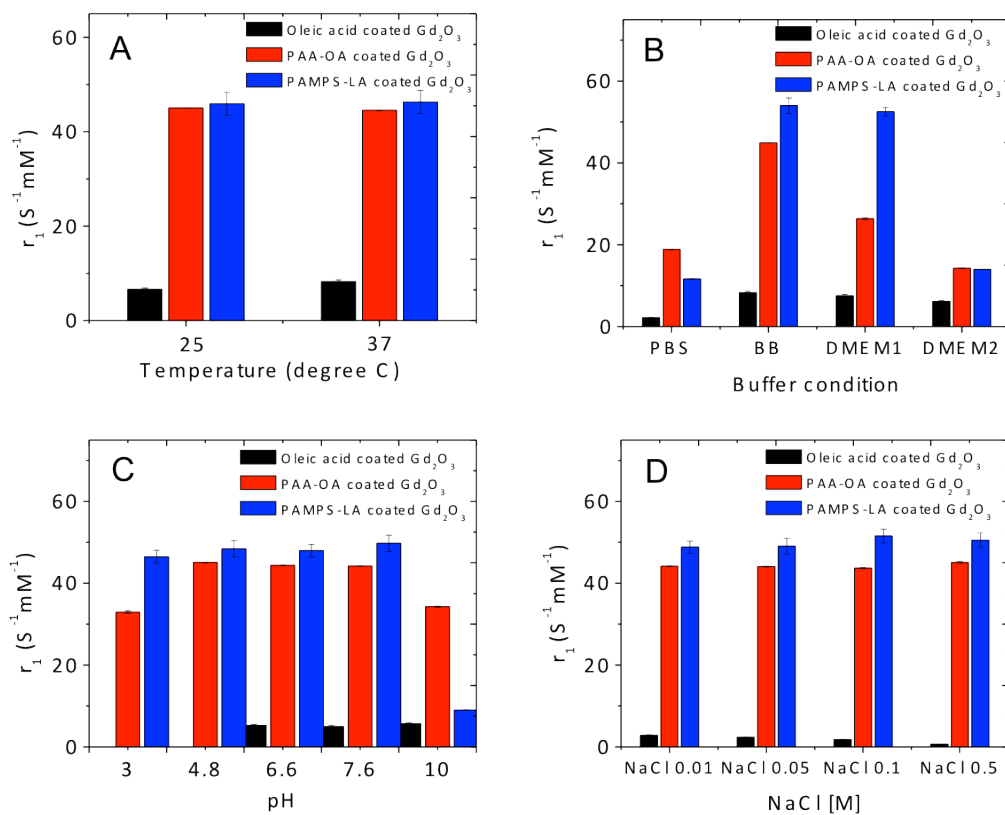
Figure 3-17 Plots of r₁ relaxivity values at different conditions

Plots of r_1 relaxivity values on the different conditions including (A) temperature (25 and 37C), (B) pH (6.6, 7.6, 10) (C) buffer conditions (PBS buffer, Borate buffer, Cell media solution DMEM 1 (low concentration), and DMEM 2(high concentration), and (D) ionic strengths (NaCl 0.01, 0.05, 0.1, 0.5M).

Table 3-6 The r_1 stability at various conditions

| | r$_1$ relaxivity (√ : stable, × : non-stable, △: little stable) | | | | | | | | | | | | | | |
| | Temperature | | Buffers | | | | pH | | | | | NaCl (M) | | | |
	R.T.	37C	PBS	BB	DMEM (1:1)	DMEM (2:1)	3	4.8	6.6	7.6	10	0.01	0.05	0.1	0.5
Oleic acid	√	√	×	√	△	×	×	√	√	√	√	√	√	√	×
PAA-OA	√	√	△	√	△	△	×	√	√	√	√	√	√	√	√
PAMPS-LA	√	√	△	√	√	△	√	√	√	√	△	√	√	√	√

3.3.4. *In vitro* toxicological study using MTS assay

Full toxicological studies are beyond the scope of this paper, but these materials were screened in an acute *in-vitro* assay designed to evaluate whether substantial leaching of gadolinium may occur in these system. *In-vitro* cell screens such as the ones employed here have been used to evaluate new materials for potential issues, and in particular for comparing materials under development. The information is not valuable as an absolute indicator of toxicology. Following past work, we have performed the MTS colorimetric assay using human dermal fibroblast (HDF) cells. It has been reported that Gd oxide nanoparticle was not toxic up to 5 uM Gd (III) concentration.[19] Here oleic acid, PAA-OA, and PAMPS-LA coated Gd$_2$O$_3$ nanoparticles with 11 nm core diameter had no effect on cells up to 0.1 to 0.3 mM concentration (Figure 3-18). Comparing with oleic acid coated Gd$_2$O$_3$ nanoparticles, the PAA-OA and PAMPS-LA coated Gd$_2$O$_3$ nanoparticles were more stable and less toxic. From the LD$_{50}$ value that can give the lethal dose required for half of the cells to die, the percentages of cell viability were calculated. The LD$_{50}$ of

oleic acid , PAA-OA, and PAMPS-LA coated nanoparticles were 120 μM, 270 μM, and 350 μM, respectively. The Gd-DTPA (Magnevist®) had no toxicological issues up to 500 μM. However, due to low relaxivity (4.3 mM^{-1}S^{-1}), it needs higher dosage (0.2 – 0.6 mL/kg of body (0.1 mmol Gd/kg)) for the enhancement in MRI.[184-187] The recommended dosage was 0.2 mL/kg of body (0.1 mmol Gd/kg) for the administration.
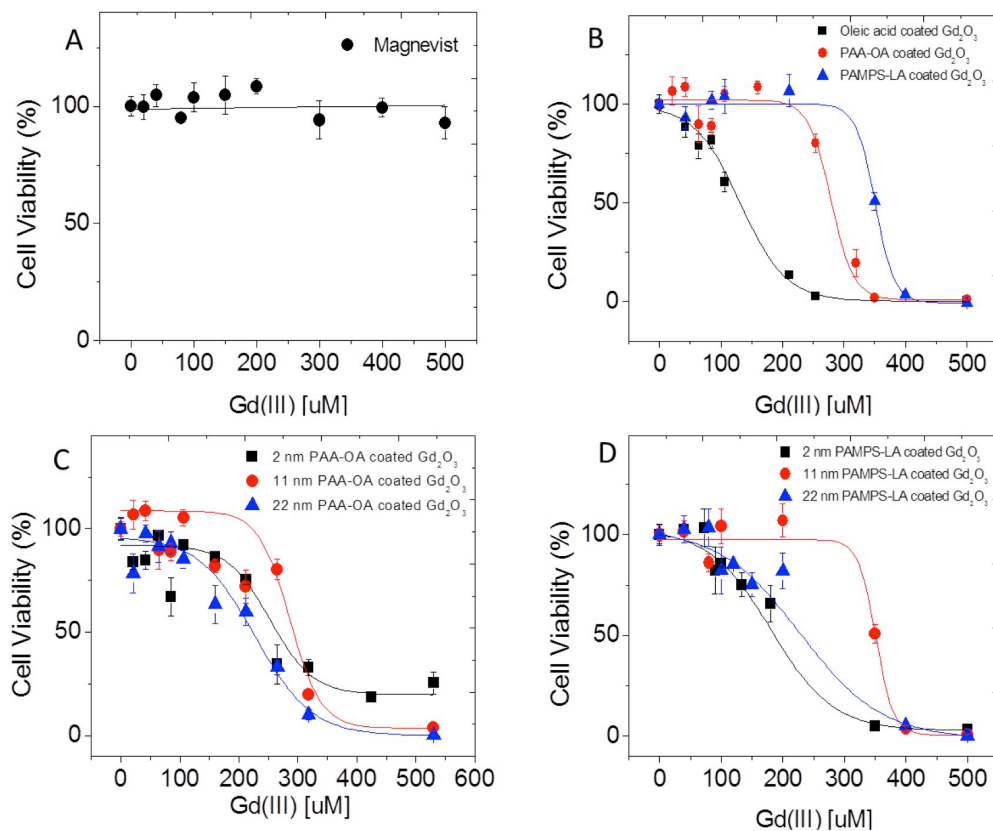
Figure 3-18 *In vitro* cytotoxicity using Human Dermal Fibroblast (HDF) cells
(A) Cell viability (%) exposed to Gd-DTPA using mitochondrial activity (MTS) assay for 24h (B) Cell viability data when introduced oleic acid, PAA-OA, and PAMPS-LA Gd_2O_3 nanoparticles (8 nm core diameter) using MTS assay. (C) Core size effects of PAA-OA Gd_2O_3 nanoparticles (D) core size effects of PAMPS-LA Gd_2O_3 nanoparticles The cells were alive up to 500 uM of Gd-DTPA. The LD_{50} of oleic acid, PAA-OA, and PAMPS-LA coated Gd_2O_3 nanoparticles were 120 uM, 270 uM, and 350 uM of Gd(III), respectively.

3.4. Conclusion

We have synthesized diameter controlled Gd_2O_3 nanoparticles ranging from 1.8 nm to 22 nm by optimization of the experimental conditions including monomer concentration, ratio of surfactant, and time. The surface engineered Gd_2O_3 nanoparticles using oleic acid, PAA-OA, and PAMPS-LA polymer were stable in various conditions including temperature, pH, buffer, and ionic strength. From the DLS and Zeta analysis, the water-soluble Gd_2O_3 nanoparticles were not aggregated and stable more than 1 month. With various core diameters and surface coatings, we optimized the relaxivity dynamics of Gd_2O_3 nanoparticles that have 15 fold higher r_1 relaxivity values (50-60 $mM^{-1}S^{-1}$) than Gd-DTPA. Moreover, we have examined the relaxivity is related to the parameters of electron spin (S) of metal ion, strength of magnetic moment (M), number of surface Gd ions (N), and rotation (R) regulated by molecular weight and internal flexibility. Based on the *in vitro* cell toxicity, the surface engineered Gd_2O_3 nanoparticles, especially PAMPS-LA coating, is non toxic up to 300 *u*M concentration of Gd(III) (LD_{50} value = 350 *u*M). We believe that PAA-OA and PAMPS-LA Gd_2O_3 nanoparticles with their high relaxivity (sensitivity), excellent water solubility, and superb stability are strong candidate MR contrast agents.

Chapter 4

The r_2 relaxation dynamics for iron oxide and ferrite nanocrystals depending on their size, coating, and composition

In this work, we have prepared size controlled iron oxide (Fe_3O_4) nanocrystals ranging from 4 to 33 nm and different types of ferrite nanocrystals (e.g. $AlFe_2O_4$, $NiFe_2O_4$, $ZnFe_2O_4$, $MnFe_2O_4$, and $MnZnFeO_4$). These size tunable iron oxide and ferrite nanocrystals are rendered water-soluble by applying various phase transfer agents, including oleic acid (OA), octylamine modified poly (acrylic acid) (PAA-OA), lauryl acrylate (LA)-poly 2-acrylamido-2-methylpropane surfonic acid (PAMPS) (PAMPS-LA), and poly (maleic anhydride-alt-1-octadecene) (PMAO)-poly (ethylene glycol)(PEG) (PMAO-PEG), to their surfaces. The r_2 magnetic resonance, (MR) relaxivity values for hydrated iron oxide magnetic nanocrystals are

strongly related to the core sizes (magnetic moments), hydrodynamic size (magnetic size regime), surface coatings (grafting density, molecular weight, and permeability), compositions (magnetic moments); the highest r_2 relaxivity is achieved using a 33 nm iron oxide particle capped with an oleic acid bilayer, which had a measured value of 510 $S^{-1}mM^{-1}$. *In vitro* cell toxicological studies were used to evaluate the various polymer coated iron oxide T_2 contrast agents, showing that none of the materials had a significant effect on human dermal fibroblasts (HDF) even at high concentration (e.g. 6000 *u*M). By designing the relaxivity dynamics with their sizes, surface coatings, and types, it will give an efficient T_2 iron oxide MRI contrast agents offering high r_2 relaxivity and low toxicity.

4.1. Introduction

Biomedical imaging has received enormous attention for their diagnostic and analytical ability at molecular level. Representative biomedical imaging tools include computed X-ray tomography (CT), magnetic resonance imaging (MRI), optical imaging (OI), positron emission tomography (PET), single-photon-emission computed tomography (SPECT), and ultrasound (US).[188,189] These imaging techniques are non-invasive and provide real-time visualization of cellular functions and molecular interactions of living organisms. They are used to diagnose diseases such as cancer and give biological or functional information for pre-clinical evaluations. Each imaging modality has its own advantages and disadvantages and a single imaging technique can not possess all required capabilities for diseases. In

particular, MRI is the most widely used non-invasive medical imaging technique.[1] It can give anatomic images of soft tissue with high spatial resolution and combine morphological and functional imaging. Therefore, MRI is one of the strongest imaging tools and will play as a molecular and cellular imaging probe. However, because of its inherent low sensitivity, there is a small difference in contrast between normal and abnormal tissues. To improve the sensitivity and visibility in MR images, nanotechnology has been called upon to develop chemical supplements, referred to as contrast agents.[35]

Magnetic nanocrystals can accelerate spin-spin relaxation times for water protons by inducing a local magnetic field and thus reduce T_2 relaxation and produce darker images.[190-194] Among various magnetic nanocrystals, iron oxide nanocrystals have been widely used as T_2 MRI contrast agents for strong contrast effect and improved biocompatibility.[195,196] Therefore, several superparamagnetic iron oxide nanocrystals (SPIOs) have been clinically approved for imaging liver tumors and metastatic lymph nodes.[123] For example, Ferridex and Combidex are approved for the detection of liver lesions and imaging of lymph node metastases. The iron oxide nanocrystals contain thousands of Fe atoms that can generate several orders of magnitude higher signal contrast. Current developments in SPIO synthesis are to yielding materials useful for advanced MRI contrast agents that possess high relaxivity, optimized surface coating, and longer blood circulation time.[100,197] Target specific functionalized SPIOs can be used as *in vivo* MR tracking and molecular markers related to the diseases. [123]

Significant advances in synthesis of iron oxide magnetic nanocrystals using thermo-decomposition has provided particles with better uniformity and high crystallinity over a broad range of sizes, from 4 to 100 nm.[50,51,171,198,199] The size and composition of iron oxide nanocrystals regulate their magnetization (μ) and MR relaxation ($R_2 = 1/T_2 = 1/T_0 + r_2$ [Fe]). Moreover, T_2 MR signal enhancements are highly dependent on hydrodynamic size related to the agglomeration and surface coating (thickness, chemical composition, grafting density).[181,200-202]

The size of iron oxide nanocrystals controls their magnetic moment (paramagnetic, superparamagnetic, ferromagnetic properties) as well as their blood circulation time and bio-distribution. The r_2 relaxivity of superparamagnetic iron oxide increases with increasing particle size (<30~50 nm) due to the fast diffusion in motional averaging regime (MAR).[200,202,203] Small particles of iron oxide nanocrystal (<50 nm) have longer plasma circulation time and are regarded as or molecular imaging probes for applications such as lymph node imaging, because they are easily distributed in the intravascular and extracellular space.[35,100,201,204] However, large magnetic nanocrystals are generally more polydisperse and aggregate in solution due to their large magnetic moments. And also, the diffusion effect of large nanocrystals is small and it is regarded as randomly distributed stationary objects (static dephasing regime, SDR). In SDR, although they exhibit high r_2 relaxivity, they are independent on their size. Their ferromagnetic dipole interaction causes the poor colloidal stability and large aggregation so that they are not suitable for *in vivo* molecular imaging probes due to their very short circulation

time.[202,204-208] In recent work, embedded multiple core iron oxides into large matrix like silica or polymers can control the ferrimagnetic dipole interaction and increased the r_2 relaxivity due to the increasing number of particles within a given aggregate. However, these aggregates become too large size problem and the r_2 value is still not maximized.[72,204,208,209] Therefore, dispersed, non-aggregated magnetic nanocrystals with high r_2 relaxivity are strongly desired for *in vivo*, targeted MR imaging.

To produce disperse iron oxide nanocrystal suspensions, as-synthesized hydrophobic materials should be transferred to aqueous solution. Surface coatings need to be biocompatible, allow the materials to possess good colloidal stability and not increasing the hydrodynamic diameter *in vivo* applications. Various surface modification methods such as ligand exchange and polymer encapsulation have been developed.[181,210-214] For ligand exchange, hydrophobic ligands initially bound to the surface of magnetic nanocrystals are displaced with hydrophilic molecules exposed to the surrounding water using carboxylic acid and dopamine.[215,216] Although ligand exchange method is simple, excess ligands, desorption or incomplete coverage can cause a decrease in the colloidal stability.

Another method requires encapsulation of the particles in silica shells or polymers via sol-gel, reverse microemulsion, or van der Waals interaction.[181,210-214] For example, phosphine oxide-poly(ethylene glycol) (PO-PEGs), 1,2 distearoyl-sn-glycero-3-phosphoethanolamine-N-[methoxy(polyethyleneglycol)copolymer (DSPE-mPEG), poly($_{D,L}$-lactide-co-glycolide) (PLGA), and poly(glycolide) (PGA) polymers

have been used.[181,210-212] These polymer encapsulated magnetic nanocrystals are very stable in water but their hydrodynamic size is relatively larger than that of ligand exchange method. The thickness, grafting density, molecular weight, and composition of the surface coatings can strongly affect the T_2 MR relaxivity, by altering the translational diffusion of water molecules in the inhomogeneous magnetic field.[193,200,203] Surface coatings can hinder water diffusion or immobilize near water molecules by forming hydrogen bonds. [181,208] Therefore, different surface coatings of iron oxide nanocrystals with same core size can have different T_2 relaxivity.[181,208]

Lastly, magnetic properties of iron oxide nanocrystals can be changed by their compositions.[100,217,218] The Fe^{2+} can be replaced with Mn^{2+}, Zn^{2+}, Ni^{2+}, and Co^{2+} in the inverse spinel structure and the magnetic properties of $MnFe_2O_4$, $ZnFe_2O_4$, $NiFe_2O_4$, $CoFe_2O_4$, and Fe_3O_4 were investigated.[218] As compositions of magnetic nanocrystals changed from $NiFe_2O_4$, to $MnFe_2O_4$, the magnetic moments and r_2 relaxivity values changed. The effects of size, surface coating, and composition on the relaxivity are very important and needed to be understood for getting best MR contrast agents.

Here, we have prepared very uniform and mono-disperse iron oxide nanocrystals with a wide range of size from 4 nm to 33 nm by thermo-decomposition method. Moreover, different compositions of iron oxide nanocrystals (e.g. $AlFe_2O_4$, $MnFe_2O_4$, $ZnFe_2O_4$, $MnZnFeO_4$) were simply prepared by adding different metal ion precursors in the synthesis. These size tunable hydrophobic iron

oxide nanocrystals were transferred to water using various phase transfer agents and evaluated for colloidal stability and hydrodynamic size. Various sizes, compositions, and coatings of iron oxide nanocrystals were investigated and optimized for MR relaxivity dynamics. Moreover, these iron oxide nanocrystals were examined *in vitro* toxicological effects with human dermal fibroblast (HDF) cells based on the size, surface coating, and composition.

4.2. Experimental sections

4.2.1. Chemicals

Iron oxide hydrated (FeO(OH), catalyst grade, 30-50 mesh), aluminium hydroxide (Al(OH)$_3$, reagent grade), nickel tetrahydrate (Ni(OCOCH$_3$)$_2 \cdot$4H$_2$O, 98 %), manganese chloride tetrahydrate (MnCl$_2 \cdot$4H$_2$O, 99 %), zinc acetate (Zn(OCOCH$_3$)$_2 \cdot$4H$_2$O, 99.99 %), oleic acid (technical grade 90%), oleylamine (technical grade 70%), oleyl alcohol (technical grade, 85 %), 1-octadecene (1-ODE, technical grade 90%), poly(acrylic acid) (PAA, Mw=1800), and octylamine (OA, 99%), poly(maleic anhydride-alt-1-octadecene) (PMAO, Mn=30,000-50,000), poly(ethylene glycol) (PEG) methyl ethers (mPEG-NH$_2$) (Mw= 2,000), acrylic acid 2-Acrylamido-2-Methylpropane sulfonic acid copolymer (AA/AMPS), lauryl acrylate (LA,technical grade 90 %) were purchased from Sigma-Aldrich. The samples were synthesized was under a flow of high purity nitrogen (N$_2$, 99.99 %). Aluminium oleate, methanol (99.8 %), acetone (99.5 %), hexanes (98.5 %), sodium bicarbonate (99.7 %), and dimethylformamide (DMF, 99.8 %), nitric acid (HNO$_3$, 70%) and

hydrogen peroxide (H_2O_2, 30%) were purchased from Fisher Scientific; 1-ethyl-3-[3-dimethylaminopropyl] carboiimide hydrochoride (EDC) was purchased from Thermo Scientific; CellTiter 96® Aqueous One solution Cell Proliferation Assay (MTS assay) was purchase from Promega; Human derman fibroblast (HDF) was purchase from Cambrex; Dulbecco's Modified Eagle's Medium (DMEM, ATTC, Mannassa, VS), fetal bovine serum (FBS),1% penicillin-streptomycin (PS), trypsin-EDTA were purchased from Sigma-Aldrich.

4.2.2. Synthesis of size tunable iron oxide nanoparticles

Magnetic iron oxide nanocrystals were synthesized using modified procedure of previously published work.[51] 0.178 g of FeO(OH), 2.26 g oleic acid and 5 g 1-ODE were mixed in a 100 ml three neck flask and heated to 120 °C for 2 hours to remove residual water and further heated to 240 °C for 30 minutes to synthesize iron carboxylate, iron-oleate. Then, the reaction mixture was heated at 320 °C for 2 hours under N_2 condition. To purify the resulting black colloidal nanocrystals, 20 ml of methanol and 20 mL acetone were added to 5 mL resulting colloidal solution and centrifuged at 4150 rpm for 30 minutes. The precipitates at the bottom were re-dispersed using hexanes and this process was repeated six times. Finally, 10 nm iron oxide nanocrystals were purified and dispersed in hexanes. For 16 nm Fe_3O_4 nanocrystals, the molar ratio between FeO(OH) and oleic acid was changed from 1:3 to 1:5 with all other conditions remaining the same.

To produce smaller iron oxide nanocrystals (<5 nm), iron oleate was used as the iron precursor. Iron oxyhydrate (FeO(OH), 20 mmol, 1.8 g), oleic acid (80 mmol, 22.4 g) and 1-ODE (60 g) were mixed in a three neck flask and heated to 240 °C for 4 hours. After purifying iron oleate precursor, the resulting black colloidal solution was stored in hexanes. 4 nm iron oxide nanocrystals were prepared using iron oleate (0.015 mmol, 0.009 g) and oleic acid (0.3 mmol, 0.08 g) in 5 g ODE at 320 °C for 3 hours under the N_2 flow. The largest iron oxide nanocrystals (33 nm), required a higher molar concentration of FeO(OH), oleic acid, and ODE. FeOOH (50 mmol, 4.5 g), oleic acid (200 mmol, 56 g), and 1-ODE (40 mmol, 10 g) were firstly heated to 240 °C for 2 hours and further heated to 320 °C for 12 hours.

4.2.3. Aluminum iron oxide ($Al_xFe_{3-x}O_4$) nanocrystals

4 nm aluminium iron oxide nanocrystals were synthesized by decomposition of iron oleate (0.05 mmol) and aluminum oleate (0.02 mmol) as metal precursors in the presence of oleic acid (2 mmol) as a surface stabilizer in 1-ODE (5 g) at 320 °C for 2 hours. 10 and 15 nm aluminum iron oxide nanocrystals were synthesized by using iron oxyhydrated (FeO(OH)) and aluminum hydroxide ($Al(OH)_3$). Specifically, 10 nm aluminum ferrite nanocrystals were prepared by heating 0.7 mmol FeO(OH), 0.3 mmol $Al(OH)_3$, 3 mmol oleic acid, and 5 g ODE at 320 °C for 1 hour. 15 nm aluminum iron oxide nanocrystals were obtained from the same conditions used to make the 10 nm aluminum iron oxide nanocrystal except changing to 4 mmol oleic acid.

4.2.4. Manganese and zinc oleate synthesis

Metal oleates (M^{x+}(oleate)$_x$, (M= Zn, Mn, and Al) were prepared as starting precursor materials to make various ferrite ($M_x Fe_{3-x}O_4$, M= Zn, Mn, Al) nanocrystals. Manganese oleate was synthesized by heating manganese chloride (10 mmol, 1.25 g) with oleic acid (20 mmol, 5.64 g) in 10 g of ODE at 180 °C for 2 hours.[219] Zinc oleate was prepared by mixing zinc acetate (10 mmol, 1.83 g) and oleic acid (20 mmol, 5.64 g) in 10 g of ODE at 210 °C for 2 hours.[220] These metal oleate precursors were purified with 20 ml of ethanol and 20 ml of acetone then centrifuged at 4150 rpm for 30 minutes then re-dispersed in 5 ml hexanes. The purification process was repeated three times.

4.2.5. Manganese iron oxide ($Mn_x Fe_{3-x}O_4$) nanocrystals

Manganese iron oxide nanocrystals were prepared from the mixture of iron oleate (0.03 mmol) and manganese oleate (from 0.0003 to 0.03 mmol) in the presence of oleic acid (2 mmol) and ODE (5 g) and heated to 320 °C for 2 hours.

4.2.6. Zinc iron oxide ($Zn_x Fe_{3-x}O_4$) nanocrystals

The mixture of iron oleate (0.03 mmol) and zinc oleate (from 0.0003 to 0.03 mmol) were used with oleic acid (2 mmol) and ODE (5 g) and heated at 320 °C for 2 hours.

4.2.7. MnZnFe oxide (MnZnFeO$_4$) nanocrystals

The mixture of iron oleate (0.03 mmol), manganese oleate (0.015 mmol), and zinc oleate (from 0.015 mmol) were used with 2 mmol of oleic acid in 5 g of 1- ODE at 320 °C for 2 hours. The resulting nanocrystals were 9.0 ± 0.6 nm in diameter.

4.2.8. Oleic acid bilayer coating

The oleic acid coated nanocrystals were modified by the previously published procedure.[165] Briefly, oleic acid (from 30 uL to 300 uL) was introduced to 1 mL of nanocrystals solution dispersed in ethyl ether (1,500 - 4,000 mg/L of iron concentration). After stirring for 24 hours, ultra pure water (MILLIPORE, 18.2 MΩ) or 0.1 M sodium bicarbonate (pH 9) solution was introduced and stirred for an additional 2 hours. Then the sample was probe sonicated (UP 50H, Dr. Hielscher) at 60 % amplitude for 10 minutes to help disperse the material in water. The nanocrystal solution was stirred, uncovered for 1 day to completely evaporate the residual ethyl ether organic solvent. The purification of water-soluble nanocrystals was carried out using ultracentrifugation (optima L-90K ultracentrifuge, Beckman coulter) at 40,000 rpm for 3 hours twice followed by syringe filteration (pore size of 0.45 uM, Whatman NYL). The resulting aqueous solutions were acquired after these ultracentrifugation and syringe filtration steps. To calculate the transfer yield of oleic acid bilayer coated materials, the concentrations of metal ion were determined using ICP-OES for the original and aqueous solutions.

4.2.9. Octylamine (OA)-modified poly(acrylic acid) (PAA-OA) coating

PAA-OA polymer and PAA-OA coated nanocrystals were prepared by the published procedure.[166] To make PAA-OA polymer, first PAA (0.6 g, 0.33 mmol) was dissolved in DMF (10 g). After stirring for 10 minutes, EDC (0.58 g, 3 mmol) was added to PAA/DMF solution, and octylamine (0.5 mL, 3 mmol) was sequentially introduced to PAA/EDC/DMF solution. After stirring overnight, the rotavap was used to remove DMF while keeping the PAA-OA solution under vacuum. The final PAA-OA solution (15 mg/mL) was dispersed in chloroform (40 mL).

PAA-OA polymer solutions from 1 to 7 mL were mixed with 1mL nanocrystal/chloroform solution (typically 1,500 to 4,000 mg/L of metal ion concentration). The mixed solution was stirred for 24 hours and then chloroform was allowed to evaporate using vacuum or air. 0.1 M sodium bicarbonate was added for every 10 mL of solution then it was sonicated using a probe sonicator (60 % amplitude) for 10 minutes. The resulting solution was purified with ultracentrifugation (40,000 rpm for 3 hours, twice) and filtered out with syringe filter (0.45 uM, Whatman NYL). The nanocrystal solution was acquired and completely dissolved in ultrapure MQ water. [138]

4.2.10. Poly (acrylic acid 2-Acrylamido-2-Methylpropane sulfonic acid) (PAMPS)- lauryl acrylate (LA) (PAMPS-LA) coating

The PAMPS-LA polymer was synthesized by copolymerization of 30 g of AMPS (0.1447 mol, 207.23 g/mol) and 22.5 mL of LA monomers (240.38 g/mol,

0.0827 mol) in 300 mL of DMF solution under UV light. The polymer solution was used to coat nanocrystals directly without further purification.

The varied ratios of PAMPS-LA polymer per nanocrystal were prepared by adding 1 to 7 mL (15 mg/ml) were mixed with 1mL nanocrystal/ethyl ether solution (typically 1,500 to 4,000 mg/L of iron concentration). When the solution was cloudy after adding excess polymer DMF was added to the solution to solubilize the polymer. The nanocrystal/polymer solution was stirred for 24 hours. After 24 hours an additional 10 mL of ultra pure MQ water was added to the mixture and the solution was stirred uncovered for another 24 hours to allow the ethyl ether to evaporate . The resulting polymer capped nanoparticles were purified of excess free polymer in solution using ultracentrifugation (40,000 rpm for 3 hours, twice) and filtered out using syringe filter (0.45 uM, Whatman NYL). The clear and cleaned nanocrystal pellet was recovered and resuspended in ultra pure MQ water.

4.2.11. Poly(maleic anhydride-alt-1-octadecene) (PMAO)- poly(ethylene glycol) (PEG) methyl ethers (mPEG-NH2) (PMAO-PEG) coating

The PMAO-PEG polymer coating method was followed and modified by the reported procedure.[221] PMAO (M_n=30,000-50,000) was reacted with mPEG-NH$_2$ (Mw 2,000) in chloroform overnight to make PMAO-PEG amphiphilic polymer (molar ratio of PMAO/PEG, 1:5 to 1:30).

The varied ratios of PMAO-PEG polymer per nanocrystal were prepared by adding 1 to 7 mL (20 mg/) were mixed with 1mL nanocrystal/ chloroform solution

(typically 1,500 to 4,000 mg/L of Fe ion concentration). The mixture was stirred for 24 hours and then the chloroform was allowed to evaporate using vacuum or air. After adding 0.1 M sodium bicarbonate solution (10 mL), the mixture was probe sonicated (60 % amplitude) for 10 minutes. The resulting solution was purified with ultracentrifugation (40,000 rpm for 3 hours, twice) and filtered out with syringe filter (0.45 uM, Whatman NYL). The purified nanocrystals were acquired and resuspended in ultrapure MQ water. The phase transfer yields were calculated based on the concentration of Fe metal ions in the purified sample divided by the original Fe ion concentration as determined using inductive coupled plasma–optical emission spectroscopy (ICP-OES).

4.2.12. MR relaxivity measurements

MR relaxivity measurement. Various concentrations of nanoparticles were prepared by the dilution from the stock solution of nanoparticles with different coatings for MR relaxivity measurement. To measure r_2 of iron oxide and ferrite nanoparticles, the MR relaxometer (NMR analyzer, mq 60, Bruker) was used at 1.41T. To get an accurate r_2 values of different coating of iron oxide and ferrite aqueous solution, various concentration of nanoparticle solution were prepared and r_2 values were come out from the slope between $1/T_2$ and concentrations.

MR phantom imaging. To get MR phantom imaging, the MRI clinical 3T scanner was used. For this measurement, the different size/coatings/composition of iron oxide aqueous solution were used.

4.2.13. Cell culture and MTS assay

Cell culture: Human derman fibroblast (HDF, Cambrex) were used and cultured in Dulbecco's Modified Eagle's Medium (DMEM, ATCC, Manassas, VS) with 10 % fetal bovine serum (FBS) and 1 % penicilin-streptomycin (PS). The cells were floated by trypsin-EDTA and re-suspended in media (DMEM with 10% FBS and 1% PS) solution for the passaging.

Cell viability test (MTS assay): To determine the nanoparticle cytotoxicity the standard colorimetric assay, MTS (CellTiter 96, Promega) was used. HDF cells were placed and grown in 96 well culture plates with over 80 % confluency. Each set was prepared with different concentrations of nanocrystal solutions. One set was treated as a blank (no nanocrystals) and last set was used for the untreated control (ethanol). The treated cells with nanocrystal aqueous solution were incubated for 24 hours. After then, the solution was suctioned out and replaced with 100 uL fresh media (DMEM with FBS 10% and 1% PS) solution and 20 uL MTS agent to each well. After incubating for 1 hour at 37 °C and 5 % CO_2, the absorbance at 490 nm of the solution was measured by using a plate reader (Spectra Max, M2, Molecular devices). The experiment was repeated three times for to determine the average. The LD_{50} for each sample., which gives the lethal dose required for half of the cells to die, was calculated by the percentage of cell viability.

4.2.14. Instruments and characterization

Transmission electron microscope (TEM). To determine the average diameter and size variation for the nanocrystal samples a JEOL 2100 field emission TEM operating at 200 kV with a single tilt holder was used. TEM samples were prepared by evaporating one drop of nanocrystals solution on an ultrathin 400 mesh copper grid (Ted Pella Inc.). The size and size histograms of each sample were determine by using Image-Pro Plus 5.0 (Media Cybernetics, Inc., Silver Spring, MD) to detect edges, smooth holes and determine the diameter for at least 500 particles per sample.

Dynamic light scattering (DLS) and zeta potential. The hydrodynamic diameter (nm) and zeta potential (mV) of all synthesized and surface functionalized materials measured on a ZEN-3600 Zetasizer Nano (Malvern, UK) equipped with a HeNe 633nm laser . The average hydrodynamic size (nm) and zeta potential (mV) were the average of five replicates for each sample.

Inductive coupled plasma-optical emission spectroscopy (ICP-OES). To measure the concentration of iron, Perkin Elmer ICP-OES equipped with auto sampler was used. Samples were prepared for ICP-OES by acid digestion using nitric acid (HNO_3, 70 %) and hydrogen peroxide (H_2O_2, 30 %).

Matrix assisted laser desorption ionization time-of-flight (MALDI-TOF) mass spectroscopy. To measure the molecular weight of polymers a MALDI-TOF mass spectroscopy, Bruker Autoflex II ToF-ToF equipped with a nitrogen laser

operated at 337 nm, was used. Polymer solutions were prepared in acetonitrile:water (4:1) and 0.1% (v/v) triflouroacetic acid and 1 uL of the sample was added on the plate. As a matrix, a saturated sample of α-cyano-4-hydroxycinnamic acid was prepared in acetonitrile:water (4:1) and 0.1% (v/v) triflouroacetic acid. After evaporating the sample solution, 1 uL of matrix solution was overlaid on sample spot and allowed to dry.

Total organic carbon (TOC). A Shimadzu TOC-L was used to measure the carbon concentration for surface functionalized gadolinium nanoparticles in water. Three replicates of each sample were prepared by adding 1 ml of the stock nanoparticle sample and diluting to 8.5 mL with Milli-Q 18 MΩ pure water. Each sample was run on a total nonpurgeable organic carbon (NPOC) assay with triplicate 50 μL injections. The calibrations from 0.5 to 60 ppm were prepared using TOC standard solution (Sigma-Adrich) (R^2 = 0.998).

Calculation of grafting density (GD). The calculation of grafting density (σ) was calculated from TOC data using the equation below, similar to previously published method.[167]

$$\sigma = \frac{[C] * MW_n}{MW_p * C_n * [NP] * (4\pi r_{core}^2)}$$

The nonpurgeable organic carbon concentration ([C]) from TOC analysis must be converted from mg/L (ppm) to mol/liter (molarity) by considering molar mass of carbon (12,010 mg/mol). To determine the number of polymer molecules

the carbon concentration is multiplied by the molecular weight of the monomer (MW_n) and divided by the polymer molecular weight (MW_p) times the number of carbons per monomer (C_n). By dividing by the molar concentration of nanoparticles, [NP], and the surface area of the particle the resulting grafting density is achieved.

4.3. Result and discussions

4.3.1. Synthesis of size tunable iron oxide and ferrites nanocrystals

We have synthesized very uniform and high crystalline iron oxide nanocrystals with a wide range of size from 4 nm to 33 nm via thermo-decomposition of iron precursors with oleic acid and 1-octadecene (ODE) at high temperature (320 °C).[51] Moreover, by adding different metal ion (Al, Mn, and Zn) precursors into iron precursors, we prepared different compositions of iron based magnetic nanocrystals. Figure 4-1(A-D) shows the TEM images of monodisperse iron oxide nanocrystals with different core diameters (4.0 ± 0.6, 10.2 ± 0.7, 16.0 ± 1.4, and 33.1 ± 2.5 nm). The experimental factors such as molar ratio of FeOOH/oleic acid, monomer concentration, and reaction time were varied to achieve the range of core diameters and uniformity. In order to have different compositions of iron based magnetic crystals, Al, Mn, and Zn metal oleates were introduced into the mixture of iron precursors by adding more surfactant (oleic acid) and solvent (ODE) based on the previous report.[51] The TEM images of different composition of ferrite samples include $AlFe_2O_4$, $MnFe_2O_4$, $ZnFe_2O_4$, and $MnZnFeO_4$ (Figure 4-1 E-H). The

core diameters for each sample were determined to be 8.8 ± 0.7, 8.9 ± 0.8, 10.4 ± 1.0, and 9.1 ± 0.6 nm, respectively.
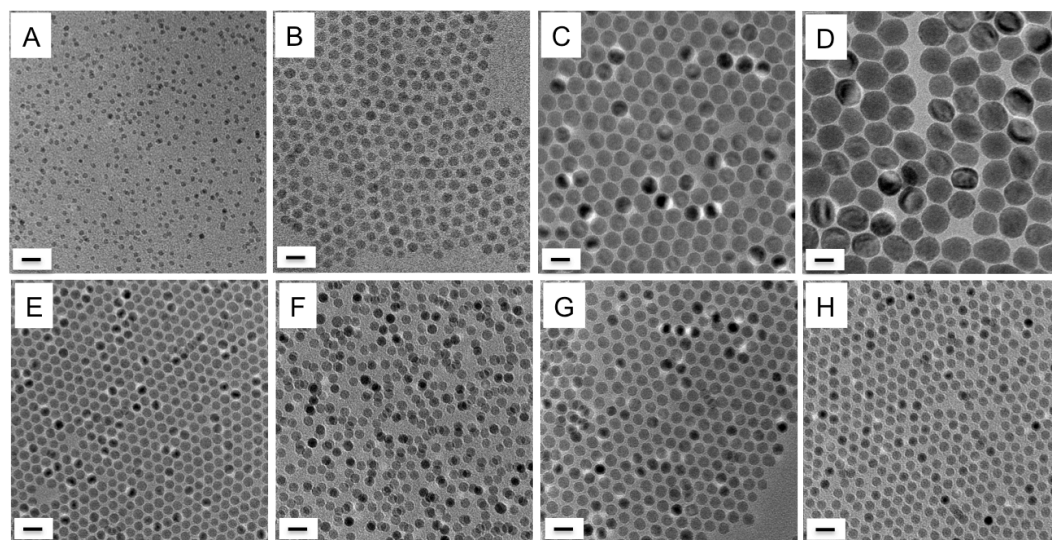
Figure 4-1 TEM images of iron oxide nanoparticles with different core diameters (A-D) and compositions (E-H).

TEM images of monodisperse iron oxide nanoparticles with different core diameters (A-D); the core diameters are 4.0 ± 0.6 (A), 10.2 ± 0.7 (B), 16.0 ± 1.4 (C), and 33.1 ± 2.5 nm (D), respectively. The TEM images of different composition of ferrite samples including $AlFe_2O_4$, $MnFe_2O_4$, $ZnFe_2O_4$, and $MnZnFeO_4$ (E-H); the core diameters are 8.8 ± 0.7 (E), 8.9 ± 0.8 (F), 10.4 ± 1.0 (G), and 9.1 ± 0.6 nm (H), respectively. All scale bars are 20 nm.

Magnetic properties are dependent on the size of iron oxide nanocrystals. When the particle size is small (< 30 nm), the superparamagnetism occurs.[100] In the

presence of an external magnetic field superparamagnetic nanocrystals respond and exhibit high saturation of magnetism whereas they have no remanence when magnetic field is removed. The Langevin equation can describe their magnetic properties.[100]

$$\frac{M}{M_s} = \frac{\coth \alpha - 1}{\alpha} \left(\alpha = \mu_0 mH \big/ K_B T \right)$$

Where, α is the ratio of magnetic to thermal energy, m is magnetic moment of a single particle, and H is magnetic field. When the particle size is very small (< 4 nm), the individual particles have very small magnetic moments ($\frac{\mu_0 mH}{K_B T}$ << 1) and show a linear relationship between magnetization and magnetic field $\left(\frac{M}{M_s} = \frac{\mu_0 mH}{3K_B T} \right)$. This is paramagnetic property and means that high saturation magnetism needs a high magnetic field. If the particle size is high (>40~50 nm), the magnetic moment ($\frac{\mu_0 mH}{K_B T}$>>1) is high and the magnetic saturation occurs ($\frac{M}{M_s}$~1). It is ferromagnetism and it has remanence and coercivity in the absence of magnetic field. If the particle size range keeps a superparamagetism in a single domain, the magnetic property increases with increasing the size and the particle has no remanence at zero magnetic field.

The magnetic properties of iron oxide nanocrystals can also be controlled by their compositions.[100,197,218,222] The iron oxide magnetite (Fe_3O_4) has an inverse spinel structure, consisting of face-centered cubic packed lattice of oxygen atoms with the tetrahedral sites (T_d) occupied by Fe^{3+} ions and octahedral sites (O_h)

occupied by Fe^{2+} and Fe^{3+} ions. When applying an external magnetic field, the magnetic spins of ions at the O_h sites are parallel to the magnetic field but those at T_d sites are antiparallel to the field. Thus, the magnetic moment of Fe^{3+} (high spin state, d^5 configuration) at different sites (T_d or O_h) cancel the magnetism and leave Fe^{2+} (d^6 configuration) in O_h site showing 4 μ_B of total magnetic moment per unit.[197,218] The Fe^{2+} in the structure of $(Fe^{3+})_{Td}(Fe^{2+}Fe^{3+})_{Oh}O_4$ can be replaced with divalent transition metal ions from Mn^{2+} and Zn^{2+}. The Zn^{2+} divalent metal ion has high T_d preference and the structure is normal spinel structure.[223] The magnetic moment dramatically increases with increasing doping ratio of Zn (x=0.4) until a certain level. Mn^{2+} can be in T_d or O_h sites and has mixed spinel structure possessing high magnetic moment of 5 μ_B.[197,218] Moreover, the trivalent Al ions (Al^{3+}) can be replaced with Fe^{3+} in either T_d or O_h sites. Therefore, different compositions of iron oxide nanocrystals such as $AlFe_2O_4$, $MnFe_2O_4$, $ZnFe_2O_4$, and $MnZnFeO_4$ have different magnetic moments.

4.3.2. Surface coatings of iron based magnetic nanoparticles

The hydrophobic iron oxide nanocrystals with a wide range of sizes and compositions are transferred into aqueous solutions using various phase transfer agents (e.g. oleic acid bilayer, PAA-OA, PAMPS-LA, and PMAO-PEG). In schematic diagram in Figure 4-2, these various phase transfer agents have different molecular weight ranges (283~50,000) and functional groups, such as carboxylic (COOH) or sulfuryl ends (SO_3H). Oleic acid and other polymer coated iron oxide nanocrystals kept their same core diameters and morphology after being transferred to water

(Figure 4-3). These water-soluble iron oxide nanocrystals were non-aggregated and retained a single core and small hydrodynamic size.
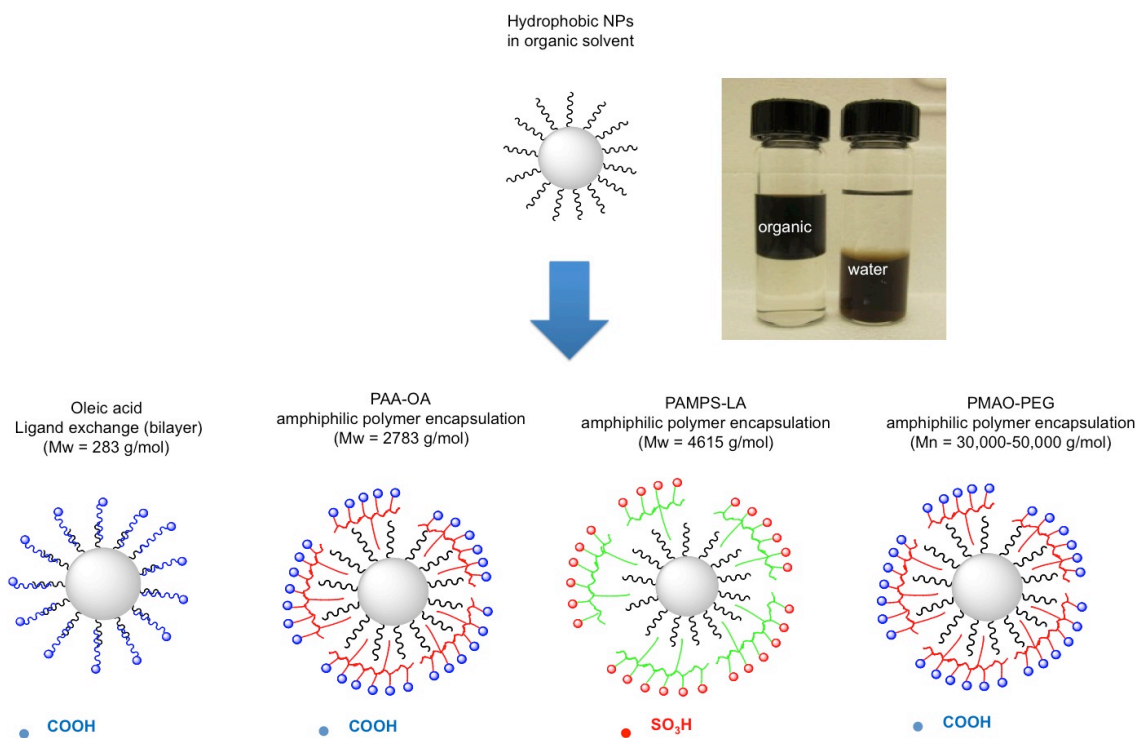
Figure 4-2 The schematic diagram of various phase transfer agents (oleic acid bilayer, PAA-OA, PAMPS-LA, and PMAO-PEG)
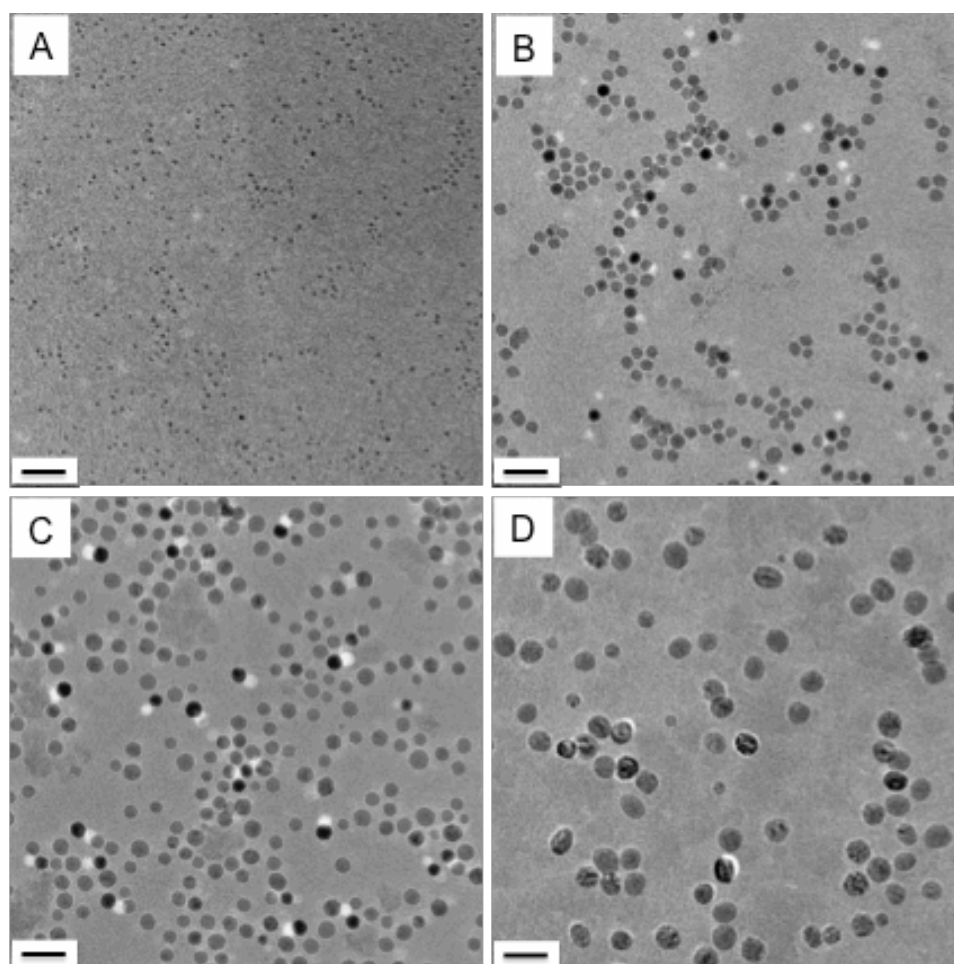
Figure 4-3 TEM images of water-soluble iron oxide nanocrystals

The water-soluble iron oxide nanocrystal suspensions using oleic acid bilayer (A), PAA-OA (B), PAMPS-LA (C), and PMAO-PEG polymers (D); the core diameters were 4.1 ± 0.8, 10.4 ± 1.2, 16.6 ± 0.8, and 33.4 ± 2.3 nm, respectively (A-D). All scale bars were 20 nm.

Dynamic light scattering (DLS) analysis shows that the core sizes and surface coatings influence the hydrodynamic sizes of magnetic nanocrystals. As the core size increased from 4 to 33 nm the bilayer of oleic acid increased the hydrodynamic size from 17 nm to 41 nm, with an average coating thickness of 3.75 nm (Figure

4-4). Polymer capping agents tended to have larger molecular weights and thicknesses therefore showed a greater increase in hydrodynamic size when applied to the nanocrystals; from 20 to 68 nm. Moreover, as coating agents varied from small molecules (oleic acid (298 g/mol) to large polymers (PMAO-PEG 30,000-50,000 g/mol), hydrodynamic sizes of iron oxide nanocrystals with 4 nm core were increased from 17 nm to 38 nm. Various iron oxide nanocrystal suspensions showed negative zeta potentials (-40 to -60 mV), which means that they were well dispersed and not aggregated.

The commercial polymers including poly (ethylene glycol) (PEG) with different molecular range (200, 1,000, 10,000 g/mol), poly vinyl pyrolidone (PVP, 1,000 g/mol), and poly acrylic acid (PAA, 15,000) were also used and measured their hydrodynamic sizes with 10 nm iron oxide nanocrystals. They kept in a small hydrodynamic range around 30 nm but the hydrodynamic size was slightly increased with increasing molecular weight. The PEG coated particles had a weak negative surface charge (-10 mV) and compared to the other polymers with large net negative potentials (-30~-40 mV).
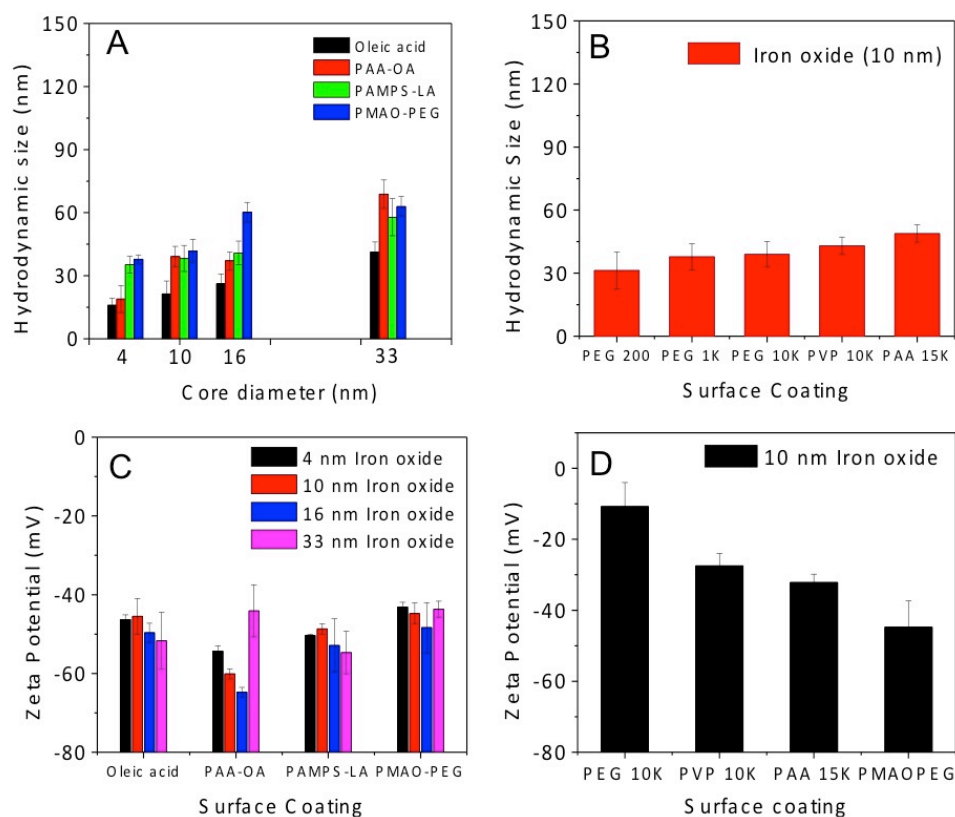
Figure 4-4 The hydrodynamic sizes and zeta potentials of iron oxide nanoparticles (A) The hydrodynamic size of iron oxide nanoparticles of different core diameter and surface coatings, (B) the hydrodynamic size of iron oxide (10 nm) with different commercial polymers, (C) The zeta potential (mV) of iron oxide nanoparticles with different sizes and coatings, (D) The zeta potential values (mV) of iron oxide (10 nm core) with different commercial polymers

Except at low pH (pH 3) or high ionic strength $CaCl_2$ conditions the iron oxide nanocrystal suspensions with various coatings were stable and all samples were stable in biological cell media solutions, different pH (5~10), and NaCl

concentrations from 0.05M to 0.5M (Figure 4-5). Especially, PAMPS-LA coated iron

oxide nanocrystals showed the greatest stability even at low pH (pH=3) and high

$CaCl_2$ (0.05 to 0.5 M) conditions.
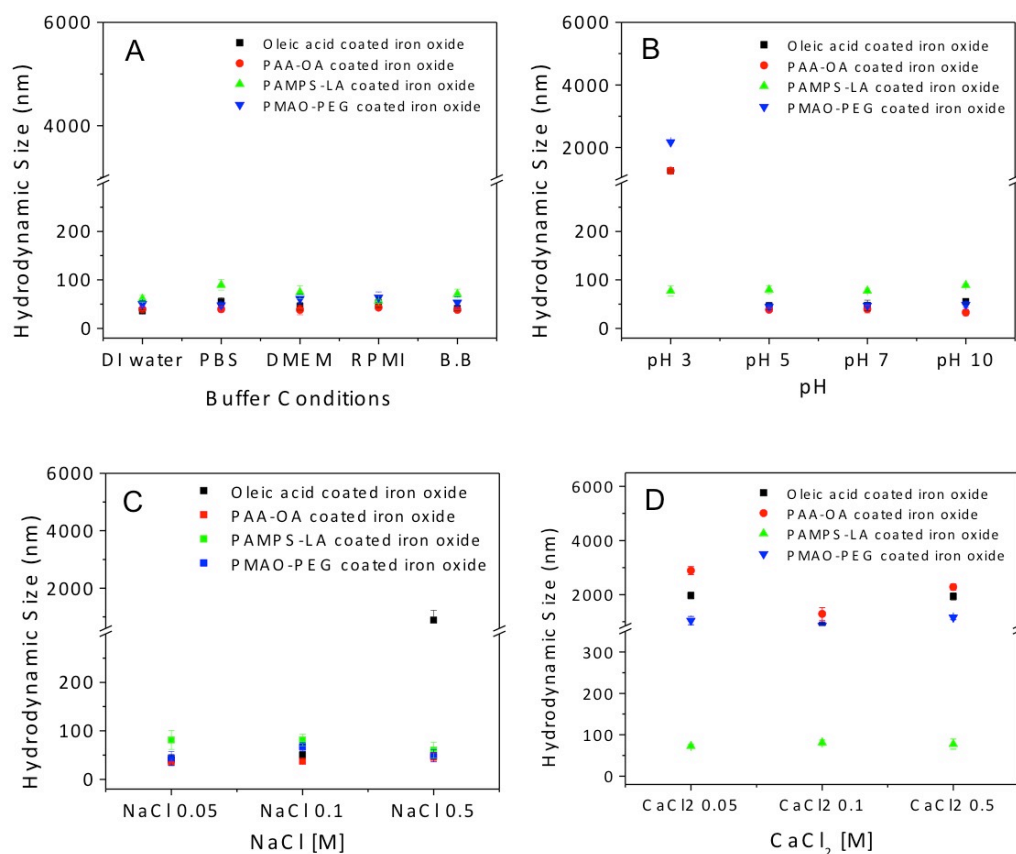
Figure 4-5 The hydrodynamic sizes of various iron oxide nanoparticles at different conditions of (A)buffers, (B) pH, (C) NaCl, and (D)$CaCl_2$.

The grafting density, or the number of bound polymers per surface area of a

nanocrystal can be determined by total organic carbon analysis (TOC).[167] It is

strongly dependent on the molecular weight of polymers and decreases with

increased polymer molecular weight.[167] Large molecular weight polymers do not

fully cover the nanoparticle surface and have low grafting densities, which allow for a high permeability/flexibility of water molecules. TOC evaluations of our nanomaterials were used to determine the grafting densities of various coating agents (bilayer oleic acid, PAA-OA, PAMPS-LA and PMAO-PEG). The molecular weights of these coating agents (oleic acid, PAA-OA, PAMPS-LA, and PMAO-PEG) are 283, 2783, 4615, 30,000-50,000 g/mol, respectively from theoretical or experimental values (Figure 4-6 and Table 4-1). With 10 nm core iron oxide nanocrystals, the grafting densities of these polymers showed the values of 12.1, 4.1, 3.7, and 0.004 molecules/nm^2, respectively (Figure 4-7).
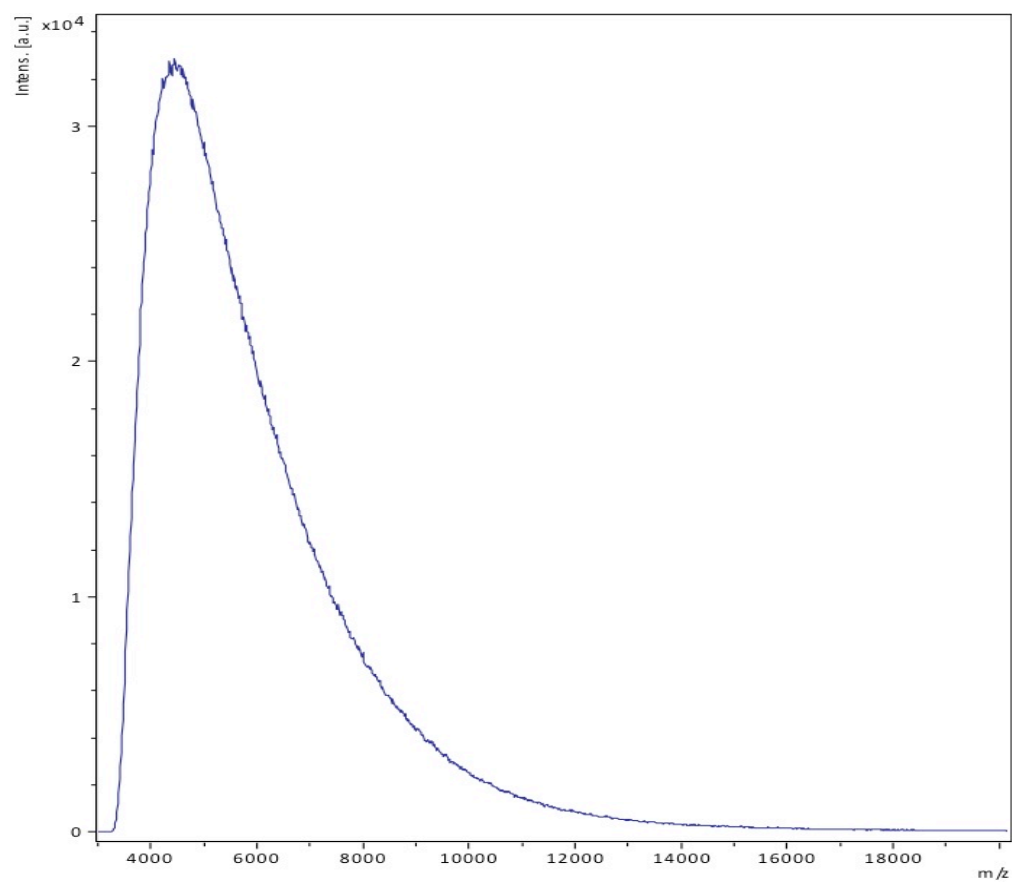
Figure 4-6 The MALDI-TOF of PAMPS-LA polymer.

The average m/z of PAMPS-LA is 4615 g/mol.

Table 4-1 The grafting densities of various phas transfer agents

Iron oxide (10 nm)	Oleic acid coating	PAA-OA coating	PAMPS-LA coating	PMAOPEG coating
Molecular weight (theoretical)	283	2783	-	30,000-50,000
Molecular weight (experimental)			4615	
Grafting density (GD)	12.13	4.11	3.67	0.00362
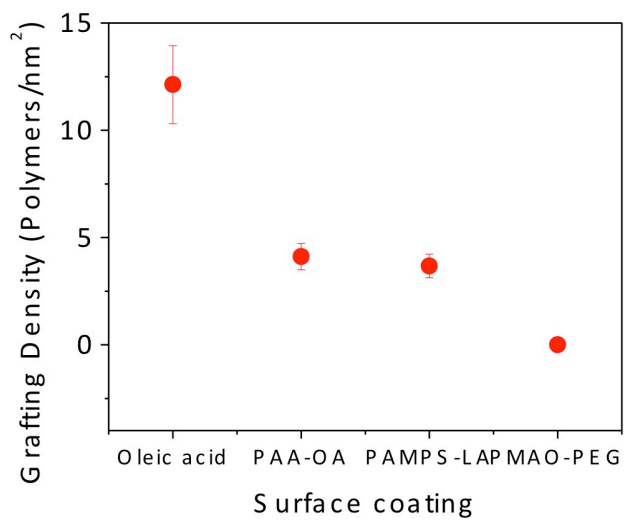
Figure 4-7 The grafting densities of various phase transfer agents (oleic acid, PAA-OA, PAMPS-LA, and PMAO-PEG)

4.3.3. MR relaxation dynamics

The magnetic nanocrystals can induce inhomogeneous local magnetic field when an external magnetic field is applied. The magnetic interaction of magnetic nanoparticles with water protons can be explained by outer sphere (OS) spin-spin relaxation model.[100,203] The diffusion time $(\tau_D = {r^2}/{D})$ is defined by the particle size (r) and diffusion coefficient of water (D). The r_2 relaxation time $(1/T_2)$ is given by:

$$R_2 = \frac{1}{T_2} = \frac{\left(\frac{64\pi}{135000}\right)\gamma^2 N_o M \mu_C^2 \tau_D}{r^3} = \frac{\left(\frac{64\pi}{135000}\right)\gamma^2 N_o M \mu_C^2}{rD} \quad (1)$$

$$v = \left(\frac{4}{3}\right)\pi r^3 N_0 M \times 10^{-3}, \quad (2)$$

$$(\Delta\omega_r)^2 = \left(\frac{4}{5}\right)\gamma^2\mu_c^2 \Big/ {r^6} \quad (3)$$

$$R_2 = \left(\frac{4}{9}\right) v\tau_D(\Delta\omega_r)^2 \quad (4)$$

where, N_o is Avogadro's number, γ is gyromagnetic ratio, M is the particle molarity (mol/L), μ_c is the magnetic moment of the nanoparticle, r is radius of particle, $1/\Delta\omega_r$ is the angular phase shift induced by the magnetic nanoparticle at the equator line on its surface, τ_D is the diffusion time (the time scale of fluctuation in the particle-water proton magnetic dipolar interaction arising from the relative diffusive motion (D) of a particle with respect to water molecules), and D is diffusion coefficient of water molecule. According these equations, the R_2 relaxivity value increases when the particle volume (v)/size (r) increases since magnetic moment is

proportional to the magnetic particle size. Regarding the relationship between R_2 and diffusion time and particle size $(R_2 \propto v, R_2 \propto \tau_D \propto r^2/D)$, three theoretical regimes of R_2 can be explained depending their size and diffusion time: the motional averaging regime (MAR), static dephasing regime (SDR), echo-limiting regime (ELR) or slow motion regime (SMR).[200,202,204,208] In MAR, the relaxivity values (R_2) increased sharply with increasing particle size (r^2, r (hydrodynamic size)< 45 nm). In SDR, the R_2 value is maximum and is not dependent on the size (r^0). Moreover, the R_2 value is decreased when the particle size is quite large (> 60 nm, r^{-1}) in ELR. In order to optimize R_2 values for magnetic nanocrystals, the hydrodynamic size (< 55 nm) should be in a range of maximum of MAR or early SDR.

The relaxivity values (r_2) of various iron oxide nanocrystals were determined from the slope in a plot of $1/T_2$ and Fe ion concentrations ($1/T_2 = 1/T_0 + r_2$ [Fe]) as shown in Figure 4-8. From these evaluations the highest r_2 value was 510 mM^{-1}S^{-1} of oleic acid bilayered iron oxide nanocrystal (33 nm core) (Table 4-2). The relaxivity r_2 is strongly dependent on the magnetic moment (μ), which is dependent on the size and composition.[190,197,201,218] Regarding to these size effects, the r_2 values of oleic acid coated iron oxide nanocrystals were 11, 51, 160, and 510 mM^{-1}S^{-1}, respectively when the core sizes increased to 4, 10, 16, and 33 nm. (Figure 4-9) In this plot, the oleic acid coated 33 nm iron oxide nanocrystals showed the highest r_2 value (510 mM^{-1}S^{-1}).

The hydrodynamic size of oleic acid coated 33 nm iron oxide nanocrystal was 41 nm, which kept a single core without agglomeration and a high r_2 value in SDR.

Due to the magnetic dipole interaction and remanence, large core size magnetic nanocrystals (>30 nm) are easily aggregated and have very large hydrodynamic size (over 200 nm).[202] When the hydrodynamic size passed over a limit of SDR (> 55 nm) and reached to ELR, the r_2 value dramatically decreased.[202,208] If the hydrodynamic size is over 100 nm, the particles are taken up by phagocytosis. [224,225] In contrast, if the hydrodynamic size is extremely small, the particles can easily pass through the renal filtration and be excreted. For biological effect the optimal nanomaterial size is between 5~60 nm, where the particles will be able to travel the blood vessels and have longer blood circulation time since they can escape phagocytosis.[224,225] Therefore large single core magnetic nanocrystal with small oleic acid coating which possess high r_2 in MAR/SDR would be ideally suited for biological used because their biodistribution is optimum for longer blood circulation time and enhance permeability and retention (EPR) effect in vivo tumor targeting.
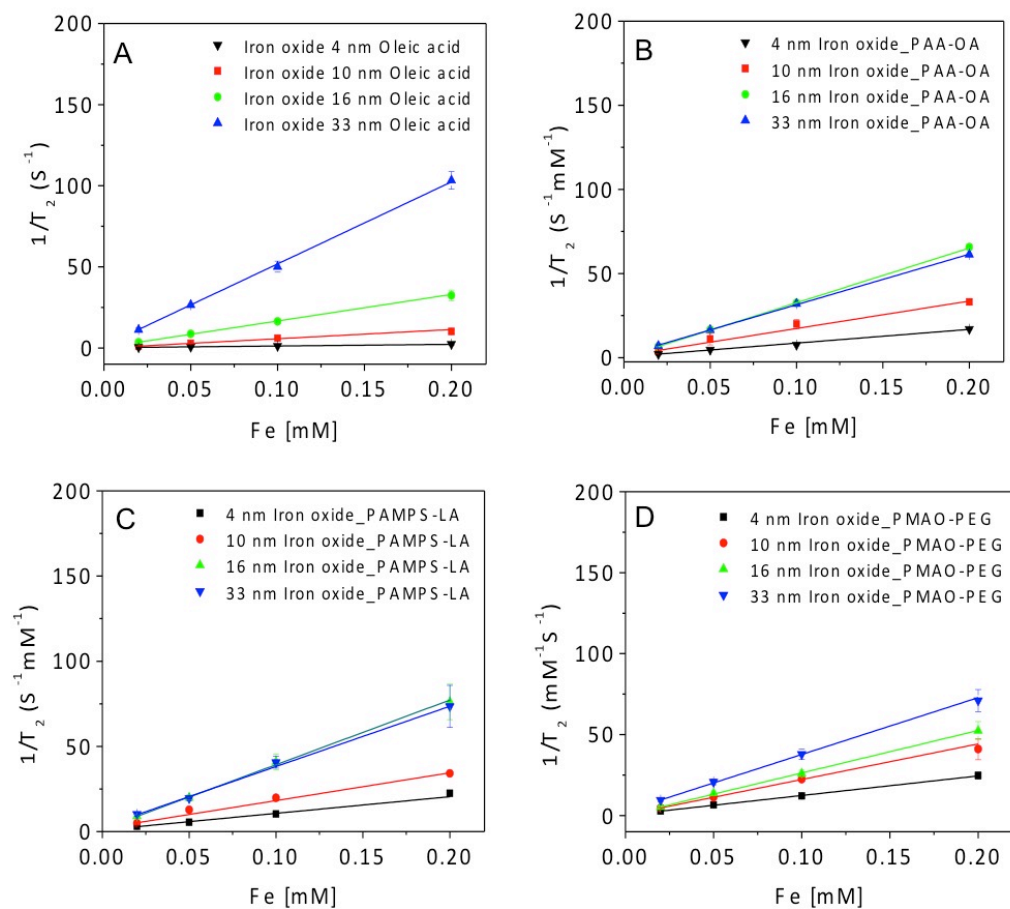
Figure 4-8 Plots of r₂ values of iron oxide nanoparticles

Plots of r₂ values of iron oxide nanoparticles depending their core diameters (4 to 33 nm) and surface coatings (oleic acid, PAA-OA, PAMPS-LA, and PAMO-PEG) (A-D)

Table 4-2 The r_2 relaxivities of iron oxide nanocrystals with different core sizes and coatings

Size/Surface effect	Average r_2 ($mM^{-1}S^{-1}$) at 1.5T			
Sample	Oleic acid	PAA-OA	PAMPS-LA	PMAO-PEG
4 nm Iron oxide	11.1 ± 3.1	81.9 ± 6.4	108.7 ± 3.9	126.6 ± 3.1
10 nm Iron oxide	50.5 ± 2.8	158.9 ± 5.9	152.4 ± 7.2	201.1 ± 5.7
16 nm Iron oxide	159.8 ± 10.7	327.7 ± 12.5	385.2 ± 10.1	260.4 ± 12.9
33 nm Iron oxide	510.3 ± 18.8	301.2 ± 10.4	355.1 ± 6.7	339.9 ± 8.3

Table 4-3. Surface effects on MR relaxivity (r_2)

Surface effect	Average r_2 ($mM^{-1}S^{-1}$) at 1.5T				
Sample	PEG 200	PEG 1K	PVP 10K	PEG 10K	PAA 15K
10 nm Iron oxide	101.5 ± 1.3	105.7 ± 3.0	138.6 ± 5.3	195.7 ± 6.7	202.3 ± 6.9
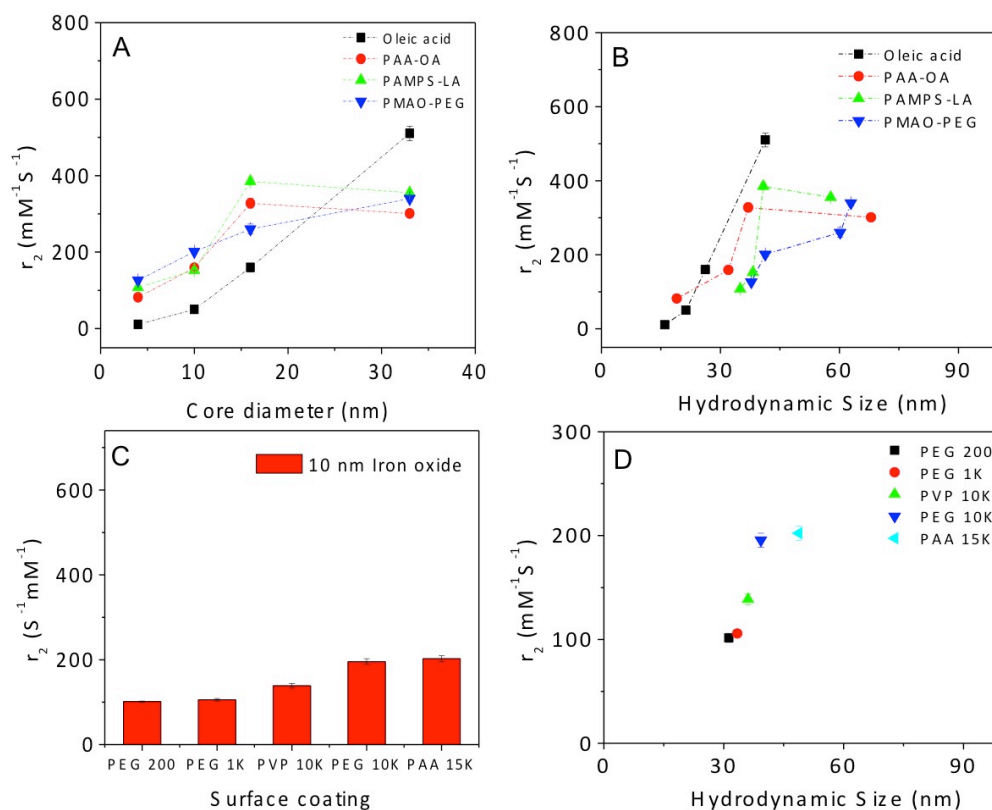
Figure 4-9 Plots of r_2 values of iron oxide nanoparticles

Plots of r_2 values of iron oxide nanoparticles depending their core diameters(A) and hydrodynamic size (B). The r_2 values of 10 nm core iron oxide nanoparticles with different molecular weight of polymers (C) and their hydrodynamic size (D)

As changing molecular weights of polymers from oleic acid to PMAO-PEG, r_2 relaxivities of 4 nm iron oxide nanocrystals increased from 11 to 127 mM^{-1}S^{-1} (Figure 4-9 (A) and (B)). Moreover, r_2 values of 10 nm iron oxide nanocrystals also increased from 51 to 201 mM^{-1}S^{-1}. In MAR, the r_2 values proportionally increased with hydrodynamic size. Furthermore, when increasing the molecular weight of PEG from 200 to 10,000 g/mol, PVP 10,000, and PAA 15,000 g/mol, the r_2 values

increased from101 to 202 $mM^{-1}S^{-1}$ (Figure 4-9 (C) and (D) and Table 4-3). If the iron oxide nanocrystals have small core (4 or 10 nm) and small hydrodynamic size (<50 nm), r_2 dynamics are strongly dependent on the magnetic moments in MAR.

High molecular weights of polymers provide larger hydrodynamic sizes, which reach to the limitation of SDR. When the hydrodynamic size was over SDR (> 60 nm) the r_2 values dramatically decrease (Figure 4-10). At 16 nm core size, the r_2 values of oleic acid, PAA-OA and PAMPS-LA coated iron oxide nanocrystals increased to 160, 328, and 385 $mM^{-1}S^{-1}$. However, the r_2 value of PMAO-PEG coated iron oxide nanocrystals decreased to 260 $mM^{-1}S^{-1}$. The hydrodynamic size of PMAO-PEG coated iron oxide nanocrystals was around 60 nm in ELR, where r_2 followed to 1/r. The size regime theory (MAR, SDR, and ELR) explained that r_2 relaxivity of 33 nm iron oxide nanocrystals dramatically decreased with increasing hydrodynamic sizes in ELR (Figure 4-10).
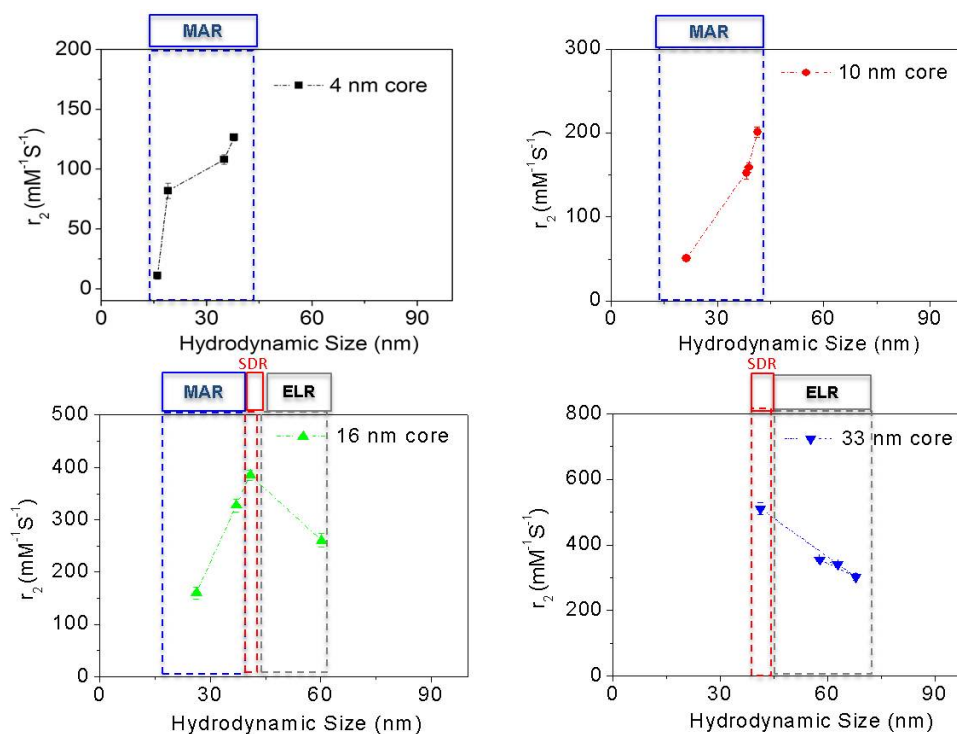
Figure 4-10 The plots of r_2 relaxivities of iron oxide nanocrystals with different cores (A-D).

The points indicate the surface coatings (left, oleic acid, PAA-OA, PAMPS-LA, PMAO-PEG).

The relaxivity value (r_2) can be also affected by surface coating. If the coating is a permeable polymer matrix where water can easily diffuse the water inside, the R_2 follows this equation[100]:

$$R_2 = \frac{1}{T_2} = \frac{\left(\frac{256\pi^2\gamma^2}{405}\right)VM_s^2a^2}{D^*} \tag{5}$$

where D* is the effective diffusion coefficient of water molecules.

If the polymer is permeable and has low grafting density (e.g. PMAO-PEG), the diffusion rate increased and the time of diffusion was faster. While keeping same hydrodynamic size, and changing only the type of polymer coated on an iron oxide nanocrystal there were different r2 relaxivity values (Figure 4-11). For example, at a hydrodynamic size between 30~40 nm in MAR, the r_2 values were strongly dependent on their coatings and decreased with increasing molecular weight of polymers. We confirmed the grafting densities of oleic acid, PAA-OA, PAMPS-LA, and PMAO-PEG were 12.1, 4.1, 3.7, and 0.004, respectively (Figure 4-7). As the grafting densities decrease, the permeability and diffusion rate increase and the r_2 value decreased.
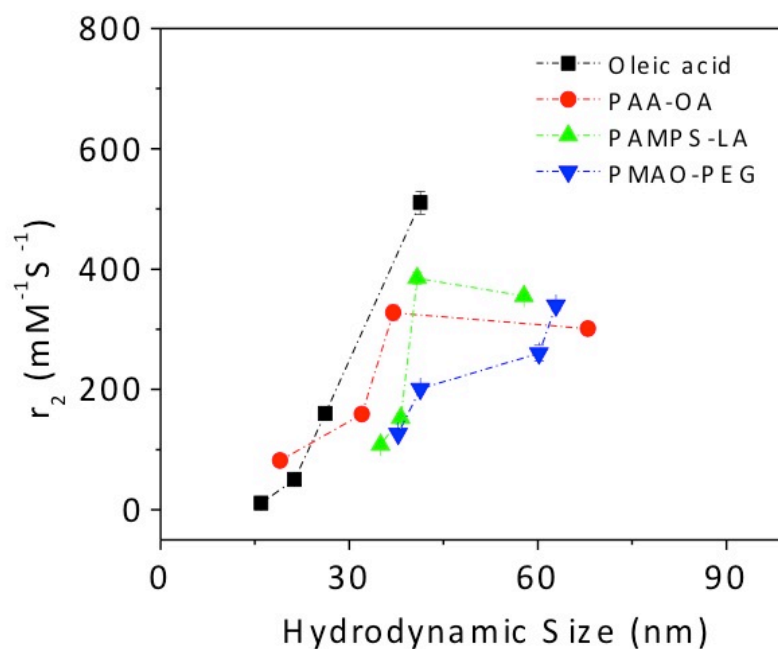
Figure 4-11 The surface coating effects at same hydrodynamic size.

Figure 4-12 showed the T_2 weighted MR phantom images for (A) three sizes of iron oxide particles at two concentrations and (B) six different coating and three different compositions of iron oxide nanocrystals on the same core (10 nm). As the particle size increased from 4 nm to 33 nm with small oleic acid coating, the T_2 MR images get darker. Also, increasing molarity (M) (0.1 mM) of iron resulted in much darker images than 0.05 mM. Increasing the molecular weight of polymer capping agents on a 10 nm iron oxide nanocrystals increased the hydrodynamic size in MAR which resulted in darker MR contrast images (Figure 4-12 (B)).
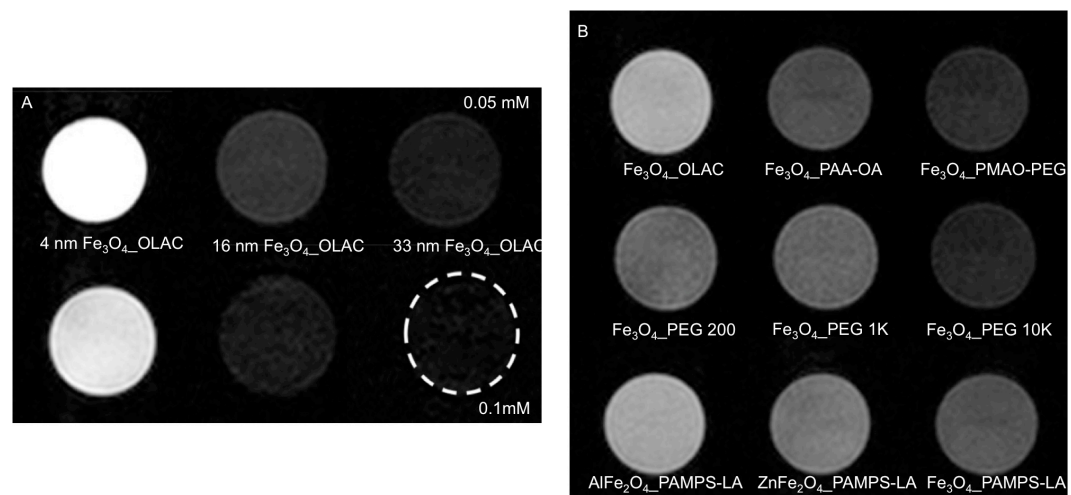
Figure 4-12 T_2 weighted MR images of iron oxide nanocrystals
(A) T_2 weighted MR image of iron oxide nanocrystals depending on their sizes (4, 16, 33 nm) at different concentration of Fe ions (0.05 mM, 0.1 mM), and (B) T_2 weighted MR image of iron oxide nanocrystals (10 nm core) depending on their coatings/compositions.

The different compositions of iron based nanocrystals ($AlFe_2O_4$, $ZnFe_2O_4$, Fe_3O_4) with PAMPS-LA coating are shown in Figure 4-12(B). Table 4-3 and Table 4-4 showed the r_2 values of iron oxide nanocrystals with various coatings and compositions. The different compositions of MFe_2O_4 iron oxide nanocrystals resulted in lower r_2 values (Figure 4-13). It was assumed that the ratio of Fe to the divalent or trivalent metal ions (Mn^{2+}, Zn^{2+}, and Al^{3+}) within a crystals would affect the magnetic moment and change the r_2 values.[100] In order to get high r_2 values, the ratio of Fe to other metal ions needs to be optimized. The r_2 values with various coatings were examined at various conditions including buffers, pH, and ionic strengths (Figure 4-14). Especially, PAMPS-LA coatings were stable at acidic condition (pH=3) and high ionic strengths. Thus it would be very useful in cellular environments because they can prevent the release of metal ions and cell damages.
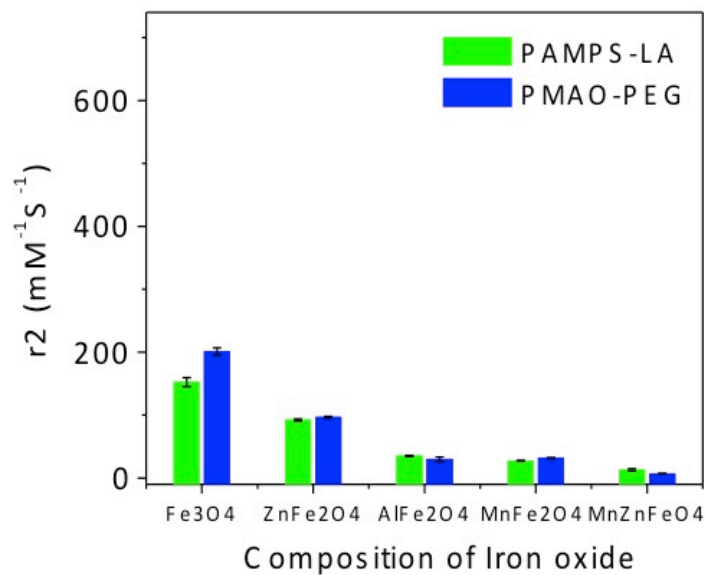
Figure 4-13 The r$_2$ relaxivites of different compositions of iron oxide nanocrystals

Table 4-4 Composition effects on MR relaxivity (r$_2$)

Composition effect	Average r$_2$ (mM^{-1} S^{-1}) at 1.5T			
Sample	Oleic acid	PAA-OA	PAMPS-LA	PMAO-PEG
10 nm Fe$_3$O$_4$	50.5 ± 2.8	158.9 ± 5.9	152.4 ± 7.2	201.1 ± 5.7
10 nm ZnFe$_2$O$_4$	15.0 ± 2.4	47.8 ± 3.6	92.4 ± 1.8	96.71 ± 1.2
10 nm AlFe$_2$O$_4$	32.6 ± 1.9	33.6 ± 2.1	35.2 ± 0.9	29.9 ± 3.4
10 nm MnFe$_2$O$_4$	16.8 ± 1.3	48.3 ± 2.2	27.4 ± 0.7	32.1 ± 0.4
10 nm MnZnFeO$_4$	37.9 ± 2.2	11.3 ± 2.2	13.0 ±1.8	7.1 ± 2.9
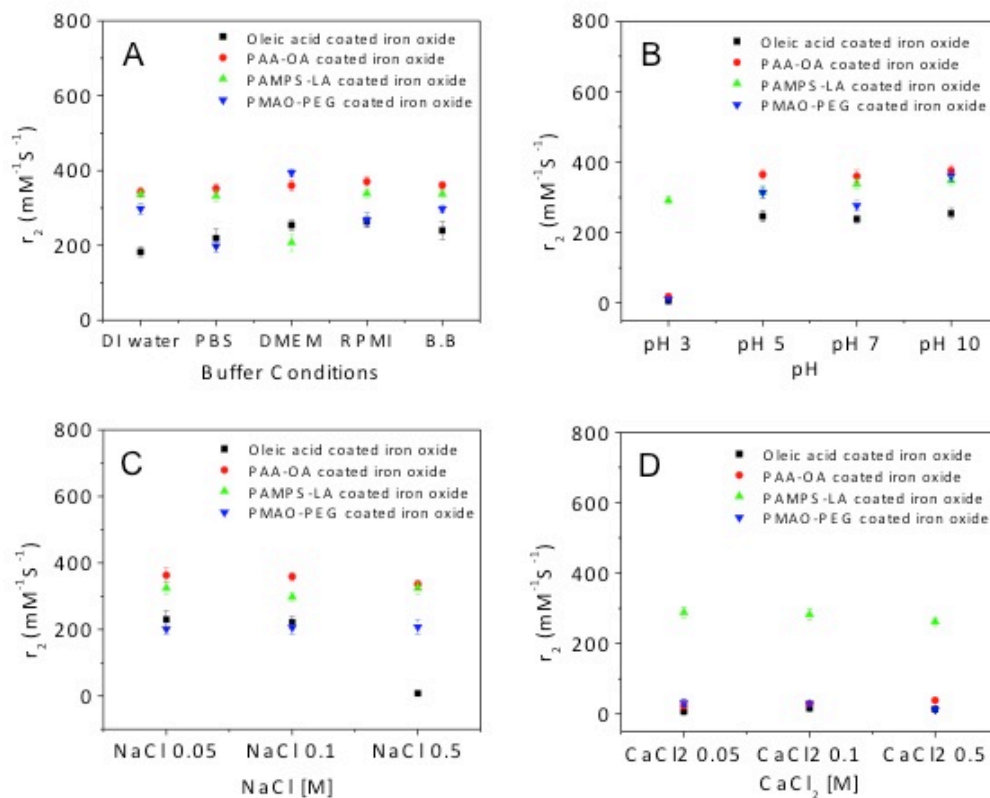
Figure 4-14 The r_2 values of iron oxide nanoparticles with different coatings at various conditions of buffers (A), pH (B), NaCl (C), and CaCl$_2$ (D).

4.3.4. *In vitro* cell toxicology study

The toxicological study is very important to apply *in vivo* MR imaging. To examine the toxicological issue of iron oxide nanocrystals depending on their sizes, coating, and compositions, we performed *in vitro* cell viability test using human dermal fibroblast (HDF). Figure 4-15 shows the percentage of cell viability with increased nanoparticle concentration measure from the amount of Fe ions in an acid digested sample. Figure 4-15 (A) confirmed that for bilayer oleic acid coated

particles the percentage of cell viability decreased as core size increased. Smaller hydrodynamic diameters would allow the particles to be internalized into the cells quicker, which result in increased toxicological effects. For iron oxide nanoparticle with the same core size (10 nm) and various polymer coatings (oleic acid bilayer, PAA-OA, PAMPS-LA, PMAO-PEG, and PEG 10K) only the bilayer oleic acid coated particles showed any toxicity up to 6000 uM Fe (Figure 4-15 (B)).

The bilayer oleic acid coating resulted in higher toxicity than any other polymer coating. The nanocrystals were densely covered with oleic acid but coating thickness is so small (2~4 nm) so that the core (iron oxide) was more exposed to the cell surface. Small hydrodynamic size would give more stress to the cells. Polymer coated materials were prepared by encapsulation. The larger hydrodynamic sizes of these materials prevent their accumulation within the cells. The oleic acid coated nanocrystals were non toxic up to 1200 uM of iron and polymer coated iron oxide suspensions were safe even at the highest concentrations tested (6,000 uM). Ferrite nanocrystals show greater toxicity to cells than pristine iron oxide nanocrystals (Figure 4-15 (C) and (D)). Comparing both bilayer oleic acid coated and PMAO-PEG coated $MnFe_2O_4$, $ZnFe_2O_4$, and Fe_3O_4, the $MnFe_2O_4$ nanocrystals were more toxic with an LD_{50} values of 600 uM for the more toxic oleic acid bilayer materials. The $ZnFe_2O_4$ and Fe_3O_4 nanocrystals showed similar toxicity with LD_{50} of 1200 uM with oleic acid bilayer coatings however with PMAO-PEG coatings the $ZnFe_2O_4$ or $MnFe_2O_4$ nanocrystals were more toxic than Fe_3O_4. The toxic metal ions (Mn and Zn) gave more toxicological effects to the cells.
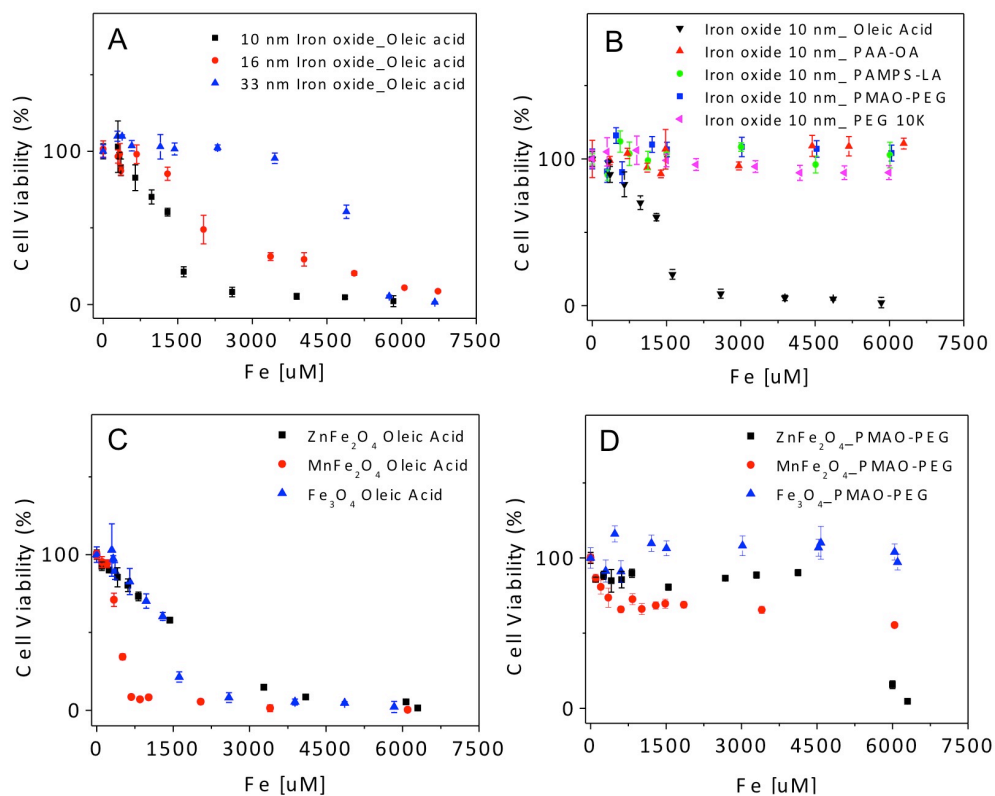
Figure 4-15 *In vitro* cell toxicological studies

In vitro cell toxocological study (A) cell viability tests of oleic acid coated iron oxide nanocrystals with different cores. (B) cell viability tests of iron oxide nanoparticles with various surface coating, (C) cell viability tests of the oleic acid coated iron oxide and ferrite nanoparticles, (D) cell viability tests of PMAO-PEG coated iron oxide and ferrite nanoparticles

4.4. Conclusion

In order to see the effects on MR relaxivity values, we prepared size tunable iron oxide nanocrystals from 4 to 33 nm with various surface coating agents (oleic acid, PAA-OA, PAMPS-LA, and PMAO-PEG). These surface-coated iron oxide suspensions gave good colloidal stability and kept small hydrodynamic size so that

they remained single core iron oxide nanocystals, which are not agglomerated and do not contain multicores in one coating. The core size (changing magnetic moment), hydrodynamic size (control size regime and aggregation), and grafting density (regulate water diffusivity) strongly affected to the MR r_2 values. The large core 33 nm iron oxide nanocrystals with small hydrodynamic size (41 nm) using oleic acid were kept in MAR/SDR and gave maximum value of r_2 (510 mM^{-1}S^{-1}). This is very promising probe for molecular and cellular labeling. Moreover, these iron oxide nanocrystals were examined to see toxicological effects on their size, surface, and composition with human dermal fibroblast (HDF) cells. The surface engineered iron oxide nanocrystals were not toxic up to 6,000 uM. The size, surface, composition tunable iron oxide nanocrystals are valuable not only high MR contrast enhancement but also excellent colloidal stability and low toxicity. It will give a variety for targeted in vivo MR imaging or drug delivery.

Chapter 5

Characterization and Optimization of the Fluorescence of Nanoscale Iron Oxide/Quantum Dots Complexes

In this work, nanoscale iron oxide/quantum dots complexes were formed in an efficient and versatile reaction that relied on the nucleation of chalcogenides on preformed iron oxide nanocrystals. Iron oxide nanocrystals acted as seeds for the growth of CdSe quantum rods (QRs), CdSe quantum dots (QDs), and CdSe@ZnS QDs. A zinc sulfide (ZnS) shell was added to protect the CdSe core in the complex chemically and to provide a reasonable fluorescence quantum yield ($\sim$ 5 %). High-resolution transmission electron microscopy (HRTEM) revealed that QDs shared an interface with iron oxide, yielding structures that resemble pincushions with QDs or QRs studding the surface of iron oxide. These complexes only formed under conditions of temperature, injection rate, and surfactant composition that

minimized the formation of unbound QDs. Because iron oxide is a ferromagnetic material, it provided a high purity (~89 %) of complexed materials without unbound QDs. The quantitative photoluminescence quantum yields (PLQY) of the purified complexes correlated with the number of QD per iron oxide. The size dependent optical and magnetic properties of each component were retained in these nanoscale complexes.

5.1. Introduction

Multifunctional nanostructures consisting of two or more functional components represent a new class of material with potential applications including multimodal imaging and simultaneous detection and therapy.[33,36,111,112,226-234] Specifically, magnetic-fluorescent hybrid nanostructures are recognized as a powerful class of multifunctional nanostructures because they combine both magnetic and fluorescent properties.[36,111,230,232] Magnetic iron oxide nanoparticles, possessing super paramagnetic property have found a variety of applications such as magnetic resonance imaging (MRI) contrast agents,[44,235,236] magnetic cell sorting and separation,[237,238] and magnetic drug delivery.[239,240] Fluorescent materials such as quantum dots (QDs) offer size-tunable optical properties and high fluorescence quantum yield.[25] As a fluorescent probe, QDs have important biomedical applications including *in vivo* cell targeting, imaging, and multiplexed biological detection.[32,53,65-67] These magnetic-fluorescent hybrid nanostructures can open new capabilities such as optical imaging combined with MRI,[107,209,211,241-244] visible

multiple cell tracking and separation.[68,108,245]   However, progress in these hybrid nanostructures is limited by many demands (stability, product yields, and size tunability) that biomedical applications place on the material.   Ideally, these assemblies would be prepared in high yield, of limited hydrodynamic size (d < 50 nm), and with controlled stoichiometry.   Three strategies have been explored to date: polymer encapsulation, ligand cross-linking, and direct seed nucleation.[36]

The first strategy relies on the encapsulation of the magnetic nanoparticles including iron oxide and QDs or fluorescent dyes inside of larger, often sub-micron, polymeric capsules or porous silica beads.[70,246-257] This method is relatively simple and is suitable for *in-vitro* applications such as multimodal imaging and drug delivery.[72-74,211,244,258,259] But, the resulting materials are relatively large (>100 nm) and easily aggregated. The second set of work examines the use of direct linking agents to coordinate magnetic particles and QDs or fluorescent dye.[77-82,260-262] Simply, iron oxide nanoparticles are covalently linked to the fluorescent dye or QDs via m-2-3-dimercaptosuccinic acid (DMSA) ligand or dodecylamine (DDA) cross linkers.[77,80] The cross-linkers can directly affect the conjugation so that the particle size remains small.   However, it is limited by its low product yield and the complicated functionality of linkers.   The third strategy exploits the observation that QDs can nucleate directly on some kinds of magnetic nanoparticles including iron oxide nanocrystals.[83-90,263-267] This method can be extended to many kinds of hybrid nanostructures including metal-metal, metal-semiconductor, metal oxide-metal, and metal oxide-semiconductor and offers products with small size,

homogeneous structures, and tunable stoichiometry.[91-96,268-271] Here, we focus on this direct nucleation route, specifically, magnetic-semiconductor hetero structures that provide small and tunable properties.

The direct nucleation of QDs on iron based magnetic nanostructure could reach to high purity and high yields of magnetic-quantum dot complex materials through the conventional high temperature metal precursor decomposition method.[83-90,263-267,272-275] More specifically, prior works have examined the formation of magnetic-semiconductor hetero structures by using a magnetic nanoparticle as a seed for the nucleation of semiconductor materials. Kwon and McDaniel *et al* described the synthesis of iron oxide/CdS heterostructures and examined the size dependence on growth rate and the effects of lattice mismatch on the heterojunctions.[272-275] Gu and Gao *et al* developed FePt-CdS, FePt-CdSe, FePt-ZnS heterodimer nanoparticles and explored the morphology of the structures by controlling various experimental conditions.[84,276,277] Recently, they demonstrated the intracellular manipulation of FePt-CdSe nanoparticles.[109] Selvan *et al* developed Fe_2O_3-CdSe nanocomposites and, by fluorescence imaging, showed internalized silica-coated magnetic quantum dots in a live cancer cell.[234,278-280]

Generally, direct nucleation produces both complexed materials and self nucleation of secondary materials as an excess. Ideally, a reaction would produce mostly complexed materials as opposed to isolated nanoparticles when the efficiency of the complex formation is optimized. In order to achieve optimal conditions, a quantitative method should be developed to understand favorable

conditions that minimize the formation of unbound QDs. Moreover, an unanswered question is the extent to which the complex reduces photoluminescence quantum yield (PLQY), and related issue of strategies to minimize quenching. The PLQYs of magnetic/QDs complexes through direct seed nucleation are generally estimated to be 3 to 38 %.[83,87,109,278-280] Because the QDs are in direct contact with the metal surface of magnetic nanoparticles, the PLQY of the complex decreases as compared with stand alone QDs.[75,76,83,87,90,109,278,279] Moreover, excess unbound QDs also affect the PLQY of the complex so that it should be removed to attain an exact value. Precise measurement is needed for an accurate PLQY value of the complex from the possible presence of excess unbound QDs.

Here we optimized the synthesis of nanoscale iron oxide/quantum dots (QDs) complexes that possess both good responsiveness to external magnetic fields and a PLQY value in excess of 5 %. The optimized synthesis permits the type and number of QD to be controlled. Because iron oxide is a strong ferromagnetic material, the complexes can be separated from unbound QDs with an external magnetic field. This magnetic capture allows for a measure of reaction yields and for the optimization of conditions to minimize excess unbound QDs. Also through this magnetic capture, the PLQY of complexes can be accurately determined because excess unbound QDs are removed. Although the photoluminescence of iron oxide/QDs complexes is lower than that found for pure QDs, it is non-bleaching and high enough to be easily visualized. Additionally, the PLQY correlates well with the number of QD per iron oxide nanoparticle. This work illustrates an efficient method

to control the synthesis of magnetic fluorescent complexes that possess variable morphology, improved fluorescent emission, and high quantum yield.

5.2. Experimental sections

5.2.1. Chemicals

Iron oxide, hydrate (FeO(OH), catalyst grade 30-50 mesh 99%), oleic acid (OA, technical grade 90%), 1-octadecene (ODE, technical grade 90%), cadmium oxide (CdO, powder 99.99%), selenium (Se, 100 mesh 99.5%), sulfur (S, powder 99.98%), zinc oxide (ZnO, powder 99%), trioctylphosphine (TOP, technical grade 90%), octadecylamine (ODA, 97%), hexadecylamine (HDA, 99%), trioctylphosphine oxide (TOPO, 99%), hexadecane (reagent plus, 99%) and phenyl ether (reagent plus, 99%) were all purchased from Sigma-Aldrich. All nanocrystals were synthesized under ultra-high purity nitrogen (N_2, 99.99 %). Methanol (99.8 %), acetone (99.5 %), hexanes (98.5 %), sodium bicarbonate (99.7 %), and dimethylformamide (DMF, 99.8 %), nitric acid (HNO_3, 70 %) and hydrogen peroxide (H_2O_2, 30 %) were purchased from Fisher Scientific. All chemicals were used without further purification.

5.2.2. Synthesis of iron oxide nanocrystals

The iron oxide nanocrystals were synthesized based on the previous work.[51] Specifically, 0.178 g of FeO(OH) was added to 2.26 g oleic acid and 5 g of 1-octadecene and this mixture was heated to 120 °C for 2 hours to evaporate residual

water. The temperature further increased to 260 °C for 30 minutes. Finally, the mixture was allowed to reflux at 320 °C for 2 hours and the solution became black. The iron oxide nanocrystals were purified and concentrated by first precipitating the product using methanol and acetone followed by centrifugation at 4150 rpm for 30 minutes (5 ml colloidal solution, 20 ml methanol, and 20 ml acetone). This process was repeated 5 or 6 times resulting in purified iron oxide nanocrystal solutions with minimal residual surfactants. The purification step is very important to make QD/iron oxide magnetic-optical complexes since unpurified iron oxide nanocrystals may prevent the nucleation and growth of QDs on the surface of iron oxide nanocrystals. The purified iron oxide solution was stored in hexanes at a concentration typically of 6,000 mg/L. Typically, nanocrystals diameters was 10 nm (± 1.5 nm). A series of iron oxide nanocrystals with various diameters from 8 to 17 nm was synthesized by controlling the ratio between FeO(OH) and OA from 1:3 to 1:6. The purified iron oxide nanocrystal solution was stored in hexanes.

5.2.3. Synthesis of iron oxide/CdSe QDs nanoparticles

To synthesize iron oxide/CdSe QDs complexes, CdO (0.0386 g, 0.3 mmol), ODA (3 g, 11 mmol), and ODE (10 g, 40 mmol) were mixed in a three-neck flask and heated to 200 °C for 1 hour. After cooling down to 60 °C, purified iron oxide nanocrystals/hexanes (1 ml, 6,000 mg/L of Fe) solution was added and the mixture was heated to 100°C for 30 min to remove the hexanes completely. Afterwards, the reaction mixture was heated to reflux at 280 °C for 1 hour under N_2 flow. After cooling down to 220 °C, Se (0.9 mmol) dissolved in 2 ml of TOP was slowly added

into the mixture solution (0.4 ml/min). The mixture was kept at 250 °C to allow for the growth of CdSe QDs at different time intervals (1 min to 25 min). Aliquots of growth solution were quenched in 10 ml hexanes.

5.2.4. Preparation of precursors for shell growth

The preparation of precursors and the shell growth for QDs was modified from published procedure.[62] The zinc precursor stock solution (0.04 M) was prepared by dissolving ZnO (0.39 g) in oleic acid (10.83 g) and 1-ODE (108 ml) at 250 °C. The sulfur precursor stock solution (0.04 M) was prepared by dissolving sulfur powder (0.128 g) in 1-ODE (100 ml) at 200 °C. Both precursor solutions were prepared under N_2 flow and clear solutions were acquired. The Zn precursor solution was preheated to ensure complete dissolution before injection. To make the shell, a specific amount of a stock solution was introduced via syringe into the hot reaction mixture.

5.2.5. Synthesis of iron oxide/CdSe@ZnS QDs nanoparticles

To synthesize iron oxide/CdSe@ZnS core/shell QDs complexes, the solution of the iron oxide/CdSe QDs complexes (growth for 20 minutes) without purification was allowed to cool down to room temperature and reheated to 220 °C to deposit ZnS shell onto CdSe QDs. At 220 °C, 1 ml of the Zn precursor (0.04 M ZnO/OA in ODE) was slowly injected into the solution and allowed to stir for 10 minutes. The same volume of sulfur in ODE was sequentially injected into the reaction and stirred for

20 minutes. Afterwards, the reaction mixture was cooled down to 60°C and dispersed in hexanes.

5.2.6. Synthesis of iron oxide/CdSe QRs nanoparticles

For synthesizing iron oxide/CdSe QRs complexes, CdO (0.0386 g, 0.3 mmol), ODA (3 g, 11 mmol), and ODE (10 g, 40 mmol) were mixed and heated to 200 °C for 1 hour. After cooling down to 60°C, purified iron oxide nanocrystal (0.023 g, 0.1 mmol) solution was added and heated to 100 °C for 30 minutes to remove the hexanes. Afterwards, the reaction mixture was heated and refluxed at 300 °C for 1 hour under N_2 to decompose the precursors. After cooling down to 200 °C, Se (0.9 mmol) dissolved in TOP (2 ml) was slowly injected into the mixture solution (0.4 ml/min). After injection, this solution was allowed to keep at 250 °C for 1 hour to synthesize the iron oxide/CdSe QRs complexes. Finally, the solution was cooled down and dispersed in hexanes.

5.2.7. Magnetic capture purification

To determine the product yield (i.e. how much Cd converted to the QDs attached on iron oxide nanoparticles), iron oxide/QDs complexes were separated and were purified from unbound QDs with the help of a magnetic force. First, iron oxide/QDs complexes were purified from excess QD precursor, surfactant, and solvent with three cycles of centrifugation by adding the methanol (20 ml) and acetone (20 ml) at 4150 rpm for 30 minutes. Afterwards, a strong handheld magnet (1/8 inch diameter, 1/8 inch long NdFeB rod magnet, United Nuclear Scientific

Equipment & Supplies) was placed for 12 hours in proximity to the purified solution in hexanes. In this magnetic capture process, the iron oxide/QDs complexes were separated from the excess unbound QDs. This process was repeated three times. The cadmium (Cd) concentrations of the captured, supernatant, and non-treated original solution were analyzed by inductive coupled plasma-optical emission spectroscopy (ICP-OES). The magnetic capturing efficiency (MCE) was calculated by the equation below.

$$MCE\ (\%) = \left[\frac{Cd_{capture}}{Cd_{capture\ +supernatant}} \right] \times 100 \quad (eq.\ 1)$$

5.2.8. Instruments and characterization

Ultraviolet-visible (UV-Vis) absorption spectroscopy: Ultraviolet-visible absorption spectra were measured by using a Varian Cary 5000 UV-VIS-NIR spectrophotometer.

Photoluminescence spectroscopy and photoluminescence quantum yield determination: Photoluminescence (PL) spectra of the iron oxide/QDs complexes were measured on a Jobin Yvon Spex Fluorolog 3 fluorescence spectrophotometer (USA). The absolute value of the iron oxide/QDs complexes was determined by the comparison of the PL integrated intensity of QDs at the same cadmium (Cd) concentration. The concentration of Cd was determined by ICP-OES. The absolute photoluminescence quantum yield (PLQY) was calculated by the gradient method of comparing the PL integrated intensity of the CdSe QDs and that

of the solution of rhodamine 6G (R6G) in ethanol. The absorption spectra of iron oxide/QDs complexes, CdSe QDs, and R6G were recorded at 480 nm excitation, with the optical intensities of all samples below 0.10 absorbance. The equation used to calculate the quantum yield follows.[117]

$$\Phi_{x=} = \Phi_r \cdot \frac{A_r}{A_x} \cdot \frac{I_r}{I_x} \cdot \frac{n_x^2}{n_r^2} \cdot \frac{D_x}{D_r} \qquad (eq.\, 2)$$

At room temperature, Φ_x and Φ_r are the absolute quantum yield of the CdSe QDs and rhodamine 6G. The Φ_r of R6G in ethanol is 95 %. A_r and A_x are, respectively, compared to the absorption value at the excitation wavelength, e.g. 480 nm in this study. I_r and I_x are the intensities of excitation, and those of the sample in our experiment are equal to the values of the standard sample. n_r and n_x are the refractive indicies of the solvents. Ethanol (n=1.359) and hexanes (n=1.372) are used in this study. D_x and D_r are the PL integrated intensities excited at 480 nm of the CdSe QDs and R6G.

For the calculation of PLQY of the iron oxide/QDs complexes, the equation was modified. The Φ_x and Φ_r are the absolute quantum yields of the iron oxide/QDs complexes and the calculated quantum yield of CdSe QDs by comparison with rhodamine 6G. The calculated value of CdSe QDs in hexanes was 10 %. A_r and A_x are the absorption values of iron oxide/QDs complexes and CdSe QDs with equivalent Cd concentration at same excitation wavelength. I_r and I_x are the intensities of excitation, and those of the sample in our experiment are equal to the values of the standard sample. n_r and n_x are the refractive indicies of the solvents. All iron

oxide/QDs complexes and CdSe QDs are both dispersed in hexanes. The refractive index n term was equal in this calculation.

Transmission electron microscopy (TEM): The TEM specimen was examined by JEOL 2100 field emission TEM operating at 200 kV with a single tilt holder. The TEM sample was made by evaporating one drop of purified solution in hexanes onto an ultra thin carbon type-A 400 mesh copper grids (Ted Pella Inc.). Energy-filtering transmission electron microscopy (EFTEM) provided the high-resolution images showing a crystalline structure and gatan imaging filter (GIF) gave the quantitative elemental maps (Fe and Cd) of a sample within narrow energy ranges. Energy-dispersive x-ray spectrometry (EDXS) detected the chemical compositions of the complexes. The average diameter was obtained by counting over 1000 individual nanocrystalline particles using Image-Pro Plus 5.0 (Media Cybernetics, Inc., Silver Spring, MD).

Inductively coupled plasma optical emission spectroscopy (ICP-OES): To determine the product yield and quantum yield of iron oxide/QD complexes, a Perkin Elmer ICP-OES equipped with auto samplers was used to measure the concentration of Cd. Purified iron oxide/QDs complexes solution was digested by using nitric acid (HNO_3, 70 %) and hydrogen peroxide (H_2O_2, 30 %) for the analysis.

X-ray diffraction (XRD): The XRD patterns were recorded using a Rigaku D/Max Ultima II with a zero-back ground sample holder and analyzed by JCPDS card. The 2θ range was measured from 10 to 80 degrees with Cu Kα radiation. The x-rays were generated at 40 kV and 40 mA.

5.3. Result and discussions

5.3.1. Synthesis of iron oxide/QD complexes

5.3.1.1. Synthesis of iron oxide/CdSe QD complexes

Nanoscale iron oxide/QDs complexes were synthesized by the nucleation and growth of QDs on preformed iron oxide nanocrystals. Monodisperse iron oxide nanocrystals were used as seeds for the nucleation sites of QDs. As shown in Figure 5-1 (A), the monodisperse iron oxide nanocrystals with narrow size distribution (<15 %) were produced using a thermal decomposition method, reported in this group; briefly, nanocrystals were stabilized with oleic acid (OA) surfactant and purified by repeated precipitation-centrifugation-redispersion using methanol, acetone, and hexanes.[51] To promote the synthesis of iron oxide/QDs complexes, cadmium oxide (CdO) was added to colloidal iron oxide nanocrystal solution forming an amorphous CdO shell around the iron oxide surface and then was converted to a cadmium precursor in the presence of octadecylamine (ODA) surfactant (see experimental section). From the TEM analysis, we confirmed that the iron oxide nanocrystals were covered by the amorphous CdO shell and were aggregated. When the Se-trioctylphosphine (Se-TOP) introduced to iron oxide-CdO shell, the QDs nucleated and grew onto the surface of iron oxide nanocrystals under optimized conditions (Figure 5-1). We speculated that due to a large lattice mismatch, the CdSe amorphous shell broke down and all CdSe nucleations occurred directly on the surface of iron oxide through de-wetting process at high

temperature.[272,273,276] The heterogeneous nucleation of QDs on iron oxide nanocrystal resulted in a pincushion structure as shown in Figure 5-1 (B). A high-resolution transmission electron microscope (HRTEM) with gatan image filter (GIF) analytical mapping confirmed that the QDs nucleated directly at the interface with iron oxide, resulting in crystalline structures (from Figure 5-2 to Figure 5-5).
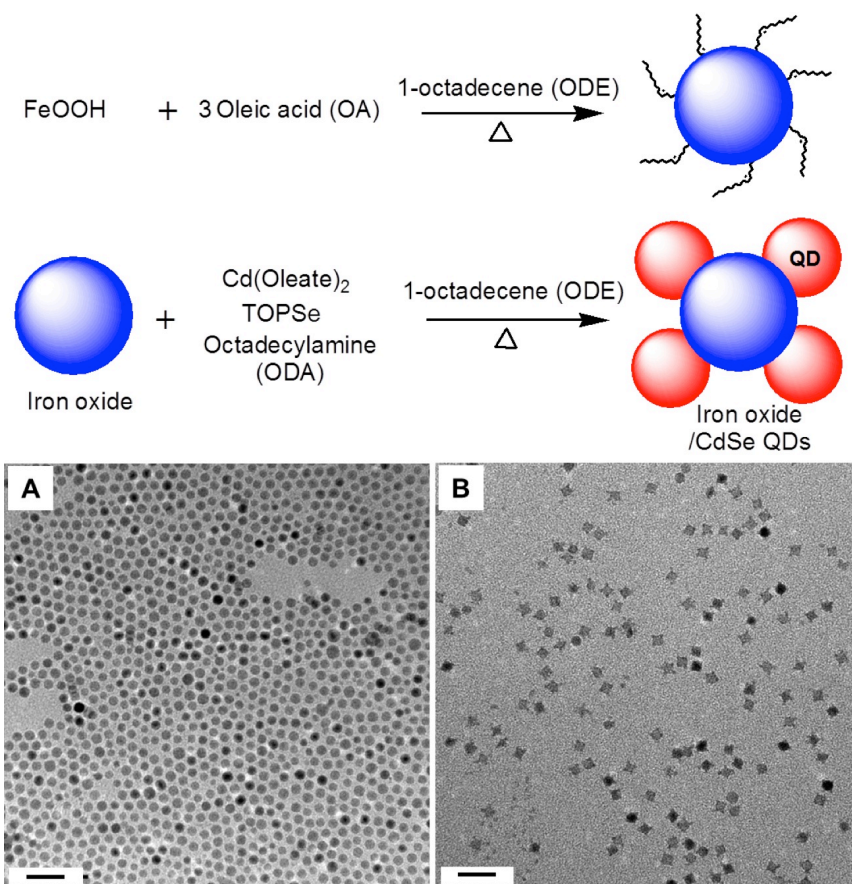
Figure 5-1 Synthesis of iron oxide nanocrystals and iron oxide/CdSe QDs complexes. The nanoscale iron oxide/QDs complexes were synthesized by using a high temperature decomposition that utilizes the nucleation of QDs on preformed iron oxide nanocrystals. The TEM images of (A) iron oxide nanocrystals and (B) iron oxide/CdSe QDs complexes (B) are shown, respectively. The size of iron oxide is 9.1 nm. The width/length of CdSe QDs is 3.0/3.4 nm. The scale bars are 50 nm.
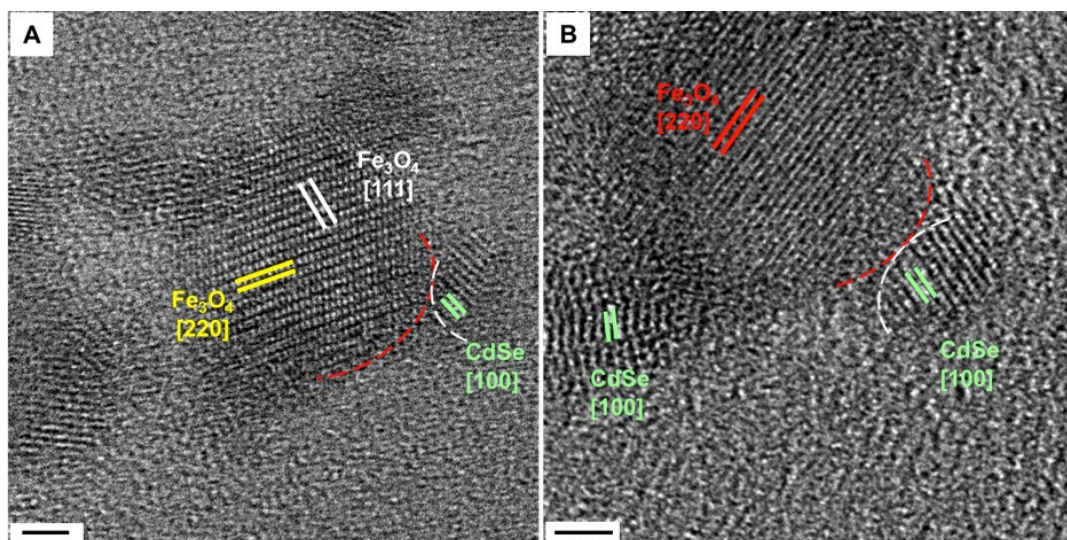
Figure 5-2 The high resolution TEM images of (A) iron oxide/CdSe QDs complexes and (B) iron oxide/CdSe/ZnS QDs complexes.

The Fe_3O_4 iron oxide region shows the (111) plane with lattice spacing of 0.458 nm (white line) and (220) plane with lattice spacing of 0.245 nm (red line). The CdSe QD region shows the (100) plane with lattice spacing 0.32 nm (blue line). The scale bars are 2 nm.
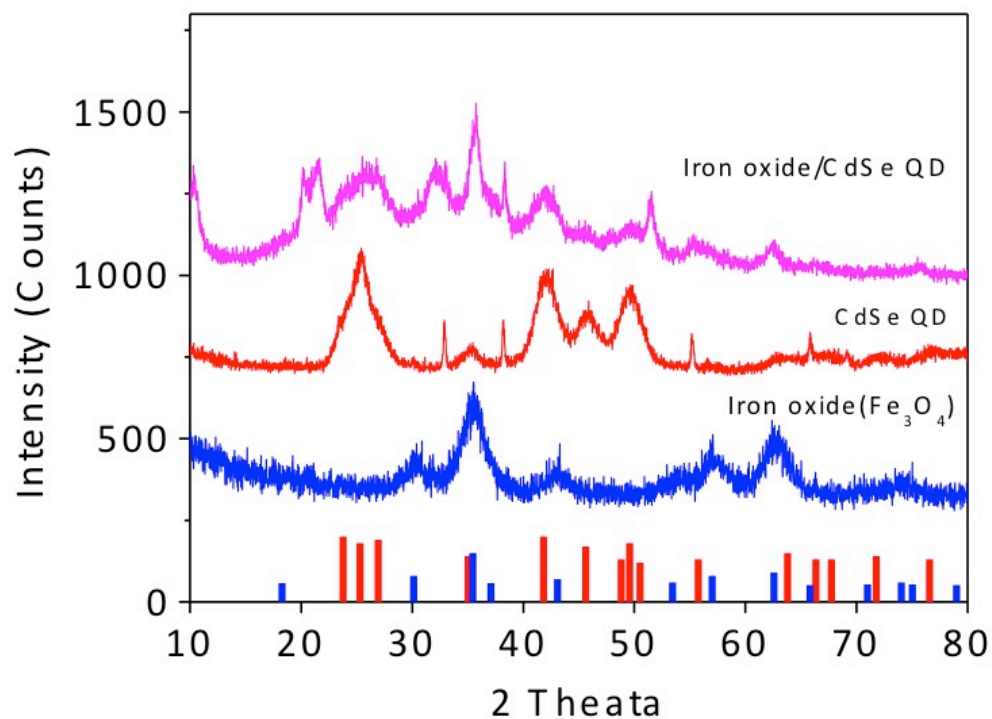
Figure 5-3 The powder XRD patterns of iron oxide/QD complexes

(A) iron oxide (Fe_3O_4)/CdSe QDs complexes, (B) CdSe QDs (wurzite), and (C) Fe_3O_4 iron oxide nanocrystals (face-centered cubic). The reference peak of face-centered cubic Fe_3O_4 (blue line) and wurzite CdSe QDs (red line) were identified from JCPDS card 19-0629 and 02-0330, respectively.
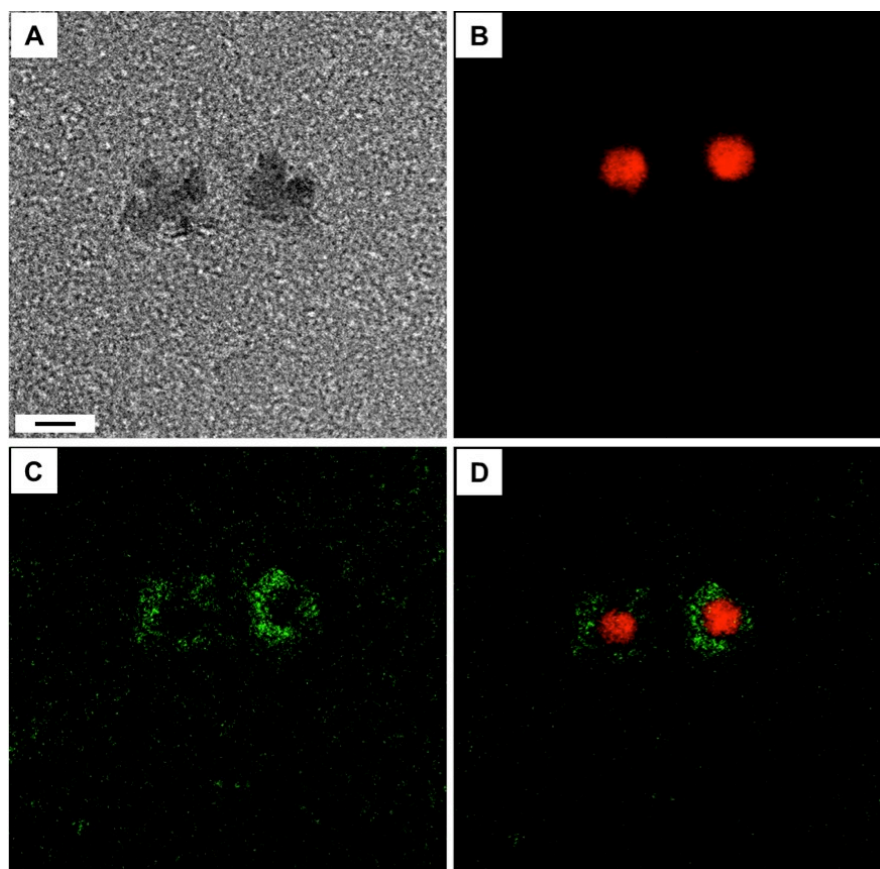
Figure 5-4 The GIF mapping of iron oxide/QD complexes

(A) The GIF frame image, (B) of iron (Fe) mapping (red), (C) Cd mapping (green), and (D) mixed mapping image of iron oxide/QDs complexes. From these images, the iron oxide nanocrystals were used as a core and QDs were grown on the surface. The scale bar is 10 nm.
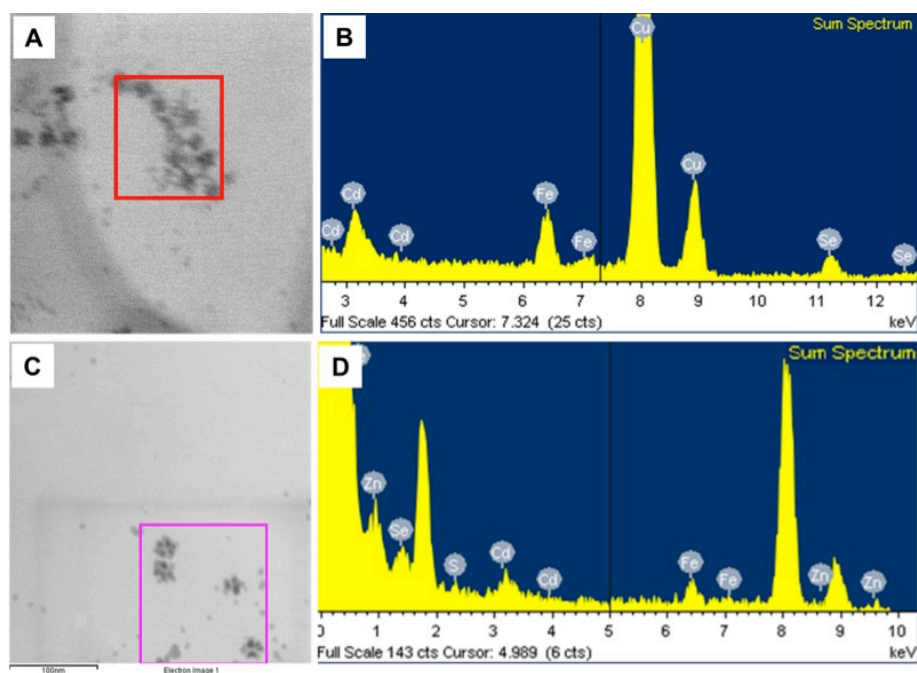
Figure 5-5 (A) STEM image and (B) EDAX of iron oxide/QDs complexes

The chemical components of Fe, Cd, and Se were detected in the iron oxide/CdSe QDs complexes. (C) The STEM image and (D) EDAX analysis of iron oxide/CdSe@ZnS QDs complexes; the chemical components of Fe, Cd, Se, Zn and S were shown in the iron oxide/CdSe@ZnS QDs complexes.

5.3.2. Shape control of iron oxide/CdSe QD complexes

The versatile method that produced heterogeneous nucleation of QDs on iron oxide nanocrystals, also controlled both the shape (iron oxide studded with core CdSe QDs, core/shell CdSe@ZnS QDs, and CdSe quantum rods (QRs)) and the composition (Figure 5-6). Various experimental reactions provided different types of iron oxide/QDs complexes such as core CdSe QDs and core/shell CdSe@ZnS QDs. For example, a zinc sulfide (ZnS) shell can be formed on iron oxide/CdSe QDs by

modified the successive ion layer adsorption and reaction (SILAR) method[62] which resulted in CdSe@ZnS QDs attached magnetic material with a fluorescence quantum yield (PLQY) of about 5 %. The improved quantum yield could be due to a ZnS wider band gap effect.[60-62,281,282] The ZnS shell that has a higher band gap than CdSe QDs, provides efficient quantum confinement of electron-hole pair inside the core. Due to the high photochemical stability of the ZnS shell, core/shell QDs exhibit stronger luminescence and higher quantum yield (3 times higher than that of core CdSe QDs). For biological and environmental applications, a ZnS coating on CdSe QDs protects from the possible release of toxic cadmium from CdSe QDs. In addition, optimized experimental conditions (reaction temperature and growth time) prepared CdSe QRs on iron oxide nanoparticle. The injection of Se-TOP into CdO/iron oxide solution at 200 °C and a growth time of 60 minutes prepared CdSe QRs on iron oxide surface even though surfactants such as octadecylphosphonic acid (ODPA)[283] or hexylphosphonic acid (HPA)[284], generally required for QR formation, were not added.
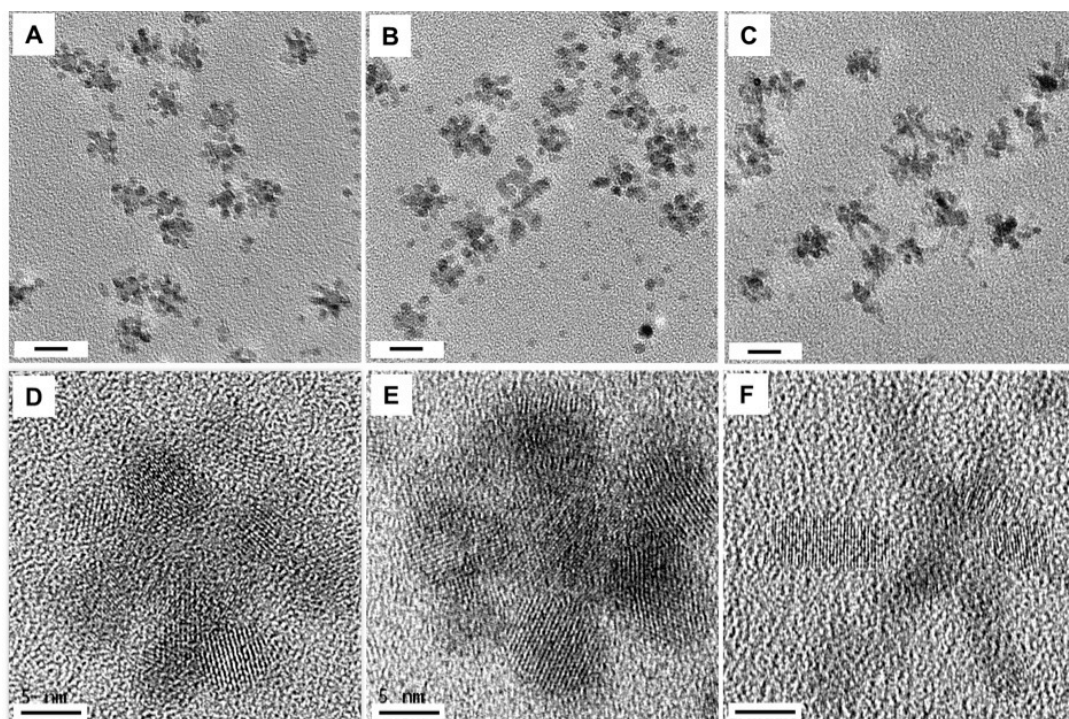
Figure 5-6 Types of the iron oxide/QDs complexes.

The TEM images of (A) iron oxide/CdSe QDs, (B) iron oxide/CdSe@ZnS QDs, and (C) iron oxide/CdSe QRs are shown. The iron oxide nanocrystal with 12 nm diameter was used as a core material. The diameter of CdSe QDs in (A) is 3.5/4.4 nm (width/length) and CdSe/ZnS QDs is 4.9/6.7 nm (width/length), respectively. The size of CdSe QRs (C) is 3.7/7.8 nm (width/length). The scale bars in A-C were 20 nm. The CdSe QRs were prepared from long time growth of QDs. Some free QDs from the reaction are seen in the TEM images, but they can be removed by magnetic capture purification. All iron oxide/QDs complexes exhibited crystalline structure as shown in high-resolution TEM images in D-F. The scale bars in D-F are 5 nm.

In these complexes, an increase in the diameter of iron oxide nanocrystals provided more nucleation sites for fluorescent QDs (Figure 5-7 and Figure 5-8). In forming this complex, the effective lattice mismatch and the presence of coincidence lattice sites are important to promote the formation of hetero structures.[273,274]

When the crystal structures are compatible and the lattice parameters of two crystalline phases are well matched, the core/shell nanostructures, such as CdSe/CdS QDs and CdSe/ZnS QDs are favored.[60-62,281,282] If the lattice mismatch is large, the interfacial lattice strain may prevent the nucleation of the second material on the first material's surface. Even with a large lattice mismatch, if preferred coincidence sites between two crystalline materials exist, then the hetero structure can be formed.[109,272-280] We examined how the diameter of initial iron oxide controlled the number of nucleation sites of CdSe QDs (Figure 5-7). As the iron oxide core size increased, multiple nucleations of QDs occurred because of the large interfacial strain effect. As the initial size of iron oxide nanocrystals ranging from 8 to 17 nm increased, the numbers of nucleation sites of QDs also increased from 4 to 10. As a result, more QDs nucleated and grew on multiple sites on larger iron oxide core. Also, since these iron oxide/QDs complexes maintained their innate magnetic and optical properties, they responded well to an external handheld magnet and showed red fluorescence under UV excitation (e.g. 365 nm) (Figure 5-9). The absorption (575 nm, black) and emission (604 nm, red) spectra also supported the sustained optical property of iron oxide/QDs complexes.
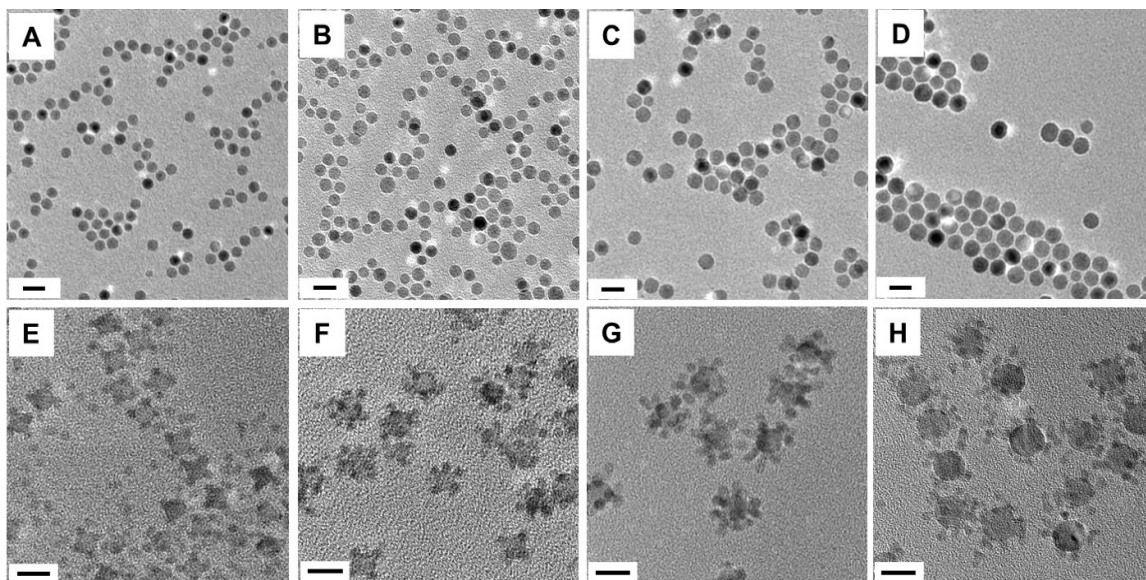
Figure 5-7 The stoichiometry of iron oxide/QDs complexes

(A-D) shows the TEM images of monodisperse iron oxide nanocrystals with diameters of 10 nm, 12 nm, 14 nm, and 17 nm, respectively. The scale bars are 20 nm. (E-H) indicates the TEM images of iron oxide/QDs complexes using different diameters of iron oxide nanocrystals from 10 nm to 17 nm. The scale bars are 10 nm. The number of nucleation/growth sites for QDs (4 to 10) directly increased with the diameter of iron oxide nanocrystals from 10 to 17 nm (A-D).
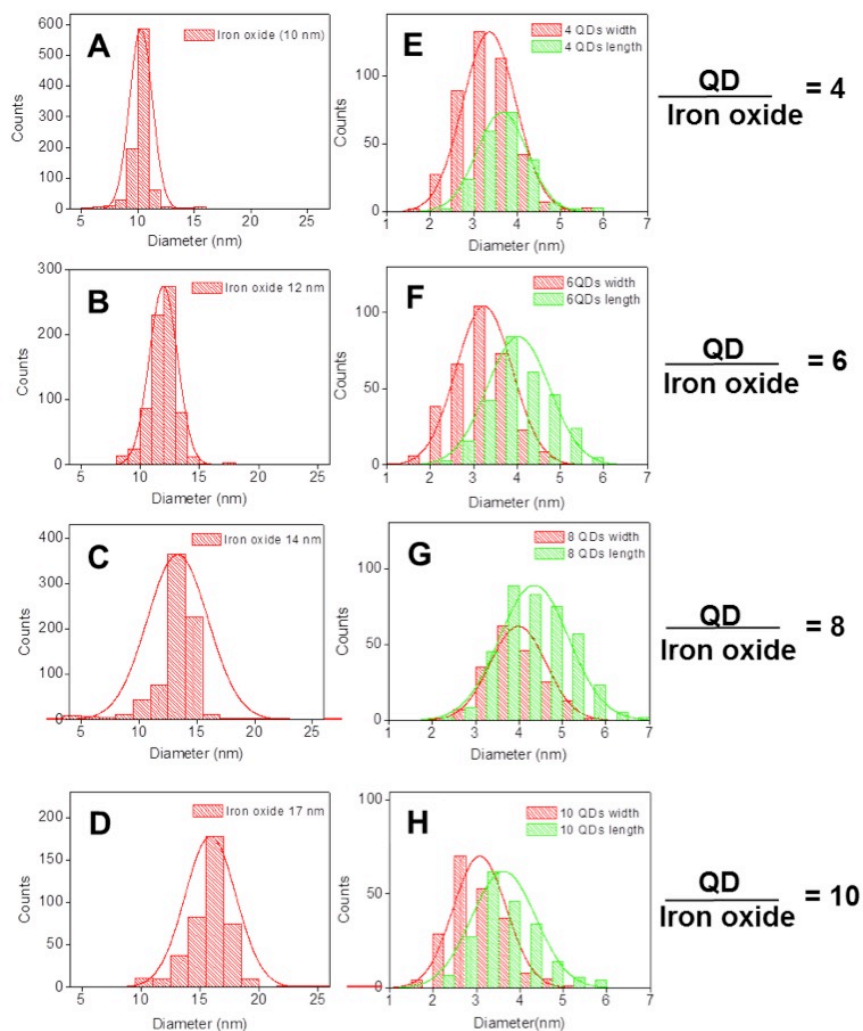
Figure 5-8 The histograms of different iron oxide/QD complexes

(A-D) shows the size histograms of iron oxide nanocrystals with diameter of (A) 10 nm, (B) 12 nm, (C) 14 nm, and (D) 17 nm, respectively. (E-F) described the size histograms of CdSe QDs in the complexes from 4 QDs per iron oxide to 10 QDs per iron oxide. The width/length of CdSe QDs in the complexes was (E) 3.1/3.7 nm, (F) 3.2/4.0 nm, (G) 4.0/4.7 nm, and (H) 3.1/3.6 nm, respectively.
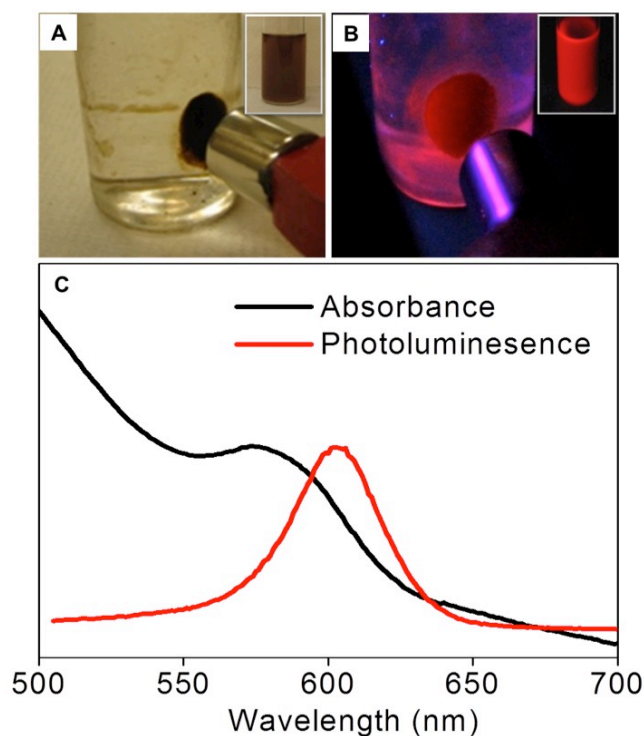
Figure 5-9 The optical and magnetic properties of iron oxide/QDs complexes. (A) The iron oxide/CdSe@ZnS QDs complexes were easily collected by handheld strong magnet. (B) The fluorescent emission was retained in the complexes under the ultraviolet light. (C) The absorption (575 nm, black line) and photoluminescence (604 nm, red line) spectra illustrate the optical property of the complexes.

5.3.3. Magnetic capture purification for the optimization

A simple magnetic capture process is an important step to measure the product yield of iron oxide/QDs complexes; the magnetic property of the complexes removed excess unbound QDs during purification (Figure 5-10). The removal of homogeneous QDs performed via a strong hand-held magnet (NdFeB, 1.25~1.28 Tesla). For the calculation of the yields of complexed materials (iron oxide/QDs), magnetic capture efficiency (MCE) was used. MCE calculates the percent product

yields with the Cd concentration of the magnetically captured materials to initial Cd concentration measured by ICP-OES. This calculation was based how much Cd converted to the QDs attached on iron oxide nanoparticles.   Figure 5-10 shows the supernatant and magnetically captured solutions before and after this purification step.   As the amount of unbound QDs decreased, fluorescence emissions sequentially decreased in the captured sample (complexed materials). From the bar graph, with the original Cd amounts of non-captured sample regarded as 100 %, the supernatant Cd amounts of unbound QDs gradually decreased (from 15 to 3 %) during the magnetic purification. The MCE suggested a quantitative way to determine the yields of iron oxide/QDs complexes, in good comparison to TEM measurements (Figure 5-11).
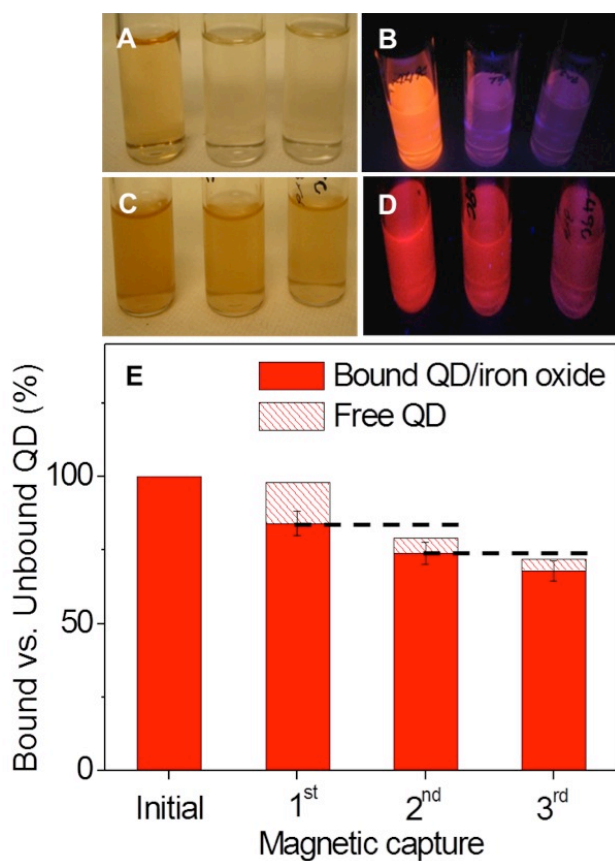
Figure 5-10 The magnetic capture process.

The photographs of supernatant solutions after 1st, 2nd, and 3rd magnetic capture process under (A) the fluorescent light and (B) the ultraviolet light. The supernatants consist of unbound QDs in the solution. The photographs of captured samples after 1st, 2nd, and 3rd magnetic capture process under (C) the fluorescent and (D) the ultraviolet light. The captured samples contained iron oxide/QD complexes with no unbound QDs. The unbound QDs decreased with multiple capturing processes. (E) The product yields of iron oxide/QDs complexes were determined via magnetic capturing process. The yields from 1st to 3rd capture are 84 %, 74 %, and 68 %, respectively.
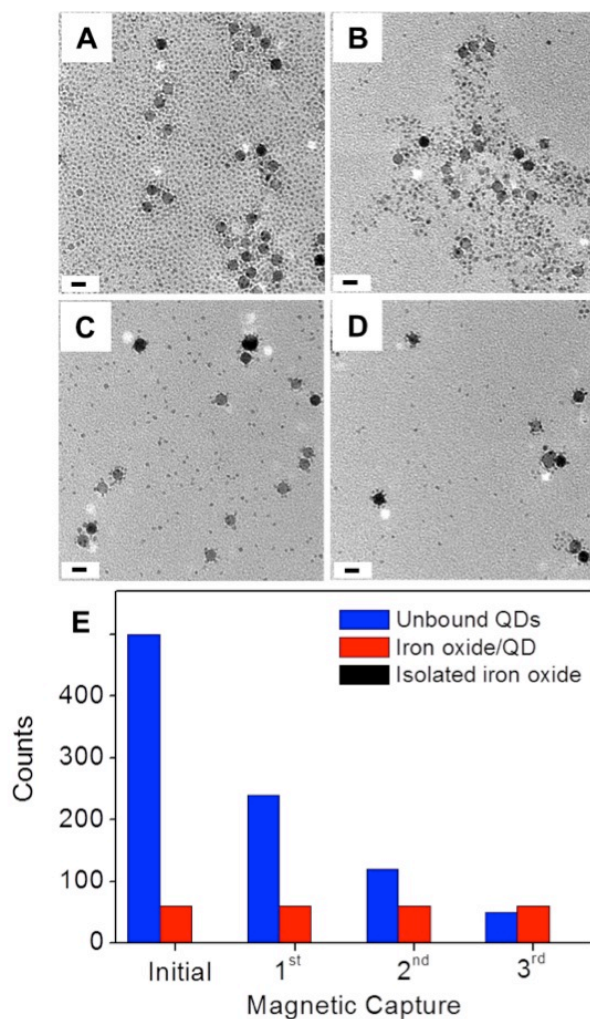
Figure 5-11 The TEM images of iron oxide/CdSe QDs complexes during magnetic capture process

The TEM images of iron oxide/CdSe QDs complexes were shown with (A) non-captured, (B) 1st magnetic capture, (C) 2nd magnetic capture, and (D) 3rd magnetic capture, respectively. As the magnetic capturing process increased, the unbound QDs were significantly reduced. Finally, purified iron oxide/CdSe QDs complexes were obtained. (E) The graph shows the relative percentages of the complexes by counting the numbers from the TEM images. The isolated iron oxide nanoparticles were not found in the TEM images. The scale bars are 20 nm.

The iron oxide/QDs complexes had high productive yield depending on the optimized experimental conditions of high temperature (280 °C), the additive (octadecylamine (ODA)), and the molar ratio between iron oxide and Cd precursor, as shown in Figure 5-12. The numerical values of product yield of iron oxide/QDs complexes were determined by MCE. Briefly, the growth temperature of 280 °C led to the highest product yield and promoted the formation of well-defined structures. In fact, at the low temperatures (200-230 °C) QD precursors did not decompose fully and too high of a temperature (300 °C) led to a high ratio of excess unbound QDs.

In the second optimized condition, the use of ODA as an additive linked Cd precursors to the iron oxide surface, with 15 mmol of ODA giving the highest yield of complexes (72 to 89 %). ODA is generally used as a ligand for high photoluminescence of core/shell nanocrystals because the alkylamine forms a weak and labile bond to the surface of the CdSe core and has good capping ability to prevent photo-oxidation.[61,62] In this complex system, ODA helped to bind QD precursors to the surface of iron oxide with a hydrophobic interaction.   Lastly, the molar ratio of iron oxides to Cd atoms was also optimized to minimize excess unbound QDs. In fact, when the molar ratio between iron oxide and Cd precursor increased from 1:4 to 3:4, iron oxide/QD complexes were produced with high yields (up to 72 %). At the higher ratio over 3:4, it kept the high yields of the complexes but excess isolated iron oxide nanoparticles were left, showing low PLQY value.
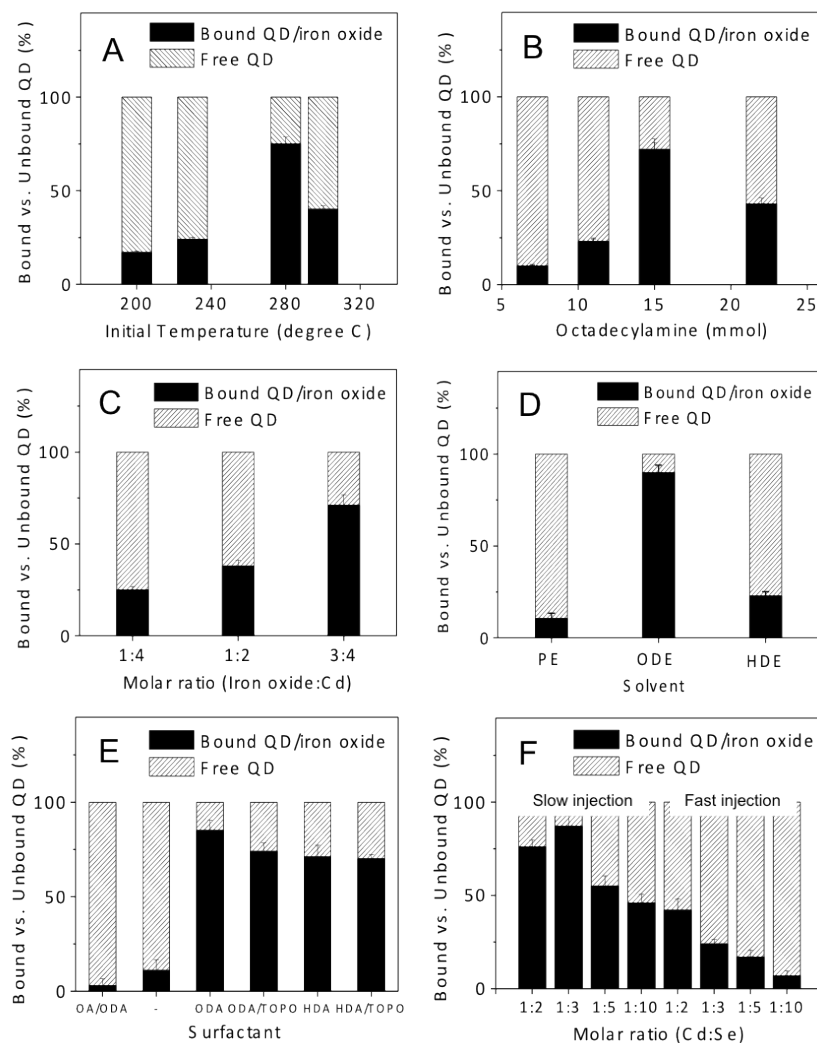
Figure 5-12 The optimization of iron oxide/QDs complexes via magnetic capture.
By magnetic-capturing, the iron oxide/QDs complex formation can be optimized.
The product yields are shown at (A) the initial temperatures from 200 °C to 300 °C,
(B) the amounts of octadecylamine (ODA), and (C) the molar ratio of iron oxide/Cd.
(D) The solvents, (E) the surfactant compositions, and (F) the injection speeds
contributed to the reaction of complexes. The solvents included phenyl ether (PE),
1-octadecene (ODE), and 1-hexadecane (HDE). The numerical values are given in
Table 5-1.

The highest product yields (about 80-89 %) of the complexes were also optimized by pure iron oxide (without excess oleic acid) and right surfactant compositions with longer carbon chain surfactant (ODA) (Figure 5-12 (E), Figure 5-13, and Figure 5-14). The nucleation of QDs on preformed iron oxide nanocrystals only occurred when the iron oxide surface was completely purified from excess iron salts and oleic acid. Unpurified iron oxide materials prevented the nucleation of secondary crystalline formation of QDs on the surface and promoted the homogenous nucleation of QDs instead (Figure 5-13).

Furthermore, surfactant composition affected the formation of the iron oxide/QDs complexes (Figure 5-12 (E) and Figure 5-14). For example, oleic acid (OA) irreversibly coated and interfered with the existing OA stabilizer of iron oxide so that OA blocked the deposition and nucleation of QDs on iron oxide surface. Instead of OA, the organoamine surfactant, ODA or hexadecylamine (HDA), was introduced to conjugate the QDs to iron oxide surface, providing a good passivation and chemical stability to the surface. In comparison with HDA, ODA had a longer hydrophobic chain and showed even higher yields than HDA.   Yet, adding trioctylphosphine oxide (TOPO) as a co-surfactant, the product yields (74 % and 70 %) were lower than that of ODA (85 %) or HDA (71 %). Organoamines and TOPO did not interfere each other but it may have competed for the binging sites producing some defects on the surface (Figure 5-14).
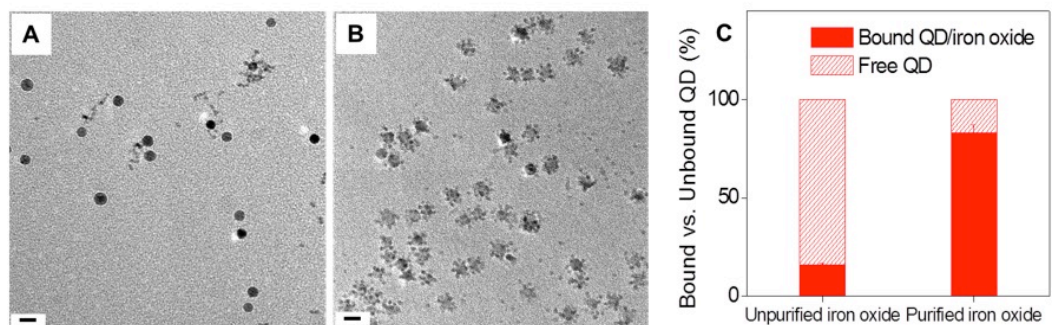
Figure 5-13 The purity of iron oxide nanocrystals for iron oxide/QD complexes
(A) and (B) show the TEM images of iron oxide/QDs mixtures using incompletely purified iron oxide (twice washing) and completely purified iron oxide (6 times washing), respectively. (C) described the product yields of iron oxide/QDs. The yields are 16 % (A) and 83 % (B), respectively. The scale bars are 20 nm.
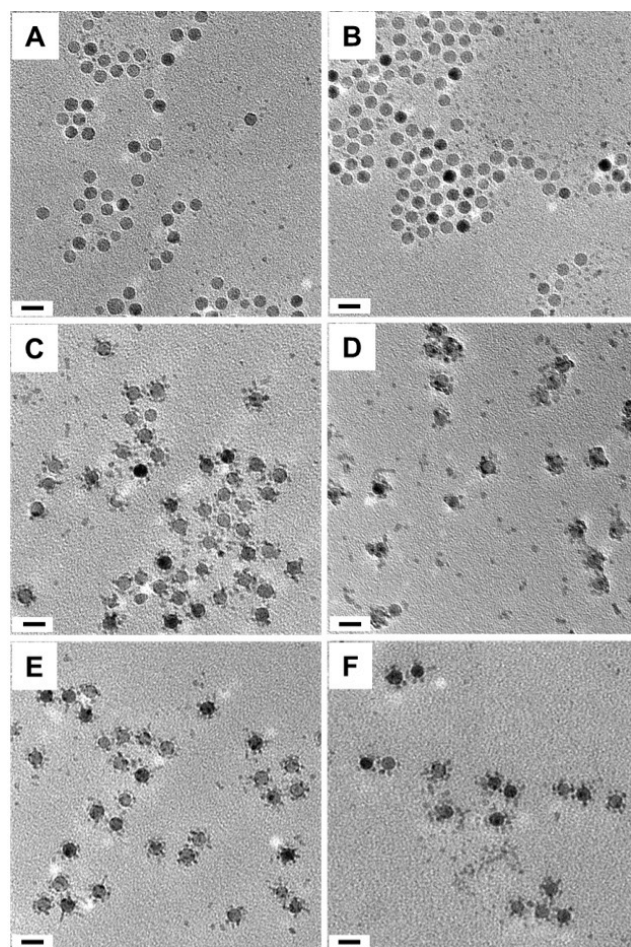
Figure 5-14 The TEM images of iron oxide/QD mixtures with various surfactants

(A) and (B) show the TEM images of iron oxide/QDs mixtures in the presence of oleic acid (OA)/octadecylamine (ODA)/1-octedecence (ODE) and only ODE without OA and ODA, respectively. The yields of captured iron oxide/QDs were (A) 3 % and (B) 11 %, respectively. (C) and (D) show the TEM images of iron oxide/QDs complexes using ODA/ODE and ODA/ODE/trioctylphosphine oxide (TOPO), respectively. The yields were (C) 85 % and (D) 74 %, respectively. (E) and (F) indicate the TEM images of iron oxide/QD complexes in the presence of hexadecylamine (HDA)/ODE and HDA/TOPO/ODE. The yields of complexes were (E) 71 % and (F) 70 %, respectively. The scale bars are 20 nm.

Another sensitive function to obtain improved product yield of iron oxide/QDs complexes was the slow and drop-wise addition of Se-TOP at high temperature (Figure 5-12 (F) and Figure 5-15). Figure 5-12 (F) shows the product yields of the complex depending on the addition speed of Se-TOP into the iron oxide/CdO solution. A fast and burst injection (2 ml/sec) caused a fast homogeneous nucleation of CdSe QDs rather than a passive continuous growth of QDs on the iron oxide. However, a slow and drop-wise addition of Se precursor (0.4 ml/min) minimized the formation of homogeneous QD nucleation, with optimized formation (46-76 %), to let QDs deposit and nucleate on the iron oxide surface. By decreasing rate of addition of Se precursor slowly deposited QDs on iron oxide surface. As a result, QDs nucleated and grew continually on the specific sites of iron oxide even though large interfacial strain and lattice mismatch effect is possible. This lattice mismatch and strain-induced contribution depends on the presence of defects and dislocations of the surface, which may vary under the conditions tested (purity of iron oxide, surfactant compositions, speed of Se-TOP addition, and etc.). The product yields of iron oxide/QDs complexes were quantitatively measured by MCE and were listed in Table 5-1.
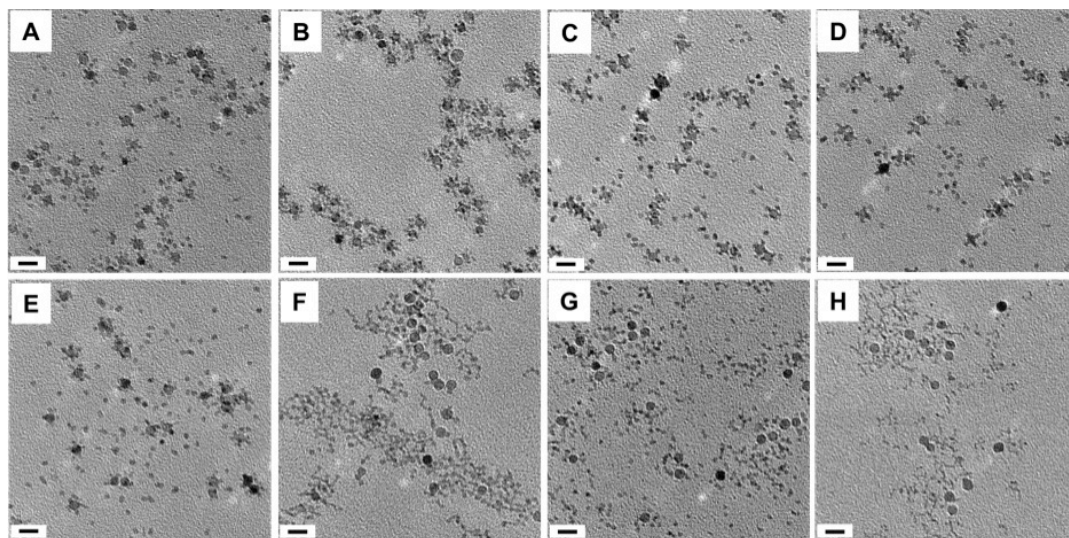
Figure 5-15 The TEM images of iron oxide/QD complexes with slow and fast injections at different molar ratios

(A-D) The TEM images of iron oxide/QDs complexes with slow injection at the different molar ratio (iron oxide/CdO/Se-TOP= 1:3:6 (A), 1:3:9 (B), 1:3:15 (C), and 1:3:30 (D)); the slow injection showed the good attachment of QDs on the iron oxide surface. The yields of iron oxide/QDs complexes from (A) to (D) were 76, 87, 55, and 46 %, respectively. (E-H) The TEM images of iron oxide/QDs complexes with fast injection at the different molar ratio (iron oxide/CdO/Se-TOP = 1:3:6 (E), 1:3:9 (F), 1:3:15 (G), and 1:3:30 (H)); the fast injection showed the poor attachment of QDs on iron oxide surface. The yields from (E) to (H) were 42, 24, 17, and 7 %, respectively. The scale bars are 20 nm.

Table 5-1 Magnetic capture efficiency (%) of the iron oxide/CdSe QDs complexes at various conditions

Sample	Magnetic Capture (Yield %)	Molar ratio (iron oxide: Cd:Se)	Molar ratio (iron oxide/Cd)	Slow injection	Fast injection	Initial Temparature (degree C)	OA (g)	ODA (g)	HDA (g)	TOPO (g)	ODE (g)	PE (g)	HDE (g)
1	17	1:3:9	1:3	O		200		4			10		
2	24	1:3:9	1:3	O		230		4			10		
3	75	1:3:9	1:3	O		280		4			10		
4	40	1:3:9	1:3	O		300		4			10		
5	10	1:3:9	1:3	O		280		2			10		
6	23	1:3:9	1:3	O		280		3			10		
7	72	1:3:9	1:3	O		280		4			10		
8	43	1:3:9	1:3	O		280		6			10		
9	25	1:4:12	1:4	O		280		4			10		
10	38	1:2:6	1:2	O		280		4			10		
11	71	3:4:12	3:4	O		280		4			10		
12	10	1:3:9	1:3	O		280		4				10	
13	89	1:3:9	1:3	O		280		4			10		
14	23	1:3:9	1:3	O		280		4					10
15	3	1:3:9	1:3	O		280	1	4			10		
16	11	1:3:9	1:3	O		280		4			10		
17	85	1:3:9	1:3	O		280		4			10		
18	74	1:3:9	1:3	O		280		4		2	10		
19	71	1:3:9	1:3	O		280			4		10		
20	70	1:3:9	1:3	O		280			4	2	10		
21	76	1:3:6	1:3	O		280		4			10		
22	87	1:3:9	1:3	O		280		4			10		
23	55	1:3:15	1:3	O		280		4			10		
24	46	1:3:30	1:3	O		280		4			10		
25	42	1:3:6	1:3		O	280		4			10		
26	24	1:3:9	1:3		O	280		4			10		
27	17	1:3:15	1:3		O	280		4			10		
28	7	1:3:30	1:3		O	280		4			10		

OA-oleic acid ($C_{18}H_{34}O_2$)
ODA-octadecylamine ($CH_3(CH_2)_{17}NH_2$)
HDA-hexadecylamine ($C_{16}H_{35}N$)
TOPO-trioctylphosphine oxide ($[CH_3(CH_2)_7]_3PO$)
ODE-1-octadecene ($CH_2=CH(CH_2)_{15}CH_3$)
PE – phenyl ether ($C_{12}H_{10}O$)
HDE- 1-hexadecene ($C_{16}H_{34}$)

5.3.4. Quantitative PLQY measurements of iron oxide/QD complex

The synthesized iron oxide/QD complexes still maintained optical property even though QDs were attached on the surface of an iron oxide nanocrystal. However, the PLQY of the QDs in the complexes is an order of magnitude (1/8) lower than that of pure QDs because QDs were attached directly to iron oxide nanocrystals. Figure 5-16 shows the results of PLQY of iron oxide/QDs complexes and isolated QDs. Iron oxide/QDs complexes had relatively lower PLQY (1~3 %) than stand alone QDs (10~20 %). Because of the direct contact to the metal surface, the metal nanoparticles quench the fluorescence of QDs gradually.[70,75,76] Many researchers reported the PLQY value of the magnetic-QD materials ranging from 2 to 38 %.[83,87,90,109,277-280] In a seed-mediated method, excess unbound QDs may affect the PLQY value. Therefore, we developed the MCE method to separate iron oxide/QDs complex only and used it before measuring PLQY value in order to eliminate excess QDs neighboring effect.
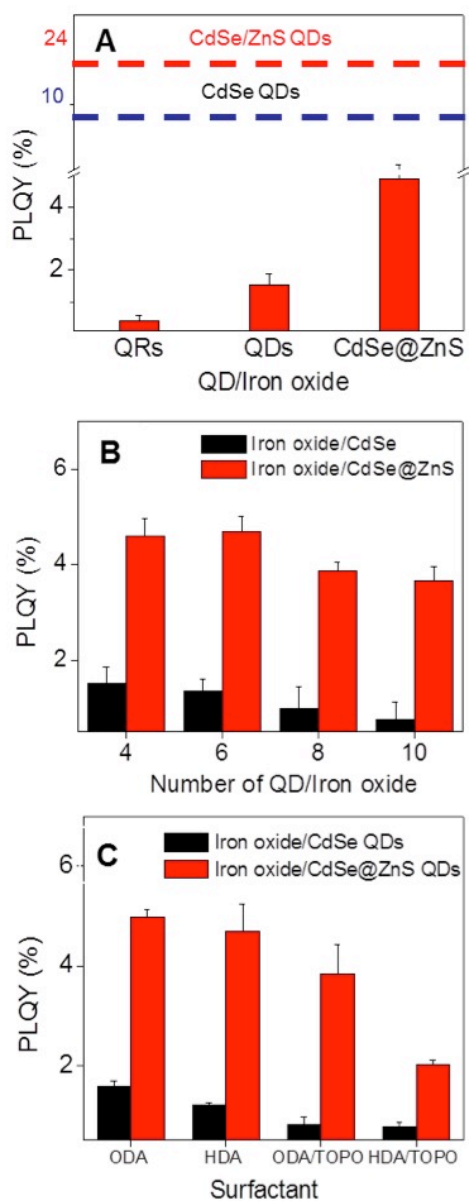
Figure 5-16 The PLQY of iron oxide/QDs complexes.

The PLQY values of iron oxide/QDs complexes at (A) the type of QD, (B) the number of QD per iron oxide, and (C) surfactant composition. The deposition of ZnS shell onto CdSe QDs improved the PLQY to 5 %.

The iron oxide/QDs (CdSe QRs and CdSe QDs) complexes have low PLQY coming from structural effect. However, the PLQY was enhanced by the deposition of a ZnS shell on the complex. Generally, the quantum yield of CdSe QRs (1-3 %) is much lower than that of CdSe QDs (10-20 %).[285,286] Due to quenching effect of metallic iron oxide, the PLQY of iron oxide/CdSe QRs complexes was 0.1 to 0.5 %, which is much lower than that of iron oxide/CdSe QDs complexes (1-3 %). Although the iron oxide/QDs complexes have a low quantum yield (< 3 %), the deposition of ZnS shell would protect the CdSe QDs on iron oxide chemically and improved the PLQY up to 5 % (Figure 5-16A). If the shell has a higher band gap than CdSe core and the band offsets of the core/shell structures are type I (where the core has a lower conduction band and a higher valence band in comparison to those of the shell), the photon generating an electron and hole inside the nanocrystals are mostly confined in the core.[281] Therefore, core/shell QDs exhibit enhanced PLQY and are more stable against photooxidation. For CdSe QDs (band gap 1.75 eV), the CdS (2.5 eV), ZnS (3.7 eV), or ZnSe (2.7 eV) which have higher band gaps can be used as shell materials with small lattice mismatch.[60,61,282,287] In the complex, although a ZnS shell gives an environmentally stable surface to prevent the release of toxic Cd to the outside, multilayered ZnS shells were not successful due to large lattice strain effect (data not shown).

Furthermore, both the number of QDs per iron oxide and surfactant composition also affected the PLQY value of iron oxide/QDs complexes (Figure 5-16 (B) and (C)). As shown in Figure 5-16 (B), the PLQY value slightly decreased as the

number of QD per iron oxide increased. Though not entirely understood, we speculate that many nucleation/growth of QDs on certain surface area may produce more defects and dislocations, leading to self-quenching effect in both iron oxide/CdSe QDs and iron oxide/CdSe@ZnS QDs systems. Figure 5-16 (C) shows that ODA surfactant gave the highest PLQY value (~5 %). However, addition of TOPO as a co-surfactant may displace and form a competitive bonding of QDs to the iron oxide surface forming the defects. As a result, the PLQY was low in both core (0.7~1 %) and core@shell iron oxide/QDs complexes (2~3 %) comparing to those of ODA (5 %) and HDA (4.5 %) stabilized complexes. In short, the organoamine surfactants (ODA and HDA) gave the most favorable environment for the nucleation/growth of CdSe QDs and CdSe@ZnS QDs.

5.4. Conclusion

In summary, we have synthesized nanoscale iron oxide/QDs complexes using high temperature decomposition of QD precursors. Under optimized conditions, the nucleation of metal chalcogenides occurred only on preformed iron oxide nanocrystals. The increase of the diameter of iron oxide nanocrystals promoted more nucleation sites for fluorescent QDs in these complexes. The purification of iron oxide/QD complexes, through a magnetic capture process, allowed us to tailor the synthetic conditions in order to minimize excess unbound QDs formation. Even though the PLQY of the QDs in these complexes is an order of magnitude lower than that of pure QDs, the PLQY of these complexes was greatly improved by a ZnS shell

in comparison to those in the literature. Moreover, the PLQY of these complexes was a sensitive function of the number of QD per iron oxide, type of QD, and surfactant stabilizer. The combination of optical and magnetic properties in these nanoscale iron oxide/QDs complexes make it possible to tailor the synthesis for potential biological applications, such as specific cell separation and drug delivery.

Chapter 6

A strategy for Visualizing Magnetic Separations: QDs/Iron Oxide Materials

Real-time quantification and visualization of magnetic separation processes involving nanoscale particles can be a challenge as these magnetic materials lack optical signatures. Here we address this problem by forming magnetic nanocrystals with quantum dots (QDs) materials affixed to their surfaces. These materials, termed here magnetic-optical complexes, consist of iron oxide cores decorated with smaller cadmium selenide (CdSe core) or cadmium selenide/zinc sulfide QDs (CdSe/ZnS core shell). Once nucleated on the surface of iron oxide nanocrystals, QDs can be grown to diameters that provide tunable emission throughout the visible. After phase transfer, the resulting aqueous suspensions of the magnetic-optical complexes were fluorescent (quantum yields of 1 – 5 %) over a range of pH, ionic strength, and buffer conditions. The size-dependent separation of iron oxide

cores could be easily visualized as larger magnetic cores tagged with red QDs came to dominate emission in the magnetic fraction of a starting mixture that included smaller cores tagged with green QDs. Additionally, optical detection could be applied to the problem of detecting small amounts material collected magnetically onto surfaces from dilute suspensions. For example, while sub nanomolar solutions of complexes had no detectable emission, complex emission could be quantified from surfaces used for magnetic collection and pre-concentration.

6.1. Introduction

The combination of magnetic and fluorescent properties in one nanocrystal has been recognized as an important goal for nano chemistry with applications ranging from material science to biotechnology.[33,36,111,112,226-228,232,234,288] Such complexes have been applied to *in vitro* and *in vivo* cell imaging with MRI, drug delivery, analytical multi-cells tracking, sorting, manipulation, and separations.[68,72,73,82,107,108,209,211,237,240-242,262,289-294] Of specific interest in this work is the development of materials that can allow for the visualization of magnetic separation processes. External magnetic fields can be used to separate magnetic materials, including nanocrystals, from stable dispersions. This principle is at the heart of the use of larger magnetic beads in bioanalytical applications, and has also motivated the use of smaller nanocrystals in magnetic cell sorting, separation, and enrichment.[108,237,238,240,288] By including a fluorescent probe such as an organic dye or quantum dot on the particle, visualization capability allows easy detection of the

target molecules.[68,73,107,209,242,245,293] For example, Wang *et al* used superparamagnetic Fe_2O_3 bead binding with CdSe/ZnS QDs to separate and detect MCF-7 breast cancer cells from serum.[289] Also, fabricated mesoporous dye-dopped silica nanocrystals immobilized with multiple magnetic nanocrystals may be applied simultaneously to enhance cell detection with MRI, fluorescence imaging, and drug delivery.[72]

Currently, most researchers have generated magnetic-fluorescent complexes by relying on the encapsulation magnetic and optical components into a larger structure.[70,74,244,247,250-252,254-259,261,295-297] What results are normally micron-sized polymer or silica beads which contain internally the active nanostructures. Using such materials, specific target (e.g. therapeutic cells, lectins, and drugs) sorting and detection with fluorescence have been reported.[74,295] It is also possible to enrich samples with one magnetic fraction and visualize this by fluorescence.[247,250,290,298,299] By incorporating QDs with tailored emission colors, it is also possible to optically encode materials for multiplexed detection.[24,65-67,300,301] This work illustrates the great value of combining optical emission with magnetic responsiveness; however, the strategies adopted to mix optical and magnetic materials in larger structures cannot easily translate to the separation of single nanocrystals with much smaller diameters.

To address the specific challenge of creating magnetic-optical complexes of small diameter (e.g. < 25 nm), several groups have developed strategies to grow emissive quantum dots (QDs) directly on magnetic nanocrystals.[83,87-89,109,265-]

[267,273,276-278,302-305] The process relies on the nucleation of QDs onto iron oxide surfaces and can provide for highly controlled QD growth and hence a wide range of well-defined emission colors.[83,87,88,276,277,303,304] While this direct nucleation process has the downside of lowering QD quantum yields as compared to isolated products, because multiple QD attach to a single particle it can still be a very bright object with stable emission relatively insensitive to bleaching. Applications of these materials to visualizing magnetic separations in relevant biological environments have not yet been reported.

Several materials issues must be addressed to realize this goal. Certainly, as is true for the larger beads it is important to be able to tag different kinds of magnetic materials with different colors to offer multiplexed optical detection.[67,70,74,295] Also possible is the ability to do multiplexed separation, or to in one separation collect several material fractions simply by varying the applied field strength.[306-308] Colloidal stability is also a critical issue; the complexes must be coated with the appropriate polymers to allow for non-bleaching QD emission as well as non-aggregation in biological media.[109,278] Finally, the size dependent magnetic properties of the complex suggest great advantages in multiple cells separation and enrichment because of its selectivity and sensitivity to a magnetic response.

In this work we applied strategies to form nanoscale magnetic-optical complexes of iron oxide and quantum dots (QDs) to developing water-soluble materials that allowed for the visualization of magnetic separations. Briefly,

purified iron oxide nanocrystals were used as nucleation sites for QDs leading to iron oxide crystallites studded with one or more QDs. The resulting complexes were highly uniform, tunable in both core and QD dimensions, with striking pin-cushion type structures. High-resolution TEM and EELS data reveal that the QDs directly nucleate at the interface of the iron oxide crystallite, and that these nanocrystals grow steadily over time. The distinctive fluorescence emission of the QDs can be tailored through the manipulation of the reaction time, and quantum yields can be optimized through the addition of ZnS shells. Water-soluble complexes could be formed using a variety of amphiphilic polymers in a conventional phase transfer process. Applications of these materials in a multiplexed magnetic separation as well as a magnetic enrichment are demonstrated.

6.1. Experimental sections

6.1.1. Chemicals

Iron oxide, hydrate (FeO(OH), 30-50 mesh), oleic acid (OA, technical grade, 90 %), 1-octadecene (ODE, technical grade 90 %), cadmium oxide (CdO, 99.99 %), selenium (Se, 99.99 %), sulfur (S, 99.5 %), zinc oxide (ZnO, 99.99 %) , trioctylphosphine oxide (TOP, technical grade 90 %), and octadecylamine (ODA, 97 %) were all purchased from Sigma-Aldrich. All nanocrystals were synthesized under ultra-high purity nitrogen (N_2, 99.99 %). Hexanes (95 %), acetone (99 %), ethanol (99.5 %), and methanol (99 %) were obtained from Sigma-Aldrich. All chemicals were used as received.

6.1.2. Synthesis of iron oxide nanoparticles

The iron oxide nanocrystals were synthesized based on the previous work.[51] Specifically, 0.178 g of FeO(OH) was added to 2.26 g oleic acid and 5 g of 1-octadecene and this mixture was heated to 120 °C for 2 hours to evaporate residual water. The temperature further increased to 260 °C for 30 minutes. During this time the iron oxyhydroxide dissolved and formed iron-oleate precursors. Finally, the mixture was allowed to reflux at 320 °C for 2 hours and the solution became black.

The iron oxide nanocrystals were purified and concentrated by first precipitating the product using methanol and acetone followed by centrifugation at 4150 rpm for 30 minutes (5 ml colloidal solution, 20 ml methanol, and 20 ml acetone). This process was repeated 5 to 6 times resulting in purified iron oxide nanocrystal solutions with minimal residual surfactants. The purification step is very important to make QD/iron oxide magnetic-optical complexes since unpurified iron oxide nanocrystals may prevent the nucleation and growth of QDs on the surface of iron oxide nanocrystals. The purified iron oxide solution was stored in hexanes at a concentration typically of 6,000 mg/L. Typically, nanocrystals diameters was 10 nm (± 1.5 nm). The larger iron oxide nanocrystals (17 nm) were prepared by increasing the amount of oleic acid relative to iron (FeOOH: oleic acid = 1:5).

6.1.3. Synthesis of iron oxide/CdSe QD nanoparticles

CdO (0.3 mmol), ODA (11 mmol), and ODE (40 mmol) were added in a 50 mL three neck flask. This mixture was ramped to 200°C and held there for one hour under nitrogen (N_2) flow. After cooling down to room temperature, 1 mL iron oxide nanocrystal solution stored in hexanes at the concentration of 6,000 mg/L Fe was injected into the mixture and the mixture was heated to 100 °C for 30 minutes for the evaporation of hexanes completely. Afterwards, the reaction mixture was allowed to heat at 280 °C for one hour under nitrogen (N_2) flow. Se (0.9 mmol) dissolved in trioctylphosphine (TOP, 2 ml) was slowly injected into the solution with the speed of 0.4 ml/min at lower temperature 220 °C and the temperature was set to 250 °C allowing to grow CdSe QDs on the iron oxide surface. By taking aliquots at the different time intervals from 1 to 25 minutes, the CdSe QDs/iron oxide magnetic-optical complexes emitted multiple fluorescence colors from green to red were obtained. The aliquots of growth solution were quenched in hexanes.

6.1.4. Synthesis of iron oxide/CdSe@ZnS core/shell QD nanoparticles

Following the procedure of Peng's group, a ZnS shell was deposited onto the CdSe QDs by introducing calculated amounts of Zn and S.[62]   The zinc precursor solution (0.04 M) was made by dissolving ZnO (0.39 g) in oleic acid (10.83 g) and ODE (108 ml) at 250 °C. The sulfur stock solution (0.04 M) was prepared by dissolving sulfur powder (0.128 g) in ODE (100 ml) at 200 °C. Both precursor solutions were prepared under nitrogen. The zinc precursor solution requires pre-

heating to ensure complete dissolution before injection. For each injection to make a shell, a certain amount of stock solution, found via calculation, was introduced to the reaction via a syringe. The CdSe QD/iron oxide magnetic-optical complexes with green and red fluorescence colors were synthesized by the procedure above. The resulting complexes were heated to 220 °C for the preparation of CdSe@ZnS QDs/iron oxide complexes and 1 ml of Zn precursor (0.04 M ZnO/OA in ODE) was slowly injected and stirred for 10 min at this temperature. The same amount of S precursor solution was sequentially injected into the reaction and stirred for 15 min. Then, the reaction mixture was cooled down to 60 °C and dispersed in hexanes solution. The resulting CdSe@ZnS QDs/iron oxide (10 nm diameter core) materials had a green fluorescence while the CdSe@ZnS QDs/iron oxide (17 nm diameter core) with red emission were prepared by these procedures.

6.1.5. Magnetic capture purification

The complexes could be purified via magnetic capture; specifically unattached QDs could be removed from the mixture as they were not magnetically responsive. To accomplish this, 15 mL of methanol was added to the hexanes solution of the complexes (5 mL). This led to some degree of aggregation and faster interaction with the strong handheld magnet (NdFeB rod magnet with 1.25 ~1.28 Tesla (T), United Nuclear Scientific Equipment & Supplies) positioned near the vial wall. After one to three minutes, the QD/iron oxide magnetic-optical complexes were concentrated on the side of the vial leaving behind any surfactant, unattached QDs, and unreacted precursors in the solution, which was discarded. 5mL hexanes

were added to dissolve complex solution and more methanol (15 ml) was further added. The solution was shaken and the cycle of magnetic capture was repeated three to five times. It is notable that this process is much faster than the conventional purification, which relies on introduction of methanol followed by centrifugation. The magnetically purified QDs/iron oxide magnetic-optical complex solution was dispersed in hexanes solution and stored under ambient conditions using dark vials and aluminum foil.

6.1.6. Phase transfer of iron oxide/QD using oleic acid

This phase transfer method was modified from that reported by Prakash et. al.[165] Various amounts of oleic acid (2~20 uL, 6 to 64 μM) were added to the 1 ml of QDs/iron oxide magnetic-optical complexes ethyl ether solution (typically, Fe 50 mg/L, Cd 200 mg/L) and stirred 24 hours without sonication. Afterwards, the same volume of 0.05 M NaOH solution was added to the solution. It was allowed to stir gently, leading to the evaporation of the organic solvent (ethyl ether) over 24 hours. Purification of as-prepared water-soluble QDs/iron oxide complexes was carried out using ultracentrifugation (Optima L-90K ultracentrifuge, BECKMAN COULTER) at 35,000 rpm for 3 h, followed by syringe filtration (pore size of 0.45 μm, WHATMAN-NYL). This purification process was repeated 2 to 3 times. Finally, the QDs/iron oxide magnetic-optical complexes were stored in ultrapure water (MILLIPORE, 18.2 MΩ·cm).

6.1.7. Magnetic column separation

The iron oxide nanocrystals (10 and 17 nm) and QDs/iron oxide complexes with different iron oxide cores (10 and 17 nm) and fluorescent colors (green and red) were used to visualize size-dependent magnetic separations. Magnetic separation were used with L-1CN S.G. Frantz Canister Separator High Gradient Magnetic Separator (HGMS) equipped with a stainless steel canister column (6.3 x 25.4 x 222.3 mm, 35.5 cm^3) packed with stainless-steel wool (~50 μm wire diameter), with a packing volume of 5 % of the canister (~15 g stainless-steel wool). Different sizes of iron oxide or iron oxide/QD complexes were passed through the HGMS at magnetic fields varying from 0 to 1.4 T to determine how efficiently the samples were retained in the column, similar to previous methods.[306-308] The samples in both hexanes and water (typically, 10 mL volume, concentration of Fe 500 mg/L) were gravity fed (~1 min) loaded into the column packed with stainless steel wool. The iron contents of initial, retained, and effluent solutions were quantitatively determined by a PerkinElmer Optima 4300 DV Inductively Coupled Plasma-Optical Emission Spectrometer (ICP-OES).

6.1.8. Magnetic enrichment

Different concentrations of QDs/iron oxide solutions were used to evaluate the pre-concentration of magnetic materials. To compare the magnetic enrichment effect, 10 ml of QD/iron oxide complex solution was loaded onto the glass slide in the small round shape petri dish, where placed on the top of a strong magnet

(NdFeB rod magnet, 1.25 ~1.28 T) for 12 hours while the control was set nearby. The fluorescent signals of both samples were detected using fluorescence microscope (Zeiss Axioimager Z2 upright microscope) and the concentrations of atomic Fe and Cd were measured by ICP-OES. The numeric values for the fluorescence intensity and populations were calculated by the integration of pixels ($\sim 10^6$ pixels) of the signals correcting for the background.

6.1.9. Instruments and characterization

Ultraviolet-visible (UV-Vis) absorption spectroscopy: Ultraviolet-visible absorption spectrum was measured by a Varian Cary 5000 UV-VIS-NIR spectrophotometer. Diluted solutions of iron oxide/QDs complexes in hexanes were placed in 1 cm quartz cuvette and their absorption spectra were acquired.

Photoluminescence (PL) spectroscopy: Photoluminescence (PL) spectra of the iron oxide/QDs complexes were recorded on a Jobin Yvon Spex Fluorolog 3 fluorescence spectrophotometer.

Transmission electron microscopy (TEM): TEM specimens were carried out by JEOL 2100 field emission gun TEM operating at 200 kV with a single tilt holder. The TEM sample was made by evaporating one drop of purified solution in hexanes on ultra thin carbon type-A 400 mesh copper grids (Ted Pella Inc.). The size and size distribution data were obtained by counting over 500 individual nanocrystalline particles using Image-Pro Plus 5.0 (Media Cybernetics, Inc., Silver Spring, MD).

High angle angular dark field-scanning transmission electron microscopy (HAADF-STEM) and electron energy loss spectroscopy (EELS) spectrum imaging: The HAADF-STEM investigation was carried out in TEM-2100F (JEOL) fitted with a spherical aberration corrector (CEOS GmbH) and a Gatan Enfina Electron Energy Loss Spectroscopy (EELS) spectrometer. The operating voltage was 200 kV. The EELS spectrum images were recorded with an energy resolution (full width at half-maximum of the zero loss peak) of 1 eV.

Inductively coupled plasma optical emission spectroscopy (ICP-OES): To determine the concentration of sample, the PERKIN ELMER ICP-OES instrument equipped with auto sampler was used. For the phase transfer efficiency, the atomic concentrations (Fe and Cd) of water-soluble QDs/iron oxide solution added with different amounts of OA were compared from the concentrations of original hexanes solution. Moreover, the percentage of the retention by magnetic separator was calculated by dividing the atomic (Fe) concentration in retained solution from the concentration measured for the initial (unseparated) solution. The iron oxide nanocrystals and QDs/iron oxide materials were digested by nitric acid (HNO_3, 70 %) and hydrogen peroxide (H_2O_2, 30 %).

Fluorescence microscope imaging: Zeiss Axio imager Z2 upright microscope (Excitation: BP 530-585, 538 nm, Beam splitter FT 600, Emission: LP615) was used for getting the fluorescence images of iron oxide/QDs complexes with captured samples on magnetic field and without the field. The fluorescence images were acquired using CCD camera and processed by the software Axio Vision.

6.2. Result and discussions

6.2.1. Synthesis of the size tunable iron oxide/QD complexes

Magnetic-optical complexes consisting of iron oxide core and CdSe QDs were synthesized by seed-mediated growth method at high temperatures (280 °C). Figure 6-1 shows that the resulting pincushion magnetic-optical complexes have tunable optical properties and collect at the site of a hand-held magnet (NdFeB rod magnet, 1.25 ~1.28 T). During synthesis, the preformed iron oxide nanocrystals act as nucleation sites for QDs, under a specific set of conditions established using pre-determined surfactant compositions, reaction temperatures, and injection speeds. The magnetic-optical complexes only form when the selenium precursor was injected drop-wise to CdO/iron oxide mixture in the presence of octadecylamine (ODA) at high temperatures (220 °C) (Figure 6-1(A)). The high angle angular dark field-scanning transmission electron microscopy (HAADF-STEM) image, Figure 6-1(B) clearly shows that QDs directly nucleated and grew directly on the surface of the iron oxide nanocrystals. Electron energy loss spectroscopy (EELS) elemental mapping was used to confirm that magnetic-optical complexes were pincushion structures that stud QDs onto iron oxide surface (Figure 6-2). EELS spectrums were also used to confirm the position and chemical composition of Fe for the iron oxide and Cd for the QDs features (Figure 6-3).
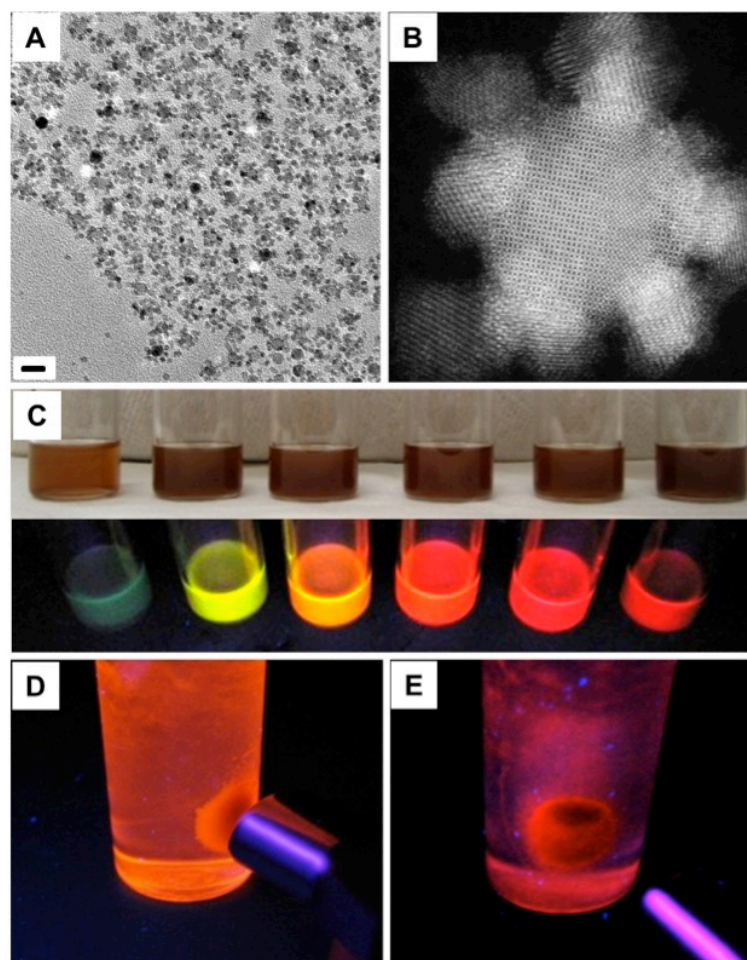
Figure 6-1 The QDs/iron oxide materials and their optical & magnetic properties. TEM images of (A) CdSe QDs/iron oxide materials and (B) HAADF-STEM image (scale: 21.2 nm x 21.2 nm). The diameter of iron oxide nanocrystals was 12 nm. The size of CdSe QD was 3.8/5.3 nm (width/length). The scale bars were 20 nm. (C) The photographs of CdSe QDs/iron oxide under the fluorescent light and ultraviolet light. By controlling the growth time from 1 to 25 minutes, the size tunable CdSe QDs/iron oxide materials showed multiple fluorescence colors. (D) and (E) The CdSe QDs/iron oxide materials collected by strong handheld magnet showed orange and red fluorescent colors.
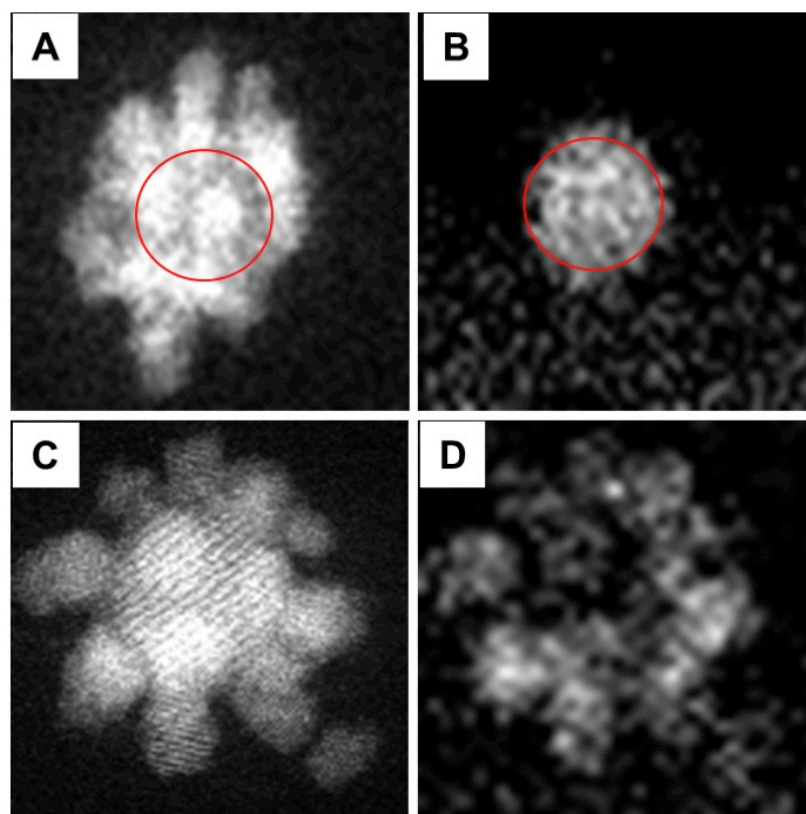
Figure 6-2 HAADF-STEM images and EELS mappings of magnetic-optical complexes (A) The HAADF-STEM image, (B) iron (Fe) mapping, (C) the HAADF-STEM image, and (D) its cadmium (Cd) mapping were acquired, respectively.
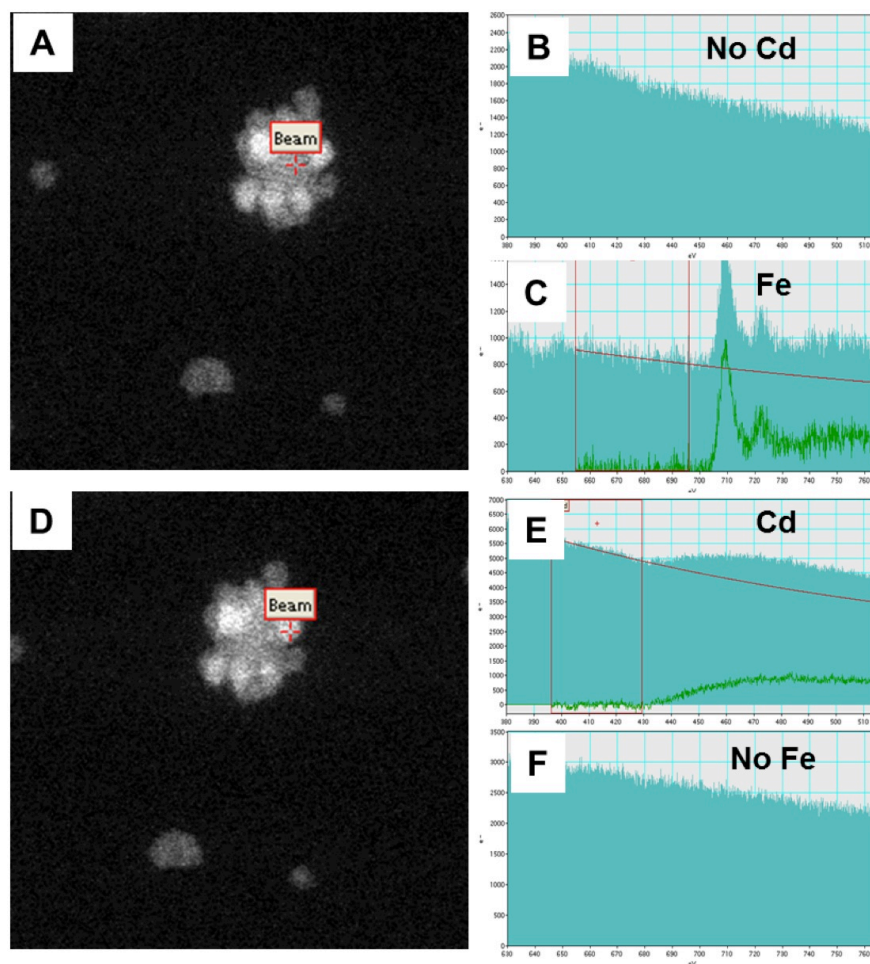
Figure 6-3 (A) EELS spectrum image and (B) and (C) chemical identification spectrums at the cross beam of (A) image.

The iron (Fe) and cadmium (Cd) were detected at 721 eV and 404 eV, respectively. The iron oxide core region in the complexes did not contain cadmium (Cd). (D) EELS spectrum and (E) and (F) the chemical identification spectrums from the cross beam of (D) image. Iron (Fe) was not detected from the QDs area in the complexes.

The diameters of QDs grown on the surface of 12 nm iron oxide nanocrystals can be tuned from 2.2 to 4.3 nm, resulting in samples with a range of distinct fluorescence emission colors. The resulting diameter of CdSe QDs in the complexes increased

causing the emission wavelength for the sample aliquot to red shift from 543-605 nm (Figure 6-4). The size dependent emission spectra of QDs can be explained by quantum confinement and band gap energy theory.[54,118,282,309] The exciton transition shifted to higher energy with an increase of molar absorption coefficient as QD diameters decreased. The size dependent optical properties of QDs were used to produce complex samples that emit at green (2.2 nm), yellow (3.0 nm), yellow-orange (3.3 nm), orange (3.8 nm), red-orange (4.0 nm), and red (4.3 nm) (Figure 6-5). Being able to achieve tunable optical property is critical for designing magnetic-optical complexes for biological applications such as multiplexed detection or multi-cell sorting.[1d, 24,62,66,310]
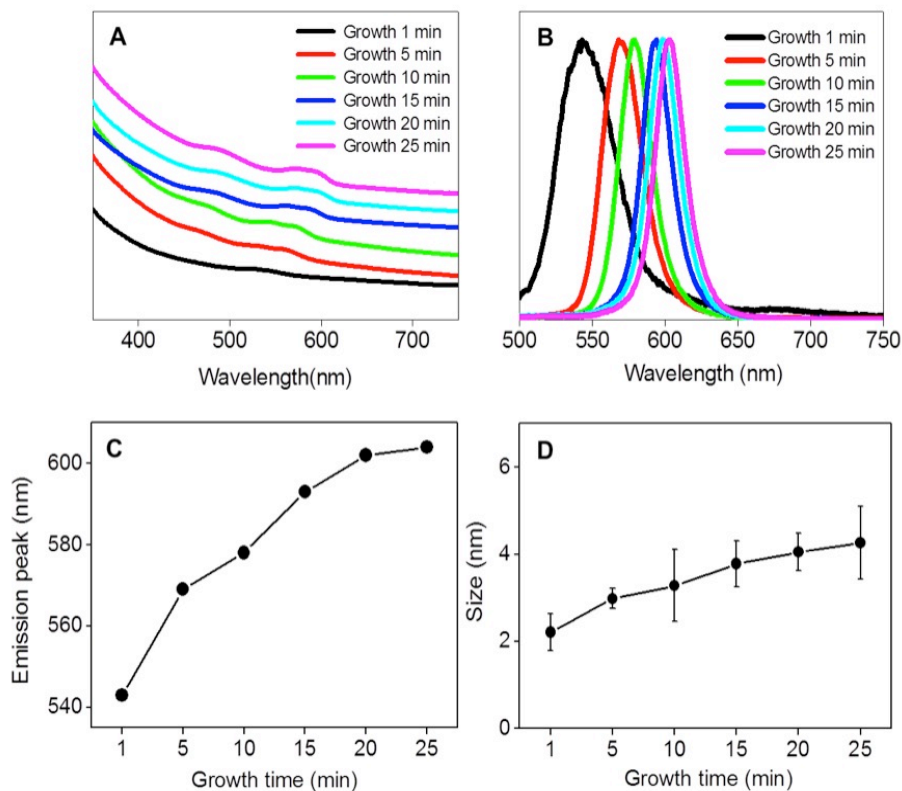
Figure 6-4 (A) Absorption spectra of CdSe QDs/iron oxide at different growth time. The absorption peaks were red-shifted from 528 nm to 589 nm. (B) Photoluminescence (PL) spectra of CdSe QDs/iron oxide materials at the different growth time. The peaks of the photoluminescence were red-shifted from 543 nm to 605 nm. (C) and (D) the emission peak positions and average TEM sizes of CdSe QDs in complexes were increased as the growth time increased from 1 to 25 min.
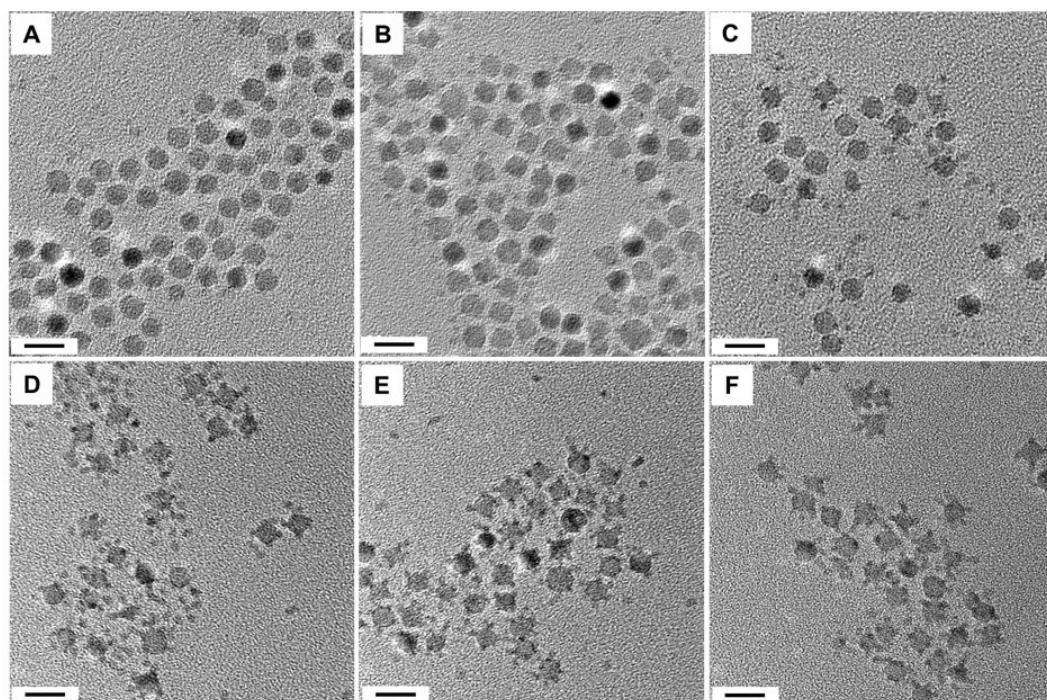
Figure 6-5 (A)-(F) The TEM images of CdSe QDs/iron oxide materials as the different growth time (1, 5, 10, 15, 20, and 25 min).

The sizes of QDs were corresponded to the emission colors. The diameter of iron oxide was 11 nm. The diameter of CdSe QD in the complexes was 2.2 nm (green), 3.0 nm (yellow), 3.3 nm (light orange), 3.8 nm (orange), 4.0 nm (deep orange), and 4.3 nm (red), respectively. The scale bars were 20 nm.

6.2.2. Phase transfer of iron oxide/QD complexes

Water-soluble magnetic-optical complexes were achieved by injecting phase transfer agents such as poly(maleic anhydride-alt-1-octadecene) (PMAO, Mn = 50,000), poly(maleic anhydride-alt-1-octadecene)(PMAO)-co-poly(ethylene glycol) (PEG, Mw = 2,000) amphiphilic polymers, and oleic acid (OA, Mw= 282 g/mol).[165,221] Among them, only OA coated magnetic-optical complex suspensionsretained their

fluorescence (Figure 6-6 and Figure 6-7). With the colloidal stability in water, the magnetic-optical complexes need to keep their optical and magnetic properties after transferring to water. However, PAMO and PMAO-PEG coated magnetic-optical complexes lost their optical properties when transferred to water (Figure 6-6). When the large, bulky polymers were introduced to the magnetic-optical complexes, a thin ZnS shell and polymer agglomeration caused magnetic-optical complexes defects on the surface and led to the quenching of fluorescence. We speculated that a thin ZnS shell does not protect the surface of CdSe QDs densely and result in the failure to trap the excitons in the CdSe QDs core. In contrast, small fatty acid, OA coated CdSe@ZnS QDs/iron oxide magnetic-optical complexes retained the fluorescence without any loss in aqueous solution.
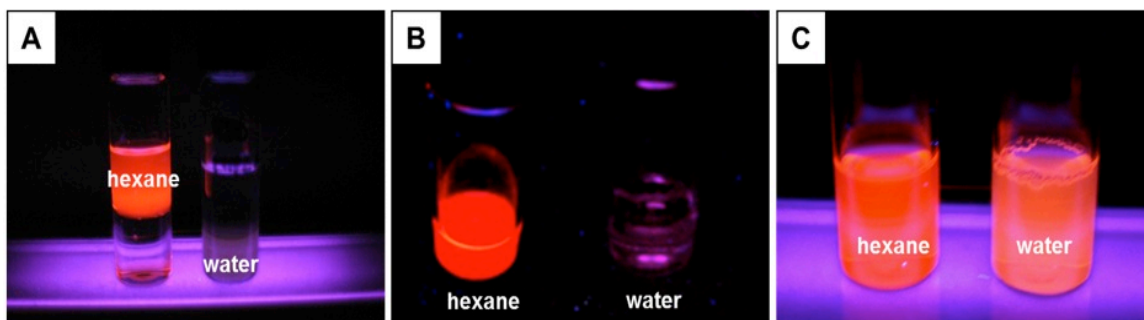
Figure 6-6 The photographs of phase transfer from organic to aqueous phase using various surface modification methods under the ultraviolet light.
The phase transfer coating were used (A) PMAO-PEG amphiphilic polymer, (B) PMAO polymer, and (C) oleic acid (fatty acid). The oleic acid coating showed the fluorescence in both solutions.
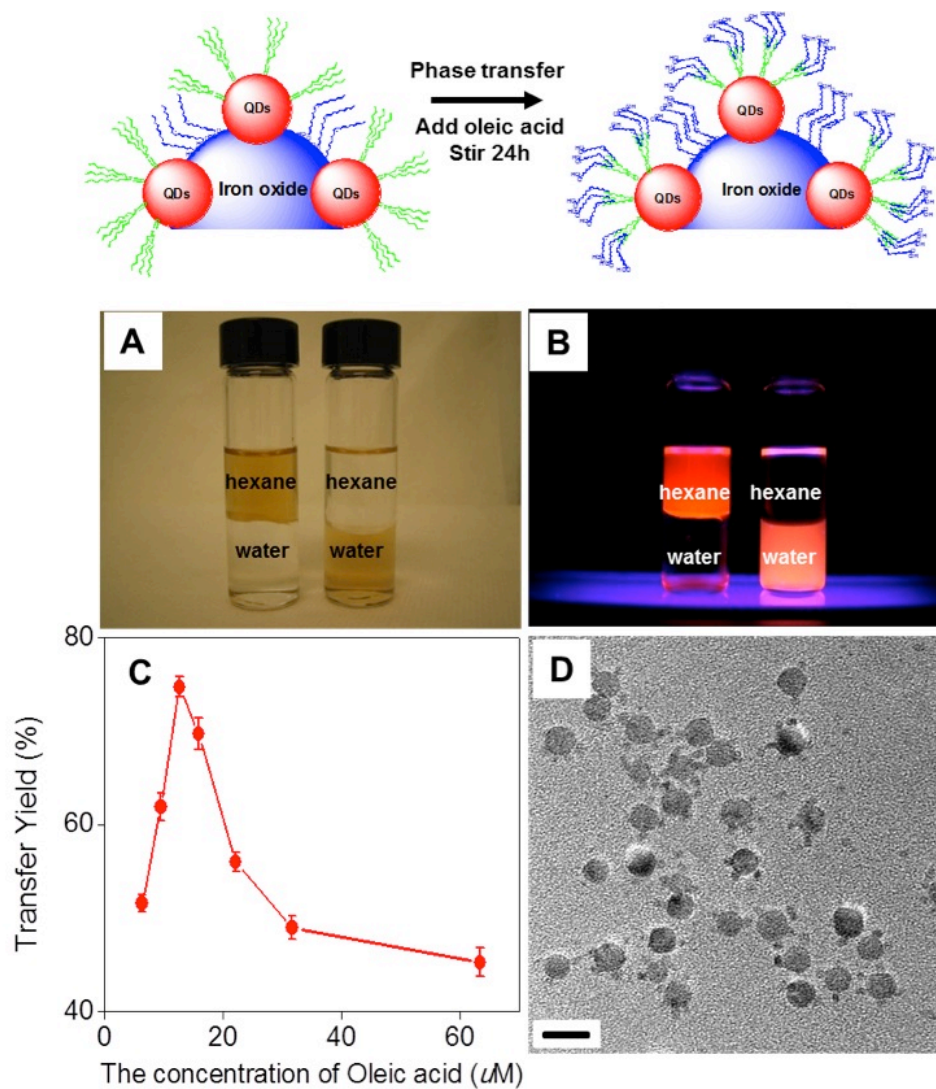
Figure 6-7 Phase transfer of QDs/iron oxide materials.

Oleic acid as was used as a phase transfer agent to bring hydrophobic QDs/iron oxide materials to water phase. The CdSe@ZnS QDs/iron oxide dispersed in hexanes and water under (A) the fluorescent and (B) the ultraviolet light. (C) The transfer yields of complexes as the increasing amounts of oleic acid. (D) The TEM image of CdSe@ZnS QDs/iron oxide materials dispersed in water. The scale bar was 20 nm.

OA-coated magnetic-optical complexes dispersed in water did not change in diameter or morphology and remained fluorescent (Figure 6-7). The average hydrodynamic diameter of the complexes was 30-35 nm, which accounted for the 10 nm of iron oxide, 9 nm of QDs, and 11-16 nm for the surface coating agents. The ration of OA per complex was varied to achieve the greatest transfer yield ($\sim$75 %). Figure 6-7 (C) shows that low concentration of OA (from 1 to 10 uM) had transfer yields of 30 – 60 % because there was not enough OA to fully cover the complex surface. However, increasing the concentration of OA (from 30 to 65 uM) resulted in cloudy solution with low transfer yields (20–30 %) due to the formation of micelles.[311] We found that 75 uM OA per 1 mL sample (CdSe@ZnS QDs/iron oxide, Fe: 50 mg/L, Cd: 200 mg/L) resulted in the best transfer yield (75 %) (Figure 6-7 (C)). The OA coated magnetic-optical complexes retained their morphology, were water-soluble, and were colloidal stable (Figure 6-7 (D)).

The optical property of the OA coated hydrophilic magnetic-optical complexes were maintained in biologically relevant solutions. The absorption and fluorescence spectra of magnetic-optical complexes did not shift while transferring from organic to aqueous phase (Figure 6-8). The colloidal and fluorescence stability of OA coated magnetic-optical complexes were evaluated in a range of buffers, pH (from 3 to 11), and ionic strength solutions (Figure 6-9). Neutral and basic solutions from 7 to 11, did not alter the fluorescence of magnetic-optical complexes. However, in acidic conditions (pH 3 and 5), the suspensions became cloudy due to precipitation and resulted in a loss of fluorescence. The magnetic-optical complexes

were stable in a range of ionic strengths from 0.01 M to 0.5 M NaCl and in various biological relavant buffers (phosphate buffered saline (PBS), borate, and sodium bicarbonate).
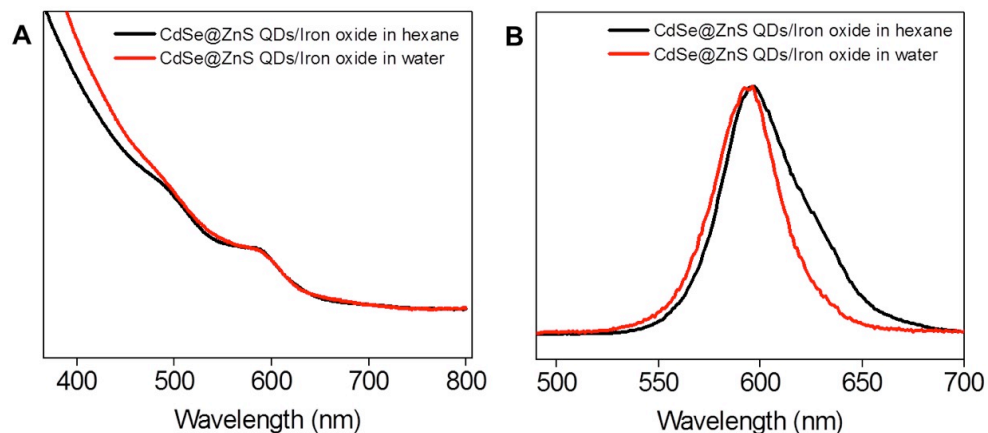
Figure 6-8 The absorption and photoluminescence spectra of QD/iron oxide complexes in hexanes and water.

(A) the absorption spectra (582 nm) and (B) the photoluminescence spectra (595 nm) of CdSe@ZnS QDs/iron oxide materials in hexanes (black) and water (red). The absorption and photoluminescence spectra of complexes were not changed after phase transfer.
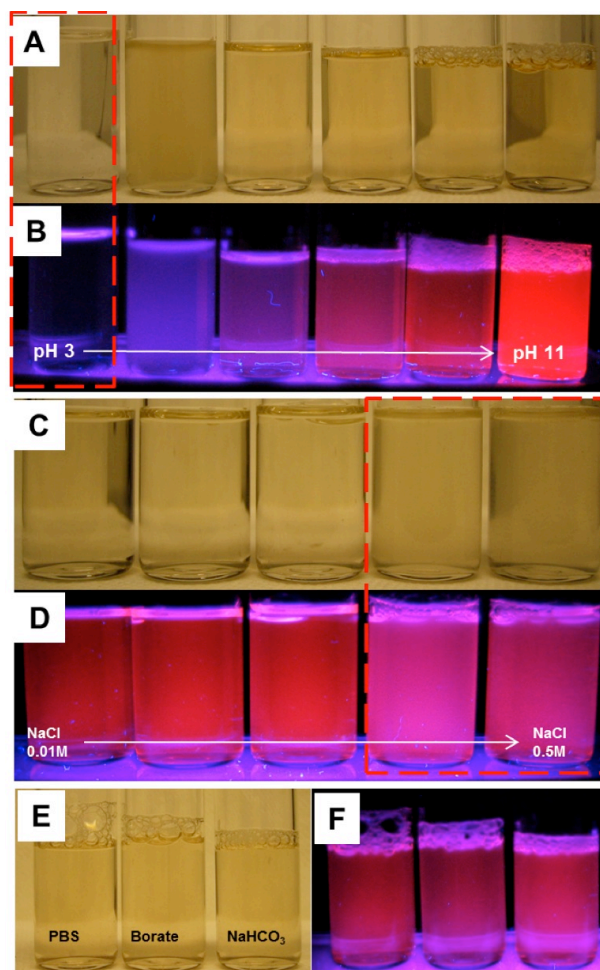
Figure 6-9 The QDs/iron oxide suspensions under various conditions

(A) and (B) The QDs/iron oxide suspensions under various pH conditions (pH 3, 5, 7, 8, 9, 11) under the fluorescent and ultraviolet light. At low pH, the samples were precipitated or cloudy. It showed the best stability in basic solution (pH 9-10). (C) and (D) The QDs/iron oxide complex suspensions under the different ionic strengths in NaCl (0.01M, 0.05M, 0.1M, 0.25M, 0.5M) under the fluorescent and ultraviolet light. At higher ionic strengths in NaCl, the suspension was cloudy. (E) and (F) The QDs/iron oxide suspensions under various buffer conditions (PBS buffer, Borate buffer, $NaHCO_3$ buffer). These photographs were taken after 7 days of the treatment.

6.2.3. Visualized magnetic separation of iron oxide/QD complex

Size dependent magnetic separation showed that larger particles have higher retention in a column for bare iron oxide and magnetic-optical complex materials. Figure 6-10 shows the percent retention of bare and complexes prepared from iron oxide nanoparticles of 10 nm and 17 nm in organic and aqueous solution. Using a conventional high gradient magnetic separator (HGMS)[306-308], we compared the percentage of retention for a sample as the applied magnetic field was increased from 0.01 to 1.4 T. As expected, for all samples the larger iron oxide nanoparticles (17 nm) had a higher percent of material retained within the column. The magnetic-optical complexes in either solution were retained in the magnetic column at a lower percentage than the same core iron oxide nanocrystals; indicating that the magnetic properties of the complexes are affected by the surrounding QDs. The difference in retention for the magnetic-optical complex was found to be more drastic in aqueous solutions, most likely due to the agglomeration effect of the double layer OA surface coatings.
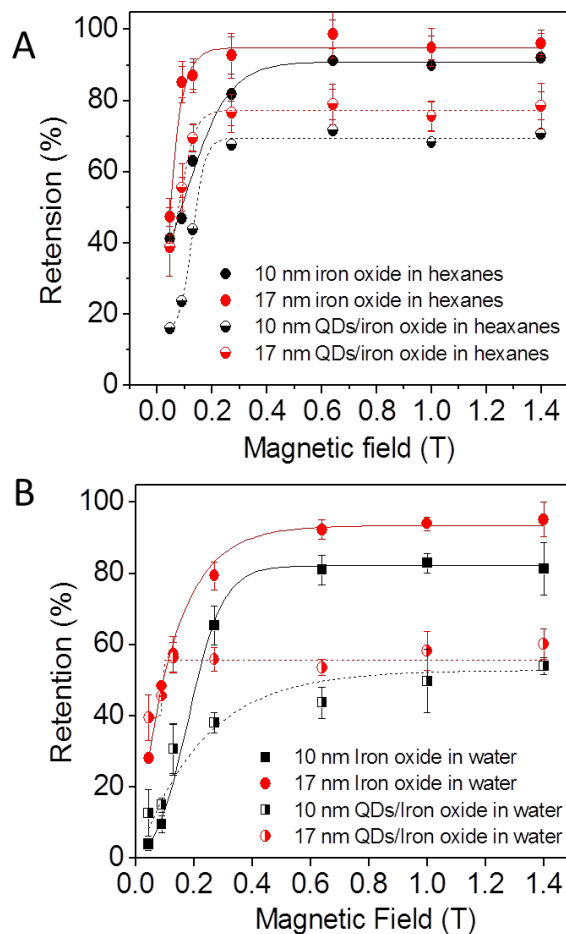
Figure 6-10 Size dependent magnetic separation with bare iron oxides and QDs/iron oxide materials in hexanes and water.

(A) Size dependent magnetic retention of iron oxide (10 nm and 17 nm) and QDs/iron oxide dispersed in hexanes using column magnetic separator (B) Magnetic retention of oleic acid coated iron oxide and QDs/iron oxide materials soluble in water using magnetic column separator. Retained fractions in a column were digested in 5% nitric acid and their concentration of iron (Fe) was analyzed by ICP-OES.

Size dependent magnetic separations selectively isolate larger magnetic-optical complexes from a mixture. Different sizes of magnetic-optical complexes were prepared where a large iron oxide nanocrystals (17 nm) were studded with 4.3 nm QDs (red) and smaller (10 nm) ones were conjugated with 2.1 nm QDs (green). Figure 6-11 shows the schematic diagram of the HGMS and TEM images of the (A) mixed, (B) retained, and (C) effluent samples during magnetic separation. First, the smaller green fluorescent complexes were mixed with large red emitting complexes in a 1:2 (v/v) ratio. The prepared mixture was passed through a packed column with an applied magnetic field of 0.09 T. Due to the size-dependent magnetic properties of the core iron oxide, most of larger (17 nm) magnetic-optical complexes were retained in the magnetic column, while the smaller complexes were eluted.[306-308] While some QDs were found to detach from the core iron oxide nanocrystals when passed through the magnetic column, most (> 80 %) of the recovered complexes were stable and intact. The separation efficiency was evaluated by TEM images and their histograms of retained (B) and effluent (C) samples, as shown in Figure 6-11. The average separation efficiency was 80 %.
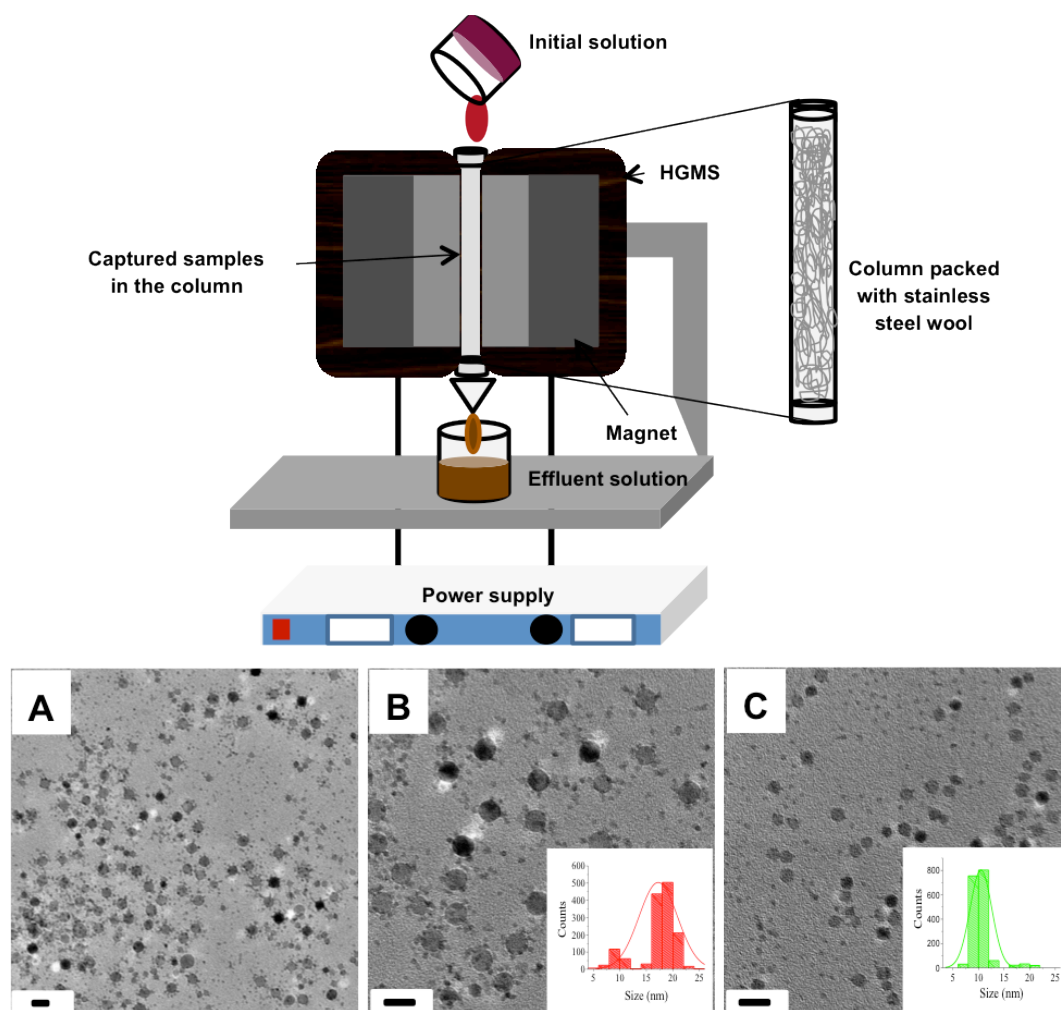
Figure 6-11 Schematic diagram of magnetic column separator and TEM images (A-C) of mixed, captured, and effluent samples.

The bare iron oxide and QDs/iron oxide solution are loaded through the column packed with stainless steel wool. The strength of magnetic field (T) can be controlled with the power supply. After turning off the magnetic field, the retained samples in the column are outflowed using clean hexanes or water. TEM images showed (A) the mixed solutions of green emitted QDs/iron oxide (10 nm) and red emitted QDs/iron oxide (17 nm) (B) the captured samples in the column, and (C) outflowed samples when the magnetic field was applied. The scale bars were 20 nm.

Fluorescence of the QDs allowed for ease of visualization for the separation of the two sizes of complexes. Figure 6-12 shows the visualized magnetic separation of the magnetic-optical complexes, which was a more effective, fast, and time saving technique since the materials can simply be monitored through their unique fluorescence spectra, instead of relying on imaging and counting the population via TEM. Figure 6-12 shows the fluorescence spectra of the magnetic-optical complexes (A & B) isolated, (C) mixed, and (D & E) after magnetic separation. The emission peak positions for the green and red magnetic-optical complexes were 574 nm and 610 nm before the separation (Figure 6-12 (A) and (B)). These complexes were mixed together in a vial and the binary emission peaks are shown in Figure 6-12 (C). Figure 6-12 (D) and (E) show the peak positions of these outflowed and retained samples were 573 nm and 607 nm, respectively, verifying the results found through TEM analysis of the same samples. This fluorescent measurement was simple and allowed for separation of two sizes of magnetic-optical complexes from a mixture.
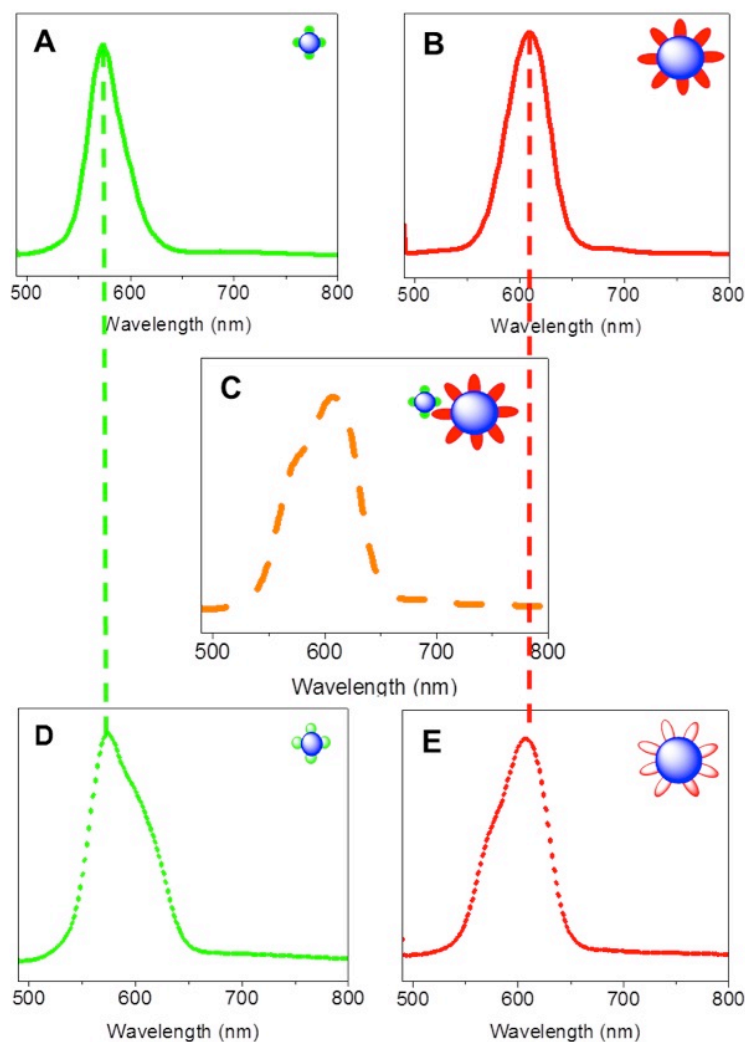
Figure 6-12 The photoluminescence (PL) spectra of two different complexes before and after magnetic separation.

(A) and (B) the photoluminescence (PL) spectra of green QDs/iron oxide (10 nm) and red QDs/iron oxide (17 nm) materials before doing magnetic capture. The PL spectra of (A) and (B) showed the maximum at 574 nm and 610 nm, respectively. (C) The PL spectrum of mixed samples. (D) and (E) the PL spectra of collected sample by strong magnet and supernatant. The PL spectra of (D) and (E) were maximum at 573 nm and 607 nm, respectively.

6.2.4. Magnetic enrichment

Nanomolar concentrations of magnetic-optical complexes can be fluorescently detected on a surface with the help of an external magnetic field (Figure 6-13). Innate magnetic properties of magnetic-optical complexes enable them to move towards an external magnetic field and are very useful for enrichment of a sample for low-level detection. Figure 6-13 shows that these materials can be easily collected using an external magnetic field (NdFeB handheld magnet, 1.25-1.28 T) and produce a visual signal even at extremely low concentrations (nanomolar level). The fluorescence microscope (Zeiss Axioimager Z2 upright microscope (excitation: 530-538 nm, emission: 615 nm) can be used to detect the signals. To compare the magnetic enrichment by applying the external magnetic field, magnetic-optical complexes were diluted from 50 to 5000 times of the starting sample concentration (Fe: 90 uM, Cd: 200 uM). The concentrations were based on the ionic concentrations of Fe and Cd in the complex determined by ICP-OES. An external magnet was placed below three of the six samples (right images in Figure 6) for 12 hours and then the surfaces were imaged. As shown in Figure 6-13, the magnetically concentrated samples were fluorescently more populated compared to the control samples prepared at the same concentration. As a result, the magnetically enriched samples could be detectable down to the nanomolar level.

Moreover, the fluorescent signal from the microscope images can be quantified through integration of the pixels compared to the background. These values are indicated on the bar line of the figure showing that the signal from a

magnetically concentration samples is enhanced at least 2 fold at each concentration. The lowest detectable concentration of the magnetic-optical complexes was 10^{-9} mol/L (nM) level; Fe and Cd ionic concentrations of the final diluted sample (5,000 times) were 18 and 40 nM, respectively. Therefore, the magnetic enrichment of magnetic-optical complexes offers the possibility of enriching the materials at a target. From this study we have shown that these magnetic-optical complexes can be used as a convenient and sensitive sensing probe for biological applications, such as multiple cell separation, multiplexed detection, and target enrichment with high sensitivities.
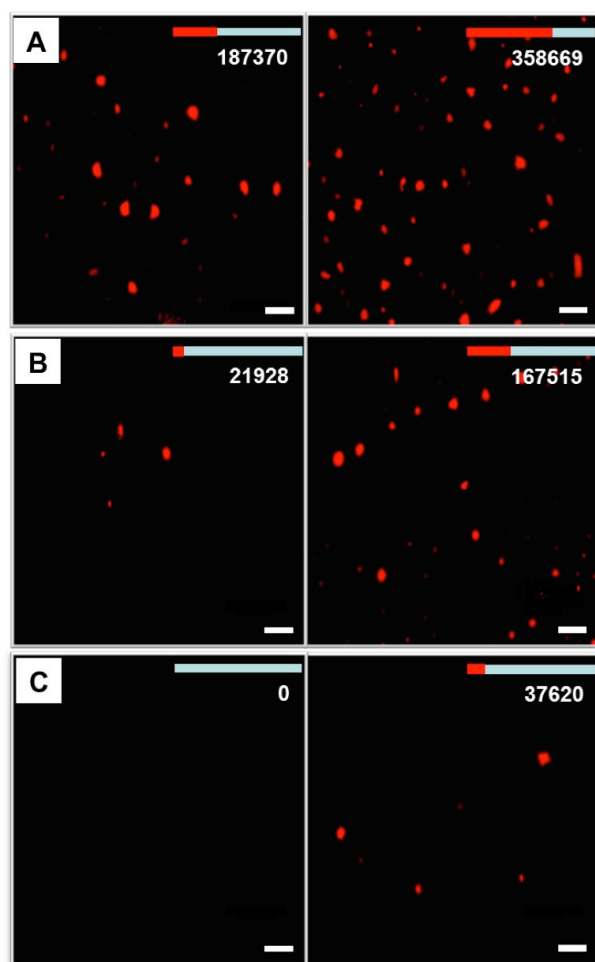
Figure 6-13 Magnetic enrichment.

The fluorescence images of CdSe@ZnS QDs/iron oxide materials were acquired with a Zeiss Axioimager Z2 upright microscope (excitation: BP 530-538 nm beam splitter:FT 600, emission: LP 615). These materials were placed on the handheld strong magnet for 12 hours. The magnetically enriched samples (right) were more concentrated in comparison of that with no magnetic field (left). (A)-(C) the fluorescent images of QDs/iron oxide materials were shown as the concentration was decreased. The concentration of iron (Fe) in complexes was (A) 1.8 uM, (B) 180 nM, and (C) 18 nM, respectively. The concentration of cadmium (Cd) in complexes was (A) 4 uM (A), (B) 400 nM, (C) 40 nM, respectively. The diameter of iron oxide and QDs were 12 nm and 4.3/4.7 nm (width/length). The scale bar was 20 um.

6.3. Conclusion

In summary, we have synthesized magnetic-optical complexes formed through the nucleation and growth of QDs on the iron oxide nanocrystals. These complexes offer tunable emission colors (green to red), size dependent magnetic response and enhanced collection at a target. Oleic acid bilayer coating renders the particles stable biologically relevant media. The magnetic-optical complexes are advantageous for visualization of magnetic separation. Moreover, the magnetically enriched samples could be optically detected down to nanomolar concentrations. Finally, these materials give us the ability to quantify and isolate specific biological targets through conjugation with the dual functional magnetic-optical complexes. Magnetic-optical complexes may enable new strategies for multiplexed cell separation, *in vivo* drug delivery, and the treatment of various diseases.

Chapter 7

Summary and Future Outlook

I have studied the design, synthesis, and their applications of biomedical nanocrystal agents from fundamental nanocrystals to multifunctional nanocomplexes. Using diameter controlled gadolinium oxide nanocrystals and iron oxide nanocrystals with various biocompatible coatings, the r_1 and r_2 MR relaxation were optimized and explored the effects of size, coating, and composition. Especially, the PAMPS-LA and PAA-OA coated ultrasmall gadolinium oxide nanoparticles (< 2 nm) showed extremely high r_1 relaxivity (50- 60 $S^{-1}mM^{-1}$), which is 10-15 fold higher than that of commercial Gd(III) chelates (4.3 ~4.6 $S^{-1}mM^{-1}$). *In vitro* toxicological studies showed that polymer coated nanocrystals suspensions had no significant effect at high concentration.

As a multi-modal imaging probe, iron oxide/QDs complexes have size tunable optical properties and variable QDs features helped to visualize and remove large

iron oxide materials in a magnetic separation. For clinical uses of these biomecial nanocrystal agents in the future, long-term toxicity, in vivo targeting, and bio-distribution should be clearly addressed. To conclude, the development of biomedical nanocrystal agents and exact investigations of their properties will give great uses for diagnosis, detection, and therapy of diseases in near future.

References

(1)   Lu, A. H.; Salabas, E. L.; Schuth, F. *Angew Chem Int Edit* **2007**, *46*, 1222.

(2)   Pankhurst, Q. A.; Thanh, N. T. K.; Jones, S. K.; Dobson, J. *J Phys D Appl Phys* **2009**, *42*.

(3)   Roca, A. G.; Costo, R.; Rebolledo, A. F.; Veintemillas-Verdaguer, S.; Tartaj, P.; Gonzalez-Carreno, T.; Morales, M. P.; Serna, C. J. *J Phys D Appl Phys* **2009**, *42*.

(4)   Pankhurst, Q. A.; Connolly, J.; Jones, S. K.; Dobson, J. *J Phys D Appl Phys* **2003**, *36*, R167.

(5)   Tartaj, P.; Morales, M. D.; Veintemillas-Verdaguer, S.; Gonzalez-Carreno, T.; Serna, C. J. *J Phys D Appl Phys* **2003**, *36*, R182.

(6)   Gupta, A. K.; Gupta, M. *Biomaterials* **2005**, *26*, 3995.

(7)   Wang, Y. X. J.; Hussain, S. M.; Krestin, G. P. *Eur Radiol* **2001**, *11*, 2319.

(8)   Weissleder, R.; Elizondo, G.; Wittenberg, J.; Rabito, C. A.; Bengele, H. H.; Josephson, L. *Radiology* **1990**, *175*, 489.

(9)   Niendorf, T.; Sodickson, D. *Rofo-Fortschr Rontg* **2006**, *178*, 15.

(10)   Sun, G. Y.; Feng, J. H.; Jing, F. Y.; Pei, F. K.; Liu, M. L. *J Magn Magn Mater* **2003**, *265*, 123.

(11)   Yang, C. T.; Chuang, K. H. *Medchemcomm* **2012**, *3*, 552.

(12)   Weinmann, H. J.; Ebert, W.; Misselwitz, B.; Schmitt-Willich, H. *Eur J Radiol* **2003**, *46*, 33.

(13)   Reichenbach, J. R.; Hacklander, T.; Harth, T.; Hofer, M.; Rassek, M.; Modder, U. *Eur Radiol* **1997**, *7*, 264.

(14)   Ahren, M.; Selegard, L.; Soderlind, F.; Linares, M.; Kauczor, J.; Norman, P.; Kall, P. O.; Uvdal, K. *J Nanopart Res* **2012**, *14*.

(15)   Hedlund, A.; Ahren, M.; Gustafsson, H.; Abrikossova, N.; Warntjes, M.; Jonsson, J. I.; Uvdal, K.; Engstrom, M. *International Journal of Nanomedicine* **2011**, *6*, 3233.

(16)   Choi, E. S.; Park, J. Y.; Baek, M. J.; Xu, W.; Kattel, K.; Kim, J. H.; Lee, J. J.; Chang, Y.; Kim, T. J.; Bae, J. E.; Chae, K. S.; Suh, K. J.; Lee, G. H. *Eur J Inorg Chem* **2010**, 4555.

(17)   Ahren, M.; Selegard, L.; Klasson, A.; Soderlind, F.; Abrikossova, N.; Skoglund, C.; Bengtsson, T.; Engstrom, M.; Kall, P. O.; Uvdal, K. *Langmuir* **2010**, *26*, 5753.

(18)   Klasson, A.; Ahren, M.; Hellqvist, E.; Soderlind, F.; Rosen, A.; Kall, P. O.; Uvdal, K.; Engstrom, M. *Contrast Media Mol I* **2008**, *3*, 106.

(19)   Park, J. Y.; Baek, M. J.; Choi, E. S.; Woo, S.; Kim, J. H.; Kim, T. J.; Jung, J. C.; Chae, K. S.; Chang, Y.; Lee, G. H. *Acs Nano* **2009**, *3*, 3663.

(20)   Passuello, T.; Pedroni, M.; Piccinelli, F.; Polizzi, S.; Marzola, P.; Tambalo, S.; Conti, G.; Benati, D.; Vetrone, F.; Bettinelli, M.; Speghini, A. *Nanoscale* **2012**, *4*, 7682.

(21)   Yoon, Y. S.; Lee, B. I.; Lee, K. S.; Heo, H.; Lee, J. H.; Byeon, S. H.; Lee, I. S. *Chem Commun* **2010**, *46*, 3654.

(22)   Jung, C. W.; Jacobs, P. *Magn Reson Imaging* **1995**, *13*, 661.

(23)   Chapon, C.; Franconi, F.; Lemaire, L.; Marescaux, L.; Legras, P.; Saint-Andre, J. P.; Denizot, B.; Le Jeune, J. J. *Invest Radiol* **2003**, *38*, 141.

(24)   Alivisatos, A. P. *Abstr Pap Am Chem S* **1999**, *218*, U296.

(25)   Bruchez, M.; Moronne, M.; Gin, P.; Weiss, S.; Alivisatos, A. P. *Science* **1998**, *281*, 2013.

(26)   Medintz, I. L.; Uyeda, H. T.; Goldman, E. R.; Mattoussi, H. *Nat Mater* **2005**, *4*, 435.

(27)   Li, Z. H.; Peng, J.; Chen, H. L. *J Nanosci Nanotechno* **2011**, *11*, 7521.

(28)   Lee, Y. K.; Hong, S. M.; Kim, J. S.; Im, J. H.; Min, H. S.; Subramanyam, E.; Huh, K. M. *Macromol Res* **2007**, *15*, 330.

(29)   Jiang, W.; Singhal, A.; Zheng, J. N.; Wang, C.; Chan, W. C. W. *Chem Mater* **2006**, *18*, 4845.

(30)   Cederquist, S. C. *Laser Focus World* **2001**, *37*, 44.

(31)   Dubertret, B.; Skourides, P.; Norris, D. J.; Noireaux, V.; Brivanlou, A. H.; Libchaber, A. *Science* **2002**, *298*, 1759.

(32)   Gao, X. H.; Cui, Y. Y.; Levenson, R. M.; Chung, L. W. K.; Nie, S. M. *Nat Biotechnol* **2004**, *22*, 969.

(33)   Kim, J.; Piao, Y.; Hyeon, T. *Chem Soc Rev* **2009**, *38*, 372.

(34)   Na, H. B.; Hyeon, T. *J Mater Chem* **2009**, *19*, 6267.

(35)   Na, H. B.; Song, I. C.; Hyeon, T. *Adv Mater* **2009**, *21*, 2133.

(36)   Quarta, A.; Di Corato, R.; Manna, L.; Ragusa, A.; Pellegrino, T. *Ieee T Nanobiosci* **2007**, *6*, 298.

(37)   Caravan, P.; Ellison, J. J.; McMurry, T. J.; Lauffer, R. B. *Chem Rev* **1999**, *99*, 2293.

(38)   Lauffer, R. B. *Chem Rev* **1987**, *87*, 901.

(39)   McDonald, M. A.; Watkin, K. L. *Acad Radiol* **2006**, *13*, 421.

(40)   Bridot, J. L.; Faure, A. C.; Laurent, S.; Riviere, C.; Billotey, C.; Hiba, B.; Janier, M.; Josserand, V.; Coll, J. L.; Vander Elst, L.; Muller, R.; Roux, S.; Perriat, P.; Tillement, O. *J Am Chem Soc* **2007**, *129*, 5076.

(41)   Evanics, F.; Diamente, P. R.; van Veggel, F. C. J. M.; Stanisz, G. J.; Prosser, R. S. *Chem Mater* **2006**, *18*, 2499.

(42)   Hifumi, H.; Yamaoka, S.; Tanimoto, A.; Citterio, D.; Suzuki, K. *J Am Chem Soc* **2006**, *128*, 15090.

(43)   Fortin, M. A.; Petoral, R. M.; Soderlind, F.; Klasson, A.; Engstrom, M.; Veres, T.; Kall, P. O.; Uvdal, K. *Nanotechnology* **2007**, *18*.

(44)   Qiao, R. R.; Yang, C. H.; Gao, M. Y. *J Mater Chem* **2009**, *19*, 6274.

(45)   Berry, C. C.; Curtis, A. S. G. *J Phys D Appl Phys* **2003**, *36*, R198.

(46)   Alexiou, C.; Arnold, W.; Klein, R. J.; Parak, F. G.; Hulin, P.; Bergemann, C.; Erhardt, W.; Wagenpfeil, S.; Lubbe, A. S. *Cancer Res* **2000**, *60*, 6641.

(47)   Qu, S. C.; Yang, H. B.; Ren, D. W.; Kan, S. H.; Zou, G. T.; Li, D. M.; Li, M. H. *J Colloid Interf Sci* **1999**, *215*, 190.

(48)   Kang, Y. S.; Risbud, S.; Rabolt, J. F.; Stroeve, P. *Chem Mater* **1996**, *8*, 2209.

(49)   Munshi, N.; De, T. K.; Maitra, A. *J Colloid Interf Sci* **1997**, *190*, 387.

(50)   Park, J.; An, K. J.; Hwang, Y. S.; Park, J. G.; Noh, H. J.; Kim, J. Y.; Park, J. H.; Hwang, N. M.; Hyeon, T. *Nat Mater* **2004**, *3*, 891.

(51)   Yu, W. W.; Falkner, J. C.; Yavuz, C. T.; Colvin, V. L. *Chem Commun* **2004**, 2306.

(52)   Dong, C. Q.; Ren, J. C. *Luminescence* **2012**, *27*, 199.

(53)   Gao, X. H.; Yang, L. L.; Petros, J. A.; Marshal, F. F.; Simons, J. W.; Nie, S. M. *Curr Opin Biotech* **2005**, *16*, 63.

(54)   Alivisatos, A. P. *Science* **1996**, *271*, 933.

(55)   Bhujval, P.; Rajaram, S.; Favretto, M. E.; Douroumis, D. *J Pharm Pharmacol* **2010**, *62*, 1296.

(56)   Han, H.; Di Francesco, G.; Maye, M. M. *J Phys Chem C* **2010**, *114*, 19270.

(57)   Moreels, I.; Justo, Y.; De Geyter, B.; Haustraete, K.; Martins, J. C.; Hens, Z. *Acs Nano* **2011**, *5*, 2004.

(58)   Slipper, I. J.; Bhujval, P.; Rajaram, S.; Favretto, M. E.; Douroumis, D. *J Nanosci Nanotechno* **2010**, *10*, 5899.

(59)   Peng, Z. A.; Peng, X. G. *J Am Chem Soc* **2001**, *123*, 183.

(60)   Hines, M. A.; Guyot-Sionnest, P. *J Phys Chem-Us* **1996**, *100*, 468.

(61)   Peng, X. G.; Schlamp, M. C.; Kadavanich, A. V.; Alivisatos, A. P. *J Am Chem Soc* **1997**, *119*, 7019.

(62)   Li, J. J.; Wang, Y. A.; Guo, W. Z.; Keay, J. C.; Mishima, T. D.; Johnson, M. B.; Peng, X. G. *J Am Chem Soc* **2003**, *125*, 12567.

(63)   Murray, C. B.; Norris, D. J.; Bawendi, M. G. *J Am Chem Soc* **1993**, *115*, 8706.

(64)   Aldana, J.; Wang, Y. A.; Peng, X. G. *J Am Chem Soc* **2001**, *123*, 8844.

(65)   Michalet, X.; Pinaud, F. F.; Bentolila, L. A.; Tsay, J. M.; Doose, S.; Li, J. J.; Sundaresan, G.; Wu, A. M.; Gambhir, S. S.; Weiss, S. *Science* **2005**, *307*, 538.

(66)   Chan, W. C. W.; Maxwell, D. J.; Gao, X. H.; Bailey, R. E.; Han, M. Y.; Nie, S. M. *Curr Opin Biotech* **2002**, *13*, 40.

(67)   Han, M. Y.; Gao, X. H.; Su, J. Z.; Nie, S. *Nat Biotechnol* **2001**, *19*, 631.

(68)   Chu, M. Q.; Song, X.; Cheng, D.; Liu, S. P.; Zhu, J. *Nanotechnology* **2006**, *17*, 3268.

(69)   Lu, C. W.; Hung, Y.; Hsiao, J. K.; Yao, M.; Chung, T. H.; Lin, Y. S.; Wu, S. H.; Hsu, S. C.; Liu, H. M.; Mou, C. Y.; Yang, C. S.; Huang, D. M.; Chen, Y. C. *Nano Lett* **2007**, *7*, 149.

(70)   Sathe, T. R.; Agrawal, A.; Nie, S. M. *Anal Chem* **2006**, *78*, 5627.

(71)   Hong, X.; Li, J.; Wang, M. J.; Xu, J. J.; Guo, W.; Li, J. H.; Bai, Y. B.; Li, T. J. *Chem Mater* **2004**, *16*, 4022.

(72)   Lee, J. E.; Lee, N.; Kim, H.; Kim, J.; Choi, S. H.; Kim, J. H.; Kim, T.; Song, I. C.; Park, S. P.; Moon, W. K.; Hyeon, T. *J Am Chem Soc* **2010**, *132*, 552.

(73)   Yang, J.; Lim, E. K.; Lee, H. J.; Park, J.; Lee, S. C.; Lee, K.; Yoon, H. G.; Suh, J. S.; Huh, Y. M.; Haam, S. *Biomaterials* **2008**, *29*, 2548.

(74)   Lim, Y. T.; Noh, Y. W.; Cho, J. H.; Han, J. H.; Choi, B. S.; Kwon, J.; Hong, K. S.; Gokarna, A.; Cho, Y. H.; Chung, B. H. *J Am Chem Soc* **2009**, *131*, 17145.

(75)   Nikoobakht, B.; Burda, C.; Braun, M.; Hun, M.; El-Sayed, M. A. *Photochem Photobiol* **2002**, *75*, 591.

(76)   Kondon, M.; Kim, J.; Udawatte, N.; Lee, D. *J Phys Chem C* **2008**, *112*, 6695.

(77)   Bertorelle, F.; Wilhelm, C.; Roger, J.; Gazeau, F.; Menager, C.; Cabuil, V. *Langmuir* **2006**, *22*, 5385.

(78)   Veiseh, O.; Sun, C.; Gunn, J.; Kohler, N.; Gabikian, P.; Lee, D.; Bhattarai, N.; Ellenbogen, R.; Sze, R.; Hallahan, A.; Olson, J.; Zhang, M. Q. *Nano Lett* **2005**, *5*, 1003.

(79)   Thakur, D.; Deng, S.; Baldet, T.; Winter, J. O. *Nanotechnology* **2009**, *20*.

(80)   Kale, A.; Kale, S.; Yadav, P.; Gholap, H.; Pasricha, R.; Jog, J. P.; Lefez, B.; Hannoyer, B.; Shastry, P.; Ogale, S. *Nanotechnology* **2011**, *22*.

(81)   Josephson, L.; Kircher, M. F.; Mahmood, U.; Tang, Y.; Weissleder, R. *Bioconjugate Chem* **2002**, *13*, 554.

(82)   Corr, S. A.; O' Byrne, A.; Gun'ko, Y. K.; Ghosh, S.; Brougham, D. F.; Mitchell, S.; Volkov, Y.; Prina-Mello, A. *Chem Commun* **2006**, 4474.

(83)   Kim, H.; Achermann, M.; Balet, L. P.; Hollingsworth, J. A.; Klimov, V. I. *J Am Chem Soc* **2005**, *127*, 544.

(84)   Gu, H. W.; Zheng, R. K.; Liu, H.; Zhang, X. X.; Xu, B. *Small* **2005**, *1*, 402.

(85)   He, S. L.; Zhang, H. W.; Delikanli, S.; Qin, Y. L.; Swihart, M. T.; Zeng, H. *J Phys Chem C* **2009**, *113*, 87.

(86)   Maynadie, J.; Salant, A.; Falqui, A.; Respaud, M.; Shaviv, E.; Banin, U.; Soulantica, K.; Chaudret, B. *Angew Chem Int Edit* **2009**, *48*, 1814.

(87)   Tian, Z. Q.; Zhang, Z. L.; Gao, J. H.; Huang, B. H.; Xie, H. Y.; Xie, M.; Abruna, H. D.; Pang, D. W. *Chem Commun* **2009**, 4025.

(88)   Tian, Z. Q.; Zhang, Z. L.; Jiang, P.; Zhang, M. X.; Xie, H. Y.; Pang, D. W. *Chem Mater* **2009**, *21*, 3039.

(89)   Du, G. H.; Liu, Z. L.; Lu, Q. H.; Xia, X.; Jia, L. H.; Yao, K. L.; Chu, Q.; Zhang, S. M. *Nanotechnology* **2006**, *17*, 2850.

(90)   Tao, K.; Zhou, H. R.; Don, H. J.; Xing, B.; Li, W. W.; Sun, K. *J Phys Chem C* **2009**, *113*, 8762.

(91)   Pellegrino, T.; Fiore, A.; Carlino, E.; Giannini, C.; Cozzoli, P. D.; Ciccarella, G.; Respaud, M.; Palmirotta, L.; Cingolani, R.; Manna, L. *J Am Chem Soc* **2006**, *128*, 6690.

(92)   Yu, H.; Chen, M.; Rice, P. M.; Wang, S. X.; White, R. L.; Sun, S. H. *Nano Lett* **2005**, *5*, 379.

(93)   Shi, W. L.; Zeng, H.; Sahoo, Y.; Ohulchanskyy, T. Y.; Ding, Y.; Wang, Z. L.; Swihart, M.; Prasad, P. N. *Nano Lett* **2006**, *6*, 875.

(94)   Figuerola, A.; Fiore, A.; Di Corato, R.; Falqui, A.; Giannini, C.; Micotti, E.; Lascialfari, A.; Corti, M.; Cingolani, R.; Pellegrino, T.; Cozzoli, P. D.; Manna, L. *J Am Chem Soc* **2008**, *130*, 1477.

(95)   Kudera, S.; Carbone, L.; Carlino, E.; Cingolani, R.; Cozzoli, P. D.; Manna, L. *Physica E* **2007**, *37*, 128.

(96)   Casavola, M.; Buonsanti, R.; Caputo, G.; Cozzoli, P. D. *Eur J Inorg Chem* **2008**, 837.

(97)   Fransson-Andreo, A. *Radiotherapy and Oncology* **2006**, *81*, S113.

(98)   Macdonald, G. A.; Peduto, A. J. *Journal of Gastroenterology and Hepatology* **2000**, *15*, 980.

(99)   Amaro, E.; Barker, G. J. *Brain and Cognition* **2006**, *60*, 220.

(100)   Lee, N.; Hyeon, T. *Chem Soc Rev* **2012**, *41*, 2575.

(101)   Das, G. K.; Heng, B. C.; Ng, S. C.; White, T.; Loo, J. S. C.; D'Silva, L.; Padmanabhan, P.; Bhakoo, K. K.; Selvan, S. T.; Tan, T. T. Y. *Langmuir* **2010**, *26*, 8959.

(102)   Faucher, L.; Gossuin, Y.; Hocq, A.; Fortin, M. A. *Nanotechnology* **2011**, *22*.

(103)   Zhou, L. J.; Gu, Z. J.; Liu, X. X.; Yin, W. Y.; Tian, G.; Yan, L.; Jin, S.; Ren, W. L.; Xing, G. M.; Li, W.; Chang, X. L.; Hu, Z. B.; Zhao, Y. L. *J Mater Chem* **2012**, *22*, 966.

(104)   Huang, H. C.; Barua, S.; Sharma, G.; Dey, S. K.; Rege, K. *J Control Release* **2011**, *155*, 344.

(105)   Harisinghani, M. G.; Weissleder, R. *Plos Med* **2004**, *1*, 202.

(106)   Harisinghani, M. G.; Barentsz, J.; Hahn, P. F.; Deserno, W. M.; Tabatabaei, S.; van de Kaa, C. H.; de la Rosette, J.; Weissleder, R. *New Engl J Med* **2003**, *348*, 2491.

(107)   Mulder, W. J. M.; Koole, R.; Brandwijk, R. J.; Storm, G.; Chin, P. T. K.; Strijkers, G. J.; Donega, C. D.; Nicolay, K.; Griffioen, A. W. *Nano Lett* **2006**, *6*, 1.

(108)   Yoon, T. J.; Yu, K. N.; Kim, E.; Kim, J. S.; Kim, B. G.; Yun, S. H.; Sohn, B. H.; Cho, M. H.; Lee, J. K.; Park, S. B. *Small* **2006**, *2*, 209.

(109)   Gao, J. H.; Zhang, W.; Huang, P. B.; Zhang, B.; Zhang, X. X.; Xu, B. *J Am Chem Soc* **2008**, *130*, 3710.

(110)   Shen, J.; Sun, L. D.; Yan, C. H. *Dalton T* **2008**, 5687.

(111)   Corr, S. A.; Rakovich, Y. P.; Gun'ko, Y. K. *Nanoscale Res Lett* **2008**, *3*, 87.

(112)   Gao, J. H.; Gu, H. W.; Xu, B. *Accounts Chem Res* **2009**, *42*, 1097.

(113)   Yang, H. S.; Lee, H.; Holloway, P. H. *Nanotechnology* **2005**, *16*, 2794.

(114)   Yu, W. W.; Peng, X. G. *Angew Chem Int Edit* **2002**, *41*, 2368.

(115)   Yu, W. W.; Falkner, J. C.; Shih, B. S.; Colvin, V. L. *Chem Mater* **2004**, *16*, 3318.

(116)   **!!! INVALID CITATION !!!**

(117)   Demas, J. N.; Crosby, G. A. *J Phys Chem-Us* **1971**, *75*, 991.

(118)   Vossmeyer, T.; Katsikas, L.; Giersig, M.; Popovic, I. G.; Diesner, K.; Chemseddine, A.; Eychmuller, A.; Weller, H. *J Phys Chem-Us* **1994**, *98*, 7665.

(119)   Werner, E. J.; Datta, A.; Jocher, C. J.; Raymond, K. N. *Angew Chem Int Edit* **2008**, *47*, 8568.

(120)   Laurent, S.; Forge, D.; Port, M.; Roch, A.; Robic, C.; Elst, L. V.; Muller, R. N. *Chemical Reviews* **2010**, *110*, 2574.

(121)   Laurent, S.; Forge, D.; Port, M.; Roch, A.; Robic, C.; Elst, L. V.; Muller, R. N. *Chemical Reviews* **2008**, *108*, 2064.

(122)   Geraldes, C. F. G. C.; Laurent, S. *Contrast Media & Molecular Imaging* **2009**, *4*, 1.

(123)   Bulte, J. W. M.; Kraitchman, D. L. *Nmr Biomed* **2004**, *17*, 484.

(124)   Aime, S.; Barge, A.; Cabella, C.; Crich, S. G.; Gianolio, E. *Current Pharmaceutical Biotechnology* **2004**, *5*, 509.

(125)   Balci, N. C.; Semelka, R. C. *Radiol Clin N Am* **2005**, *43*, 887.

(126)   Reimer, P.; Balzer, T. *Eur Radiol* **2003**, *13*, 1266.

(127)   Stark, D. D.; Weissleder, R.; Elizondo, G.; Hahn, P. F.; Saini, S.; Todd, L. E.; Wittenberg, J.; Ferrucci, J. T. *Radiology* **1988**, *168*, 297.

(128)   Clement, O.; Guimaraes, R.; Dekerviler, E.; Frija, G. *Invest Radiol* **1994**, *29*, S226.

(129)   Bellin, M. F.; Lebleu, L.; Meric, J. B. *Abdom Imaging* **2002**, *28*, 155.

(130)   Bulte, J. W. M.; Douglas, T.; Witwer, B.; Zhang, S. C.; Strable, E.; Lewis, B. K.; Zywicke, H.; Miller, B.; van Gelderen, P.; Moskowitz, B. M.; Duncan, I. D.; Frank, J. A. *Nature Biotechnology* **2001**, *19*, 1141.

(131)   Cabella, C.; Crich, S. G.; Corpillo, D.; Barge, A.; Ghirelli, C.; Bruno, E.; Lorusso, V.; Uggeri, F.; Aime, S. *Contrast Media & Molecular Imaging* **2006**, *1*, 23.

(132)   Herborn, C. U.; Honold, E.; Wolf, M.; Kemper, J.; Kinner, S.; Adam, G.; Barkhausen, J. *Invest Radiol* **2007**, *42*, 58.

(133)   Tanimoto, A.; Kadoya, M.; Kawamura, Y.; Kuwatsuru, R.; Gokan, T.; Hirohashi, S. *J Magn Reson Imaging* **2006**, *23*, 499.

(134)   Tanimoto, A.; Kadoya, M.; Kawamura, Y.; Kuwatsuru, R.; Gokan, T.; Hirohashi, S. *Acad Radiol* **2002**, *9*, S457.

(135)   Pereira, R. S.; Wisenberg, G.; Prato, F. S.; Yvorchuk, K. *Magn Reson Mater Phy* **2000**, *11*, 104.

(136)   Kono, M.; Adachi, S.; Kusumoto, M.; Sakai, E. *J Thorac Imag* **1993**, *8*, 18.

(137)   Schwaighofer, B. W.; Klein, M. V.; Wesbey, G.; Hesselink, J. R. *J Comput Assist Tomo* **1990**, *14*, 11.

(138)   Imakita, S.; Nishimura, T.; Naito, H.; Yamada, N.; Takamiya, M.; Minamikawa, J.; Kikuchi, H.; Nakamura, M.; Sawada, T.; Choki, J.; Yamaguchi, T.; Terada, T. *Neuroradiology* **1987**, *29*, 600.

(139)   Brantzawadzki, M.; Berry, I.; Osaki, L.; Brasch, R.; Murovic, J.; Norman, D. *Am J Neuroradiol* **1986**, *7*, 781.

(140)   Berry, I.; Brantzawadzki, M.; Osaki, L.; Holland, B. A.; Rosenbloom, S.; Mcmurdo, S. K.; Haas, D. K.; Harper, P. S.; Keyes, W. D.; Norman, D.; Newton, T. H.; Brasch, R. C.; Wilson, C. B. *Am J Neuroradiol* **1986**, *7*, 540.

(141)   Berry, I.; Brantzawadzki, M.; Osaki, L.; Brasch, R.; Murovic, J.; Newton, T. H. *Am J Roentgenol* **1986**, *147*, 1231.

(142)   Toth, E.; Helm, L.; Merbach, A. E. *Contrast Agents I* **2002**, *221*, 61.

(143)   Marckmann, P.; Skov, L.; Rossen, K.; Dupont, A.; Damholt, M. B.; Heaf, J. G.; Thomsen, H. S. *Journal of the American Society of Nephrology* **2006**, *17*, 2359.

(144)   Grobner, T. *Nephrol Dial Transpl* **2006**, *21*, 1745.

(145)   Sadowski, E. A.; Bennett, L. K.; Chan, M. R.; Wentland, A. L.; Garrett, A. L.; Garrett, R. W.; Djamali, A. *Radiology* **2007**, *243*, 148.

(146)   Broome, D. R.; Girguis, M. S.; Baron, P. W.; Cottrell, A. C.; Kjellin, I.; Kirk, G. A. *Am J Roentgenol* **2007**, *188*, 586.

(147)   Kuo, P. H.; Kanal, E.; Abu-Alfa, A. K.; Cowper, S. E. *Radiology* **2007**, *242*, 647.

(148)   Engstrom, M.; Klasson, A.; Pedersen, H.; Vahlberg, C.; Kall, P. O.; Uvdal, K. *Magnetic Resonance Materials in Physics Biology and Medicine* **2006**, *19*, 180.

(149)   Miyawaki, J.; Yudasaka, M.; Imai, H.; Yorimitsu, H.; Isobe, H.; Nakamura, E.; Iijima, S. *Journal of Physical Chemistry B* **2006**, *110*, 5179.

(150)   Li, I. F.; Su, C. H.; Sheu, H. S.; Chiu, H. C.; Lo, Y. W.; Lin, W. T.; Chen, J. H.; Yeh, C. S. *Adv Funct Mater* **2008**, *18*, 766.

(151)   Hu, K. W.; Jhang, F. Y.; Su, C. H.; Yeh, C. S. *J Mater Chem* **2009**, *19*, 2147.

(152)   Seo, S.; Yang, H.; Holloway, P. H. *J Colloid Interf Sci* **2009**, *331*, 236.

(153)   Paek, J.; Lee, C. H.; Choi, J.; Choi, S. Y.; Kim, A.; Lee, J. W.; Lee, K. *Crystal Growth & Design* **2007**, *7*, 1378.

(154)   Mahajan, S. V.; Dickerson, J. H. *Nanotechnology* **2007**, *18*.

(155)   Bazzi, R.; Flores-Gonzalez, M. A.; Louis, C.; Lebbou, K.; Dujardin, C.; Brenier, A.; Zhang, W.; Tillement, O.; Bernstein, E.; Perriat, P. *J Lumin* **2003**, *102*, 445.

(156)   Bazzi, R.; Flores, M. A.; Louis, C.; Lebbou, K.; Zhang, W.; Dujardin, C.; Roux, S.; Mercier, B.; Ledoux, G.; Bernstein, E.; Perriat, P.; Tillement, O. *J Colloid Interf Sci* **2004**, *273*, 191.

(157)   Abrikossova, N.; Skoglund, C.; Ahren, M.; Bengtsson, T.; Uvdal, K. *Nanotechnology* **2012**, *23*.

(158)   Azizian, G.; Riyahi-Alam, N.; Haghgoo, S.; Moghimi, H. R.; Zohdiaghdam, R.; Rafiei, B.; Gorji, E. *Nanoscale Res Lett* **2012**, *7*.

(159)   Cao, Y. C. *J Am Chem Soc* **2004**, *126*, 7456.

(160)   Si, R.; Zhang, Y. W.; Zhou, H. P.; Sun, L. D.; Yan, C. H. *Chem Mater* **2007**, *19*, 18.

(161)   Park, J. Y.; Choi, E. S.; Baek, M. J.; Lee, G. H.; Woo, S.; Chang, Y. *Eur J Inorg Chem* **2009**, 2477.

(162)   Faucher, L.; Tremblay, M.; Lagueux, J.; Gossuin, Y.; Fortin, M. A. *Acs Appl Mater Inter* **2012**, *4*, 4506.

(163)   Xu, W.; Park, J. Y.; Kattel, K.; Bony, B. A.; Heo, W. C.; Jin, S.; Park, J. W.; Chang, Y.; Do, J. Y.; Chae, K. S.; Kim, T. J.; Park, J. A.; Kwak, Y. W.; Lee, G. H. *New J Chem* **2012**, *36*, 2361.

(164)   Zhang, B. B.; Jin, H. T.; Li, Y.; Chen, B. D.; Liu, S. Y.; Shi, D. L. *J Mater Chem* **2012**, *22*, 14494.

(165)   Prakash, A.; Zhu, H. G.; Jones, C. J.; Benoit, D. N.; Ellsworth, A. Z.; Bryant, E. L.; Colvin, V. L. *Acs Nano* **2009**, *3*, 2139.

(166)   Lee, S. S.; Zhu, H. G.; Contreras, E. Q.; Prakash, A.; Puppala, H. L.; Colvin, V. L. *Chem Mater* **2012**, *24*, 424.

(167)   Benoit, D. N.; Zhu, H. G.; Lilierose, M. H.; Verm, R. A.; Ali, N.; Morrison, A. N.; Fortner, J. D.; Ayendano, C.; Colvin, V. L. *Anal Chem* **2012**, *84*, 9238.

(168)   Bronstein, L. M.; Huang, X. L.; Retrum, J.; Schmucker, A.; Pink, M.; Stein, B. D.; Dragnea, B. *Chem Mater* **2007**, *19*, 3624.

(169) Chaubey, G. S.; Barcena, C.; Poudyal, N.; Rong, C. B.; Gao, J. M.; Sun, S. H.; Liu, J. P. *J Am Chem Soc* **2007**, *129*, 7214.

(170) Jackson, C. L.; Mckenna, G. B. *Journal of Chemical Physics* **1990**, *93*, 9002.

(171) Park, J.; Joo, J.; Kwon, S. G.; Jang, Y.; Hyeon, T. *Angew Chem Int Edit* **2007**, *46*, 4630.

(172) Peng, X. G.; Wickham, J.; Alivisatos, A. P. *J Am Chem Soc* **1998**, *120*, 5343.

(173) Petruska, M. A.; Bartko, A. P.; Klimov, V. I. *J Am Chem Soc* **2004**, *126*, 714.

(174) Sharma, M.; Yashonath, S. *J Phys Chem B* **2007**, *111*, 7928.

(175) Subramanian, Y.; Ghorai, P. K.; Sastry, S. *Abstr Pap Am Chem S* **2005**, *229*, U794.

(176) Dickson, D. P. E. *Journal of Magnetism and Magnetic Materials* **1999**, *203*, 46.

(177) Wan, J. Q.; Jiang, X. H.; Li, H.; Chen, K. Z. *J Mater Chem* **2012**, *22*, 13500.

(178) Kim, B. H.; Lee, N.; Kim, H.; An, K.; Park, Y. I.; Choi, Y.; Shin, K.; Lee, Y.; Kwon, S. G.; Na, H. B.; Park, J. G.; Ahn, T. Y.; Kim, Y. W.; Moon, W. K.; Choi, S. H.; Hyeon, T. *J Am Chem Soc* **2011**, *133*, 12624.

(179) Tromsdorf, U. I.; Bruns, O. T.; Salmen, S. C.; Beisiegel, U.; Weller, H. *Nano Lett* **2009**, *9*, 4434.

(180) Baek, M. J.; Park, J. Y.; Xu, W. L.; Kattel, K.; Kim, H. G.; Lee, E. J.; Patel, A. K.; Lee, J. J.; Chang, Y. M.; Kim, T. J.; Bae, J. E.; Chae, K. S.; Lee, G. H. *Acs Appl Mater Inter* **2010**, *2*, 2949.

(181) Tong, S.; Hou, S. J.; Zheng, Z. L.; Zhou, J.; Bao, G. *Nano Lett* **2010**, *10*, 4607.

(182) Caravan, P. *Accounts Chem Res* **2009**, *42*, 851.

(183) Caravan, P. *Chem Soc Rev* **2006**, *35*, 512.

(184) Heverhagen, J. T.; Reitz, I.; Pavlicova, M.; Levine, A. L.; Klose, K. J.; Wagner, H. J. *Eur Radiol* **2007**, *17*, 626.

(185) Vehmas, T.; Markkola, A. T. *Acta Radiol* **1998**, *39*, 223.

(186) Erb, G.; Benner, T.; Heiland, S.; Reith, W.; Sartor, K.; Forsting, M. *Rofo-Fortschr Rontg* **1997**, *167*, 599.

(187) LeBedis, C.; Luna, A.; Soto, J. A. *Magn Reson Imaging C* **2012**, *20*, 715.

(188) Faulkner, S.; Long, N. J. *Dalton T* **2011**, *40*, 6067.

(189) Massoud, T. F.; Gambhir, S. S. *Gene Dev* **2003**, *17*, 545.

(190) Cheon, J.; Lee, J. H. *Accounts Chem Res* **2008**, *41*, 1630.

(191) Mahmoudi, M.; Hosseinkhani, H.; Hosseinkhani, M.; Boutry, S.; Simchi, A.; Journeay, W. S.; Subramani, K.; Laurent, S. *Chem Rev* **2011**, *111*, 253.

(192) Long, C. M.; van Laarhoven, H. W. M.; Bulte, J. W. M.; Levitsky, H. I. *Cancer Res* **2009**, *69*, 3180.

(193) Gillis, P.; Koenig, S. H. *Magnet Reson Med* **1987**, *5*, 323.

(194) Koenig, S. H.; Kellar, K. E. *Magnet Reson Med* **1995**, *34*, 227.

(195) Bourrinet, P.; Bengele, H. H.; Bonnemain, B.; Dencausse, A.; Idee, J. M.; Jacobs, P. M.; Lewis, J. M. *Invest Radiol* **2006**, *41*, 313.

(196) Jain, T. K.; Reddy, M. K.; Morales, M. A.; Leslie-Pelecky, D. L.; Labhasetwar, V. *Mol Pharm* **2008**, *5*, 316.

(197) Jun, Y. W.; Lee, J. H.; Cheon, J. *Angew Chem Int Edit* **2008**, *47*, 5122.

(198) Ho, D.; Sun, X. L.; Sun, S. H. *Accounts Chem Res* **2011**, *44*, 875.

(199) Park, J.; Lee, E.; Hwang, N. M.; Kang, M. S.; Kim, S. C.; Hwang, Y.; Park, J. G.; Noh, H. J.; Kini, J. Y.; Park, J. H.; Hyeon, T. *Angew Chem Int Edit* **2005**, *44*, 2872.

(200) Gillis, P.; Moiny, F.; Brooks, R. A. *Magnet Reson Med* **2002**, *47*, 257.

(201) Jun, Y. W.; Huh, Y. M.; Choi, J. S.; Lee, J. H.; Song, H. T.; Kim, S.; Yoon, S.; Kim, K. S.; Shin, J. S.; Suh, J. S.; Cheon, J. *J Am Chem Soc* **2005**, *127*, 5732.

(202) Lee, N.; Choi, Y.; Lee, Y.; Park, M.; Moon, W. K.; Choi, S. H.; Hyeon, T. *Nano Lett* **2012**, *12*, 3127.

(203) Brooks, R. A.; Moiny, F.; Gillis, P. *Magnetic Resonance in Medicine* **2001**, *45*, 1014.

(204) Yoon, T. J.; Lee, H.; Shao, H. L.; Hilderbrand, S. A.; Weissleder, R. *Advanced Materials* **2011**, *23*, 4793.

(205) Kim, D.; Lee, N.; Park, M.; Kim, B. H.; An, K.; Hyeon, T. *Journal of the American Chemical Society* **2009**, *131*, 454.

(206) Lee, N.; Kim, H.; Choi, S. H.; Park, M.; Kim, D.; Kim, H. C.; Choi, Y.; Lin, S.; Kim, B. H.; Jung, H. S.; Kim, H.; Park, K. S.; Moon, W. K.; Hyeon, T. *Proceedings of the National Academy of Sciences of the United States of America* **2011**, *108*, 2662.

(207) Moroz, P.; Metcalf, C.; Gray, B. N. *Biometals* **2003**, *16*, 455.

(208) Poselt, E.; Kloust, H.; Tromsdorf, U.; Janschel, M.; Hahn, C.; Masslo, C.; Weller, H. *Acs Nano* **2012**, *6*, 1619.

(209) Lee, J. H.; Jun, Y. W.; Yeon, S. I.; Shin, J. S.; Cheon, J. *Angew Chem Int Edit* **2006**, *45*, 8160.

(210) Bin Na, H.; Lee, I. S.; Seo, H.; Park, Y. I.; Lee, J. H.; Kim, S. W.; Hyeon, T. *Chemical Communications* **2007**, 5167.

(211) Kim, J.; Lee, J. E.; Lee, S. H.; Yu, J. H.; Lee, J. H.; Park, T. G.; Hyeon, T. *Adv Mater* **2008**, *20*, 478.

(212) Panyam, J.; Labhasetwar, V. *Advanced Drug Delivery Reviews* **2003**, *55*, 329.

(213) Kim, J.; Lee, J. E.; Lee, J.; Yu, J. H.; Kim, B. C.; An, K.; Hwang, Y.; Shin, C. H.; Park, J. G.; Kim, J.; Hyeon, T. *J Am Chem Soc* **2006**, *128*, 688.

(214) Kohler, N.; Fryxell, G. E.; Zhang, M. Q. *Journal of the American Chemical Society* **2004**, *126*, 7206.

(215) Song, H. T.; Choi, J. S.; Huh, Y. M.; Kim, S.; Jun, Y. W.; Suh, J. S.; Cheon, J. *Journal of the American Chemical Society* **2005**, *127*, 9992.

(216) Xu, C. J.; Xu, K. M.; Gu, H. W.; Zheng, R. K.; Liu, H.; Zhang, X. X.; Guo, Z. H.; Xu, B. *Journal of the American Chemical Society* **2004**, *126*, 9938.

(217) Sun, S. H.; Zeng, H.; Robinson, D. B.; Raoux, S.; Rice, P. M.; Wang, S. X.; Li, G. X. *Journal of the American Chemical Society* **2004**, *126*, 273.

(218) Lee, J. H.; Huh, Y. M.; Jun, Y.; Seo, J.; Jang, J.; Song, H. T.; Kim, S.; Cho, E. J.; Yoon, H. G.; Suh, J. S.; Cheon, J. *Nature Medicine* **2007**, *13*, 95.

(219) Anisur, R. M.; Shin, J.; Choi, H. H.; Yeo, K. M.; Kang, E. J.; Lee, I. S. *Journal of Materials Chemistry* **2010**, *20*, 10615.

(220) Xu, J.; Zhu, Y. G.; Huang, H. T.; Xie, Z.; Chen, D.; Shen, G. Z. *Crystengcomm* **2011**, *13*, 2629.

(221) Yu, W. W.; Chang, E.; Falkner, J. C.; Zhang, J. Y.; Al-Somali, A. M.; Sayes, C. M.; Johns, J.; Drezek, R.; Colvin, V. L. *J Am Chem Soc* **2007**, *129*, 2871.

(222) Topfer, J.; Schops, W.; Nauber, P.; Katzel, D. *Cfi-Ceram Forum Int* **1999**, *76*, 49.

(223) Jang, J. T.; Nah, H.; Lee, J. H.; Moon, S. H.; Kim, M. G.; Cheon, J. *Angew Chem Int Edit* **2009**, *48*, 1234.

(224) Tanimoto, A.; Kuribayashi, S. *Eur J Radiol* **2006**, *58*, 200.

(225) Gupta, A. K.; Wells, S. *Ieee T Nanobiosci* **2004**, *3*, 66.

(226) Fang, C.; Zhang, M. Q. *J Mater Chem* **2009**, *19*, 6258.

(227) Hao, R.; Xing, R. J.; Xu, Z. C.; Hou, Y. L.; Gao, S.; Sun, S. H. *Adv Mater* **2010**, *22*, 2729.

(228) Behrens, S. *Nanoscale* **2011**, *3*, 877.

(229) Carbone, L.; Cozzoli, P. D. *Nano Today* **2010**, *5*, 449.

(230) Janczewski, D.; Zhang, Y.; Das, G. K.; Yi, D. K.; Padmanabhan, P.; Bhakoo, K. K.; Tan, T. T. Y.; Selvan, S. T. *Microsc Res Techniq* **2011**, *74*, 563.

(231) Louie, A. Y. *Chem Rev* **2010**, *110*, 3146.

(232) Mulder, W. J. M.; Griffioen, A. W.; Strijkers, G. J.; Cormode, D. P.; Nicolay, K.; Fayad, Z. A. *Nanomedicine-Uk* **2007**, *2*, 307.

(233) Bigall, N. C.; Parak, W. J.; Dorfs, D. *Nano Today* **2012**, *7*, 282.

(234) Selvan, S. T.; Tan, T. T. Y.; Yi, D. K.; Jana, N. R. *Langmuir* **2010**, *26*, 11631.

(235) Mornet, S.; Vasseur, S.; Grasset, F.; Duguet, E. *J Mater Chem* **2004**, *14*, 2161.

(236) Lee, H.; Lee, E.; Kim, D. K.; Jang, N. K.; Jeong, Y. Y.; Jon, S. *J Am Chem Soc* **2006**, *128*, 7383.

(237) Lee, K. B.; Park, S.; Mirkin, C. A. *Angew Chem Int Edit* **2004**, *43*, 3048.

(238) Gu, H. W.; Ho, P. L.; Tsang, K. W. T.; Wang, L.; Xu, B. *J Am Chem Soc* **2003**, *125*, 15702.

(239) Sun, C.; Lee, J. S. H.; Zhang, M. Q. *Advanced Drug Delivery Reviews* **2008**, *60*, 1252.

(240) Liong, M.; Lu, J.; Kovochich, M.; Xia, T.; Ruehm, S. G.; Nel, A. E.; Tamanoi, F.; Zink, J. I. *Acs Nano* **2008**, *2*, 889.

(241) Huh, Y. M.; Jun, Y. W.; Song, H. T.; Kim, S.; Choi, J. S.; Lee, J. H.; Yoon, S.; Kim, K. S.; Shin, J. S.; Suh, J. S.; Cheon, J. *J Am Chem Soc* **2005**, *127*, 12387.

(242) Kircher, M. F.; Mahmood, U.; King, R. S.; Weissleder, R.; Josephson, L. *Cancer Res* **2003**, *63*, 8122.

(243) Howes, P.; Green, M.; Bowers, A.; Parker, D.; Varma, G.; Kallumadil, M.; Hughes, M.; Warley, A.; Brain, A.; Botnar, R. *J Am Chem Soc* **2010**, *132*, 9833.

(244)   Li, K.; Ding, D.; Huo, D.; Pu, K. Y.; Ngo, N. P. T.; Hu, Y.; Li, Z.; Liu, B. *Adv Funct Mater* **2012**, *22*, 3107.

(245)   Song, E. Q.; Hu, J.; Wen, C. Y.; Tian, Z. Q.; Yu, X.; Zhang, Z. L.; Shi, Y. B.; Pang, D. W. *Acs Nano* **2011**, *5*, 761.

(246)   Roullier, V.; Grasset, F.; Boulmedais, F.; Artzner, F.; Cador, O.; Marchi-Artzner, V. *Chem Mater* **2008**, *20*, 6657.

(247)   Law, W. C.; Yong, K. T.; Roy, I.; Xu, G.; Ding, H.; Bergey, E. J.; Zeng, H.; Prasad, P. N. *J Phys Chem C* **2008**, *112*, 7972.

(248)   Gaponik, N.; Radtchenko, I. L.; Sukhorukov, G. B.; Rogach, A. L. *Langmuir* **2004**, *20*, 1449.

(249)   Wang, G. P.; Song, E. Q.; Xie, H. Y.; Zhang, Z. L.; Tian, Z. Q.; Zuo, C.; Pang, D. W.; Wu, D. C.; Shi, Y. B. *Chem Commun* **2005**, 4276.

(250)   Zebli, B.; Susha, A. S.; Sukhorukov, G. B.; Rogach, A. L.; Parak, W. J. *Langmuir* **2005**, *21*, 4262.

(251)   Guo, J.; Yang, W. L.; Wang, C. C.; He, J.; Chen, J. Y. *Chem Mater* **2006**, *18*, 5554.

(252)   V, S.-M.; Correa-Duarte, M. A.; Spasova, M.; Liz-Marzan, L. M.; Farle, M. *Adv Funct Mater* **2006**, *16*, 509.

(253)   Mandal, S. K.; Lequeux, N.; Rotenberg, B.; Tramier, M.; Fattaccioli, J.; Bibette, J.; Dubertret, B. *Langmuir* **2005**, *21*, 4175.

(254)   Sun, L.; Zang, Y.; Sun, M. D.; Wang, H. G.; Zhu, X. J.; Xu, S. F.; Yang, Q. B.; Li, Y. X.; Shan, Y. M. *J Colloid Interf Sci* **2010**, *350*, 90.

(255)   Wan, J. Q.; Meng, X. X.; Liu, E. Z.; Chen, K. Z. *Nanotechnology* **2010**, *21*.

(256)   Pfaff, A.; Schallon, A.; Ruhland, T. M.; Majewski, A. P.; Schmalz, H.; Freitag, R.; Muller, A. H. E. *Biomacromolecules* **2011**, *12*, 3805.

(257)   Tu, C. F.; Yang, Y. H.; Gao, M. Y. *Nanotechnology* **2008**, *19*.

(258)   Kim, J.; Kim, H. S.; Lee, N.; Kim, T.; Kim, H.; Yu, T.; Song, I. C.; Moon, W. K.; Hyeon, T. *Angew Chem Int Edit* **2008**, *47*, 8438.

(259)   Li, L. L.; Li, H. B.; Chen, D.; Liu, H. Y.; Tang, F. Q.; Zhang, Y. Q.; Ren, J.; Li, Y. *J Nanosci Nanotechno* **2009**, *9*, 2540.

(260)   Fernandez, B.; Galvez, N.; Cuesta, R.; Hungria, A. B.; Calvino, J. J.; Dominguez-Vera, J. M. *Adv Funct Mater* **2008**, *18*, 3931.

(261)   Sun, B.; Sun, M. J.; Gu, Z.; Shen, Q. D.; Jiang, S. J.; Xu, Y.; Wang, Y. *Macromolecules* **2010**, *43*, 10348.

(262)   Koktysh, D.; Bright, V.; Pham, W. *Nanotechnology* **2011**, *22*.

(263)   Zhan, F. M.; Zhang, C. Y. *J Mater Chem* **2011**, *21*, 4765.

(264)   Deng, S.; Ruan, G.; Han, N.; Winter, J. O. *Nanotechnology* **2010**, *21*.

(265)   Trinh, T. T.; Mott, D.; Thanh, N. T. K.; Maenosono, S. *Rsc Adv* **2011**, *1*, 100.

(266)   Zhou, H. R.; Tao, K.; Sui, Y. Q.; Sun, K. *Physica E* **2011**, *44*, 597.

(267)   Zhou, H. R.; Tao, K.; Ding, J.; Zhang, Z. F.; Sun, K.; Shi, W. B. *Colloid Surface A* **2011**, *389*, 18.

(268)   Wang, C.; Xu, C. J.; Zeng, H.; Sun, S. H. *Adv Mater* **2009**, *21*, 3045.

(269)   Zeng, H.; Sun, S. H. *Adv Funct Mater* **2008**, *18*, 391.

(270)   Costi, R.; Saunders, A. E.; Banin, U. *Angew Chem Int Edit* **2010**, *49*, 4878.

(271)   Zanella, M.; Falqui, A.; Kudera, S.; Manna, L.; Casula, M. F.; Parak, W. J. *J Mater Chem* **2008**, *18*, 4311.

(272)   Kwon, K. W.; Shim, M. *J Am Chem Soc* **2005**, *127*, 10269.

(273)   Kwon, K. W.; Lee, B. H.; Shim, M. *Chem Mater* **2006**, *18*, 6357.

(274)   McDaniel, H.; Shim, M. *Acs Nano* **2009**, *3*, 434.

(275)   Shim, M.; McDaniel, H. *Curr Opin Solid St M* **2010**, *14*, 83.

(276)   Gu, H. W.; Zheng, R. K.; Zhang, X. X.; Xu, B. *J Am Chem Soc* **2004**, *126*, 5664.

(277)   Gao, J. H.; Zhang, B.; Gao, Y.; Pan, Y.; Zhang, X. X.; Xu, B. *J Am Chem Soc* **2007**, *129*, 11928.

(278)   Selvan, S. T.; Patra, P. K.; Ang, C. Y.; Ying, J. Y. *Angew Chem Int Edit* **2007**, *46*, 2448.

(279)   Ang, C. Y.; Giam, L.; Chan, Z. M.; Lin, A. W. H.; Gu, H.; Devlin, E.; Papoefthymiou, G. C.; Selvan, S. T.; Ying, J. Y. *Adv Mater* **2009**, *21*, 869.

(280)   Lin, A. W. H.; Ang, C. Y.; Patra, P. K.; Han, Y.; Gu, H.; Le Breton, J. M.; Juraszek, J.; Chiron, H.; Papaefthymiou, G. C.; Selvan, S. T.; Ying, J. Y. *J Solid State Chem* **2011**, *184*, 2150.

(281)   Talapin, D. V.; Mekis, I.; Gotzinger, S.; Kornowski, A.; Benson, O.; Weller, H. *J Phys Chem B* **2004**, *108*, 18826.

(282)   Dabbousi, B. O.; RodriguezViejo, J.; Mikulec, F. V.; Heine, J. R.; Mattoussi, H.; Ober, R.; Jensen, K. F.; Bawendi, M. G. *J Phys Chem B* **1997**, *101*, 9463.

(283)   Peng, Z. A.; Peng, X. G. *J Am Chem Soc* **2002**, *124*, 3343.

(284)   Fu, A. H.; Gu, W. W.; Boussert, B.; Koski, K.; Gerion, D.; Manna, L.; Le Gros, M.; Larabell, C. A.; Alivisatos, A. P. *Nano Lett* **2007**, *7*, 179.

(285)   Mokari, T.; Banin, U. *Chem Mater* **2003**, *15*, 3955.

(286)   Peng, X. G.; Manna, L.; Yang, W. D.; Wickham, J.; Scher, E.; Kadavanich, A.; Alivisatos, A. P. *Nature* **2000**, *404*, 59.

(287)   Zhu, H. G.; Prakash, A.; Benoit, D. N.; Jones, C. J.; Colvin, V. L. *Nanotechnology* **2010**, *21*.

(288)   Yang, J.; Lee, J.; Kang, J.; Chung, C. H.; Lee, K.; Suh, J. S.; Yoon, H. G.; Huh, Y. M.; Haam, S. *Nanotechnology* **2008**, *19*.

(289)   Wang, D. S.; He, J. B.; Rosenzweig, N.; Rosenzweig, Z. *Nano Lett* **2004**, *4*, 409.

(290)   Aung, W.; Hasegawa, S.; Koshikawa-Yano, M.; Obata, T.; Ikehira, H.; Furukawa, T.; Aoki, I.; Saga, T. *Gene Ther* **2009**, *16*, 830.

(291)   Bardhan, R.; Chen, W. X.; Perez-Torres, C.; Bartels, M.; Huschka, R. M.; Zhao, L. L.; Morosan, E.; Pautler, R. G.; Joshi, A.; Halas, N. J. *Adv Funct Mater* **2009**, *19*, 3901.

(292)   Gallagher, J. J.; Tekoriute, R.; O'Reilly, J. A.; Kerskens, C.; Gun'ko, Y. K.; Lynch, M. *J Mater Chem* **2009**, *19*, 4081.

(293)   Ke, J. H.; Lin, J. J.; Carey, J. R.; Chen, J. S.; Chen, C. Y.; Wang, L. F. *Biomaterials* **2010**, *31*, 1707.

(294)   Shi, D. L.; Cho, H. S.; Chen, Y.; Xu, H.; Gu, H. C.; Lian, J.; Wang, W.; Liu, G. K.; Huth, C.; Wang, L. M.; Ewing, R. C.; Budko, S.; Pauletti, G. M.; Dong, Z. Y. *Adv Mater* **2009**, *21*, 2170.

(295)   Hu, J.; Xie, M.; Wen, C. Y.; Zhang, Z. L.; Xie, H. Y.; Liu, A. A.; Chen, Y. Y.; Zhou, S. M.; Pang, D. W. *Biomaterials* **2011**, *32*, 1177.

(296)   Ruan, G.; Vieira, G.; Henighan, T.; Chen, A. R.; Thakur, D.; Sooryakumar, R.; Winter, J. O. *Nano Lett* **2010**, *10*, 2220.

(297)   Kim, B. S.; Taton, T. A. *Langmuir* **2007**, *23*, 2198.

(298)   Zhang, B. B.; Chen, B. D.; Wang, Y. L.; Guo, F. F.; Li, Z. Q.; Shi, D. L. *J Colloid Interf Sci* **2012**, *372*, 261.

(299)   Zhang, B. B.; Chen, B. D.; Wang, Y. L.; Guo, F. F.; Li, Z. Q.; Shi, D. L. *J Colloid Interf Sci* **2011**, *353*, 426.

(300)   Wilson, R.; Spiller, D. G.; Prior, I. A.; Veltkamp, K. J.; Hutchinson, A. *Acs Nano* **2007**, *1*, 487.

(301)   Wang, G. N.; Gao, Y. A.; Huang, H.; Su, X. G. *Anal Bioanal Chem* **2010**, *398*, 805.

(302)   Ang, C. Y.; Giam, L.; Chan, Z. M.; Lin, A. W. H.; Gu, H.; Devlin, E.; Papoefthymiou, G. C.; Selvan, S. T.; Ying, J. Y. *Adv Mater* **2009**, *21*, 869.

(303)   McDaniel, H.; Shim, M. *Acs Nano* **2009**, *3*, 434.

(304)   Tao, K.; Zhou, H. R.; Dou, H. J.; Xing, B.; Li, W. W.; Sun, K. *J Phys Chem C* **2009**, *113*, 8762.

(305)   Lin, A. W. H.; Ang, C. Y.; Patra, P. K.; Han, Y.; Gu, H.; Le Breton, J. M.; Juraszek, J.; Chiron, H.; Papaefthymiou, G. C.; Selvan, S. T.; Ying, J. Y. *J Solid State Chem* **2011**, *184*, 2150.

(306)   Yavuz, C. T.; Mayo, J. T.; Yu, W. W.; Prakash, A.; Falkner, J. C.; Yean, S.; Cong, L. L.; Shipley, H. J.; Kan, A.; Tomson, M.; Natelson, D.; Colvin, V. L. *Science* **2006**, *314*, 964.

(307)   Mayo, J. T.; Lee, S. S.; Yavuz, C. T.; Yu, W. W.; Prakash, A.; Falkner, J. C.; Colvin, V. L. *Nanoscale* **2011**, *3*, 4560.

(308)   Mayo, J. T.; Yavuz, C.; Yean, S.; Cong, L.; Shipley, H.; Yu, W.; Falkner, J.; Kan, A.; Tomson, M.; Colvin, V. L. *Sci Technol Adv Mat* **2007**, *8*, 71.

(309)   Trindade, T.; O'Brien, P.; Pickett, N. L. *Chem Mater* **2001**, *13*, 3843.

(310)   Smith, A. M.; Duan, H. W.; Mohs, A. M.; Nie, S. M. *Adv Drug Deliver Rev* **2008**, *60*, 1226.

(311)   Murakami, K.; Chan, S. Y.; Routtenberg, A. *J Biol Chem* **1986**, *261*, 5424.